

DISSERTATION

**Toward a Precise Measurement of Weak Lensing Signals through CMB
Experiments and Galaxy Imaging Surveys:
A Theoretical Development and Its Cosmological Implications**

by

Toshiya Namikawa

submitted

in partial fulfillment of the requirements

for the degree of

Doctor of Philosophy in Science

The University of Tokyo

Tokyo, Japan

December 2012

© Copyright 2012 by Toshiya Namikawa
All right reserved.

Abstract

Numerous progress in cosmology in the last decade have successfully established a fundamental framework in cosmology. In the coming decade, based on our current knowledge of the universe, the cosmology should focus on more advanced and fundamental issues; what drove cosmic acceleration of the universe? how much does a neutrino weigh? is there evidence for new physics in the early Universe? One of the powerful probe to tackle these advanced issues is weak gravitational lensing; a deflection of photons emitted from, e.g., last scattering surface of CMB or galaxies.

In this thesis, we investigate what we can probe by measuring weak lensing signals of CMB and galaxy images, and how accurately the lensing signals can be measured. In general, the observables of weak lensing are decomposed into two quantities according to the parity symmetry. The even-parity mode is generated by scalar metric perturbations such as matter density fluctuations of the large-scale structure, and utilized in constraining properties of dark energy and massive neutrinos. In contrast, the odd-parity quantities are produced by the vector and tensor perturbations, but not by the scalar perturbations. Hence, any signals of odd-parity quantities on large angular scales would be a direct evidence for non-scalar metric perturbations such as the primordial gravitational waves and cosmic strings.

In the first main part of this thesis, we explore observational signatures of weak gravitational lensing, in the presence of scalar, vector and tensor perturbations. Solving the geodesic and geodesic deviation equations, we obtain explicit expressions for even and odd parity modes of cosmic shear and deflection angle. Then we derive the full-sky formulas for angular power spectra of lensing observables, i.e., even and odd parity quantities of deflection angle and shear of galaxy images. We find that, in the presence of tensor perturbations, there is a non-trivial relation between the deflection angle and cosmic shear.

Next we develop a method for measuring weak lensing of CMB on the full sky, in the presence of both even and odd parity quantities. We find that the gradient and curl modes can be reconstructed separately, thanks to the distinctive feature in the parity symmetry. The expected signal-to-noise ratio of the odd parity modes produced by the primordial gravitational-waves and a specific model of cosmic strings are estimated, and prospects for future observations of CMB and galaxies are discussed.

Finally, we explore how accurately CMB lensing can be measured. We present new methods for lensing reconstruction from CMB temperature fluctuations which are less sensitive than the standard estimators to several potential experimental systematics. These “bias-hardened” estimators are more reliable than the standard estimators when applied to realistic CMB observations, at a small cost of signal-to-noise. This method is quite useful in analysis of CMB lensing reconstruction for a cross-check on standard results, and could also be generalized to the case with polarization which is an important signal for lensing reconstruction in upcoming and next generation CMB experiments.

Contents

1	Introduction	2
2	Review of CMB Anisotropies and Weak Lensing	7
2.1	Background Evolution	7
2.1.1	Background evolution	7
2.1.2	Cosmological distances	9
2.2	Anisotropies of Cosmic Microwave Background	10
2.2.1	Intensity and Polarization of Photons	10
2.2.2	Measuring CMB fluctuations	12
2.2.3	CMB anisotropies	15
2.2.4	Angular power spectrum of temperature and polarization	16
2.3	Evolution of Gravitational Fields in the Universe	17
2.3.1	Evolution of scalar components	18
2.3.2	Evolution of vector perturbations	18
2.3.3	Evolution of tensor components	20
2.4	Weak Gravitational Lensing	20
2.4.1	Lensing effect on CMB	21
2.4.2	Lensing effect on galaxy images	28
3	Weak Lensing from Scalar, Vector and Tensor Perturbations	31
3.1	Lensing observables	31
3.1.1	Geodesic equation and deflection angle	31
3.1.2	Geodesic deviation equation and Jacobi mapping	36
3.2	Formulation of Angular Power Spectrum	39
3.2.1	Angular power spectrum of lensing potentials	39
3.2.2	Angular power spectrum of shear fields	41
4	Cosmological Implications from Weak Lensing	43
4.1	Cosmological information from CMB lensing and cosmic shear	43
4.2	Forecasts for Future CMB Experiments and Galaxy Imaging Surveys	45
4.2.1	Fisher Formalism	45
4.2.2	Forecast results	50
5	CMB Lensing Reconstruction for Gradient and Curl Modes	55
5.1	Estimating CMB lensing potentials	55
5.1.1	Formalism of standard optimal quadratic estimator	55
5.1.2	Lensing estimator in flat-sky	61
5.1.3	Maximum likelihood estimator	64

5.2	Estimating CMB lensing power spectrum	65
5.2.1	From lensing potentials to lensing power spectrum	65
5.2.2	Estimating bias terms from Monte Carlo simulation	68
6	An Improved Method For CMB Lensing Reconstruction	70
6.1	Formalism of Estimators	71
6.1.1	Conventional approach	71
6.1.2	Bias-reduced lensing estimator	73
6.1.3	Gaussian noise estimator	77
6.2	Numerical Tests	78
6.2.1	Filtering	78
6.2.2	Mean-field power spectrum	81
6.2.3	Power spectrum of lensing estimator	82
6.3	Application of Bias-Reduced Estimator to CMB data	84
6.3.1	Maps used for reconstruction and measured temperature angular power spectrum	84
6.3.2	Angular power spectra of lensing potentials	85
7	Summary and Conclusion	90
A	Evolution Equations for Fluctuations	93
A.1	Evolution Equations for Fluctuations	93
A.1.1	Scalar Perturbations	93
A.1.2	Vector Perturbations	95
A.1.3	Tensor Perturbations	97
B	Note for Weak Lensing from Scalar, Vector and Tensor Perturbations	99
B.1	Useful formulas for computing weak lensing effect	99
B.1.1	Properties of orthonormal space-like basis	99
B.1.2	Derivatives with orthonormal space-like basis	99
B.1.3	Perturbed optical tidal matrix	99
B.2	Derivation of angular power spectrum	100
B.2.1	E-/B-mode cosmic shear	100
B.2.2	Lensing potential and curl mode	103
B.2.3	Derivation of shear-deflection relation	103
C	Note for derivation of lensing estimator	105
C.1	Noise covariance	105
C.1.1	Relation between noise and estimator covariance	105
C.1.2	Estimator covariance	106
C.2	Flat-sky limit	108
D	Derivation of correlations of a cosmic string network	112
E	Conjugate Gradient Method for Inpainting	114
F	Mathematical Note	117
F.1	Kronecker product	117
F.2	Special Functions	117
F.2.1	Wigner- $3j$ symbols	117

F.2.2	Legendre Polynomials	118
F.2.3	Associated Legendre polynomials	118
F.2.4	Spin operators	119
F.2.5	Spherical harmonics	120
F.2.6	Bessel function	124
G	Numerical simulation of lensed CMB maps	126
G.1	<i>N</i> -body Simulations	126
G.2	Ray-tracing Simulations	126
G.3	Lensed CMB Temperature Map	128

Chapter 1

Introduction

Cosmological observations in the last decade have successfully led to the establishment of a fundamental framework in cosmology. In particular, the observations of cosmic microwave background radiation (CMB), type-Ia supernovae, and large scale structure revealed that the energy composition of the universe is well described by a flat Lambda Cold Dark Matter (Λ CDM) model (see e.g., [1, 2]). Taking seriously account of our current understanding and lack of our knowledge of the universe, cosmology in the coming decade should focus on more advanced and fundamental issues. Dark energy is introduced to explain the late-time acceleration of the universe, but the origin and nature of the dark energy are unknown and this is one of the fundamental issues in cosmology. In the standard model of particle physics, neutrinos are considered as massless particles, but neutrino oscillation experiments imply non-zero mass of neutrinos. The evolution of the large-scale structure depends on the mass of neutrinos, and a measurement of neutrino mass is important for both physics beyond standard model of particle physics and cosmology. We still do not have a complete picture about how the early stage of the universe looked like. Inflation is a successful phenomenological model to describe the early universe, but the physical description are still challenging. The answers to these questions are important, and would shed light on new physics beyond our current knowledge.

One of the powerful probes to address these fundamental issues is weak gravitational lensing; a deflection of photons emitted from, e.g., last scattering surface of CMB or galaxy, by gravitational field of large-scale structure. Weak lensing effect leads to distortions in spatial pattern of CMB anisotropies and the resultant CMB anisotropies exhibit weak non-Gaussianity. Observed galaxy images are also distorted by the weak lensing effect. In cosmology, weak gravitational lensing has several advantages compared to other cosmological probes. Although weak lensing effect has smaller signal-to-noise ratio compared to a measurement of galaxy clustering, it is induced by gravitational field itself and free from galaxy bias which may potentially affect the cosmological parameter estimation. Statistics of weak lensing is sensitive to evolution of both background geometry and density fluctuations, and is complementary to other cosmological probes.

In this thesis, we focus on what we can probe from the weak gravitational lensing of CMB and galaxies, for which we hereafter call CMB lensing and cosmic shear, respectively. The CMB lensing can be measured in two different techniques. One is to measure the CMB angular power spectrum and to look for a characteristic excess on small angular scales. From this method, combining Wilkinson Microwave Anisotropy Probe (WMAP) data, multiple high-resolution CMB observations, such as Arcminute Cosmology Bolometer Array Receiver (ACBAR) [3], Atacama Cosmology Telescope (ACT) [4], and South Pole Telescope (SPT) [5] have detected the lensing effect on CMB temperature angular power spectrum. The other method, usually referred to as the lensing reconstruction, is to map the deflection angle through the mode mixing of observed CMB anisotropies [6, 7, 8, 9, 10]. With lensing reconstruction, the cross-correlation with the density fluctuations of large scale structure is detected from the data set of WMAP combined with observations of large scale structure such as Sloan Digital Sky Survey (SDSS) and NRAO VLA Sky Survey (NVSS) [11, 12, 13, 14]. Recently, the auto-correlation of lensing potential is also detected from ACT with WMAP, and SPT with WMAP [15, 16]. In the upcoming and next-generation CMB experiments, such as PLANCK [17], PolarBear [18], SPTpol [19], ACTPol [20] and CMBPol [21] would detect the lensing effect with high

significance, and would provide us valuable cosmological information. The weak lensing effect on galaxy is estimated through measurements of ellipticity of each galaxy image. Measurements of cosmic shear have been reported from, e.g., Canada France Hawaii Telescope (CFHT) [22, 23, 24, 25], Hubble Space Telescope Cosmic Evolution Survey (COSMOS) [26], SDSS [27, 28] and Deep Lens Survey (DLS) [29]. With upcoming and future galaxy imaging surveys, e.g., Dark Energy Survey (DES), [30], SuMIRE Hyper Suprime Cam (HSC) [31] and Large Synoptic Legacy Survey (LSST) [32], cosmic shear would be a key probe of fundamental issues in cosmology.

In general, the observables of weak lensing are decomposed into two quantities by the parity symmetry. Since the deflection angle is a two dimensional vector field projected on unit sphere, the deflection angle has two degrees of freedom and decomposed into two components by parity; a gradient of scalar lensing potential and a rotation of pseudo-scalar lensing potential [33, 10, 34, 35]. Similarly, the spatial pattern of cosmic shear fields is generally described by a two-dimensional symmetric traceless field on the sky, and it can be decomposed into two parts; even-parity mode (E-mode shear) and odd-parity mode (B-mode shear) (e.g., [33, 36]).

Cosmological applications of the even-parity modes of weak lensing signals (i.e., scalar lensing potential and E-mode shear) have been widely discussed in the literature. Since the even-parity modes are generated by scalar metric perturbations through matter density fluctuations, we would constrain, e.g., properties of dark energy and massive neutrinos through a measurement of scalar lensing potential and E-mode shear. Recent several studies show that measurement of the lensing information from upcoming and next generation experiments of CMB and galaxies would constrain properties of dark energy, as stringently as those from other dark energy probes such as type-Ia supernovae, baryon acoustic oscillation, and cluster abundance (e.g., [37, 38, 39, 40]). Similarly, these observations would significantly improve the constraints on total mass of neutrinos (e.g., [41, 42, 43, 44]), and provide clues for physics beyond the standard model of particle physics.

The B-mode shear and the curl-mode deflection angle are produced by the vector and tensor perturbations, but not by the scalar perturbations. Hence, the non-vanishing B-mode or curl-mode signal especially on large angular scales would be a smoking gun of non-scalar metric perturbations. The weak lensing effect by the tensor perturbations has been previously studied in the cases of primordial gravitational waves (GWs) [45, 34, 46] and secondary GWs generated by the second-order primordial density perturbations [47], but the effect turns out to be very small and difficult to observe (see Refs. [48, 49]). However, several active sources such as cosmic strings, which may give clues about the mechanism of inflationary scenario at the early universe and implications for high-energy physics, are possible sources of vector and tensor metric perturbations even at late time of the universe. Note that, even in the absence of the vector and tensor sources, the higher-order density perturbations and foreground contaminations generate not only the even-parity quantities but also odd-parity quantities. These sources would act as systematic errors in the estimation of the even-parity mode. Thus, the evaluation of the contaminations of these sources in the odd-parity mode would be helpful to estimate the contributions of these sources in the even-parity mode.

Although a measurement of weak lensing from upcoming and future observations would be a powerful probe in cosmology, signal itself is primarily very small, and precise and accurate estimation of these signals is highly required. For CMB lensing reconstruction, we assume that the primordial CMB anisotropies are Gaussian, but there are several possible sources to generate mode coupling in the anisotropies such as mask of Galactic emission and point sources [50, 51], inhomogeneous noise, beam asymmetry [52], relative velocity of the Earth with respect to the rest frame of CMB [53] and patchy reionization [54, 55]. These contaminations potentially lead to significant bias on the estimation of lensing potentials and we should construct a method to mitigate these systematic biases for upcoming and future experiments. Similar practical issues are also problematic for measurements of cosmic shear. In the presence of mask, E and B mode shears are mixed each other and should be corrected for using, e.g., pseudo power spectrum method [56]. The intrinsic ellipticity and alignment of galaxies [57, 58, 59, 60], their correlation [61], inaccurate calibration of shear amplitude [62], anisotropy of point-spread function [63, 64] and uncertainties of photometric redshift error [65, 66, 67] are also sources of spurious biases in the estimation of cosmic shear. Moreover, there are theoretical issues in the estimation of cosmological parameters from cosmic shear measurement; although there are several theoretical developments (e.g., [68, 69, 70, 71, 72, 73]), it is still hard to give an accurate theoretical prediction for lensing observables including the effect of non-linear evolution of density fluctuations. For accurate

cosmology with future observations, methods for reducing all these biases are highly desirable.

In this thesis, we first derive the deflection angle and cosmic shear in the presence of scalar, vector and tensor perturbations, and formulate the angular power spectrum of these observables. We give expressions for both even and odd-parity modes of weak lensing signals in terms of the metric perturbations, and find that there is a non-trivial relation between deflection angle and cosmic shear in the presence of tensor perturbations.

To measure signatures of all components of metric perturbations on the lensing observables, we next develop a method for CMB lensing reconstruction in the presence of both gradient and curl modes of deflection angle. We show that the gradient and curl modes can be reconstructed separately, thanks to the distinctive feature in the parity symmetry between the gradient and curl modes. Based on our formalism, we also discuss the expected signal-to-noise ratio of the curl mode produced by the primordial gravitational-waves and a specific model of cosmic strings are estimated, and prospects for future observations.

Finally, to apply CMB data, we construct a method for CMB lensing reconstruction which has reduced sensitivity to bias from non-lensing sources compared to the current estimator. We also measure gradient and curl modes of deflection angle from publicly available CMB data, and discuss cosmological implications.

This thesis is organized as follows:

- **Chapter 2**

We briefly review fundamentals of cosmology in the framework of Λ CDM model. In particular, we focus on the generation of CMB anisotropies and weak gravitational lensing.

- **Chapter 3**

We give a formulation of weak gravitational lensing in the presence of scalar, vector and tensor metric perturbations, following our work [74]. Note that the details of our formulation is given in appendix B.

- **Chapter 4**

Based on Fisher formalism, we discuss expected constraints on massive neutrinos, GWs and cosmic strings with weak lensing observations, following our works [35, 74].

- **Chapter 5**

We present a method for CMB lensing reconstruction in the presence of both gradient and curl modes of deflection angle following our work [35]. A method to measure power spectrum of lensing potentials is also discussed.

- **Chapter 6**

We present new methods for lensing reconstruction from CMB temperature fluctuations which have smaller mean-field and reconstruction noise bias corrections than current lensing estimators, with minimal loss of signal-to-noise, according to our work [75].

- **Chapter 7**

This chapter is devoted to summary and conclusion.

Before closing this chapter, we summarize the notations used in this thesis. The basis vectors of the polar coordinate is defined as

$$e_\chi^i(\hat{\mathbf{n}}) = e_x^i \sin \theta \cos \varphi + e_y^i \sin \theta \sin \varphi + e_z^i \cos \theta, \quad (1.1)$$

$$e_\theta^i(\hat{\mathbf{n}}) = e_x^i \cos \theta \cos \varphi + e_y^i \cos \theta \sin \varphi - e_z^i \sin \theta, \quad (1.2)$$

$$e_\varphi^i(\hat{\mathbf{n}}) = -e_x^i \sin \theta \sin \varphi + e_y^i \sin \theta \cos \varphi, \quad (1.3)$$

where $\hat{\mathbf{n}} = (\theta, \varphi)$ is a position on the unit sphere.

Throughout this thesis, we assume that the background unperturbed metric is described by the isotropic and homogeneous metric:

$$a^2(\eta)\bar{g}_{\mu\nu}dx^\mu dx^\nu = a^2(\eta)[-d\eta^2 + \gamma_{ij}dx^i dx^j], \quad (1.4)$$

where a is the scale factor and η is the conformal time. The unperturbed three-dimensional spatial metric, γ_{ij} , is given by

$$\gamma_{ij}dx^i dx^j = \delta_{ij} + K \frac{x^i x^j}{1 - Kr^2} dx^i dx^j = \frac{dr^2}{1 - Kr^2} + r^2 \omega_{ab} d\theta_a d\theta_b. \quad (1.5)$$

Here, K is the curvature and

$$\omega_{ab} d\theta_a d\theta_b = d\theta^2 + \sin^2 \theta d\varphi^2, \quad (1.6)$$

is the metric on the sphere. The metric perturbations are expressed as a sum of unperturbed and perturbed metrics, $\bar{g}_{\mu\nu}$ and $h_{\mu\nu}$, as

$$ds^2 = a^2(\eta)g_{\mu\nu}dx^\mu dx^\nu = a^2(\eta)[\bar{g}_{\mu\nu} + h_{\mu\nu}]dx^\mu dx^\nu, \quad (1.7)$$

where $h_{\mu\nu}$ is the metric perturbations. We use the conformal Newtonian gauge in which the metric perturbations are decomposed into

$$h_{00} = -2\Phi, \quad (1.8)$$

$$h_{0i} = -\sigma_i, \quad (1.9)$$

$$h_{ij} = 2\Psi\gamma_{ij} + 2D_{ij}, \quad (1.10)$$

where Φ and Ψ are the scalar components, σ_i is the vector component ($\sigma_{i|i} = 0$), and D_{ij} is the tensor component ($D_{ij|i} = 0$, and $D_{ii} = 0$) of the metric perturbations. The bar ($\bar{|}$) denotes the covariant derivative with respect to the three dimensional metric.

In this thesis, Fourier modes of scalar, vector, and tensor perturbations are given by [76] (see also appendix A):

$$\Psi(\mathbf{x}, \eta) = \int \frac{d^3 k}{(2\pi)^3} \Psi(\mathbf{k}, \eta) Q^{(0)}(\mathbf{k}, x), \quad (1.11)$$

$$\Phi(\mathbf{x}, \eta) = \int \frac{d^3 k}{(2\pi)^3} \Phi(\mathbf{k}, \eta) Q^{(0)}(\mathbf{k}, x), \quad (1.12)$$

$$\sigma_i(\mathbf{x}, \eta) = \int \frac{d^3 k}{(2\pi)^3} \sum_{m=\pm 1} \sigma^{(m)}(\mathbf{k}, \eta) Q_i^{(m)}(\mathbf{k}, x), \quad (1.13)$$

$$D_{ij}(\mathbf{x}, \eta) = \int \frac{d^3 k}{(2\pi)^3} \sum_{m=\pm 2} D^{(m)}(\mathbf{k}, \eta) Q_{ij}^{(m)}(\mathbf{k}, x). \quad (1.14)$$

Finally, throughout this thesis, we calculate the power spectra for a fiducial set of cosmological parameters in Table 1.1, i.e., the density parameter of baryon $\Omega_b h^2$, of matter $\Omega_m h^2$, dark energy density Ω_Λ , scalar spectral index n_s , and scalar amplitude A_s at $k = 0.002 \text{ Mpc}^{-1}$, reionization optical depth τ , total neutrino mass $\sum m_\nu$, dark energy equation-of-state parameters, w_0 and w_a , with the functional form of $w(a) = w_0 + w_a(1 - a)$, and the tensor-to-scalar ratio, r .

$\Omega_b h^2$	$\Omega_m h^2$	Ω_Λ	n_s	$A_s \times 10^9$	τ	$\sum m_\nu$	w_0	w_a	r
0.022	0.13	0.72	0.96	2.4	0.086	0.1 eV	-1.0	0.0	0.1

Table 1.1: Fiducial values of cosmological parameters used in this thesis. These values are favored or consistent with the WMAP results [77]. We assume the flat Λ CDM model with three massive neutrinos.

Chapter 2

Review of CMB Anisotropies and Weak Lensing

From many observations including CMB and large-scale structure (LSS), the universe seems to be homogeneous and isotropic, at least, on scales larger than several hundreds Mpc [78]. Therefore, the cosmological principle may be validated and the background metric is well described by the Friedman-Lemaître-Robertson-Walker (FLRW) metric.

In this chapter, we first briefly review the background evolution in the homogeneous-isotropic universe in Sec. 2.1. Then based on the homogeneous-isotropic background we summarize the generation of CMB anisotropies in Sec. 2.2. In Sec. 2.3 the evolution of fluctuations at linear order is discussed, particularly focusing on the evolution of gravitation fields for discussion of weak lensing effect given in Sec. 2.4.

2.1 Background Evolution

2.1.1 Background evolution

From the Einstein equation, in the absence of fluctuations, the energy-momentum tensor should be the following form:

$$\bar{T}^{\mu}_{\nu} = \begin{pmatrix} \bar{\rho} & 0 & 0 & 0 \\ 0 & -\bar{p} & 0 & 0 \\ 0 & 0 & -\bar{p} & 0 \\ 0 & 0 & 0 & -\bar{p} \end{pmatrix}. \quad (2.1)$$

This implies that the Universe is filled with a perfect fluid with an energy density, $\bar{\rho}$, and pressure, \bar{p} . The Einstein equation without any fluctuations leads to

$$H^2 + \frac{K}{a^2} = \frac{8\pi G}{3}\rho + \frac{\Lambda}{3}, \quad (2.2)$$

$$\frac{d\rho}{dt} + 3H(\rho + p) = 0, \quad (2.3)$$

where $H = a\mathcal{H} = a'$ is the cosmic expansion rate and Λ is the cosmological constant. Eq. (2.2) is usually referred to as the Friedman equation while Eq. (2.3) is the continuity equation in the expanding universe.

In the Λ CDM model, the energy density in Eq. (2.2) is given by a sum of the energy densities of photons, ρ_γ , neutrinos, ρ_ν , baryons, ρ_b , and CDM, ρ_C . Then, Eq. (2.2) becomes

$$H^2 + \frac{K}{a^2} = \frac{8\pi G}{3}(\rho_\gamma + \rho_\nu + \rho_b + \rho_C + \rho_\Lambda), \quad (2.4)$$

where $\rho_\Lambda \equiv \Lambda/8\pi G$. Eq. (2.2) at $\eta = \eta_0$ is rewritten as

$$1 = \Omega_\gamma + \Omega_\nu + \Omega_b + \Omega_C + \Omega_\Lambda + \Omega_K. \quad (2.5)$$

Here, using the present value of the energy density, $\rho_{i,0}$, we define

$$\Omega_i \equiv \frac{8\pi G \rho_{i,0}}{3H_0^2}, \quad (i = b, C, \gamma, \nu) \quad (2.6)$$

We also use $\Omega_K = -K/H_0^2$ with H_0 being the expansion rate today. A dimensionless parameter $h = H_0/100\text{Mpc}$ is also frequently used in several context. Hereafter, we denote the matter component as the sum of the baryon and CDM, and define the energy density of the matter components as

$$\rho_m \equiv \rho_b + \rho_C, \quad (2.7)$$

$$\Omega_m \equiv \frac{8\pi G \rho_{m,0}}{3H_0^2} = \Omega_b + \Omega_C, \quad (2.8)$$

where $\rho_{m,0}$ is the present value of ρ_m . If the neutrino masses are included, the above quantities have additional contributions from non-relativistic neutrinos which are typically important after $a \simeq 10^{-2}$. Similarly, the radiation component is the sum of photons and neutrinos:

$$\rho_r \equiv \rho_\gamma + \rho_\nu, \quad (2.9)$$

$$\Omega_r \equiv \frac{8\pi G \rho_{r,0}}{3H_0^2} = \Omega_\gamma + \Omega_\nu, \quad (2.10)$$

where $\rho_{r,0}$ is the present value of ρ_r .

We consider the universe which is dominated by one component whose equation-of-state is expressed as $p = w\rho$, with the quantity, w , denoting the the equation-of-state parameter. If $w \neq -1$, the evolution of energy density and scale factor are given by

$$\rho \propto \frac{1}{a^{3(1+w)}} \propto \frac{1}{t^2}, \quad (2.11)$$

$$a \propto t^{2/(3+3w)}, \quad (2.12)$$

where we use Eqs. (2.2) and (2.3). If $w = -1$, the energy density, ρ , is constant, and then the scale factor, a , increases exponentially. For relativistic particles where the energy density from the rest mass is negligible compared to the kinetic energy, the equation-of-state parameter is $w = 1/3$. In this case, the energy density decreases as $\rho \propto 1/a^4$ where $a \propto t^{1/2}$. On the other hand, for non-relativistic particles, the kinetic energy is negligible compared to the energy of the rest mass, and $w = 0$. Then, we obtain $\rho \propto 1/a^3$ and $a \propto t^{2/3}$. From the above discussions, the expansion rate is written as

$$H = \begin{cases} \frac{1}{t} & \text{if } w \neq -1 \\ \text{const.} & \text{if } w = -1 \end{cases}. \quad (2.13)$$

Finally, let us compute the range of w in which the universe expands with acceleration. Considering the energy component whose energy density is ρ_Λ and pressure is p_Λ , these two values should satisfy

$$\frac{1}{a} \frac{d^2a}{dt^2} = -\frac{4\pi G}{3}(3p_\Lambda + \rho_\Lambda) > 0, \quad (2.14)$$

where we use Eqs. (2.2) and (2.3). This leads to $w < -1/3$.

2.1.2 Cosmological distances

Comoving distance

The comoving distance is defined as the distance between observer and an object along a path defined by an observer at $\eta = \eta_0$, i.e.,

$$\chi = \int_0^r \frac{dr}{\sqrt{1 - Kr^2}} . \quad (2.15)$$

With the redshift, $z \equiv 1/a - 1$, the comoving distance is rewritten as

$$\chi = \int_\eta^{\eta_0} d\eta = \int_0^z \frac{dz}{H(z)} . \quad (2.16)$$

The radial coordinate, r , is related to the comoving distance, χ , through Eq. (2.15). Calculating the integral in Eq. (2.15), we obtain

$$r = S_K(\chi) \equiv \frac{1}{\sqrt{-K}} \sinh(\sqrt{-K}\chi) . \quad (2.17)$$

From Eq. (2.16), the radial coordinate is related to the redshift as

$$r = S_K \left(\int_0^z \frac{dz}{H(z)} \right) . \quad (2.18)$$

Luminosity distance

Once luminosity of an object is given, a distance to that object is measured by comparing an observed luminosity. To see this, we consider an luminous object at redshift z which emits photons with total energy per time is L_t . If these photons are emitted isotropically, the observed energy flux is given by

$$L_{\text{flux}} = \frac{L_t}{4\pi r^2} , \quad (2.19)$$

where r is the distance to the object. This relation is valid for Euclidian space, however, this equation is modified in the expanding universe.

Let us consider photons of wavelength, λ , emitted at time t , with energy $E(\lambda)$. In the coordinate system whose center is the object, the number of photons, $N(\lambda)$, emitted during a time interval, Δt , decreases by $1/4\pi r^2$. Thus, the photon flux in unit of area, observed between a time interval of $\Delta t'$ at an observer, is

$$N_{\text{flux}}(\lambda')\Delta t'\Delta\lambda' = \frac{N(\lambda)}{4\pi r^2} \Delta t \Delta\lambda . \quad (2.20)$$

Using $\lambda' = (1+z)\lambda$ and $\Delta t' = (1+z)\Delta t$, the above relation is rewritten as

$$N_{\text{flux}}(\lambda')\Delta t'\Delta\lambda' = \frac{N(\lambda'/(1+z))}{4\pi r^2} \frac{\Delta t'}{1+z} \frac{\Delta\lambda'}{1+z} . \quad (2.21)$$

Since the photon number, $N(\lambda)$, is proportional to $\frac{E(\lambda)}{2\pi/\lambda}$, the energy flux at wavelength, $\lambda' = (1+z)\lambda$, is given by

$$E_{\text{flux}}(\lambda') = \frac{1}{4\pi r^2} \frac{E(\lambda'/(1+z))}{(1+z)^3} . \quad (2.22)$$

Integrating in terms of λ' , we obtain

$$L_{\text{flux}} = \frac{L_t}{4\pi r^2(1+z)^2} . \quad (2.23)$$

Using the luminosity distance, $d_L \equiv r(1+z)$, Eq. (2.23) becomes

$$L_{\text{flux}} = \frac{L_t}{4\pi d_L^2} . \quad (2.24)$$

Angular diameter distance

Let us consider two points, A and B, at redshift z , and these two points are separate with

$$\ell = \int_A^B ar d\theta = \frac{r}{1+z} \Delta\theta; \quad \Delta\theta \equiv \int_A^B d\theta. \quad (2.25)$$

The angular diameter distance, d_A , is defined as

$$d_A \equiv \frac{\ell}{\Delta\theta} = \frac{r}{1+z}. \quad (2.26)$$

Using cosmological parameters, the above equation is rewritten as

$$d_A = \frac{1}{(1+z)H_0\sqrt{\Omega_K}} \sinh\left(\sqrt{\Omega_K} \int_0^z \frac{dz}{H(z)}\right). \quad (2.27)$$

The relation between d_A and d_L , which is usually referred to as the duality relation, is

$$d_A = \frac{d_L}{(1+z)^2}. \quad (2.28)$$

2.2 Anisotropies of Cosmic Microwave Background

The cosmic microwave background (CMB) is the most distant source of photons that we can observe. At an early stage of the universe, photons and electrons are tightly coupled by Thomson scattering. Around redshift $z \sim 1100$, these two components are decoupled, and then photons can move freely through the universe without scattering by electrons. These photons are observed today as CMB. The CMB temperature and polarization have fruitful information on not only the early stage of the universe but also the late-time evolution of the universe. Until now, measurements of CMB have successfully revealed many aspects of the universe. In this section, we briefly summarize the fundamentals of CMB fluctuations, following Refs. [79, 2]. Note that the full evolution equations are summarized in appendix A.1 following Ref. [76].

2.2.1 Intensity and Polarization of Photons

Stokes parameters

Here we introduce the Stokes parameter to express the intensity and polarization of CMB photons. We choose a coordinate system so that one of three basis vectors corresponds to a radial vector, e_r , and the other two basis vectors, e_1 and e_2 , are chosen so as to perpendicular to e_r . Considering CMB photons coming from $\hat{n} = e_r$, the electromagnetic field of CMB photons observed with a mean frequency ν_0 is expressed by a sum of plane waves with frequency, ν :

$$\mathcal{E}(\nu, \hat{n}) = \mathcal{E}_1(\nu, \hat{n})e_1 + \mathcal{E}_2(\nu, \hat{n})e_2, \quad (2.29)$$

where, with $a = 1, 2$,

$$\mathcal{E}_a(\nu, \hat{n}) = A_a(\nu, \hat{n}) \exp[-2\pi i\nu t + i\alpha_a(\nu, \hat{n})], \quad (2.30)$$

and A_a and α_a are the amplitude and phase of a -th component, respectively. Averaging over frequency, we define the intensity matrix of the CMB photons with

$$\begin{aligned} \mathbf{J}(\hat{n}) &\equiv \langle \mathcal{E}(\nu, \hat{n}) \otimes \mathcal{E}^*(\nu, \hat{n}) \rangle_\nu \\ &= \frac{1}{2} \left[I(\hat{n})(e_1 \otimes e_1 + e_2 \otimes e_2) + Q(\hat{n})(e_1 \otimes e_1 - e_2 \otimes e_2) \right. \\ &\quad \left. + U(\hat{n})(e_1 \otimes e_2 + e_2 \otimes e_1) + iV(\hat{n})(e_1 \otimes e_2 - e_2 \otimes e_1) \right], \end{aligned} \quad (2.31)$$

where I , Q , U and V are the Stokes parameters, and the operator, $\langle \cdot \cdot \cdot \rangle_\nu$, means the average over frequency. From the above definition, the Stokes parameters are related to the electro-magnetic field as

$$I(\hat{\mathbf{n}}) = \langle A_1^2(\nu, \hat{\mathbf{n}}) + A_2^2(\nu, \hat{\mathbf{n}}) \rangle_\nu, \quad (2.32)$$

$$Q(\hat{\mathbf{n}}) = \langle A_1^2(\nu, \hat{\mathbf{n}}) - A_2^2(\nu, \hat{\mathbf{n}}) \rangle_\nu, \quad (2.33)$$

$$U(\hat{\mathbf{n}}) = \langle 2A_1(\nu, \hat{\mathbf{n}})A_2(\nu, \hat{\mathbf{n}}) \cos[\alpha_1(\nu, \hat{\mathbf{n}}) - \alpha_2(\nu, \hat{\mathbf{n}})] \rangle_\nu, \quad (2.34)$$

$$V(\hat{\mathbf{n}}) = \langle -2A_1(\nu, \hat{\mathbf{n}})A_2(\nu, \hat{\mathbf{n}}) \sin[\alpha_1(\nu, \hat{\mathbf{n}}) - \alpha_2(\nu, \hat{\mathbf{n}})] \rangle_\nu. \quad (2.35)$$

For linearly polarized photons, the relationship between the phases of $a = 1$ and 2 components is $\alpha_1 - \alpha_2 = m\pi$ with $m = 0, \pm 1, \pm 2$, and thus $V = 0$. On the other hand, for circularly polarized photons, we have $\alpha_1 - \alpha_2 = 2m\pi \pm \pi/2$ and $A_1 = A_2$, so $Q = U = 0$. This implies that the quantity, Q and U , are associated with the linearly polarized photon, and V is non-zero when the photon is circularly polarized.

Spin

To generalize the definition of intensity matrix given in Eq. (2.31) for arbitrary observers with another set of basis vectors, we have to take into account the spin property of the Stokes parameters under the rotation of a coordinate system. We first rewrite the intensity matrix as

$$\begin{aligned} \mathbf{J}(\hat{\mathbf{n}}) &= \frac{1}{2} \left[I(\hat{\mathbf{n}})(\mathbf{e}_+ \otimes \mathbf{e}_- + \mathbf{e}_- \otimes \mathbf{e}_+) + Q(\hat{\mathbf{n}})(\mathbf{e}_+ \otimes \mathbf{e}_+ + \mathbf{e}_- \otimes \mathbf{e}_-) \right. \\ &\quad \left. - iU(\hat{\mathbf{n}})(\mathbf{e}_+ \otimes \mathbf{e}_+ - \mathbf{e}_- \otimes \mathbf{e}_-) + V(\hat{\mathbf{n}})(\mathbf{e}_+ \otimes \mathbf{e}_- - \mathbf{e}_+ \otimes \mathbf{e}_-) \right] \\ &= \frac{1}{2} \left[I(\hat{\mathbf{n}})(\mathbf{e}_+ \otimes \mathbf{e}_- + \mathbf{e}_- \otimes \mathbf{e}_+) + V(\hat{\mathbf{n}})(\mathbf{e}_+ \otimes \mathbf{e}_- - \mathbf{e}_+ \otimes \mathbf{e}_-) \right. \\ &\quad \left. + [Q(\hat{\mathbf{n}}) + iU(\hat{\mathbf{n}})]\mathbf{e}_+ \otimes \mathbf{e}_+ + [Q(\hat{\mathbf{n}}) - iU(\hat{\mathbf{n}})]\mathbf{e}_- \otimes \mathbf{e}_- \right], \end{aligned} \quad (2.36)$$

where we introduce the polarization vectors:

$$\mathbf{e}_\pm \equiv \mathbf{e}_1 \pm i\mathbf{e}_2. \quad (2.37)$$

Now we consider an observer who uses a different coordinate system, \mathbf{e}'_r , \mathbf{e}'_1 and \mathbf{e}'_2 , and measures the same CMB photons discussed above. The relation between the two coordinate systems, $(\mathbf{e}_r, \mathbf{e}_1, \mathbf{e}_2)$, and $(\mathbf{e}'_r, \mathbf{e}'_1, \mathbf{e}'_2)$ is obtained by, first, rotating the primed coordinate system with a rotation matrix, \mathbf{R} , so that $\mathbf{e}_r = \mathbf{R}\mathbf{e}'_r$, and then rotating the system around the axis, \mathbf{e}_r , by an angle, ψ , so that

$$\mathbf{e}_1 = \mathbf{R}\mathbf{e}'_1 \cos \psi + \mathbf{R}\mathbf{e}'_2 \sin \psi, \quad (2.38)$$

$$\mathbf{e}_2 = -\mathbf{R}\mathbf{e}'_1 \sin \psi + \mathbf{R}\mathbf{e}'_2 \cos \psi. \quad (2.39)$$

Then, the polarization vectors defined in the two coordinate systems are related as

$$\mathbf{e}_\pm = e^{\pm i\psi} \mathbf{R}\mathbf{e}'_\pm, \quad (2.40)$$

Note that the intensity matrix, which is a Kronecker product of three-dimensional vector, is transformed as

$$\mathbf{J}(\hat{\mathbf{n}}) = \mathbf{R}\mathbf{J}'(\hat{\mathbf{n}})\mathbf{R}^t. \quad (2.41)$$

With Eqs. (2.40) and (2.41), the Stokes parameters in the different two coordinate systems are related as

$$I(\hat{\mathbf{n}}) = I'(\hat{\mathbf{n}}), \quad (2.42)$$

$$[Q \pm iU](\hat{\mathbf{n}}) = e^{\pm 2i\psi} [Q' \pm iU'](\hat{\mathbf{n}}), \quad (2.43)$$

$$V(\hat{\mathbf{n}}) = V'(\hat{\mathbf{n}}). \quad (2.44)$$

The above means that the polarization parameters, $Q \pm iU$, are transformed as a spin-2 quantity.

2.2.2 Measuring CMB fluctuations

Fluctuations of CMB

We assume that the CMB photons are unpolarized if averaged over directions, $\hat{\mathbf{n}}$. Thus, the Stokes parameters, $[Q \pm iU](\hat{\mathbf{n}})$ and $V(\hat{\mathbf{n}})$, averaged over $\hat{\mathbf{n}}$ vanishes, and the averaged intensity matrix is given by

$$\bar{\mathbf{J}} = \frac{\bar{I}}{2} (\mathbf{e}_+ \otimes \mathbf{e}_- + \mathbf{e}_- \otimes \mathbf{e}_+) , \quad (2.45)$$

Then, the fluctuations of intensity matrix are defined as

$$\begin{aligned} \delta \mathbf{J}(\hat{\mathbf{n}}) &\equiv \frac{\mathbf{J}(\hat{\mathbf{n}}) - \bar{\mathbf{J}}}{\bar{I}} \\ &= 2 \left[\Theta(\hat{\mathbf{n}}) (\mathbf{e}_+ \otimes \mathbf{e}_- + \mathbf{e}_- \otimes \mathbf{e}_+) + \Upsilon(\hat{\mathbf{n}}) (\mathbf{e}_+ \otimes \mathbf{e}_- - \mathbf{e}_- \otimes \mathbf{e}_-) \right. \\ &\quad \left. + \Pi^+(\hat{\mathbf{n}}) \mathbf{e}_+ \otimes \mathbf{e}_+ + \Pi^-(\hat{\mathbf{n}}) \mathbf{e}_- \otimes \mathbf{e}_- \right], \end{aligned} \quad (2.46)$$

where we define the fluctuations as

$$\Theta(\hat{\mathbf{n}}) = \frac{I(\hat{\mathbf{n}}) - \bar{I}}{4\bar{I}}, \quad (2.47)$$

$$\Pi^\pm(\hat{\mathbf{n}}) = \frac{Q(\hat{\mathbf{n}}) \pm iU(\hat{\mathbf{n}})}{4\bar{I}}, \quad (2.48)$$

$$\Upsilon(\hat{\mathbf{n}}) = \frac{V(\hat{\mathbf{n}})}{4\bar{I}}. \quad (2.49)$$

Note that, since the intensity, I , is proportional to the fourth power of the temperature, T^4 , for a black-body radiation, the fluctuations of the intensity equals to four times the temperature fluctuations, 4Θ . Hereafter, we ignore the circular polarization, Υ , since there are no natural mechanism for generating observable circular polarization.

Fourier Transform of Temperature Anisotropies

To analyze the CMB fluctuations, we usually use the Fourier transform of the temperature and polarization fluctuations.

First we consider the observation of CMB temperature fluctuations, $\Theta(\hat{\mathbf{n}})$. If we observe fluctuations within a narrow region of the sky, i.e., the fluctuations can be approximately defined on a two-dimensional plane (hereafter this approximation is called as the flat-sky approximation), the observed fluctuations are transformed into the Fourier space with the plane wave basis. Considering a polar coordinate $\hat{\mathbf{n}} = \mathbf{e}_1 \theta \cos \psi + \mathbf{e}_2 \theta \sin \psi$, the Fourier transform of the CMB temperature fluctuations is defined as

$$\Theta_\ell = \int d^2 \hat{\mathbf{n}} e^{-i\hat{\mathbf{n}} \cdot \ell} \Theta(\hat{\mathbf{n}}), \quad (2.50)$$

where, with the basis vectors in Fourier space, \mathbf{e}'_1 and \mathbf{e}'_2 , the two-dimensional vector, ℓ , is given by $\ell = \mathbf{e}'_1 \ell \cos \varphi_\ell + \mathbf{e}'_2 \ell \sin \varphi_\ell$. The inverse of the Fourier transform is defined by

$$\Theta(\hat{\mathbf{n}}) = \int \frac{d^2 \hat{\mathbf{n}}}{(2\pi)^2} e^{i\hat{\mathbf{n}} \cdot \ell} \Theta_\ell, \quad (2.51)$$

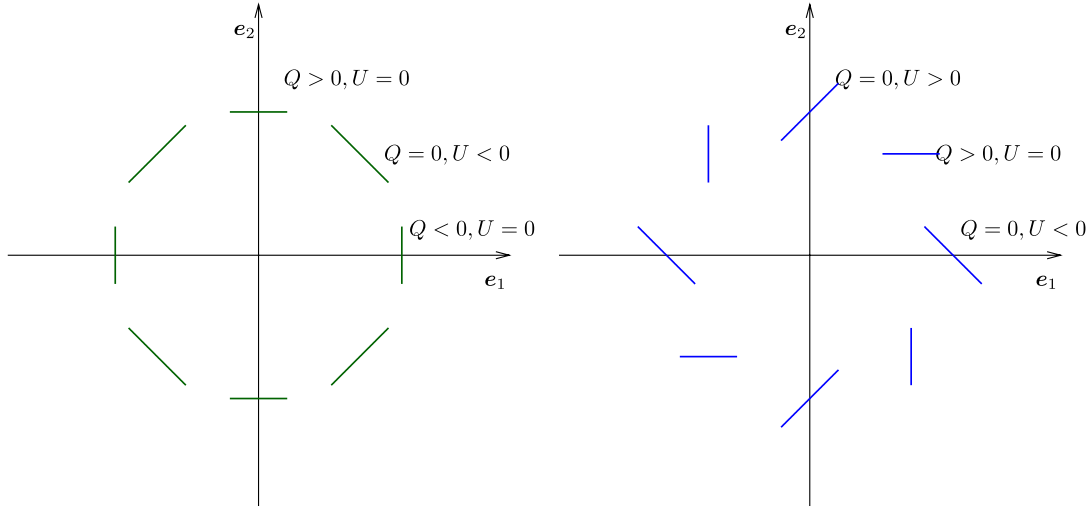


Figure 2.1: Examples of spatial pattern of E- and B-mode polarizations. The lines express the vector of the electro-magnetic fields at each position, $\mathcal{E}(\hat{n})$. In the left panel, the electro-magnetic fields are given by $\mathcal{E}_1 = \cos(\varphi - \pi/2)$ and $\mathcal{E}_2 = \sin(\varphi - \pi/2)$, where φ is the angle measured from the axis, e_1 , with counterclockwise. On the other hand, in the right panel, the electro-magnetic fields are expressed as $\mathcal{E}_1 = \cos(\varphi - \pi/4)$ and $\mathcal{E}_2 = \sin(\varphi - \pi/4)$. The resultant Stokes parameters, Q and U , are also shown.

Then, the expressions of the delta function in real and Fourier space, $\delta(\hat{n})$ and δ_ℓ , associated with the above Fourier basis are given by

$$\delta(\hat{n}) = \int \frac{d^2\hat{n}}{(2\pi)^2} e^{i\hat{n}\cdot\ell}, \quad (2.52)$$

$$\delta_\ell = \int d^2\hat{n} e^{-i\hat{n}\cdot\ell}. \quad (2.53)$$

On the other hand, if we take into account the sky curvature of the sphere (hereafter this case is denoted as full sky), the observed temperature anisotropies in a direction \hat{n} are expanded with the spherical harmonics $Y_{\ell m}(\hat{n})$ as

$$\Theta_{\ell m} = \int d\hat{n} \Theta(\hat{n}) Y_{\ell m}^*(\hat{n}). \quad (2.54)$$

Note that the inverse of this expansion is given by

$$\Theta(\hat{n}) = \sum_\ell \sum_{m=-\ell}^\ell \Theta_{\ell m} Y_{\ell m}(\hat{n}). \quad (2.55)$$

Fourier Transform of Polarization Anisotropies and E/B Decomposition

For the polarization anisotropies, the Fourier transforms of Q and U are not convenient in analyzing CMB fluctuations because these parameters are coordinate dependent. Alternatively, we usually use the parity even and odd modes of the polarization fluctuations, E and B , defined as

$$E_\ell \pm iB_\ell = - \int d^2\hat{n} e^{-i\hat{n}\cdot\ell} e^{\pm 2i(\varphi - \varphi_\ell)} \Pi^\pm(\hat{n}), \quad (2.56)$$

in the flat-sky approximation, and, with the spin-2 spherical harmonics, $\pm_2 Y_{\ell m}(\hat{\mathbf{n}})$,

$$E_{\ell m} \pm iB_{\ell m} = \int d\hat{\mathbf{n}} (Y_{\ell m}^{\pm 2})^*(\hat{\mathbf{n}}) \Pi^{\pm}(\hat{\mathbf{n}}). \quad (2.57)$$

for full sky case. The even and odd parity modes are called E and B mode polarizations, respectively.

In Fig. 2.1, to see whether the above quantities represent the even and odd parity modes of the polarization pattern, we show an example polarization pattern of even and odd parity modes. In the left panel, the electro-magnetic fields which is expressed as solid lines are given by $\mathcal{E}_1 = \cos(\varphi - \pi/2)$ and $\mathcal{E}_2 = \sin(\varphi - \pi/2)$, where ϖ is the angle measured from the axis, e_1 , with counterclockwise. On the other hand, in the right panel, the electro-magnetic fields are expressed as $\mathcal{E}_1 = \cos(\varphi - \pi/4)$ and $\mathcal{E}_2 = \sin(\varphi - \pi/4)$. From the definition of Q and U given in Eq. (2.35), we obtain

$$Q(\varphi) = \mathcal{E}_1^2(\varphi) - \mathcal{E}_2^2(\varphi) = \cos(2\varphi - \pi), \quad (2.58)$$

$$U(\varphi) = 2\mathcal{E}_1(\varphi)\mathcal{E}_2(\varphi) = \sin(2\varphi - \pi), \quad (2.59)$$

for the left panel, and

$$Q(\varphi) = \cos(2\varphi - \pi/2), \quad (2.60)$$

$$U(\varphi) = \sin(2\varphi - \pi/2), \quad (2.61)$$

for the right panel. According to Eq. (2.56) we obtain

$$E_{\ell} \pm iB_{\ell} = - \int d^2\hat{\mathbf{n}} e^{-i\hat{\mathbf{n}} \cdot \ell} e^{\mp 2i\varphi} e^{\pm i(2\varphi - \pi)} = \delta_{\ell}, \quad (2.62)$$

for the even parity mode (left panel) and

$$E_{\ell} \pm iB_{\ell} = - \int d^2\hat{\mathbf{n}} e^{-i\hat{\mathbf{n}} \cdot \ell} e^{\mp 2i\varphi} e^{\pm i(2\varphi - \pi/2)} = \pm i\delta_{\ell}, \quad (2.63)$$

for the odd parity mode (right panel). Thus the quantities, E and B , represent the even and odd parity patterns of polarization.

Angular power spectrum

In analyzing the statistical property of temperature and polarization fluctuations, the angular power spectrum is widely used. For $X, Y = \Theta_{\ell m}, E_{\ell m}$ and $B_{\ell m}$, we define the angular power spectrum, C_{ℓ}^{XY} , as

$$\langle X_{\ell m} Y_{\ell' m'}^* \rangle = \delta_{\ell\ell'} \delta_{mm'} C_{\ell}^{XY}, \quad (2.64)$$

where $\langle \dots \rangle$ means the statistical ensemble average. Similarly, we define the angular power spectrum in the flat-sky approximation as

$$\langle X_{\ell} Y_{\ell'}^* \rangle = \delta_{\ell\ell'} C_{|\ell|}^{XY}. \quad (2.65)$$

Since the B -mode anisotropies have odd parity, if the universe conserves the parity, the angular power spectra, $C_{\ell}^{\Theta B}$ and C_{ℓ}^{EB} , vanish.

Relation between full and flat sky fluctuations

Eqs. (2.51) and (2.56) imply that the Fourier modes, Z_ℓ ($= \Theta_\ell, E_\ell$ and B_ℓ), are related to the harmonic coefficients, $Z_{\ell m}$ ($= \Theta_{\ell m}, E_{\ell m}$ and $B_{\ell m}$), through the following equations for $\ell \gg 1$ [80]:

$$Z_\ell = \sqrt{\frac{4\pi}{2\ell+1}} \sum_m i^{-m} Z_{\ell m} e^{im\varphi_\ell}, \quad (2.66)$$

$$Z_{\ell m} = \sqrt{\frac{2\ell+1}{4\pi}} i^m \int \frac{d\varphi_\ell}{2\pi} e^{-im\varphi_\ell} Z_\ell. \quad (2.67)$$

From the above relations the angular power spectrum in the full and flat-sky case satisfy

$$C_\ell^{XY} = C_{|\ell|}^{XY}. \quad (2.68)$$

2.2.3 CMB anisotropies

Here we summarize the signatures imprinted on the CMB anisotropies.

Oscillation in the baryon-photon fluid

Before the last scattering baryons and photons interact each other by Thomson scattering. This leads to an oscillation in the baryon-photon plasma. The pattern of the oscillation is imprinted in the CMB fluctuations we observe.

Silk damping

At $\ell \gtrsim 1000$ the amplitude of temperature anisotropies are exponentially decreased. This is because at such scales the tight coupling between baryons and photons is broken and the difference of velocities between photons and baryons induces the energy and momentum exchange between these components. It leads to the heat conduction and viscosity in the photon-baryon fluid. This effect is usually referred to as Silk damping.

Generation of CMB polarizations

E-mode polarizations are generated by the quadrupole moment of temperature fluctuations through Thomson scattering. As long as the tight-coupling approximation is valid, however, the quadrupole moment of temperature fluctuations is negligible compared to the monopole and dipole, and thus polarizations. To generate the polarizations the time scale of Thomson scattering $\eta_T = 1/(n_e \sigma_{T a})$ should be large by decreasing the number density of electrons, i.e., at the recombination or reionization. After the decoupling of photons and baryons the polarization anisotropies are no longer generated by Thomson scattering. Thus the polarizations are generated only at the epoch of recombination or reionization. This leads to lower amplitude of the polarization fluctuations compared to the temperature fluctuations.

On the other hand the B-mode polarization is not generated through Thomson scattering because of parity symmetry. However, unlike the scalar perturbations, the vector or tensor perturbations could be a source of B-mode polarization.

Sachs-Wolfe and Integrated Sachs-Wolfe effect

The fluctuations of CMB are generated by the difference of gravitational potentials between at the observer and the last scattering surface. This effect is called the Sachs-Wolfe effect [81]. The fluctuations are also generated by the time variation of gravitational potential during the propagation of CMB photons. This effect is referred to as the integrated Sachs-Wolfe (ISW) effect. The time variation of gravitational potential is caused by (1) the non-negligible contribution of radiation components, and (2) the accelerated expansion at late time of the universe.

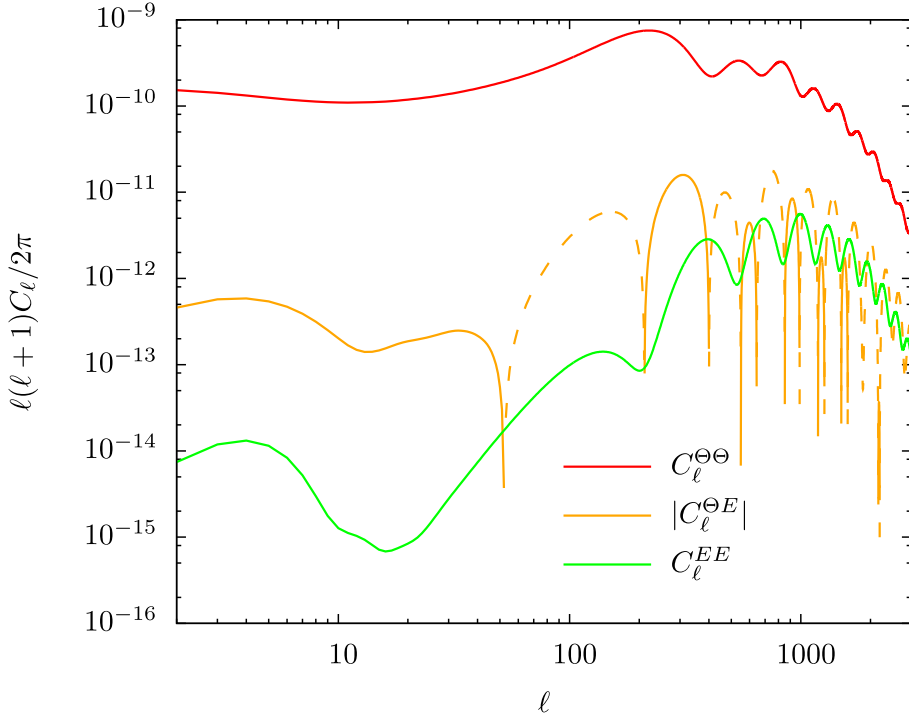


Figure 2.2: The angular power spectrum of CMB anisotropies generated by the scalar perturbations; the temperature, $C_\ell^{\Theta\Theta}$, E -mode polarization, C_ℓ^{EE} , and cross-correlation of temperature and E -mode polarization, $C_\ell^{\Theta E}$. For $C_\ell^{\Theta E}$, we plot the absolute value, and the negative values are expressed as thin line.

Weak gravitational lensing

The path of the CMB photons is deflected by the gravitational potential of LSS, and the resultant spatial pattern of the CMB fluctuations is distorted. This effect is referred to as CMB lensing. The details of the effect are given in section 2.4.

Reionization

Just after recombination, the universe is mostly filled with neutral hydrogen. But our current universe is highly ionized, implying that, at some redshift, neutral hydrogens are ionized by some mechanism, e.g., ultraviolet photons emitted from first stars. When neutral hydrogens are ionized, the CMB photons interact with electrons again, and the CMB polarization is induced, in a similar way as polarization at recombination.

Sunyaev-Zel'dovich effect

The CMB photon are interact with electrons associated with galaxies or galaxy clusters. Then, the energy of CMB photons are enhanced by scattering of the hot electrons. This effect is called Sunyaev-Zel'dovich effect.

2.2.4 Angular power spectrum of temperature and polarization

We summarize the effects of generating CMB anisotropies by showing the theoretical angular power spectrum of CMB temperature and polarization.

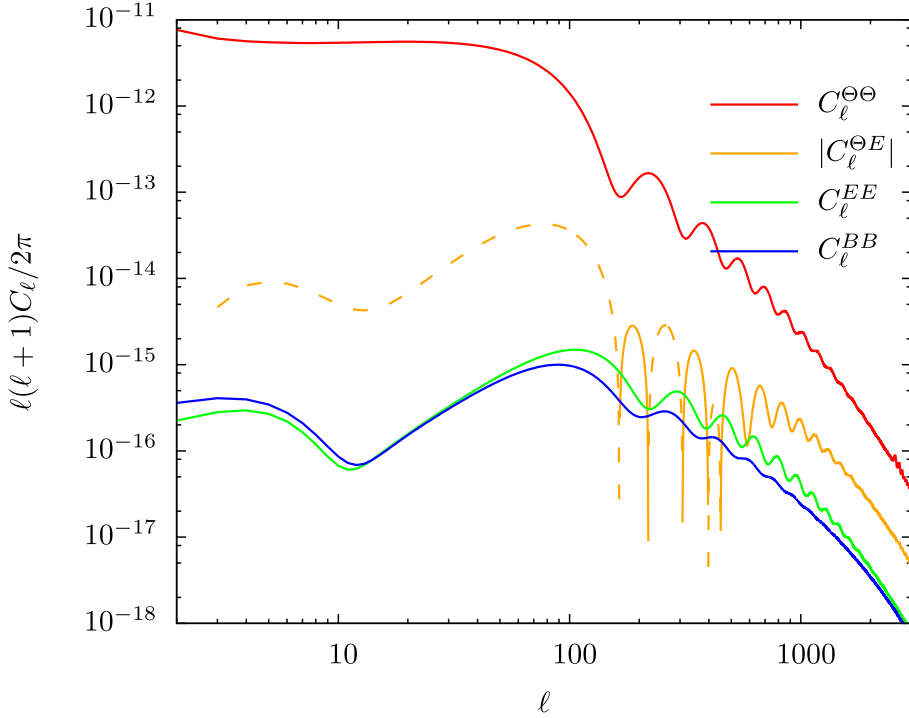


Figure 2.3: Same as Fig.2.2, but for the tensor perturbations.

Fig. 2.2 shows an example of angular power spectra. The angular power spectra shown here are computed by the Code for Anisotropies in the Microwave Background (CAMB; [82]). The cosmological parameters which are adopted in computing the angular power spectra is given in Table 1.1, and are consistent with the results obtained from Ref.[77].

In the temperature angular power spectrum, $C_\ell^{\Theta\Theta}$, the first acoustic peak is located at $\ell = 200$ which roughly corresponds to the scale of the sound horizon. The acoustic feature can be seen in the scales smaller than $\ell \sim 200$, and, at $\ell \sim 1000$, the amplitude of the angular power spectrum exponentially decreases by Silk damping. From $\ell \sim 100$ to the first acoustic scale, the temperature anisotropies are also generated by the early-type ISW effect, and, at $\ell < 10$, there are contributions from late-type ISW effect. The acoustic peaks also appear in the E -mode angular power spectrum, C_ℓ^{EE} , and has a maximum around $\ell \sim 1000$. Beyond $\ell \sim 1000$, the E -mode angular power spectrum also suppressed by the Silk damping. The effect of reionization is appeared at large scales, $\ell < 10$.

Fig. 2.3 shows the same plot but for tensor perturbations. Comparing with the power spectra of scalar perturbations, the amplitude of the angular power spectra from tensor perturbations is by several order of magnitudes lower than that from scalar perturbations. The power spectrum of E and B modes has roughly same amplitude and exhibits similar behavior. There are oscillation features in the power spectra with the first peak around the horizon scale. Since the gravitational waves are damped at sub-horizon scales, the angular power spectrum decreases as the multipole increases.

2.3 Evolution of Gravitational Fields in the Universe

The origin of the structure that we observe today is considered as the fluctuations generated at the early stage of the universe, which evolve through gravitational interaction, and form galaxy and galaxy halos. One of the candidates to explain generation of the initial fluctuations is the inflation. With a sudden exponential expansion of the universe, the initial quantum fluctuations are extended beyond the horizon size, $\lambda_H \equiv 1/\mathcal{H}$. After the end of inflation, the length

λ_H becomes large, and the fluctuations at the super-horizon scale re-enter the sub-horizon scale. The fluctuations re-entered in the sub-horizon scale evolve and form in galaxies and galaxy clusters through gravitational clustering and the LSS that we observe today. At late time of the universe, although the main source of the gravitational fields is the matter density fluctuations, there may exist some additional sources, e.g., gravitational waves and cosmic strings.

To discuss weak gravitational lensing, we have to know the evolution of gravitational fields between the sources and observer. For this purpose, in this section, we briefly summarize the evolution of fluctuations, focusing on the gravitational fields, following Refs. [1, 2], for the evolutions of the scalar perturbations, Ref. [43] for the case including massive neutrinos, and Refs. [76, 2], for the evolution of vector and tensor perturbations.

2.3.1 Evolution of scalar components

For the scalar perturbations, the solution of the evolution equation can be obtained analytically when we assume the radiation/matter-dominated era, or super/sub-horizon scales [2].

Radiation/matter-dominated era and super/sub-horizon scales

When the radiation components dominate the universe, at super-horizon scales ($k\eta \ll 1$), the gravitational potentials i.e. Φ and Ψ given in Eq. (1.10) are constant. On the other hand, when a mode enters the horizon during the radiation-dominated era, the potential oscillates with its amplitude decaying. This behavior comes from the fact that, at sub-horizon scales, the photon temperature fluctuations oscillate through interaction with baryons, and the potentials decay and oscillate as well. On the other hand, in the matter-dominated era, the radiation components are negligible and the gravitational potentials are constant even at the sub-horizon scales.

Presence of hot dark matter

Here we consider the evolution of gravitational potential in the presence of hot dark matter. One of the hot dark matter is the massive neutrinos. Although the neutrinos are treated as relativistic particles at the early epoch of the universe, massive neutrinos behave as non-relativistic particles. But the mass of neutrinos is very small compared to that of CDM and the velocity dispersion is significantly large on small scales.

This leads to a difference in the growth of the density fluctuations at large and small scales separated with the free-streaming scale, k_{FS} , which is determined by the Jeans equation of neutrinos. At scales larger than k_{FS} the density fluctuations of neutrinos grows gravitationally. At smaller scales the fluctuations do not grow since the neutrinos have large velocity dispersion and suppress the gravitational growth.

This also leads to the difference between the evolution of gravitational potentials at $k \ll k_{\text{FS}}$ and $k \gg k_{\text{FS}}$. At scales, $k \ll k_{\text{FS}}$, the massive neutrinos behave as CDM, and the evolution of gravitational potentials is the same as we discussed previously. On the other hand, at scales, $k \gg k_{\text{FS}}$, the massive neutrinos do not contribute to the gravitational clustering, and gravitational potentials become shallow compared to the case without massive neutrinos.

2.3.2 Evolution of vector perturbations

Evolution equation of vector perturbations with seed

Let us consider the evolution equations of vector perturbations. In addition to the cosmological fluid, there exists another “seed” of vector perturbations that does not change the evolution of the scalar perturbations. From Eq. (A.37) the linearized Einstein equation for the vector perturbations is given by

$$\frac{1}{a^2} \frac{d(a^2 \sigma^{(1)})}{dt} = -\frac{8\pi G a^2}{k} \pi_s^{(1)}, \quad (2.69)$$

where $\pi_s^{(1)}$ is the vector mode of the anisotropic stress for seed and we assume that the vector perturbations of cosmological fluids are negligible. From the momentum conservation we obtain

$$\frac{1}{a^4} \frac{d(a^4 v_s^{(1)})}{dt} + \frac{k}{2} \pi_s^{(1)} = 0, \quad (2.70)$$

where $v_s^{(1)}$ are the vector components of the velocity perturbations for seed. From the above equations (2.69) and (2.70), we obtain

$$\sigma^{(1)} = -\frac{16\pi G a^2}{k^2} v_s^{(1)}. \quad (2.71)$$

Example of vector source: cosmic string network

Here, as an example of the vector sources, we summarize a specific model of cosmic string network described in Ref.[74].

We assume that the string network is described by the velocity-dependent one-scale (VOS) model [83, 84, 85, 86]. In this model, the string network is characterized by only two physical quantities; the correlation length and mean-square-root velocity, ξ and v_{rms} , and, instead of ξ , we use $\gamma_s = 1/(H\xi)$. We take into account the energy loss of strings due to loop formation. The intercommuting process provides an essential mechanism for a string network to lose its energy due to loop formation. It is widely believed that the energy-loss mechanism allows the network to relax towards an cosmological attractor solution, in which γ_s and v_{rms} remain constant: this is so-called scaling solution. In the VOS model, γ_s and v_{rms} are approximately described by $\gamma_s = (\pi\sqrt{2}/3\tilde{c}P)^{1/2}$ and $v_{\text{rms}}^2 = (1 - \pi/3\gamma_s)/2$ [86], where $\tilde{c} \approx 0.23$ quantifies the efficiency of loop formation [84] and P is the intercommuting probability.

To obtain v_{rms} , we consider a Nambu-Goto string segment at the position $\mathbf{r} = \mathbf{r}(\Sigma, \eta)$, where η and Σ are the time and position on the string world-sheet. In the transverse gauge, the stress-energy tensor for a string segment can be described as [87]

$$\delta T^{\mu\nu}(\mathbf{r}, \eta) = \mu \int d\Sigma \begin{pmatrix} 1 & -\dot{r}^i \\ -\dot{r}^j & \dot{r}^i \dot{r}^j - r^{i'} r^{j'} \end{pmatrix} \delta_D^3(\mathbf{r} - \mathbf{r}(\Sigma, \eta)), \quad (2.72)$$

where the dot () and the prime (') denote the derivative with respect to η and Σ , respectively. The velocity perturbations, $v^{(\pm 1)}$, due to a segment are given by

$$v^{(\pm 1)}(\mathbf{k}, \eta) = \mu \int d\Sigma \dot{r}^i(\Sigma, \eta) e_{\pm, i}^*(\hat{\mathbf{k}}) e^{i\mathbf{k}\cdot\mathbf{r}(\Sigma, \eta)}. \quad (2.73)$$

For a tractable analytic estimate, we assume that the correlations between the string segments are characterized by a simple model developed in Refs. [88, 89, 90]. Then, we obtain the equal-time auto power spectrum for the vector perturbations as [74]

$$\begin{aligned} P_{\sigma\sigma}(k; \eta, \eta) &= 2 \frac{(16\pi G)^2 a^4}{k^4} \frac{1}{\mathcal{V}} \langle v^{(\pm 1)*}(\mathbf{k}, \eta) v^{(\pm 1)}(\mathbf{k}, \eta) \rangle \\ &= (16\pi G \mu)^2 \frac{2\sqrt{6\pi} v_{\text{rms}}^2}{3(1 - v_{\text{rms}}^2)} \frac{4\pi \chi^2 a^4}{H} \left(\frac{a}{k\xi} \right)^5 \text{erf} \left(\frac{k\xi/a}{2\sqrt{6}} \right), \end{aligned} \quad (2.74)$$

where $\mathcal{V} = (2\pi)^3 \delta(\mathbf{0})$ is the comoving box size, and $\text{erf}(x)$ is the error function:

$$\text{erf}(x) = \frac{2}{\sqrt{\pi}} \int_0^x dy e^{-y^2}. \quad (2.75)$$

To compute the weak lensing power spectra, we further need the unequal-time auto-power spectrum. Here, as a crude estimate, we adopt the following approximation (e.g., [91]):

$$P_{\sigma\sigma}(k; \eta_1, \eta_2) = \sqrt{P_{\sigma\sigma}(k, \eta_1, \eta_1) P_{\sigma\sigma}(k, \eta_2, \eta_2)}. \quad (2.76)$$

Note that the model and assumptions given above would be too simple and might not be realistic for a precision study of lensing signals. Further, Eqs. (2.74) and (2.76) may have additional modifications from the contributions of the loop strings or non-negligible correlations between different string segments [92]. Though these effects are expected to be small, they would certainly enhance the lensing signals, and the expected signal-to-noise ratios discussed in chapter 4 will be increased. In this respect, the analysis with the above simple model may give a rather conservative estimate for the detectability of cosmic strings.

2.3.3 Evolution of tensor components

Here we summarize the evolution of the tensor perturbations. Ignoring the anisotropic stress from the radiation components, the evolution equation of gravitational waves, Eq. (A.47), reduces to

$$(1+y)\frac{d^2D}{dy^2} + \left(\frac{2(1+y)}{y} + \frac{1}{2}\right)\frac{dD}{dy} + k_{\text{eq}}^2 D = 0, \quad (2.77)$$

where $k_{\text{eq}} = \sqrt{2}/a_{\text{eq}}H_{\text{eq}}$. At super-horizon scales, the above equation implies that the two solutions are constant, D_0 , or decaying mode. Thus, we focus on the solution which is constant at super-horizon scales.

First we consider the solution in a radiation-dominated era, $y \ll 1$. In this epoch, the above equation becomes

$$\frac{d^2D}{dy^2} + \frac{2}{y}\frac{dD}{dy} + k_{\text{eq}}^2 D = 0. \quad (2.78)$$

For any k_{eq} , the solution that approaches a constant D_0 at an early time, $y \rightarrow 0$, is given by

$$D = \frac{\sin(k_{\text{eq}}y)}{k_{\text{eq}}y} D_0. \quad (2.79)$$

Next we consider the solution at a matter-dominated era, $y \gg 1$. The evolution equation becomes

$$y\frac{d^2D}{dy^2} + \frac{5}{2}\frac{dD}{dy} + k_{\text{eq}}^2 D = 0. \quad (2.80)$$

This has two independent solutions:

$$\frac{2j_1(2k_{\text{eq}}\sqrt{y})}{k_{\text{eq}}\sqrt{y}}, \quad -\frac{2n_1(2k_{\text{eq}}\sqrt{y})}{k_{\text{eq}}\sqrt{y}}. \quad (2.81)$$

In order to become constant at super-horizon scales, the second function, n_1 , is excluded. On the other hand, for $k_{\text{eq}}\sqrt{y} \ll 1$, the first solution becomes $4/3$. Thus, the solution of the tensor perturbation is given by

$$D = \frac{3D_0}{2} \frac{j_1(2k_{\text{eq}}\sqrt{y})}{k_{\text{eq}}\sqrt{y}}. \quad (2.82)$$

2.4 Weak Gravitational Lensing

The CMB photons emitted at the last scattering move through the gravitational fields generated by the large scale structure, and their path is deflected. As a result the spatial pattern of observed anisotropies are distorted and the CMB angular power spectrum is modified (e.g.,[93, 94, 95, 96, 97]). Similarly, the observed galaxy images are distorted by gravitational field between observer and sources.

In this section, we briefly summarize the weak gravitational lensing. We first summarize the lensing effect on CMB, following Refs. [98, 99], and discuss the lensing effect on CMB temperature and polarization power spectrum. Note that the detailed calculation for angular power spectrum of CMB temperature and polarization is presented in, e.g., Ref.[80] in the absence of the curl mode, and in Ref.[46] including the curl mode. We also discuss the lensing effect on galaxies, and show angular power spectrum of weak lensing observables.

2.4.1 Lensing effect on CMB

Lensed temperature anisotropies in harmonic space

The lensed temperature fluctuations are expressed as remapping of unlensed temperature fluctuations, $\Theta(\hat{\mathbf{n}})$, by deflection angle, $\mathbf{d}(\hat{\mathbf{n}})$:

$$\tilde{\Theta}(\hat{\mathbf{n}}) = \Theta(\hat{\mathbf{n}} + \mathbf{d}(\hat{\mathbf{n}})), \quad (2.83)$$

where, in general, the deflection angle is decomposed into

$$\mathbf{d}(\hat{\mathbf{n}}) = \nabla\phi(\hat{\mathbf{n}}) + (\star\nabla)\varpi(\hat{\mathbf{n}}). \quad (2.84)$$

The operator, \star , denotes the counterclockwise rotation of a two dimensional vector. Hereafter, we call the quantities, ϕ and ϖ , the lensing potential and curl-modes, respectively.

Usually, the deflection angle is a small perturbed quantity, $|\mathbf{d}| \ll 1$, and the lensed temperature fluctuations may be expressed as

$$\tilde{\Theta}(\hat{\mathbf{n}}) = \Theta(\hat{\mathbf{n}}) + \mathbf{d} \cdot \nabla\Theta(\hat{\mathbf{n}}) + \frac{(\mathbf{d} \cdot \nabla)^2}{2}\Theta(\hat{\mathbf{n}}) + \mathcal{O}(|\mathbf{d}|^3), \quad (2.85)$$

where we expand $\Theta(\hat{\mathbf{n}} + \mathbf{d})$ in terms of the deflection angle. The harmonic coefficients of the lensed quantities are obtained by converting Eq. (2.85) into the harmonic space with the spin-0 spherical harmonics. From Eq. (2.84), the lensed temperature anisotropies in the harmonic space are given by

$$\begin{aligned} \tilde{\Theta}_{\ell m} &= \Theta_{\ell m} + \int d\hat{\mathbf{n}} Y_{\ell m}^*(\hat{\mathbf{n}}) [\mathbf{d} \cdot \nabla] \Theta(\hat{\mathbf{n}}) + \int d\hat{\mathbf{n}} Y_{\ell m}^*(\hat{\mathbf{n}}) \frac{(\mathbf{d} \cdot \nabla)^2}{2} \Theta(\hat{\mathbf{n}}) + \mathcal{O}(|\mathbf{d}|^3) \\ &= \Theta_{\ell m} + \sum_{x=\phi,\varpi} \sum_{\ell_1 m_1 \ell_2 m_2} x_{\ell_1 m_1} \Theta_{\ell_2 m_2} \mathcal{I}_{\ell m \ell_1 m_1 \ell_2 m_2}^x \\ &\quad + \frac{1}{2} \sum_{x,y=\phi,\varpi} \sum_{\ell_1 m_1 \ell_2 m_2 \ell_3 m_3} x_{\ell_1 m_1} \Theta_{\ell_2 m_2} y_{\ell_3 m_3}^* \mathcal{J}_{\ell m \ell_1 m_1 \ell_2 m_2 \ell_3 m_3}^{xy}. \end{aligned} \quad (2.86)$$

Here we define

$$\mathcal{I}_{\ell m \ell_1 m_1 \ell_2 m_2}^x \equiv c_{ij}^x \int d\hat{\mathbf{n}} Y_{\ell m}^* \partial^i Y_{\ell_1 m_1} \partial^j Y_{\ell_2 m_2}, \quad (2.87)$$

$$\mathcal{J}_{\ell m \ell_1 m_1 \ell_2 m_2 \ell_3 m_3}^{xy} \equiv c_{ij}^x c_{kl}^y \int d\hat{\mathbf{n}} Y_{\ell m}^* \partial^i Y_{\ell_1 m_1} \partial^k Y_{\ell_3 m_3}^* \partial^j \partial^l Y_{\ell_2 m_2}, \quad (2.88)$$

with $c_{ij}^\phi = \delta_{ij}$ and $c_{ij}^\varpi = \epsilon_{ij}$. The coefficients, $\mathcal{I}_{\ell m \ell_1 m_1 \ell_2 m_2}^x$, are written as

$$\mathcal{I}_{L M \ell m \ell' m'}^x = (-1)^M \begin{pmatrix} L & \ell & \ell' \\ -M & m & m' \end{pmatrix} S_{L \ell \ell'}^{0,x}. \quad (2.89)$$

As shown in appendix F, the quantities, $S_{L \ell \ell'}^{0,\phi}$ and $S_{L \ell \ell'}^{0,\varpi}$, are expressed in terms of the Wigner-3j symbols, and the results are

$$S_{L \ell \ell'}^{0,\phi} = \sqrt{\frac{(2\ell+1)(2\ell'+1)(2L+1)}{16\pi}} [-L(L+1) + \ell(\ell+1) + \ell'(\ell'+1)] \begin{pmatrix} L & \ell & \ell' \\ 0 & 0 & 0 \end{pmatrix}, \quad (2.90)$$

$$\begin{aligned} S_{L \ell \ell'}^{0,\varpi} &= -i \sqrt{\frac{(2\ell+1)(2\ell'+1)(2L+1)}{16\pi}} \sqrt{\ell(\ell+1)} \sqrt{\ell'(\ell'+1)} \\ &\quad \times \left[\begin{pmatrix} L & \ell & \ell' \\ 0 & -1 & 1 \end{pmatrix} - \begin{pmatrix} L & \ell & \ell' \\ 0 & 1 & -1 \end{pmatrix} \right]. \end{aligned} \quad (2.91)$$

We note that the quantities $S_{L\ell\ell'}^{0,\phi}$ and $S_{L\ell\ell'}^{0,\varpi}$ satisfy

$$S_{L\ell\ell'}^{0,\phi} = (-1)^{L+\ell+\ell'} S_{L\ell\ell'}^{0,\phi}, \quad (2.92)$$

$$S_{L\ell\ell'}^{0,\varpi} = -(-1)^{L+\ell+\ell'} S_{L\ell\ell'}^{0,\varpi}. \quad (2.93)$$

The above equations come from the parity symmetry of Θ , ϕ and ϖ ; the temperature anisotropies and the lensing potential are even parity, while the curl mode has odd parity. In fact, Eqs. (2.92) and (2.93) are confirmed by changing the variable, $\hat{\mathbf{n}} \rightarrow -\hat{\mathbf{n}}$ in the r.h.s of Eq. (2.87). Under this transformation, the spin-0 spherical harmonics are multiplied by a factor of $(-1)^\ell$, and the derivatives become $\nabla \rightarrow \nabla$ and $(\star\nabla) \rightarrow -(\star\nabla)$, respectively. As a result, the r.h.s of Eq. (2.87) is multiplied by a factor of $(-1)^{L+\ell+\ell'}$ and $-(-1)^{L+\ell+\ell'}$, for $x = \phi$ and $x = \varpi$. Eqs. (2.92) and (2.93) are also confirmed with the formulas of Wigner $3j$ symbols.

From Eqs. (2.92) and (2.93) the quantity, $S_{L\ell\ell'}^{0,\phi}$ becomes zero if $L + \ell + \ell'$ is an odd integer, and the coefficient $S_{L\ell\ell'}^{0,\varpi}$ vanishes if $L + \ell + \ell'$ is an even integer. These properties are essential for a separate reconstruction of gradient and curl modes as discussed in the next chapter.

Lensed temperature angular power spectrum

With the multipole coefficients of lensed temperature anisotropies, $\tilde{\Theta}_{\ell m}$, the lensed temperature angular power spectrum is defined as

$$\delta_{\ell\ell'}\delta_{mm'}\tilde{C}_\ell^{\Theta\Theta} \equiv \langle \tilde{\Theta}_{\ell m}\tilde{\Theta}_{\ell' m'}^* \rangle. \quad (2.94)$$

From Eq. (2.86) we obtain the expression of the angular power spectrum:

$$\tilde{C}_\ell^{\Theta\Theta} = C_\ell^{\Theta\Theta} + \sum_{x=\phi,\varpi} \left[\sum_{\ell_1\ell_2} C_{\ell_1}^{xx} C_{\ell_2}^{\Theta\Theta} I_{\ell\ell_1\ell_2}^x + C_\ell^{\Theta\Theta} \sum_{\ell_1} C_{\ell_1}^{xx} J_{\ell\ell_1\ell_2}^x \right], \quad (2.95)$$

where we define

$$I_{\ell\ell_1\ell_2}^x \equiv \sum_{m_1m_2} (I_{\ell m_1 m_1 \ell_2 m_2}^x)^2, \quad (2.96)$$

$$J_{\ell\ell_1\ell_2}^x \equiv \frac{1}{2} \sum_{m_1} J_{\ell m_1 m_1 \ell_2 m_2 \ell_3 m_1}^{xx} + \text{c.c.} \quad (2.97)$$

Note that we assume that the cross-correlation between ϕ and ϖ vanishes.

Lensed polarization anisotropies in harmonic space

Next we consider the lensing effect on the CMB polarizations, $\Pi^\pm(\hat{\mathbf{n}}) = Q(\hat{\mathbf{n}}) \pm iU(\hat{\mathbf{n}})$:

$$\tilde{\Pi}^\pm(\hat{\mathbf{n}}) = \Pi^\pm(\hat{\mathbf{n}} + \mathbf{d}(\hat{\mathbf{n}})). \quad (2.98)$$

Lensing effect on polarization has an interesting feature; even in the absence of primary B-mode polarization, pattern of lensed polarization anisotropies could have odd-parity mode. Generation of B-mode polarization by lensing would be understood from Fig. 2.1. Primary E-mode polarization given in left panel of Fig. 2.1 is remapped by deflection angle at each position. By shifting “bars” slightly at each point, the resultant pattern is no longer pure even parity mode, but mixed pattern of even and odd-parity mode. Thus, even in the absence of sources which generate B-mode polarization in primary CMB anisotropies, observed anisotropies include B-mode polarization.

To consider the lensing effect on polarization anisotropies quantitatively, we expand the lensed polarization anisotropies in terms of deflection angle, as similar to the case of temperature anisotropies:

$$\tilde{\Pi}^\pm(\hat{n}) = \Pi^\pm(\hat{n}) + \mathbf{d} \cdot \nabla \Pi^\pm(\hat{n}) + \frac{(\mathbf{d} \cdot \nabla)^2}{2} \Pi^\pm(\hat{n}) + \mathcal{O}(|\mathbf{d}|^3), \quad (2.99)$$

We are especially concerned with the rotationally invariant combinations, i.e., E - and B -mode polarizations. Denoting $X_{\ell m}^\pm = E_{\ell m} \pm iB_{\ell m}$, the lensing effect on X^\pm is given by transforming the above equation with spin-2 spherical harmonics:

$$\begin{aligned} \tilde{X}_{\ell m}^\pm &= X_{\ell m}^\pm + \int d\hat{n} (Y_{LM}^{\pm 2}(\hat{n}))^* \mathbf{d}(\hat{n}) \cdot \nabla \Pi^\pm(\hat{n}) + \int d\hat{n} (Y_{LM}^{\pm 2}(\hat{n}))^* \frac{[\mathbf{d}(\hat{n}) \cdot \nabla]^2}{2} \nabla^2 \Pi^\pm(\hat{n}) \\ &= X_{\ell m}^\pm + \sum_{x=\phi,\varpi} \sum_{\ell_1 m_1 \ell_2 m_2} x_{\ell_1 m_1} X_{\ell_2 m_2}^\pm I_{\ell m \ell_1 m_1 \ell_2 m_2}^{\pm 2, x} \\ &\quad + \frac{1}{2} \sum_{x,y=\phi,\varpi} \sum_{\ell_1 m_1 \ell_2 m_2 \ell_3 m_3} x_{\ell_1 m_1} X_{\ell_2 m_2}^\pm y_{\ell_3 m_3}^* J_{\ell m \ell_1 m_1 \ell_2 m_2 \ell_3 m_3}^{\pm 2, xy}, \end{aligned} \quad (2.100)$$

where we define

$$\begin{aligned} I_{\ell m \ell_1 m_1 \ell_2 m_2}^{\pm 2, x} &\equiv c_{ij}^x \int d\hat{n} {}_{\pm 2} Y_{\ell m}^* \partial^i Y_{\ell_1 m_1} \partial^j {}_{\pm 2} Y_{\ell_2 m_2}, \\ J_{\ell m \ell_1 m_1 \ell_2 m_2 \ell_3 m_3}^{\pm 2, xy} &\equiv c_{ij}^x c_{kl}^y \int d\hat{n} {}_{\pm 2} Y_{\ell m}^* \partial^i Y_{\ell_1 m_1} \partial^k Y_{\ell_3 m_3} \partial^j \partial^l {}_{\pm 2} Y_{\ell_2 m_2}. \end{aligned} \quad (2.101)$$

The quantity, $I_{\ell m \ell_1 m_1 \ell_2 m_2}^{\pm 2, x}$, is related to $S_{L\ell\ell'}^{\pm 2, \phi}$ and $S_{L\ell\ell'}^{\pm 2, \varpi}$ as

$$I_{LM \ell m \ell' m'}^{\pm 2, x} = (-1)^M \begin{pmatrix} L & \ell & \ell' \\ -M & m & m' \end{pmatrix} S_{L\ell\ell'}^{\pm 2, x}. \quad (2.102)$$

The quantities, $S_{L\ell\ell'}^{\pm 2, \phi}$ and $S_{L\ell\ell'}^{\pm 2, \varpi}$, are written as

$$\begin{aligned} S_{L\ell\ell'}^{\pm 2, \phi} &= \sqrt{\frac{(2\ell+1)(2\ell'+1)(2L+1)}{16\pi}} \\ &\quad \times [\ell(\ell+1) + \ell'(\ell'+1) - L(L+1)] \begin{pmatrix} L & \ell & \ell' \\ \pm 2 & 0 & \mp 2 \end{pmatrix}, \end{aligned} \quad (2.103)$$

$$\begin{aligned} S_{L\ell\ell'}^{\pm 2, \varpi} &= -i \sqrt{\frac{(2\ell+1)(2\ell'+1)(2L+1)}{16\pi}} \sqrt{\ell(\ell+1)} \sqrt{(\ell' \pm 2)(\ell'+1 \pm 2)} \\ &\quad \times \left[\sqrt{\frac{\ell'+1 \mp 2}{\ell'+1 \pm 2}} \begin{pmatrix} L & \ell & \ell' \\ \pm 2 & -1 & 1 \mp 2 \end{pmatrix} - \sqrt{\frac{\ell' \mp 2}{\ell' \pm 2}} \begin{pmatrix} L & \ell & \ell' \\ \pm 2 & 1 & -1 \mp 2 \end{pmatrix} \right]. \end{aligned} \quad (2.104)$$

Up to the first order of lensing potentials (2.100) is rewritten in the separable form for E - and B -mode polarizations:

$$\begin{aligned} \tilde{E}_{LM} &= E_{LM} + \sum_{\ell m \ell' m'} (-1)^M \begin{pmatrix} L & \ell & \ell' \\ -M & m & m' \end{pmatrix} \\ &\quad \times \sum_{x=\phi,\varpi} x_{\ell m} \{S_{L\ell\ell'}^{+,x} E_{\ell' m'} - S_{L\ell\ell'}^{-,x} B_{\ell' m'}\}, \end{aligned} \quad (2.105)$$

$$\begin{aligned} \tilde{B}_{LM} &= B_{LM} + \sum_{\ell m \ell' m'} (-1)^M \begin{pmatrix} L & \ell & \ell' \\ -M & m & m' \end{pmatrix} \\ &\quad \times \sum_{x=\phi,\varpi} x_{\ell m} \{S_{L\ell\ell'}^{-,x} E_{\ell' m'} + S_{L\ell\ell'}^{+,x} B_{\ell' m'}\}, \end{aligned} \quad (2.106)$$

where we define

$$S_{L\ell\ell'}^{+,x} = \frac{S_{L\ell\ell'}^{2,x} + S_{L\ell\ell'}^{-2,x}}{2}, \quad (2.107)$$

$$S_{L\ell\ell'}^{-,x} = \frac{S_{L\ell\ell'}^{2,x} - S_{L\ell\ell'}^{-2,x}}{2i}. \quad (2.108)$$

Note again that, for an even integer of $L + \ell + \ell'$, the coefficients $S^{+,\varpi}$ and $S^{-,\phi}$ vanish. On the other hand, the quantities $S^{+,\phi}$ and $S^{-,\varpi}$ vanish when $L + \ell + \ell'$ is an odd integer. Similar to the case of temperature, these properties come from the fact that the E -mode polarization and lensing potential have even parity, while the B -mode polarization and curl mode have odd parity.

Lensed angular power spectrum for polarization

Using the multipole coefficients of lensed E and B modes, the angular power spectrum of lensed E and B mode are given by

$$\begin{aligned} \tilde{C}_\ell^{\text{EE}} &= C_\ell^{\text{EE}} + \frac{1}{2} \sum_{x=\phi,\varpi} \sum_{\ell_1 \ell_2} C_{\ell_1}^{xx} [(C_{\ell_2}^{\text{EE}} + C_{\ell_2}^{\text{BB}}) + (-1)^L (C_{\ell_2}^{\text{EE}} - C_{\ell_2}^{\text{BB}})] I_{\ell\ell_1\ell_2}'^{22,x} \\ &\quad + \frac{1}{2} C_\ell^{\text{EE}} \sum_{x=\phi,\varpi} \sum_{\ell_1} C_{\ell_1}^{xx} (J_{\ell\ell_1}'^{2,x} + J_{\ell\ell_1}'^{-2,x}) \end{aligned} \quad (2.109)$$

$$\begin{aligned} \tilde{C}_\ell^{\text{BB}} &= C_\ell^{\text{BB}} + \frac{1}{2} \sum_{x=\phi,\varpi} \sum_{\ell_1 \ell_2} C_{\ell_1}^{xx} [(C_{\ell_2}^{\text{BB}} + C_{\ell_2}^{\text{EE}}) + (-1)^L (C_{\ell_2}^{\text{BB}} - C_{\ell_2}^{\text{EE}})] I_{\ell\ell_1\ell_2}'^{22,x} \\ &\quad + \frac{1}{2} C_\ell^{\text{BB}} \sum_{x=\phi,\varpi} \sum_{\ell_1} C_{\ell_1}^{xx} (J_{\ell\ell_1}'^{2,x} + J_{\ell\ell_1}'^{-2,x}), \end{aligned} \quad (2.110)$$

where $L = \ell + \ell_1 + \ell_2$ and

$$I_{\ell\ell_1\ell_2}'^{22,x} \equiv \sum_{m_1 m_2} (I_{\ell m \ell_1 m_1 \ell_2 m_2}^{2,x})^2, \quad (2.111)$$

$$J_{\ell\ell_1}'^{\pm 2,x} \equiv \frac{1}{2} \sum_{m_1} J_{\ell m \ell_1 m_1 \ell_1 m_1 \ell m}^{\pm 2,xx} + \text{c.c.} \quad (2.112)$$

Eq. (2.110) implies that, even if the primordial B -mode power spectrum is zero, the lensing effect induces the B -mode polarization. Combining the expression of lensed temperature anisotropies, the cross-power spectrum of lensed temperature and E-mode polarization is

$$\begin{aligned} \tilde{C}_\ell^{\Theta\text{E}} &= C_\ell^{\Theta\text{E}} + \frac{1}{2} \sum_{x=\phi,\varpi} \sum_{\ell_1 \ell_2} C_{\ell_1}^{xx} C_{\ell_2}^{\Theta\text{E}} [1 + (-1)^L] I_{\ell\ell_1\ell_2}'^{02,x} \\ &\quad + \frac{1}{4} C_\ell^{\Theta\text{E}} \sum_{x=\phi,\varpi} \sum_{\ell_1} C_{\ell_1}^{xx} (J_{\ell\ell_1}'^{2,x} + J_{\ell\ell_1}'^{-2,x} + 2J_{\ell\ell_1}'^x), \end{aligned} \quad (2.113)$$

where

$$J_{\ell\ell_1}'^x \equiv -\frac{1}{2} \ell(\ell+1) \ell_1(\ell_1+1) \frac{2\ell_1+1}{4\pi}, \quad (2.114)$$

$$I_{\ell\ell_1\ell_2}'^{02,x} \equiv \sum_{m_1 m_2} (I_{\ell m \ell_1 m_1 \ell_2 m_2}^x I_{\ell m \ell_1 m_1 \ell_2 m_2}^{2,x}). \quad (2.115)$$

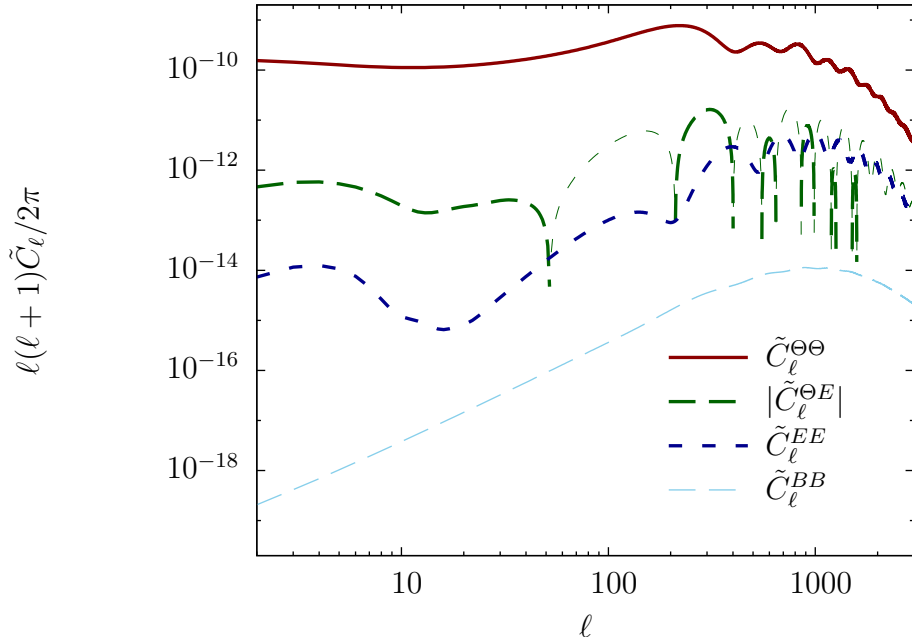


Figure 2.4: The lensed angular power spectrum of temperature, $\tilde{C}_\ell^{\Theta\Theta}$, E -mode polarization, \tilde{C}_ℓ^{EE} , B -mode polarization, \tilde{C}_ℓ^{BB} and cross-power spectrum of temperature and E -mode polarization, $\tilde{C}_\ell^{\Theta E}$.

To see the lensing effect on the angular power spectrum, we plot in Fig. 2.4 the lensed angular power spectrum. The lensed B mode power spectrum has a peak around $\ell \sim 1000$. On the other hand, the primary B -mode power spectrum generated by primordial gravitational waves has peak at large scales ($\ell \sim 100 - 200$), and the primary signal of B -mode from gravitational waves would be observed without delensing when tensor-to-scalar ratio is larger than $r \sim 0.01$.

Also, in Fig. 2.5, we show the ratio of the lensed angular power spectrum to the unlensed angular power spectrum. The lensing effect on temperature and E -mode polarization power spectrum is significant only on large scales ($\ell \gtrsim 2000$). This is because, on these scales, the primary CMB fluctuations are suppressed by Silk damping, and the lensing effect dominates the primary signals. This implies that, to measure the lensing effect through temperature anisotropies, experiments with high angular resolution ($\lesssim 5$ arcmin) are required.

Lensed anisotropies in flat sky limit

In the flat-sky approximation, we expand the real space quantities in the plane wave:

$$\Theta(\hat{n}) = \int \frac{d^2 \hat{n}}{(2\pi)^2} e^{i \hat{n} \cdot \ell} \Theta_\ell, \quad (2.116)$$

$$X^\pm(\hat{n}) = \pm i \int \frac{d^2 \hat{n}}{(2\pi)^2} e^{i \hat{n} \cdot \ell} X_\ell^\pm e^{\pm i(\varphi_\ell - \varphi_\theta)}, \quad (2.117)$$

where we define

$$\ell = \ell(\cos \varphi_\ell, \sin \varphi_\ell), \quad (2.118)$$

$$\hat{n} = \theta(\cos \varphi_\theta, \sin \varphi_\theta). \quad (2.119)$$

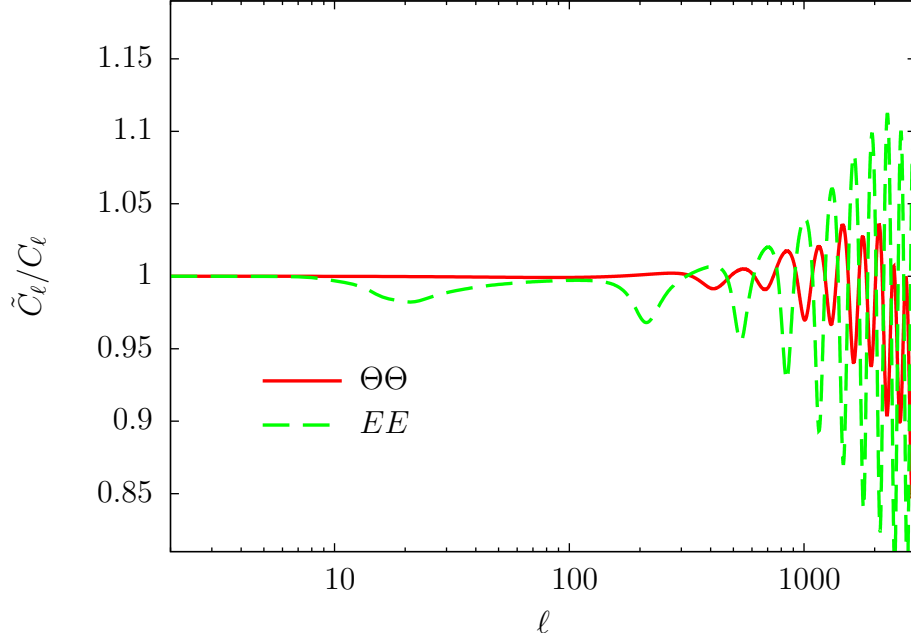


Figure 2.5: The ratio of lensed angular power spectrum to the unlensed angular power spectrum for temperature and E -mode polarization.

Then, the lensed anisotropies for temperature and polarizations become [80]

$$\begin{aligned} \tilde{\Theta}_\ell &= \Theta_\ell + \sum_{x=\phi,\varpi} \int \frac{d^2 L}{(2\pi)^2} \Theta_L L_{\ell,L}^x \\ &\quad + \frac{1}{2} \sum_{x,y=\phi,\varpi} \int \frac{d^2 L}{(2\pi)^2} \int \frac{d^2 L'}{(2\pi)^2} \Theta_L L_{\ell,L,L'}^{xy} + \mathcal{O}(|\mathbf{d}|^3), \end{aligned} \quad (2.120)$$

$$\begin{aligned} \tilde{X}_\ell^\pm &= X_\ell^\pm + \sum_{x=\phi,\varpi} \int \frac{d^2 L}{(2\pi)^2} e^{\pm i(\varphi_L - \varphi_\ell)} X_L^\pm L_{\ell,L}^x \\ &\quad + \frac{1}{2} \sum_{x,y=\phi,\varpi} \int \frac{d^2 L}{(2\pi)^2} e^{\pm i(\varphi_L - \varphi_\ell)} \int \frac{d^2 L'}{(2\pi)^2} X_L^\pm L_{\ell,L,L'}^{xy} + \mathcal{O}(|\mathbf{d}|^3). \end{aligned} \quad (2.121)$$

where

$$L_{\ell,L}^x = [(\mathbf{L} - \ell) \odot_x \mathbf{L}] x_{\ell-L}, \quad (2.122)$$

$$L_{\ell,L,L'}^{xy} = [\mathbf{L}' \odot_x \mathbf{L}] [(\ell - \mathbf{L} - \mathbf{L}') \odot_y \mathbf{L}'] x_{\ell-L-L'} y_{\ell-L-L'}, \quad (2.123)$$

and, for arbitrary two vectors, \mathbf{a} and \mathbf{b} , we define the products, \odot_ϕ and \odot_ϖ , as

$$\mathbf{a} \odot_\phi \mathbf{b} \equiv \mathbf{a} \cdot \mathbf{b}, \quad \mathbf{a} \odot_\varpi \mathbf{b} \equiv (\star \mathbf{a}) \cdot \mathbf{b} = -(\star \mathbf{b}) \cdot \mathbf{a}. \quad (2.124)$$

Lensed angular power spectrum in flat-sky limit

To analyze the asymptotic property of lensed angular power spectrum, it is convenient to express the angular power spectrum in the flat-sky approximation. Here we derive the angular power spectrum in the flat-sky formalism, and give asymptotic functional form of lensed B -mode angular power spectrum.

Using Eqs. (2.116) and (2.117), we obtain the lensed angular power spectrum for temperature in the flat-sky approximation

$$\begin{aligned}\tilde{C}_\ell^{\Theta\Theta} &= \tilde{C}_\ell^{\Theta\Theta} + \sum_{x=\phi,\omega} \int \frac{d^2\ell'}{(2\pi)^2} [\ell' \odot_x (\ell - \ell')]^2 C_{|\ell-\ell'|}^{xx} C_{\ell'}^{\Theta\Theta} \\ &\quad - C_\ell^{\Theta\Theta} \sum_{x=\phi,\omega} \int \frac{d^2\ell}{(2\pi)^2} (\ell \odot_x \ell')^2 C_\ell^{xx},\end{aligned}\tag{2.125}$$

and polarizations

$$\begin{aligned}\tilde{C}_\ell^{EE} &= C_\ell^{EE} + \frac{1}{2} \sum_{x=\phi,\omega} \int \frac{d^2\ell'}{(2\pi)^2} [\ell' \odot_x (\ell - \ell')]^2 C_{|\ell-\ell'|}^{xx} [(C_{\ell'}^{EE} + C_{\ell'}^{BB}) + (C_{\ell'}^{EE} - C_{\ell'}^{BB}) \cos 4\varphi_{\ell'}] \\ &\quad - C_\ell^{EE} \sum_{x=\phi,\omega} \int \frac{d^2\ell'}{(2\pi)^2} (\ell \odot_x \ell')^2 C_{\ell'}^{xx},\end{aligned}\tag{2.126}$$

$$\begin{aligned}\tilde{C}_\ell^{BB} &= C_\ell^{BB} + \frac{1}{2} \sum_{x=\phi,\omega} \int \frac{d^2\ell'}{(2\pi)^2} [\ell' \odot_x (\ell - \ell')]^2 C_{|\ell-\ell'|}^{xx} [(C_{\ell'}^{EE} + C_{\ell'}^{BB}) - (C_{\ell'}^{EE} - C_{\ell'}^{BB}) \cos 4\varphi_{\ell'}] \\ &\quad - C_\ell^{BB} \sum_{x=\phi,\omega} \int \frac{d^2\ell'}{(2\pi)^2} (\ell \odot_x \ell')^2 C_{\ell'}^{xx},\end{aligned}\tag{2.127}$$

$$\begin{aligned}\tilde{C}_\ell^{\Theta E} &= C_\ell^{\Theta E} + \sum_{x=\phi,\omega} \int \frac{d^2\ell'}{(2\pi)^2} [\ell' \odot_x (\ell - \ell')]^2 C_{|\ell-\ell'|}^{xx} C_{\ell'}^{\Theta E} \cos 2\varphi_{\ell'} \\ &\quad - C_\ell^{\Theta E} \sum_{x=\phi,\omega} \int \frac{d^2\ell'}{(2\pi)^2} (\ell \odot_x \ell')^2 C_{\ell'}^{xx}.\end{aligned}\tag{2.128}$$

Let us consider the approximate expression for lensed B -mode power spectrum. If we ignore the angular power spectra of the primary B modes and curl modes, the lensed B -mode power spectrum is given by

$$\tilde{C}_\ell^{BB} = \int \frac{d^2\ell'}{(2\pi)^2} [\ell' \cdot (\ell - \ell')]^2 C_{|\ell-\ell'|}^{\phi\phi} C_{\ell'}^{EE} \sin^2 2\varphi_{\ell'}.\tag{2.129}$$

At large angular scales, the integral is evaluated by assuming $\ell \ll \ell'$. In this approximation, the above equation becomes

$$\tilde{C}_\ell^{BB} \simeq \int \frac{d^2\ell'}{(2\pi)^2} \ell'^2 C_{\ell'}^{\phi\phi} C_{\ell'}^{EE} \sin^2 2\varphi_{\ell'}.\tag{2.130}$$

Note that the lensed B -mode angular power spectrum does not depend on the multipole, ℓ . This behavior is consistent with the result shown in Fig. 2.4, where the lensed B -mode angular power spectrum is multiplied by $\ell(\ell+1)/2\pi$ and proportional to ℓ^2 .

Next we consider the small angular scales. In this case, the integral is calculated by assuming $\ell \gg \ell'$ in the integrand, and the result is

$$\begin{aligned}\tilde{C}_\ell^{BB} &\simeq C_\ell^{\phi\phi} \int \frac{d^2\ell'}{(2\pi)^2} [\ell' \cdot \ell]^2 C_{\ell'}^{EE} \sin^2 2\varphi_{\ell'} \\ &= \ell^2 C_\ell^{\phi\phi} \int \frac{d^2\ell'}{(2\pi)^2} \ell'^2 C_{\ell'}^{EE}.\end{aligned}\tag{2.131}$$

Note that the lensed E -mode spectrum also exhibits similar behavior on small angular scales.

2.4.2 Lensing effect on galaxy images

To characterize the distortion on galaxy images, let us consider the Jacobi matrix which transforms a circle into an ellipse in two dimensional plane. For a galaxy at distance, $\tilde{\chi}$, the Jacobi matrix is usually decomposed into four components, i.e., convergence, κ , shear, γ_1 and γ_2 , and rotation, ω , as [100]

$$\frac{1}{\tilde{\chi}} \mathcal{D}_b^a(\tilde{\chi}) = \delta_b^a - \begin{pmatrix} \kappa + \gamma_1 & \gamma_2 + \omega \\ \gamma_2 - \omega & \kappa - \gamma_1 \end{pmatrix}. \quad (2.132)$$

The convergence, shear and rotation are related to the metric perturbations which can be calculated theoretically. These relations are given in the next chapter, and, in the following, we show how to obtain the convergence, shear and rotation from observation of galaxy images.

Ellipticity of galaxies

Here we discuss the relation between the observables and convergence, shear and rotation. In a measurement of weak lensing effect on the shape of galaxies, what we can derive from observation is the ellipticity of the galaxy image, e , and the observed ellipticity is related to the intrinsic ellipticity of galaxy, e_{int} , through [101]

$$e_{\text{int}} = \frac{e - 2g + g^2 e^*}{1 + g^2 - 2\Re(g e^*)}, \quad (2.133)$$

where we define the reduced shear as

$$g = \frac{\gamma}{1 - \kappa}. \quad (2.134)$$

The quantity, $\gamma = \gamma_1 + i\gamma_2$, is the complex shear. Since the reduced shear fields transform as the spin- ± 2 quantities, with the similar analogy of the CMB polarization, we define the E - and B -modes shear as the two parity eigenstates as

$$\mathcal{E}(\hat{n}) = -\frac{1}{2} \left(\bar{\partial}^2 g(\hat{n}) + \partial^2 g(\hat{n}) \right), \quad (2.135)$$

$$\mathcal{B}(\hat{n}) = -\frac{1}{2i} \left(\bar{\partial}^2 g(\hat{n}) - \partial^2 g(\hat{n}) \right), \quad (2.136)$$

where $\bar{\partial}$ and ∂ are the spin-raising/lowering operator (see appendix F). For weak lensing, we assume $\kappa \ll 1$, and the reduced shear becomes the complex shear. Thus, the quantity obtained from a measurement of galaxy shapes is complex shear, although accurate information on the intrinsic shape of galaxies should be required.

Distribution of galaxies

In a photometric survey, we divide observed galaxies into redshift bins. Shear fields in the i -th redshift bin is expressed as

$$\gamma_i = \int_0^\infty N_i(z) \gamma(z) dz, \quad (2.137)$$

where $N_i(z)$ is galaxy distribution in the i -th redshift bin. The functional form of $N_i(z)$ is usually assumed as an empirical form, e.g., the Schechter function:

$$N_i(z) = \begin{cases} z^\alpha \exp \left[-\left(\frac{z}{z_0} \right)^\beta \right] & (z_{i-1} < z < z_i) \\ 0 & (\text{otherwise}) \end{cases}, \quad (2.138)$$

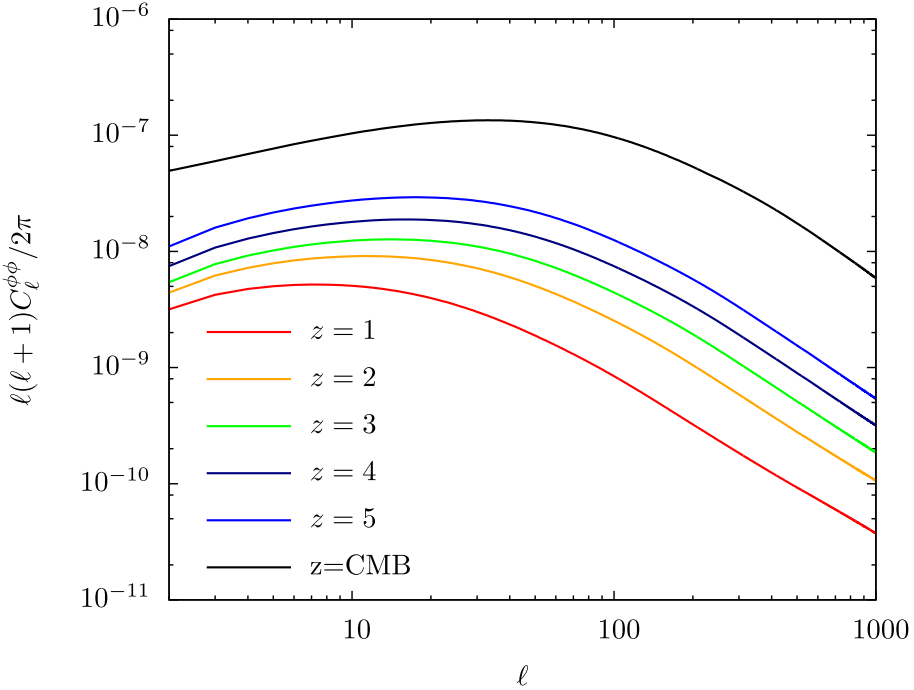


Figure 2.6: The angular power spectrum of scalar lensing potential (or E -mode shear), $C_\ell^{\phi\phi} = C_\ell^{\mathcal{EE}} \times (\ell-2)!/(\ell+2)!$, generated by linear matter density fluctuations.

where α , β and z_0 are constants, and z_{i-1} and z_i are minimum and maximum redshifts in the i -th bin.

For the photometric redshift determination, the uncertainty arising from the photometric redshift error is crucial in the cosmological analysis [102]. To mimic this effect, we assume that the photometric redshift estimates are distributed as a Gaussian with rms fluctuation $\sigma(z)$. Then the actual redshift distribution for i -th galaxy subsamples over the range, $z_{i-1} < z < z_i$, is related to the redshift distribution of galaxies, $N(z)$, as [103]

$$N_i(z) = \frac{1}{2} \left[\operatorname{erfc} \left(\frac{z_{i-1} - z}{\sqrt{2}\sigma(z)} \right) - \operatorname{erfc} \left(\frac{z_i - z}{\sqrt{2}\sigma(z)} \right) \right] z^\alpha \exp \left[- \left(\frac{z}{z_0} \right)^\beta \right], \quad (2.139)$$

where the function $\operatorname{erfc}(x)$ is the complementary error function:

$$\operatorname{erfc}(x) \equiv \frac{2}{\sqrt{\pi}} \int_x^\infty dz \exp(-z^2). \quad (2.140)$$

Example of power spectrum

Here we show examples of the angular spectrum assuming a single source located at a redshift, z . Fig. 2.6 shows the spectrum of the scalar lensing potential (or the E -mode shear), $C_\ell^{\phi\phi}$, generated by the matter density fluctuations with varying the source redshift from 1 to the CMB last-scattering surface (~ 1100). The amplitude of the angular spectra is larger at higher redshifts because the spectrum is given as the integral of the gravitational potential along the line-of-sight. The contribution to the power spectrum comes mostly from $z \sim z/2$ in each spectrum.

Systematics in cosmic shear measurements

Here we summarize systematics in the estimation of the cosmic shear.

- Reduced shear

As in Eq. (2.133), what we can estimate from galaxy's ellipticities is the reduced shear, $g = \gamma/(1 - \kappa)$, which is a combination of shear and convergence. Eq. (2.134) means that the shear can be estimated directly from the reduced shear only if $\kappa \ll 1$. Refs. [104, 105] estimate how the approximation, $\kappa \ll 1$, affects estimate of the shear in next generation galaxy surveys such as LSST and show size of systematic biases on dark energy constraints.

- Born approximation

In the Born approximation, the lensing effect is computed with the metric perturbations along the unperturbed path. For an accurate treatment of the lensing effect, however, we have to take into account higher-order corrections from metric perturbations on the “perturbed” geodesic. The correction terms are evaluated in Ref. [106].

- Baryon physics

At small scales where the lensing effect becomes significant, to accurately compute evolution of baryons, we should consider several physical process affecting on baryons. Refs. [107, 108] show how the physical process affects the lensing at small scales based on numerical simulation. But an accurate treatment of the physical process is still quite difficult, and uncertainties in the estimation of physical process would cause systematics for future surveys.

- Nonlinear evolution of density fluctuations

One of the most crucial uncertainties is the theoretical treatment of the nonlinear evolution of the density fluctuations. There are several fitting formulas to mimic the results of numerical simulations [109, 110]. But its accuracy heavily relies on the resolution of numerical simulation. Alternative approach such as analytic calculation with the perturbation theory would help to construct reliable fitting formulas.

Chapter 3

Weak Lensing from Scalar, Vector and Tensor Perturbations

Among various cosmological observations, a measurement of weak lensing signals is one of the direct probe of intervening gravitational fields along a line of sight. The weak lensing effect on background sources such as galaxies and CMB has been widely studied and now been accepted as a standard cosmological observable [111, 112, 113, 33, 114, 36, 80] (for reviews, see [101, 98]).

In this chapter, based on our work [74], including contributions from all components of metric perturbations, i.e., scalar, vector and tensor perturbations, we compute the deflection angle and deformation matrix (section 3.1), and its angular power spectrum (section 3.2). An interesting observation is that the curl-mode deflection angle and B-mode shear are produced by the vector and tensor perturbations, but not by the scalar perturbations. Hence, the non-vanishing curl mode or B-mode signal would be a direct evidence for non-scalar metric perturbations. Note that, for computing weak lensing effect from scalar, vector and tensor perturbations, we summarize useful formulas in appendix B. In Table 3.1, we summarize the definition of the quantities used throughout this thesis.

3.1 Lensing observables

Weak lensing effect is characterized in two ways, i.e., the deflection angle of light rays between the observer and sources, and the distortion of images. In the following, we derive the deflection angle and distortion of images using the geodesic equation, and geodesic deviation equations, respectively, following Yamauchi *et al* [74].

3.1.1 Geodesic equation and deflection angle

Geodesic equation

We consider a photon geodesic, $x^\mu(v)$, where v is the affine parameter. The geodesic lie in the past light cone of an observer at the origin of the coordinate system, O . Since null geodesic is not affected by conformal transformations, it is sufficient to consider the spacetime without the expansion of the universe [98]. Hence, along the geodesic, we introduce a tangent vector, k^μ , on the conformally transformed spacetime with the affine parameter λ [115]:

$$k^\mu \equiv a^2 \frac{dx^\mu}{dv} = \frac{dx^\mu}{d\lambda}. \quad (3.1)$$

The above four vector satisfies the null condition, $k^\mu k_\mu$, and

$$\frac{Dk^\mu}{D\lambda} \equiv k^\mu_{;\nu} k^\nu = \frac{d^2x^\mu}{d\lambda^2} + \Gamma^\mu_{\nu\rho} \frac{dx^\nu}{d\lambda} \frac{dx^\rho}{d\lambda} = 0. \quad (3.2)$$

Table 3.1: Notations for quantities used in the calculation of weak lensing observables and its power spectra.

Symbol	eq.	Definition
$\bar{g}_{\mu\nu}$	Eq. (1.4)	4-dimensional metric on background spacetime
γ_{ij}	Eq. (1.5)	3-dimensional spatial metric
$\omega_{ab}, \epsilon_{ab}$	Eq. (1.6)	Metric/Levi-Civita pseudo-tensor on unit sphere
semi-colon (;)	-	Covariant derivative associated with $\bar{g}_{\mu\nu}$
vertical bar ()	-	Covariant derivative associated with $\bar{\gamma}_{ij}$
colon (:)	Eq. (3.18)	Covariant derivative associated with ω_{ab}
∇^2	-	Laplace operator on the unit sphere
(...)	Eq. (3.65)	symmetric sum
{...}	Eq. (3.72)	antisymmetric sum
[...]	Eq. (3.67)	sum of symmetric trace-free part
e_χ^i	-	photon propagation direction
e_a^i	-	orthonormal space-like basis on the unit sphere
σ_χ, σ_a	Eq. (3.14)	projected quantities for vector perturbations
$D_{\chi\chi}, D_{a\chi}, D_{ab}$	Eq. (3.15)	projected quantities for tensor perturbations

where the semi-colon (;) denotes the covariant derivative in terms of $g_{\mu\nu}$, and $\Gamma^\mu_{\nu\rho}$ is the Christoffel symbols associated with $g_{\mu\nu}$. The above equation is called geodesic equation. In the following, we perturbatively solve Eq. (3.2) to obtain the unperturbed path, $\bar{x}^\mu(\lambda)$, and the small deviation from the unperturbed path, $\xi^\mu(\lambda)$. The former is obtained by solving the geodesic equation in the absence of the metric perturbations.

Unperturbed Geodesics

In the absence of metric perturbation, the Christoffel symbol in the Cartesian coordinate vanishes. Then, the geodesic equation becomes

$$\frac{d^2\bar{x}^\mu}{d\lambda^2} = 0. \quad (3.3)$$

The affine parameter at the observer is set to zero. Imposing the initial condition as

$$\bar{x}^\mu|_{\lambda=0} = 0, \quad \left. \frac{d\bar{x}^0}{d\lambda} \right|_{\lambda=0} = 1, \quad \left. \frac{d\bar{x}^i}{d\lambda} \right|_{\lambda=0} = -e_\chi^i, \quad (3.4)$$

the solution of the above equation is

$$\bar{x}^0(\lambda) = \lambda, \quad (3.5)$$

$$\bar{x}^i(\lambda) = -\lambda e_\chi^i, \quad (3.6)$$

where e_χ^i is the photon propagation direction measured from the observer in the background flat spacetime. Without the loss of generality, the energy of photon can be set to unity and the vector e_χ^i is the unit vector tangent to a geodesic on the flat three-space satisfying

$$\gamma_{ij} e_\chi^i e_\chi^j = 1, \quad (e_\chi^i)_{|j} e_\chi^j = 0. \quad (3.7)$$

From Eq. (3.6), the comoving distance are given by

$$\chi(\lambda) = \gamma_{ij} \bar{x}^i(\lambda) e_\chi^j = -\lambda. \quad (3.8)$$

Orthonormal space-like basis

Before solving the perturbed geodesic equation, we choose the basis vectors associated with the unperturbed path. Denoting the observer's 4-velocity at the observer position as u^μ , the orthonormal space-like basis, e_a^μ , with $a = \theta$ or φ , are chosen so that the basis are orthogonal to u^μ and the propagation direction, $\bar{k}^\mu = d\bar{x}^\mu/d\lambda$:

$$\bar{g}_{\mu\nu}\bar{k}^\mu e_a^\nu = \bar{g}_{\mu\nu}u^\mu e_a^\nu = 0. \quad (3.9)$$

The basis are also normalized as

$$\bar{g}_{\mu\nu}e_a^\mu e_b^\nu = \omega_{ab}. \quad (3.10)$$

They are parallelly transported along the geodesics as

$$u^\mu_{;\nu}\bar{k}^\nu = 0, \quad (3.11)$$

$$e_a^\mu_{;\nu}\bar{k}^\nu = 0. \quad (3.12)$$

For a static observer, we assume

$$u^0 = 1, \quad u^i = 0, \quad e_a^0 = 0. \quad (3.13)$$

We use the spatial basis vectors on the background spacetime in the Cartesian given in Eq. (1.3).

Given a vector quantity, X_i , the projected quantities are denoted as

$$X_\chi = X_i e_\chi^i, \quad X_a = X_i e_a^i. \quad (3.14)$$

Similarly, for a tensor quantity, X_{ij} , we define

$$X_{\chi\chi} = X_{ij} e_\chi^i e_\chi^j, \quad X_{a\chi} = X_{ij} e_a^i e_\chi^j, \quad X_{ab} = X_{ij} e_a^i e_b^j. \quad (3.15)$$

The angular index are raised or lowered by the two-dimensional metric on the sphere, e.g., $X^a = \omega^{ab}X_b$.

For a given quantity, X , we define the radial and angular derivative as

$$X_{,\chi} \equiv \frac{\partial X}{\partial \chi} \equiv e_\chi^i X_{,i}, \quad (3.16)$$

$$X_{,a} \equiv \frac{\partial X}{\partial a} \equiv \chi e_a^i X_{,i}, \quad (3.17)$$

On the other hand, for a projected-vector quantity, X_a , the covariant derivative on the unit sphere in terms of the two-dimensional basis is

$$X_{a:b} \equiv X_{a,b} - {}^{(2)}\bar{\Gamma}_{ab}^c X_c, \quad {}^{(2)}\bar{\Gamma}_{ab}^c \equiv e_i^c e_{a,b}^i. \quad (3.18)$$

where ${}^{(2)}\bar{\Gamma}_{ab}^c$ is the two dimensional Christoffel symbol defined on the unit sphere, and we have introduced the colon (:) as the covariant derivative with respect to the unit sphere metric ω_{ab} .

Perturbed Geodesic Equation

Now we derive the solution for the deviation vector, $\xi^\mu(\lambda)$. We set the metric perturbations at the observer position to zero because they can be absorbed into the homogeneous mapping. To derive the linear-order geodesic equation from Eq. (3.2), we expand the a photon geodesics as $x^\mu = \bar{x}^\mu + \xi^\mu$. In the Cartesian coordinate, the Christoffel symbols is the liner-order quantity, and we can rewrite Eq. (3.2) as

$$\frac{d^2\xi^\rho}{d\lambda^2} + \delta\Gamma_{\mu\nu}^\rho \bar{k}^\mu \bar{k}^\nu = 0. \quad (3.19)$$

At the linear-order in metric perturbations, the gravitational lensing effect generates the angular deviations on the geodesic equation. To extract the angular components of the deviation vector, $\xi^a = \xi^\mu e_\mu^a$, we multiply e_μ^a in both sides of Eq. (3.19), and the result is

$$\frac{d^2\xi^a}{d\lambda^2} = -e_i^a \delta\Gamma_{\mu\nu}^i \bar{k}^\mu \bar{k}^\nu, \quad (3.20)$$

where we use

$$\frac{d}{d\lambda} e_\mu^a = 0. \quad (3.21)$$

Perturbed Christoffel symbol

To solve the above equation, here we summarize the Christoffel symbol associated with the perturbed metric, $g_{\mu\nu}$. The first-order perturbation of the Christoffel symbol, $\delta\Gamma_{\nu\lambda}^\mu$, is given by

$$\delta\Gamma_{\nu\lambda}^\mu = \frac{1}{2} \bar{g}^{\mu\rho} [-2h_{\rho\sigma}\bar{\Gamma}_{\nu\lambda}^\sigma + h_{\rho\nu,\lambda} + h_{\rho\lambda,\nu} - h_{\nu\lambda,\rho}]. \quad (3.22)$$

In the Cartesian coordinate system, the unperturbed quantity vanishes, and the covariant derivative with respect to the unperturbed three-dimensional metric, $\gamma_{ij} = \delta_{ij}$, reduces to the usual derivative. Using the metric perturbation described in Eq. (1.10)), the Christoffel symbol for $\mu = 0$ including both unperturbed and perturbed contributions becomes

$$\Gamma_{00}^0 = \frac{\partial\Phi}{\partial\eta}, \quad \Gamma_{0i}^0 = \Gamma_{i0}^0 = \Phi_{,i}, \quad \Gamma_{ij}^0 = \frac{1}{2}(\sigma_{i,j} + \sigma_{j,i}) + \frac{\partial C_{ij}}{\partial\eta}, \quad (3.23)$$

where the linear perturbation of the spacial components are decomposed into the scalar and tensor parts:

$$C_{ij} = \Psi\delta_{ij} + D_{ij}. \quad (3.24)$$

For $\mu = i$, the components of the Christoffel symbols are given by

$$\Gamma_{00}^i = \Phi^{,i} - \frac{\partial\sigma^i}{\partial\eta}, \quad \Gamma_{0j}^i = \frac{1}{2}(\sigma_j^{,i} - \sigma_i^{,j}) + \frac{\partial C^i_j}{\partial\eta}, \quad \Gamma_{jk}^i = C^i_{j,k} + C^i_{k,j} - C^i_{jk}. \quad (3.25)$$

Note that all the Christoffel symbols are first order quantity.

Solution of Geodesic Equations

The source terms given in the right-hand side of Eq. (3.20) is decomposed into

$$e_i^a \delta\Gamma_{\mu\nu}^i \bar{k}^\mu \bar{k}^\nu = e_i^a \delta\Gamma_{00}^i - 2e_i^a \delta\Gamma_{0j}^i e_\chi^j + e_i^a \delta\Gamma_{jk}^i e_\chi^j e_\chi^k. \quad (3.26)$$

To go further, we combine the expression of the perturbed Christoffel symbols described in Eqs. (3.23) and (3.25). Then, the first term in the right-hand side of the above equation becomes

$$e_i^a \delta\Gamma_{00}^i = \frac{\Phi^{,a}}{\chi} - \frac{\partial\sigma^a}{\partial\eta}. \quad (3.27)$$

Similarly, the second term becomes

$$\begin{aligned} e_i^a \delta\Gamma_{0j}^i e_\chi^j &= \frac{1}{2} \left(e_\chi^j \frac{\sigma_j^{,a}}{\chi} - e_i^a \frac{\partial\sigma^i}{\partial\chi} \right) + e_i^a e_\chi^j \frac{\partial C^i_j}{\partial\eta} \\ &= \frac{1}{2} \left(e_\chi^j \frac{\sigma_j^{,a}}{\chi} - \frac{\partial\sigma^a}{\partial\chi} \right) + e_i^a e_\chi^j \frac{\partial D^i_j}{\partial\eta}, \end{aligned} \quad (3.28)$$

and the third term is given by

$$\begin{aligned} e_i^a \delta \Gamma_{jk}^i e_\chi^j e_\chi^k &= e_i^a \left[C_{j,k}^i + C_{k,j}^i - C_{jk}^{,i} \right] e_\chi^j e_\chi^k \\ &= e_i^a e_\chi^j \frac{\partial C_j^i}{\partial \chi} + e_i^a e_\chi^k \frac{\partial C_k^i}{\partial \chi} - e_\chi^j e_\chi^k C_{jk}^a \\ &= -\frac{\Psi,^a}{\chi} + 2e_i^a e_\chi^j \frac{\partial D_j^i}{\partial \chi} - e_\chi^j e_\chi^k \frac{D_{jk}^a}{\chi}, \end{aligned} \quad (3.29)$$

Substituting Eqs. (3.27) - (3.29) into Eq. (3.26), the angular components of Eq. (3.20) becomes

$$\begin{aligned} \frac{d^2 \xi^a}{d\chi^2} &= \frac{\Phi,^a}{\chi} + \frac{\partial \sigma^a}{\partial \eta} + e_\chi^j \frac{\sigma_j^a}{\chi} - \frac{\partial \sigma^a}{\partial \chi} + 2e_i^a e_\chi^j \frac{\partial D_j^i}{\partial \eta} - \frac{\Psi,^a}{\chi} - 2e_i^a e_\chi^j \frac{\partial D_j^i}{\partial \chi} + e_\chi^j e_\chi^k \frac{D_{jk}^a}{\chi} \\ &= \frac{(\Phi - \Psi),^a}{\chi} - \frac{d\sigma^a}{d\chi} + e_\chi^j \frac{\sigma_j^a}{\chi} - 2e_i^a e_\chi^j \frac{dD_j^i}{d\chi} + e_\chi^j e_\chi^k \frac{D_{jk}^a}{\chi} \\ &= \frac{\omega^{ab}}{\chi} \left[(\Phi - \Psi),_b + (\sigma_\chi),_b - \frac{d(\chi \sigma_b)}{d\chi} + (D_{\chi\chi}),^b - 2 \frac{d(\chi D_{b\chi})}{d\chi} \right], \end{aligned} \quad (3.30)$$

where we use $d/d\lambda = -d/d\chi$. We also use the fact that, for a perturbed quantity, X ,

$$\frac{dX}{d\lambda} = -\frac{d\bar{x}^\mu}{d\lambda} X,_\mu = -\frac{\partial X}{\partial \eta} + \frac{\partial X}{\partial \chi}, \quad (3.31)$$

Imposing the initial conditions, $\xi^a|_O = 0$ and $(d\xi^a/d\chi)|_O = \delta\theta_O^a$, where $\delta\theta_O^a$ denotes the angular coordinate at the observer position, the solution of Eq. (3.30) becomes

$$\frac{\xi^a(\chi)}{\chi} = \delta\theta_O^a + \omega^{ab} \int_0^\chi d\chi' \frac{\chi - \chi'}{\chi \chi'} \left\{ \mathcal{A},_b(\bar{x}^i) - \frac{d[\chi' \mathcal{B}_b(\bar{x}^i)]}{d\chi'} \right\}, \quad (3.32)$$

where we define the three vector, $\bar{x}^i = \chi' e_\chi^i$, and

$$\mathcal{A} = \Phi - \Psi + \sigma_\chi + D_{\chi\chi}, \quad \mathcal{B}_b = \sigma_b - 2D_{b\chi}. \quad (3.33)$$

In the above, the integral at the right-hand-side is evaluated along the unperturbed light path according to the Born approximation.

Deflection Angle

Provided the deviation vector at the both end points, the deflection angle, $\Delta^a \equiv \mathbf{d} \cdot \mathbf{e}^a$, is defined as [33]

$$\Delta^a(\chi) \equiv \frac{\xi^a(\chi)}{\chi} - \delta\theta_O^a. \quad (3.34)$$

With Eq. (??) the deflection angle is described by the sum of the two terms (e.g., [10]):

$$\Delta_a = \phi,_a + \varpi,_b \epsilon^b_a, \quad (3.35)$$

where ϵ^b_a denotes the two dimensional Levi-Civita pseudo-tensor. The lensing potential and curl mode in the case of the vector perturbations can be written as

$$\nabla^2 \phi = \Delta^a,_a = \int_0^\chi \frac{d\chi'}{\chi'} \left\{ \frac{\chi - \chi'}{\chi} \nabla^2 \mathcal{A} - \mathcal{B}^a,_a \right\}, \quad (3.36)$$

$$\nabla^2 \varpi = \Delta^a,_b \epsilon^b_a = - \int_0^\chi \frac{d\chi'}{\chi'} \mathcal{B}^a,_b \epsilon^b_a, \quad (3.37)$$

where ∇^2 is the Laplace operator on the sphere; $\nabla^2\phi = \phi_{:ab}\omega^{ab} = \phi^{:a}_{:a}$. Note that Eq. (3.37) coincides with Eq. (1.4) of Ref. [35]. The curl component of the deflection becomes non-vanishing in the presence of vector or tensor component, \mathcal{B}_b .

Finally, to relate the deflection angle to observables, we express the affine parameter, χ , in terms of some observable quantities. In the first-order perturbation, the parameter, χ , can be considered as the comoving distance computed in the unperturbed metric, since the all quantities in the expression of deflection angle is linear order quantities. Then, the parameter, χ , is given by the redshift through Eq. (2.16).

3.1.2 Geodesic deviation equation and Jacobi mapping

Geodesic deviation equation

Here, following Refs. [116, 113, 117, 100], we derive the geodesic deviation equation, and introduce the Jacobi matrix. Let us consider the propagation of a light bundle, i.e., a collection of nearby light rays expressed by two geodesics, $x^\mu(\lambda)$ and $y^\mu(\lambda) = x^\mu(\lambda) + \xi^\mu(\lambda)$. These two paths are connected by the deviation vector, ξ^μ . We assume that the affine parameter at the observer is $\lambda = 0$, and $\xi^\mu(\lambda = 0) = 0$. Using the wave vector, $k^\mu = dx^\mu/d\lambda$, the derivative along the path for ξ^μ is

$$\frac{D}{D\lambda}\xi^\mu = \xi^\mu_{;\alpha}k^\alpha = \xi^\mu_{,\alpha}\frac{dx^\alpha}{d\lambda} + \Gamma^\mu_{\alpha\beta}k^\alpha\xi^\beta = \frac{d\xi^\mu}{d\lambda} + \Gamma^\mu_{\alpha\beta}k^\alpha\xi^\beta. \quad (3.38)$$

The derivative of the deviation vector along the path becomes

$$\frac{d\xi^\mu}{d\lambda} = \frac{dy^\mu}{d\lambda} - \frac{dx^\mu}{d\lambda} = k^\mu(x + \xi) - k^\mu(x) = \xi^\alpha k^\mu_{;\alpha}. \quad (3.39)$$

This leads to

$$\frac{D}{D\lambda}\xi^\mu = \xi^\nu k^\mu_{;\nu}. \quad (3.40)$$

Differentiating both sides of the above equation along the path of geodesic again, we obtain

$$\begin{aligned} \frac{D^2}{D\lambda^2}\xi^\mu &= \frac{D}{D\lambda}\xi^\alpha k^\mu_{;\alpha} = k^\mu_{;\alpha}\frac{D}{D\lambda}\xi^\alpha + \xi^\beta\frac{D}{D\lambda}k^\mu_{;\beta} \\ &= \xi^\beta k^\alpha_{;\beta}k^\mu_{;\alpha} + \xi^\beta k^\alpha k^\mu_{;\beta\alpha} \\ &= -\xi^\beta k^\alpha k^\mu_{;\alpha\beta} + \xi^\beta k^\alpha k^\mu_{;\beta\alpha} \\ &= -\xi^\beta k^\alpha [k^\mu_{;\alpha\beta} - k^\mu_{;\beta\alpha}], \end{aligned} \quad (3.41)$$

where, in the last line, we use $k^\alpha k^\mu_{;\alpha} = 0$. Using the Bianchi identity,

$$k^\mu_{;\alpha\beta} - k^\mu_{;\beta\alpha} = -R^\mu_{\nu\alpha\beta}k^\nu, \quad (3.42)$$

evolution equation of the deviation vector, ξ^μ , is described by

$$\frac{D^2}{D\lambda^2}\xi^\mu = R^\mu_{\nu\alpha\beta}\xi^\beta k^\nu k^\alpha, \quad (3.43)$$

where $R^\mu_{\nu\alpha\beta}$ is the Riemann tensor.

Next, we introduce the Jacobi matrix which relates the coordinate systems between image and source planes. We use the coordinate system whose basis vectors are the four-velocity at the observer, u^μ , wave vector, $k^\mu = dx^\mu/d\lambda$,

and the two transverse vectors, n_a^μ . The two-dimensional plane given by two basis, n_θ^μ and n_φ^μ , is usually referred to as screen. The quantity, ξ^μ , is decomposed into the line-of sight and transverse components:

$$\xi^\mu = \xi^a n_a^\mu + \xi^0 k^\mu. \quad (3.44)$$

The angular component, ξ^a , is the angle separation between two paths for arbitrary affine parameter, λ . Given the initial conditions at the observer, $\xi^a|_O = 0$ and $(d\xi^a/d\lambda)|_O = \delta\theta_O^a$, the solution of Eq. (3.43) is generally given by

$$\xi^a(\lambda) = \mathcal{D}^a{}_b(\lambda)\theta_O^b, \quad (3.45)$$

where the matrix, $\mathcal{D}^a{}_b$, is the Jacobi matrix.

To derive the evolution equation of the Jacobi matrix, we consider the equation of ξ^a . From Eq. (3.43), we obtain

$$\frac{d^2\xi^a}{d\lambda^2} = \mathcal{T}^a{}_b \xi^b, \quad (3.46)$$

where we define the optical tidal matrix as

$$\mathcal{T}_{ab} = R_{\mu\nu\rho\sigma} k^\nu k^\rho n_a^\mu n_b^\sigma. \quad (3.47)$$

This gives the evolution equation for the Jacobi matrix

$$\frac{d^2\mathcal{D}^a{}_b}{d\lambda^2} = \mathcal{T}^a{}_c \mathcal{D}^c{}_b, \quad (3.48)$$

with the initial condition at the observer O rewritten with

$$\mathcal{D}^a{}_b|_O = 0, \quad \frac{d}{d\lambda}\mathcal{D}^a{}_b|_O = \delta^a{}_b. \quad (3.49)$$

Solution of geodesic deviation equation in the perturbed universe

To get the expressions for the unperturbed and perturbed solutions, we expand Eq. (3.48) with

$$\mathcal{D}^a{}_b = \bar{\mathcal{D}}^a{}_b + \delta\mathcal{D}^a{}_b, \quad (3.50)$$

$$\mathcal{T}^a{}_b = \delta\mathcal{T}^a{}_b, \quad (3.51)$$

where we use the fact that the tidal matrix vanishes in the unperturbed space-time. Substituting the above quantities into Eq. (3.48) we obtain the zeroth and first order equations of Jacobi map:

$$\frac{d^2\bar{\mathcal{D}}^a{}_b}{d\lambda^2} = 0, \quad (3.52)$$

$$\frac{d^2\delta\mathcal{D}^a{}_b}{d\lambda^2} = \delta\mathcal{T}^a{}_c \bar{\mathcal{D}}^c{}_b. \quad (3.53)$$

With the initial conditions (3.49), the zeroth-order solution is given by

$$\bar{\mathcal{D}}^a{}_b(\lambda) = \lambda\delta^a{}_b. \quad (3.54)$$

Next we consider the first-order solution of the Jacobi matrix. Using the zeroth-order solution, we obtain

$$\frac{d\delta\mathcal{D}^a{}_b}{d\lambda} = \int_0^\lambda d\lambda' \lambda' \delta\mathcal{T}^a{}_c. \quad (3.55)$$

Then, integrate both sides of the above equation again, we obtain the expression valid up to the linear-order in metric perturbations:

$$\mathcal{D}^a{}_b(\lambda) = \lambda \delta^a{}_b + \int_0^\lambda d\lambda' (\lambda - \lambda') \lambda' \delta \mathcal{T}^a{}_b(\lambda') + \mathcal{O}(h^2), \quad (3.56)$$

where we use

$$\int_0^\lambda d\lambda' \int_0^{\lambda'} d\lambda'' = \int_0^\lambda d\lambda'' \int_{\lambda''}^\lambda d\lambda'. \quad (3.57)$$

In the above, an important observation is that the resultant Jacobi map is always symmetric. Hence, the anti-symmetric part of the Jacobi map, which is directly related to the rotation mode, does not appear at the linear order. Note that it is convenient to transform the variable from λ to the conformal distance including the effect of perturbation:

$$d\tilde{\chi} = -k^0 d\lambda. \quad (3.58)$$

Using the variable, $\tilde{\chi}$, Eq. (3.56) is rewritten as

$$\mathcal{D}^a{}_b(\tilde{\chi}) = - \int_0^{\tilde{\chi}} d\tilde{\chi} (2 - k^0) \delta^a{}_b - \int_0^{\tilde{\chi}} d\chi' (\chi - \chi') \chi' \delta \mathcal{T}^a{}_b(\chi'), \quad (3.59)$$

where, in the second term, we use the unperturbed quantity, χ , instead of $\tilde{\chi}$, and we use

$$\frac{1}{k^0} = \frac{1}{1 + (k^0 - 1)} \simeq 2 - k^0. \quad (3.60)$$

To relate the Jacobi matrix with the metric perturbations given in Eq. (1.10), we have to explicitly write down the tidal matrix (3.47) in terms of the metric perturbations which is given in appendix B. The Jacobi matrix is finally given by

$$\mathcal{D}_{ab}(\tilde{\chi}) = \tilde{\chi} \omega_{ab} + \sum_{I=S,V,T} \int_0^{\tilde{\chi}} d\chi' \chi' (\chi - \chi') \delta \mathcal{T}_{ab}^{(I)}, \quad (3.61)$$

with

$$\mathcal{T}_{ab}^{(S)} = -\frac{1}{\chi^2} (\Phi - \Psi)_{:ab} - \frac{1}{\chi} \omega_{ab} \frac{\partial(\Phi - \Psi)}{\partial \chi} + \omega_{ab} \frac{d^2 \Psi}{d\chi^2}, \quad (3.62)$$

$$\mathcal{T}_{ab}^{(V)} = \frac{1}{\chi^2} \left\{ (\sigma_\chi)_{:ab} - \frac{d}{d\chi} (\chi \sigma_{(a:b)}) + \chi \omega_{ab} \frac{\partial \sigma_\chi}{\partial \eta} \right\}, \quad (3.63)$$

$$\mathcal{T}_{ab}^{(T)} = \frac{1}{\chi^2} \left\{ (D_{\chi\chi})_{:ab} - 2 \frac{d}{d\chi} [\chi D_{\chi(a:b)}] + \chi \frac{d^2}{d\chi^2} [\chi D_{ab}] + \chi \omega_{ab} \left(\frac{d}{d\chi} D_{\chi\chi} - \frac{\partial}{\partial \eta} D_{\chi\chi} \right) \right\}. \quad (3.64)$$

Note that we define an operator as

$$\sigma_{(a:b)} = \frac{\sigma_{a:b} + \sigma_{b:a}}{2}, \quad D_{\chi(a:b)} = \frac{D_{\chi a:b} + D_{\chi b:a}}{2}. \quad (3.65)$$

From Jacobi matrix to observables

Since we are interested in the shear field, here we relate the shear fields with the metric perturbations. For shear field, from Eq. (2.132), it is sufficient to consider the symmetric trace-free part of the Jacobi map:

$$\gamma_{ab} \equiv \frac{1}{\tilde{\chi}} \mathcal{D}_{[ab]}(\tilde{\chi}), \quad (3.66)$$

where the angle bracket $[\dots]$ denotes the symmetric trace-free part taken in the two-dimensional space:

$$X_{[ab]} \equiv \frac{X_{ab} + X_{ba} - X^c{}_c \omega_{ab}}{2}. \quad (3.67)$$

The symmetric trace-free part of Eq. (3.61) is (see also [100, 118])

$$\begin{aligned} \gamma_{ab} = & [D_{[ab]}]_0^\chi + \int_0^\chi d\chi' \frac{\chi - \chi'}{\chi\chi'} \\ & \times \left\{ \mathcal{A}_{:[ab]} - \frac{d}{d\chi'} [\chi' \mathcal{B}_{[a:b]}] + \chi' \frac{d^2}{d\chi'^2} [\chi' D_{[ab]}] \right\}. \end{aligned} \quad (3.68)$$

We will use it to derive the formulas for angular power spectra of the E-/B-mode cosmic shear. Finally, we note that the rotation is not generated from the linear perturbations.

Relation between Jacobi map and deflection angle

It is interesting to mention on the relation between the Jacobi map and deflection angle in the presence of vector and tensor metric perturbations. In the presence of tensor perturbations, the relation between the shear matrix and deflection angle becomes

$$\gamma_{ab} = \Delta_{[a:b]} + \frac{1}{2} [D_{[ab]}]_0^\chi. \quad (3.69)$$

This relation is valid at linear order, and in the absence of the tensor perturbations, the above relation reduces to the one empirically defined in [33]:

$$\gamma_{ab} = \Delta_{[a:b]}. \quad (3.70)$$

On the other hand, no such expression is obtained for the relation between $\mathcal{D}^a{}_b$ and $\Delta^a{}_{:b}$ because of the non-vanishing trace part.

3.2 Formulation of Angular Power Spectrum

In this section, we briefly summarize the angular power spectrum of the gradient/curl modes and E/B mode shear. The formula of the angular power spectra are respectively given in Eqs. (3.78), (3.80) and (3.85) for the gradient-/curl-mode deflection angle, and in Eqs. (3.90), (3.92) and (3.97), for the E -/ B -mode shear. We then discuss an interesting relation for angular power spectra between the deflection angle and the cosmic shear.

3.2.1 Angular power spectrum of lensing potentials

Based on the expressions (3.36) and (3.37), let us consider the angular spectrum of the gradient and curl modes of the deflection angle. First notice that the metric on the sphere, ω^{ab} , and the Levi-Civita pseudo-tensor, ϵ^{ab} , can be rewritten in terms of the basis vectors e_\pm^a with [98]

$$\omega^{ab} = e_+^{(a} e_-^{b)}, \quad \epsilon^{ab} = i e_+^{\{a} e_-^{b\}}, \quad (3.71)$$

where we have introduced the anti-symmetric operation defined by

$$A_{\{a} B_{b\}} = \frac{1}{2} (A_a B_b - A_b B_a). \quad (3.72)$$

From Eqs. (3.36) and (3.37), the gradient and curl modes are recast as

$$\nabla^2 \phi = \int_0^\chi \frac{d\chi'}{\chi'} \left\{ \frac{\chi - \chi'}{\chi} (\mathcal{A})_{:ab} - \mathcal{B}_{a:b} \right\} e_+^{(a} e_-^{b)} , \quad (3.73)$$

$$\nabla^2 \varpi = -i \int_0^\chi \frac{d\chi'}{\chi'} \mathcal{B}_{a:b} e_-^{(a} e_+^{b)} . \quad (3.74)$$

In the above, the metric perturbations contain statistical information for spatial randomness, which can be decomposed into the Fourier modes according to Eqs. (1.11) - (1.14). For scalar modes, we assume

$$\langle \Psi(\mathbf{k}, \eta) \Psi(\mathbf{k}, \eta') \rangle = (2\pi)^3 \delta_D(\mathbf{k} - \mathbf{k}') P^{(0)}(k, \eta, \eta') , \quad (3.75)$$

and $\Phi = \Psi$. Similarly, for vector mode, assuming the unpolarized state of vector fluctuations, their statistical properties are characterized by

$$\langle \sigma^{(m)*}(\mathbf{k}, \eta) \sigma^{(m')}(\mathbf{k}', \eta') \rangle = \begin{cases} \frac{1}{2} P^{(1)}(k; \eta, \eta') (2\pi)^3 \delta_D(\mathbf{k} - \mathbf{k}') & : m = m' = \pm 1 \\ 0 & : \text{otherwise} \end{cases} . \quad (3.76)$$

For tensor modes, we assume

$$\langle D^{(m)*}(\mathbf{k}, \eta) D^{(m')}(\mathbf{k}', \eta') \rangle = \begin{cases} \frac{1}{2} P^{(2)}(k; \eta, \eta') (2\pi)^3 \delta_D(\mathbf{k} - \mathbf{k}') & : m = m' = \pm 2 \\ 0 & : \text{otherwise} \end{cases} . \quad (3.77)$$

Finally, the angular power spectra are decomposed into the contributions from the scalar, vector and tensor perturbations as

$$C_\ell^{xx} = \frac{2}{\pi} \int_0^\infty k^3 d \ln k \int_0^\chi k d\chi' \int_0^\chi k d\chi'' \times \sum_{m=-2}^2 S_{x,\ell}^{(m)}(k, \chi') S_{x,\ell}^{(m)}(k, \chi'') P^{(m)}(k; \eta_0 - \chi', \eta_0 - \chi'') , \quad (3.78)$$

$$C_\ell^{\phi\varpi} = 0 . \quad (3.79)$$

The expressions of the transfer function, $S_{x,\ell}^{(m)}$, are summarized as follows

- scalar perturbations

$$S_{\phi,\ell}^{(0)}(k, \chi') = \frac{\chi - \chi'}{\chi} {}_0\epsilon_\ell^{00}(k\chi') , \quad (3.80)$$

$$S_{\varpi,\ell}^{(0)}(k, \chi') = 0 . \quad (3.81)$$

- vector perturbations

$$S_{\phi,\ell}^{(\pm 1)}(k, \chi') = \frac{\chi - \chi'}{\chi} {}_0\epsilon_\ell^{1,\pm 1}(k\chi') - \sqrt{\frac{2}{\ell(\ell+1)}} {}_1\epsilon_\ell^{1,\pm 1}(k\chi') , \quad (3.82)$$

$$S_{\varpi,\ell}^{(\pm 1)}(k, \chi') = \sqrt{\frac{2}{\ell(\ell+1)}} {}_1\beta_\ell^{1,\pm 1}(k\chi') , \quad (3.83)$$

- tensor perturbations

$$S_{\phi,\ell}^{(\pm 2)}(k, \chi') = \frac{\chi - \chi'}{\chi} \sqrt{\frac{4}{3}} {}_0\epsilon_\ell^{2,\pm 2}(k\chi') - \sqrt{\frac{2}{\ell(\ell+1)}} {}_1\epsilon_\ell^{2,\pm 2}(k\chi') + \frac{2}{5} \delta_{\ell,2} \delta(k\chi') , \quad (3.84)$$

$$S_{\varpi,\ell}^{(\pm 2)}(k, \chi') = {}_1\beta_\ell^{2,\pm 2}(k\chi') . \quad (3.85)$$

3.2.2 Angular power spectrum of shear fields

Shear fields

In discussing the spatial patterns of shear fields on celestial sphere, it is convenient to express the quantities with the polarization vectors. With the polarization basis, the Jacobi map can be decomposed into the spin-0 and spin- ± 2 components as similar to the intensity matrix:

$${}_0\mathcal{D} = \mathcal{D}_{ab}e_+^a e_-^b, \quad {}_{\pm 2}\mathcal{D} = \mathcal{D}_{ab}e_\pm^a e_\pm^b. \quad (3.86)$$

As we mentioned, the Jacobi map at the linear order is symmetric, and the spin-0 part of the linear-order Jacobi map contains only the trace part, which is related to the convergence field κ . On the other hand, the spin- ± 2 parts give the shear fields, γ and γ^* :

$$\begin{aligned} \gamma &= -\frac{{}^{+2}\mathcal{D}}{2\chi_S} = -\frac{1}{2}\gamma_{ab}e_+^a e_+^b, \\ \gamma^* &= -\frac{{}^{-2}\mathcal{D}}{2\chi_S} = -\frac{1}{2}\gamma_{ab}e_-^a e_-^b. \end{aligned} \quad (3.87)$$

Then, the reduced shear is related to the spin-weighted Jacobi map as

$$g = \frac{\gamma}{1 - \kappa} = -\frac{{}^{+2}\mathcal{D}}{{}_0\mathcal{D}}, \quad g^* = -\frac{{}^{-2}\mathcal{D}}{{}_0\mathcal{D}}. \quad (3.88)$$

Using the reduced shear given in the above equations, we can obtain the E and B mode shear, \mathcal{E} and \mathcal{B} , with Eqs. (2.135) and (2.136).

With the preliminary setup mentioned above, let us show the explicit expression for E/B-mode shear power spectra. Multiplying $e_+^a e_+^b$ in both side of Eq. (3.68), the spin +2 part of the reduced shear, Eq. (3.88), is written as (see also [100])

$$\begin{aligned} g &= -\frac{1}{2}e_+^a e_+^b \left\{ [D_{\langle ab \rangle}]_0^\chi + \int_0^\chi d\chi' \frac{\chi - \chi'}{\chi\chi'} \right. \\ &\quad \times \left. \left[(\Phi - \Psi + \sigma_\chi + D_{\chi\chi})_{\langle ab \rangle} - \frac{d}{d\chi'} [\chi'(\sigma_{\langle a:b \rangle} + D_{\chi\langle a:b \rangle})] + \chi' \frac{d^2}{d\chi'^2} [\chi' D_{\langle ab \rangle}] \right] \right\}. \end{aligned} \quad (3.89)$$

Similar to the case of lensing potentials, an efficient way to compute the angular power spectrum is to expands E and B mode shear in terms of the total-angular momentum method. Expanding Eq. (3.89) with the spin-2 total-angular momentum basis, and substituting it into Eqs. (2.135) and (2.136), we obtain expressions of the coefficients, $\mathcal{E}_\ell^{(m)}$ and $\mathcal{B}_\ell^{(m)}$, in terms of the metric perturbations (the details of calculation is presented in appendix B). The resultant expressions become

$$\begin{aligned} C_\ell^{XX} &= \frac{2}{\pi} \int_0^\infty k^2 dk \int_0^\chi k d\chi' \int_0^\chi k d\chi'' \\ &\quad \times \sum_{m=-2}^2 S_{X,\ell}^{(m)}(k, \chi') S_{X,\ell}^{(m)}(k, \chi'') P_{(m)}(k; \eta_0 - \chi', \eta_0 - \chi''), \end{aligned} \quad (3.90)$$

$$C_\ell^{\mathcal{EB}} = 0. \quad (3.91)$$

The transfer functions, $S_{X,\ell}^{(m)}$ are summarized in the following:

- scalar perturbations

$$S_{\mathcal{E},\ell}^{(0)}(k, \chi') = \frac{1}{2} \sqrt{\frac{(\ell+2)!}{(\ell-2)!}} S_{\phi,\ell}^{(0)}(k, \chi'), \quad (3.92)$$

$$S_{\mathcal{B},\ell}^{(0)}(k, \chi') = 0 \quad (3.93)$$

- vector perturbations

$$S_{\mathcal{E},\ell}^{(\pm 1)}(k, \chi') = \frac{1}{2} \sqrt{\frac{(\ell+2)!}{(\ell-2)!}} S_{\phi,\ell}^{(\pm 1)}(k, \chi'), \quad (3.94)$$

$$S_{\mathcal{B},\ell}^{(\pm)}(k, \chi') = \frac{1}{2} \sqrt{\frac{(\ell+2)!}{(\ell-2)!}} S_{\varpi,\ell}^{(\pm 1)}(k, \chi'). \quad (3.95)$$

- tensor perturbations

$$\begin{aligned} S_{\mathcal{E},\ell}^{(\pm 2)}(k, \chi') &= \frac{1}{2} \sqrt{\frac{(\ell+2)!}{(\ell-2)!}} S_{\phi,\ell}^{(\pm 2)}(k, \chi') \\ &\quad + \frac{1}{\sqrt{2}} {}^2\epsilon_\ell^{2,\pm 2}(k\chi') \delta(k\chi' - k\chi_s) + \frac{1}{5} \delta_{\ell,2} \delta(k\chi'), \end{aligned} \quad (3.96)$$

$$S_{\mathcal{B},\ell}^{(\pm 2)}(k, \chi') = \frac{1}{2} \sqrt{\frac{(\ell+2)!}{(\ell-2)!}} S_{\varpi,\ell}^{(\pm 2)}(k, \chi') + \frac{1}{\sqrt{2}} {}^2\beta_\ell^{2,\pm 2}(k\chi') \delta(k\chi' - k\chi_s). \quad (3.97)$$

Shear-deflection relation

Here, we briefly mention the relation between E/B-mode cosmic shear and gradient-/curl-mode deflection angle. From Eq. (3.69), with only vector perturbations, the symmetric trace-free part of the Jacobi map (shear) is directly related to the deflection angle which can be decomposed into the gradient and curl modes:

$$\Delta_{\langle ab \rangle} = \phi_{\langle ab \rangle} + \varpi_{:c \langle a} \epsilon^c_{\rangle b} = \gamma_{ab}. \quad (3.98)$$

This means that we can extract the vector-induced gradient-/curl-modes from the vector-induced shear. Taking the divergence and then taking the divergence or curl again on Eq. (3.98), we find

$$\gamma_{ab}^{:ab} = \frac{1}{2} \nabla^2 (\nabla^2 + 2) \phi, \quad \epsilon^{ca} \gamma_{ab}^{:b:c} = \frac{1}{2} \nabla^2 (\nabla^2 + 2) \varpi. \quad (3.99)$$

The above relation can be further reduced to simplified forms if we move to the harmonic space. After lengthy calculation presented in Ref. [74], we obtain the explicit relation between the lensing potentials and the shear fields:

$$\phi_{\ell m} = 2 \sqrt{\frac{(\ell-2)!}{(\ell+2)!}} \mathcal{E}_{\ell m}, \quad (3.100)$$

$$\varpi_{\ell m} = 2 \sqrt{\frac{(\ell-2)!}{(\ell+2)!}} \mathcal{B}_{\ell m}. \quad (3.101)$$

Thus, we reach at the relation between angular power spectra for shear and deflection angle:

$$C_\ell^{\phi\phi} = 4 \frac{(\ell-2)!}{(\ell+2)!} C_\ell^{\mathcal{E}\mathcal{E}}, \quad C_\ell^{\varpi\varpi} = 4 \frac{(\ell-2)!}{(\ell+2)!} C_\ell^{\mathcal{B}\mathcal{B}}, \quad C_\ell^{\phi\varpi} = C_\ell^{\mathcal{E}\mathcal{B}} = 0. \quad (3.102)$$

These relations are nontrivial, but are generally valid as long as the relation between the deflection angle and the Jacobi map, Eq. (3.98), holds. In other words, in the presence of tensor perturbations, the relations given here does not hold.

Chapter 4

Cosmological Implications from Weak Lensing

In this chapter, we discuss cosmological implications from measurements of weak lensing spectra, i.e., gradient/curl modes, $C_\ell^{\phi\phi}$, $C_\ell^{\varpi\varpi}$, and E/B-mode shear, $C_\ell^{\mathcal{E}\mathcal{E}}$, $C_\ell^{\mathcal{B}\mathcal{B}}$.

4.1 Cosmological information from CMB lensing and cosmic shear

Here we show how the lensing spectra depend on cosmological parameters. In particular, for later analysis in this chapter, we consider dependence on the total mass of neutrinos, primordial GWs and cosmic strings.

Gradient mode/ E-mode shear

Massive neutrinos lead to a characteristic suppression on the growth of large scale structure below the free-streaming scale. Since the characteristic wavenumber of the free-streaming scale becomes large as increasing the neutrino mass, as a consequence, the logarithmic derivative of lensing spectra can be negative, and decreases as increasing multipoles. That is, the amplitude of lensing spectra is reduced with the effect of neutrino mass at small scales, and with a high angular resolution lensing experiment, we would detect a clear signature of free-streaming suppression.

Fig. 4.1 shows the logarithmic derivatives of angular spectra, $C_\ell^{\phi\phi}$, and $C_\ell^{\mathcal{E}_3\mathcal{E}_3}$, with respect to the neutrino mass (right). Here, the quantity \mathcal{E}_3 represents the shear field estimated from the galaxy at redshift $z \sim 1.5$. For comparison, we also show the dependence on matter density, i.e., the logarithmic derivative $d \ln C_\ell / d \ln \Omega_m h^2$. It is clearly shown that the derivative of angular power spectra in terms of neutrino mass has scale-dependence. Although this scale-dependent nature of the lensing power spectra is, in principle, very powerful to constrain the neutrino mass, we note here that there exist some parameters that exhibit a similar scale-dependence, which can be the source of parameter degeneracy. As shown in Fig. 4.1, the logarithmic derivative of the lensing spectra with respect to the quantity $\ln \Omega_m h^2$ gives a similar trend to that of the neutrino mass parameter, and thus the density parameter $\Omega_m h^2$ can mimic a scale-dependent suppression by massive neutrino. For more quantitative aspect of the parameter estimation, we will proceed to the Fisher analysis.

Curl mode/ B-mode shear

The GWs can produce the metric perturbations which have odd parity symmetry. This means that the lensing effect induced by the GWs cause the curl mode of deflection angle and B-mode shear [45, 47, 34, 46]). Since the B-mode shear is related to the curl mode as Eq. (3.101), here we focus on the curl mode.

The curl-mode angular power spectrum generated by primordial GWs is given by [47]

$$C_\ell^{\varpi\varpi} = \frac{8}{\pi \ell^2 (\ell + 1)^2} \frac{(\ell + 2)!}{(\ell - 2)!} r A_s \int \frac{dk}{k} [\Delta_\ell^{\text{GW}}(k, \eta)]^2, \quad (4.1)$$

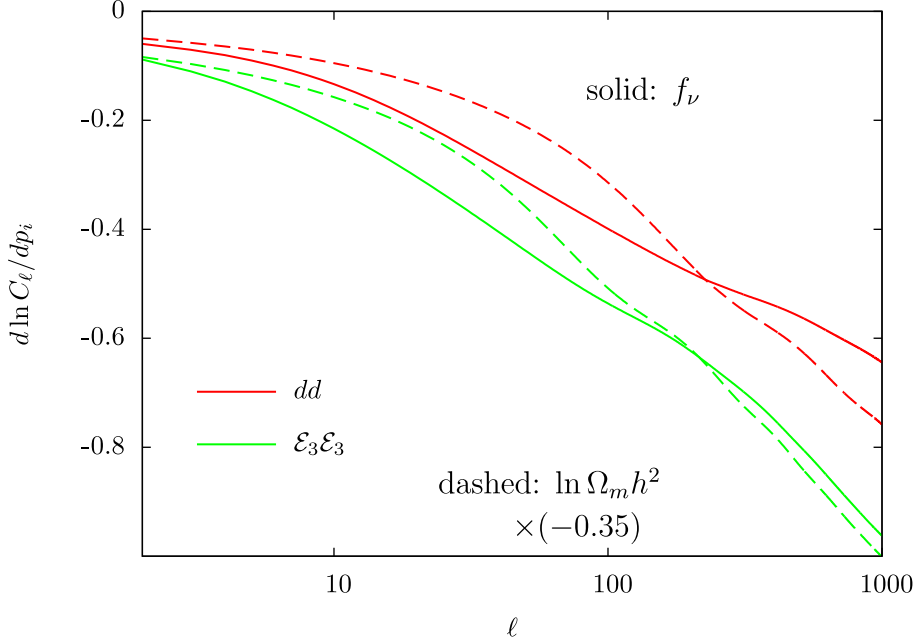


Figure 4.1: Logarithmic derivatives of the lensing spectra, $C_\ell^{\phi\phi}$ and $C_\ell^{\mathcal{E}_3\mathcal{E}_3}$, with respect to $\sum m_\nu$ and $\Omega_m h^2$. The galaxies are divided into three redshift bins and we plot the results for the highest redshift subsample ($1.14 < z$). For illustrative purpose, $d \ln C_\ell / d \ln \Omega_m h^2$ is multiplied by -0.35 . The derivatives are evaluated around the fiducial set of cosmological parameters summarized in Table 1.1.

with

$$\Delta_\ell^{\text{GW}}(k, \eta) = \int_{\eta_*}^{\eta_0} k d\eta \left(\frac{3j_1(k\eta)}{k\eta} \right) \frac{j_\ell(x)}{x^2} \Big|_{x=k(\eta_0-\eta)}. \quad (4.2)$$

The quantity, η_* , denotes the conformal time at the last scattering surface, and the quantity r is the tensor-to-scalar ratio.

On the other hand, extended objects such as cosmic strings produce not only the scalar perturbations but also the vector/tensor perturbations, and induce the curl mode and B-mode shear. For simplicity, we focus on the odd-parity quantities only from vector perturbations for cosmic strings. To compute the curl mode, we consider a string network model given in section 2.3.2. If the string tension, $G\mu$, and intercommuting probability, P , are given, the curl mode from cosmic strings are computed as follows [74]:

$$C_\ell^{\varpi\varpi} = \frac{4}{\ell(\ell+1)} (16\pi G\mu)^2 \sqrt{\frac{2}{3\pi}} \frac{v^2}{1-v^2} \int \frac{dk}{k} [\Delta_\ell^{\text{CS}}(k, \eta)]^2, \quad (4.3)$$

with [74]

$$\Delta_\ell^{\text{CS}}(k, \eta) = \int_{\eta_*}^{\eta_0} k d\eta \left[\frac{4\pi a^4 k}{H} \left(\frac{a}{k\xi} \right)^5 \operatorname{erf} \left(\frac{k\xi}{2\sqrt{6}a} \right) \right]^{1/2} j_\ell(x) \Big|_{x=k(\eta_0-\eta)}. \quad (4.4)$$

The quantities, ξ and v , are the correlation length and root-mean-square velocity, respectively, and determined from

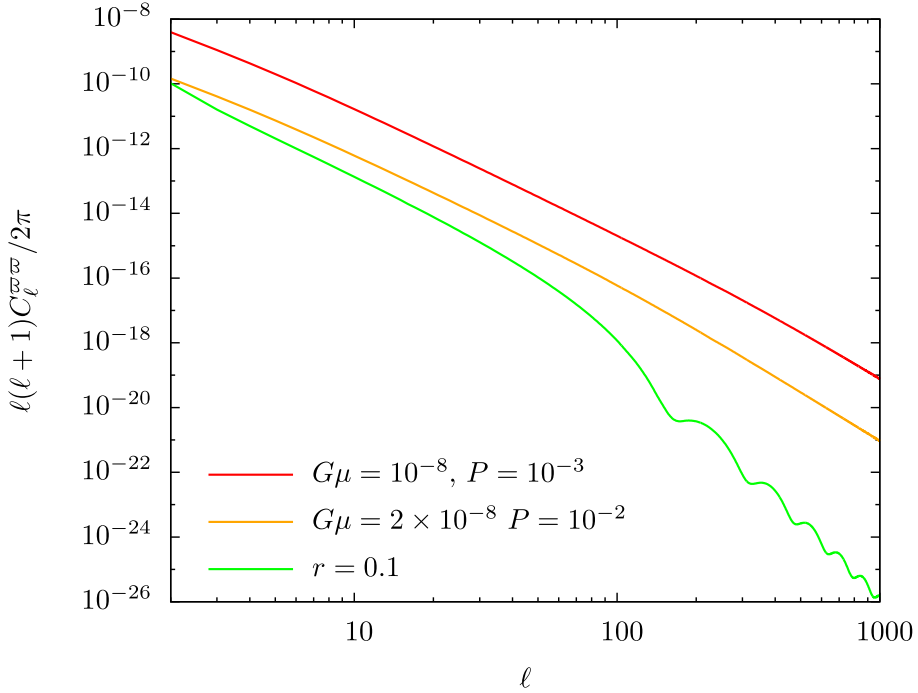


Figure 4.2: Angular spectra of the curl mode from the primordial GWs and a specific model of cosmic string network.

[92]

$$2v^2 \left(1 + \frac{\pi}{2\sqrt{2}} 0.23P \frac{1+8v^6}{1-8v^6} \right) = 1, \quad (4.5)$$

$$\xi = \frac{2\sqrt{2}}{\pi} \frac{1-8v^6}{2Hv(1+8v^6)}. \quad (4.6)$$

Fig. 4.2 shows the curl-mode angular power spectrum of assuming the specific model of cosmic string network and the primordial GWs. The cosmic string model depends on the tension, $G\mu$, and reconnection probability, P , and we fix $G\mu = 10^{-8}$ and $P = 10^{-3}$. The primordial GWs depend on the tensor-to-scalar ratio, r , and we set $r = 0.1$ which is close to the current upper bound [77]. It is clearly shown that the signals would be significant on large scales. This is because the vector and tensor perturbations are damped when they enter the sub-horizon scales. Note that, in the scalar lensing potential, the contributions from primordial GWs or cosmic strings are much smaller than that from the matter density fluctuations. However, the matter density fluctuations do not generate the curl-part of deflection angle, thus the curl mode would be a unique probe of any vector and tensor sources.

4.2 Forecasts for Future CMB Experiments and Galaxy Imaging Surveys

4.2.1 Fisher Formalism

One of the methods to theoretically estimate the expected constraints on cosmological parameters is the Fisher analysis which is based on the maximum likelihood approach. Here we summarize the Fisher matrix formalism used in analysis of this chapter, and describe the canonical setup for CMB and cosmic shear experiments, for which forecast results are presented in next section.

Table 4.1: Experimental specifications for space/ground-based CMB experiments in this thesis, denoting CMB-S and CMB-G, respectively. Note that CMB-S is a PLANCK-like experiment [17], and CMB-G is considered as a CMB experiment aimed to measure weak lensing effect such as ACTPol [20], SPTpol [19] and PolarBear. The quantity θ_{FWHM} is the beam size, and σ_T represents the sensitivity to the temperature. We assume the polarization sensitivity is given by $\sigma_P = \sqrt{2}\sigma_T$.

Experiment	f_{sky}	θ_{FWHM} [arcmin]	σ_T [$\mu\text{K}/\text{pixel}$]
CMB-S	0.65	7.0	4.3
CMB-G	0.10	1.4	3.6

Fisher information matrix

Given the angular spectra theoretically parametrized by a set of parameters \mathbf{p} , cosmological information on these parameters obtained from the combination of several experiments is quantified by the Fisher matrix [119]:

$$F_{ij} = \sum_{\ell=2}^{\ell_{\max}} \frac{2\ell+1}{2} f_{\text{sky}} \text{Tr} \left(\mathbf{C}_{\ell}^{-1}(\mathbf{p}) \frac{\partial \mathbf{C}_{\ell}}{\partial p_i}(\mathbf{p}) \mathbf{C}_{\ell}^{-1}(\mathbf{p}) \frac{\partial \mathbf{C}_{\ell}}{\partial p_j}(\mathbf{p}) \right) \Big|_{\mathbf{p}=\mathbf{p}_{\text{fid}}}, \quad (4.7)$$

where \mathbf{C}_{ℓ} is the covariance matrix of the angular power spectra given below, p_i is a cosmological parameter which we want to estimate, and the f_{sky} is the sky coverage. The Fisher matrix is evaluated with the fiducial cosmological parameter, \mathbf{p}_{fid} . With the Fisher matrix given above, the 1σ (68% C.L.) statistical uncertainties for the cosmological parameters, p_i , marginalized over other parameters, $\sigma(p_i)$, are estimated as

$$\sigma(p_i) = \sqrt{\{\mathbf{F}^{-1}\}_{ii}}. \quad (4.8)$$

Eq. (4.7) relies on the assumption of the Gaussian likelihood which is not accurate in some situations. In particular, cosmic shear is sensitive to the nonlinear gravitational evolution, leading to the non-Gaussian covariance. However, the actual impact of non-Gaussian covariance on the parameter estimation is not significant, and it degrades the parameter constraints at most few percent level [120, 121]. Although this does not imply the validity of the error estimation with Gaussian likelihood function (for example, in the case of neutrino mass, the condition, $\sum m_{\nu} > 0$, leads to non-Gaussian error [122]), we adopt Eq. (4.7) to explore the potential power of weak lensing experiments.

Covariance matrix

In our analysis, CMB and cosmic shear experiments are considered, and the cosmological analysis is based on primary temperature (Θ) and (E-mode) polarization (E) data which are obtained with the de-lensing technique, the gradient and curl mode of deflection angle (ϕ and ϖ) data for the CMB lensing reconstruction, and the data of E and B mode shear for galaxies divided into three redshift bins (\mathcal{E}_i ; $i = 1, \dots, 3$).

To estimate neutrino mass constraints, we use the temperature, E-mode polarization, ϕ and E-mode shear. The full covariance matrix of these signals, \mathbf{C}_{ℓ} , is given by

$$\mathbf{C}_{\ell} = \begin{pmatrix} C_{\ell}^{\Theta\Theta} + N_{\ell}^{TT} & C_{\ell}^{\Theta E} & C_{\ell}^{\Theta\phi} & C_{\ell}^{\Theta\mathcal{E}_1} & \dots & C_{\ell}^{\Theta\mathcal{E}_n} \\ C_{\ell}^{\Theta E} & C_{\ell}^{EE} + N_{\ell}^{PP} & 0 & 0 & \dots & 0 \\ C_{\ell}^{\Theta\phi} & 0 & C_{\ell}^{\phi\phi} + N_{\ell}^{\phi} & C_{\ell}^{\phi\mathcal{E}_1} & \dots & C_{\ell}^{\phi\mathcal{E}_n} \\ C_{\ell}^{\Theta\mathcal{E}_1} & 0 & C_{\ell}^{\mathcal{E}_1\mathcal{E}_1} & C_{\ell}^{\mathcal{E}_1\mathcal{E}_1} + N_{\ell}^{\mathcal{E}_1\mathcal{E}_1} & \dots & C_{\ell}^{\mathcal{E}_1\mathcal{E}_3} \\ \vdots & 0 & \vdots & \vdots & \ddots & \vdots \\ C_{\ell}^{\Theta\mathcal{E}_3} & 0 & C_{\ell}^{\mathcal{E}_3\mathcal{E}_3} & C_{\ell}^{\mathcal{E}_3\mathcal{E}_3} & \dots & C_{\ell}^{\mathcal{E}_3\mathcal{E}_3} + N_{\ell}^{\mathcal{E}_3\mathcal{E}_3} \end{pmatrix}. \quad (4.9)$$

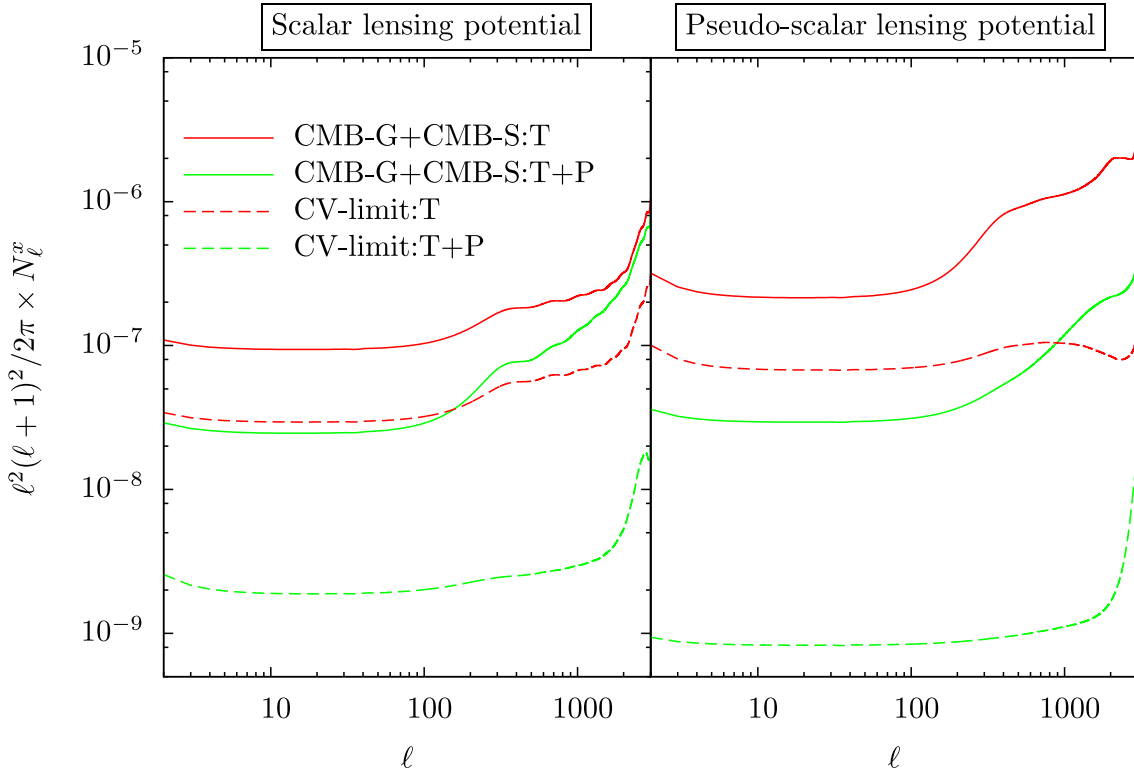


Figure 4.3: Comparison of the reconstruction noise spectra in the lensing potential (left) and curl mode (right) using the temperature map alone, $\alpha = \Theta\Theta$ (T; red lines), and the temperature and polarization maps (T+P; green lines). We assume two cases; CMB-G combined with CMB-S (CMB-G+CMB-S; solid lines), and cosmic-variance limit (CV-limit; dashed lines). We compute noise spectra according to Eq. (5.26) for T and Eq. (5.30) for T+P, with $\ell_{\text{max}} = 3000$, and take into account the effect of finite sky coverage.

Here, N_ℓ^{TT} , N_ℓ^{PP} , N_ℓ^ϕ and $N_\ell^{\mathcal{E}_i\mathcal{E}_i}$ are the noise power spectra. The amplitude and shape of the noise spectra depends on the survey design for the CMB and lensing experiments, which will be discussed below.

The elements of covariance matrix, i.e., the angular power spectra of primary CMB anisotropies ($C_\ell^{\Theta\Theta}$, $C_\ell^{\Theta E}$, C_ℓ^{EE}), scalar lensing potentials ($C_\ell^{\phi\phi}$), and E-mode shear ($C_\ell^{\mathcal{E}\mathcal{E}}$) are computed by modifying public code, CAMB [82], with the fiducial value of cosmological parameters described in chapter 1. Note that the angular power spectrum of the scalar lensing potential and E-mode shear is obtained by integrating the matter power spectrum along the line-of-sight, for which we adopt the fitting formula of the non-linear matter power spectrum given in Ref. [109].

CMB Experiments

For CMB experiments, we consider a nearly full-sky survey with the fraction of sky coverage, $f_{\text{sky}} = 0.65$, such as PLANCK, denoted by CMB-S. As for the ground-based experiment denoted by CMB-G, we assume a high-resolution experiments with $\theta_{\text{FWHM}} = 1$ arcmin, and $f_{\text{sky}} = 0.1$, such as ACTPol, SPTpol and PolarBear, which have high sensitivity to the CMB lensing power spectrum. The noise level is assumed to be $\sigma_T = \sigma_P/\sqrt{2} = 1\mu\text{K}$. When estimating the temperature and polarization power spectra from ground-based experiment, we combine CMB-S data at $\ell < 700$, in order to remedy a large uncertainty at large angular scales arising from the atmospheric temperature

fluctuations. The isotropic homogeneous instrumental noise power spectra are given by [123]

$$N_\ell^{XX} \equiv \left(\frac{\sigma_x \theta_{\text{FWHM}}}{T_{\text{CMB}}} \right)^2 \exp \left[\frac{\ell(\ell+1)\theta_{\text{FWHM}}^2}{8 \ln 2} \right], \quad (4.10)$$

with $T_{\text{CMB}} = 2.7\text{K}$ being mean temperature of CMB and X denoting the temperature (T) or polarization (P). Here, the quantity θ_{FWHM} is the beam size, and σ_x represents the sensitivity to the temperature σ_T or polarizations σ_P . The specific values for CMB-S and CMB-G are summarized in Table 4.1. Note that the foregrounds contamination in the CMB data would be additional noise source for estimating angular power spectra, and it could not only degrade but also bias the cosmological constraints. Recent estimate by Ref. [124] suggests that the foregrounds contribution to the angular power spectrum would become less than the instrumental noise, if foregrounds can be successfully subtracted at a 1% level. Although this is still challenging and a more elaborative study is necessary for the foreground removal, we here ignore the effect of foreground contamination in order to explore the potential and complementarity of the lensing experiment.

CMB Lensing

For the CMB lensing data, we must consider the errors associated with reconstruction technique. The details of the reconstruction technique is given in the next chapter, and here we compute the noise spectrum based on Eq. (5.30) given in the next chapter, with the modified version of FuturCMB code¹ [122], assuming that the lensing effect on the CMB comes only from the large-scale structure, and no source to produce the curl mode. We assume that the survey region of CMB-G is entirely overlapped with that of CMB-S, and compute the following noise spectrum

$$N_\ell^\phi \equiv \left[\frac{f_{\text{sky}}^G}{(N_{\ell;G}^\phi)^2} + \frac{(f_{\text{sky}}^S - f_{\text{sky}}^G)}{(N_{\ell;S}^\phi)^2} \right]^{-1/2}, \quad (4.11)$$

where $f_{\text{sky}}^G = 0.1$ and $f_{\text{sky}}^S = 0.65$ are the fractional sky-coverage of CMB-G and CMB-S, respectively. In computing the noise of reconstruction within the survey region of CMB-G, $N_{\ell;G}^\phi$, we use the lensed angular power spectra from CMB-S instead of CMB-G, at $\ell < 700$, in order to remedy a large uncertainty at large angular scales arising from the atmospheric temperature fluctuations. On the other hand, the noise, $N_{\ell;S}^\phi$, is calculated with CMB-S experimental specification. Also note that, for cosmic-variance limit, the reconstruction noise is computed with the instrumental noise being $N_\ell^{XX} = 0$. Fig. 4.3 shows the expected noise spectrum in the full-sky case for both gradient and curl modes. The left and right panels show the expected noise spectra, N_ℓ^ϕ and N_ℓ^ϖ , respectively. The resultant curl-mode noise spectra have amplitude comparable to those for the lensing potential. In the cosmic-variance limit, the reconstruction noise is improved by more than an order of magnitude compared to the case with CMB-G+CMB-S. Notice that the curl-mode noise spectra is sensitive to the inclusion of polarizations compared to the estimator of the lensing potential. In our calculation, the curl-mode angular power spectrum is set to zero. Although the primordial GWs or cosmic strings induces the curl mode, the amplitude of $C_\ell^{\varpi\varpi}$ is at least two orders of magnitude smaller than that of $C_\ell^{\phi\phi}$, as long as we consider the model parameters consistent with observations. Thus, the inclusion of the curl mode would hardly change the result in Fig. 4.3.

Cosmic shear survey

In general, the bulk properties of a photometric survey are characterized by the sky coverage, f_{sky} , the mean redshift, z_m , and the total number of galaxies per square arcminute, N_g . We compute the Fisher matrix in the three representative photometric surveys; a deep survey ($f_{\text{sky}} = 0.05$, $z_m = 1.0$ and $N_g = 35 \text{ arcmin}^{-2}$) such as SuMIR-HSC [31] and a wide imaging survey ($f_{\text{sky}} = 0.2$, $z_m = 0.5$ and $N_g = 12 \text{ arcmin}^{-2}$) like DES [30], denoted by CS-D and

¹<http://lpsc.in2p3.fr/perotto>

Table 4.2: Characterization of galaxy imaging surveys, i.e., the sky coverage, f_{sky} , the mean redshift, z_m , and the number of galaxies per square arcminute, N_g . We consider two surveys: a deep survey such as Subaru-HSC [31] and a wide survey like DES [30], denoted by CS-D and CS-W, respectively with the similar set up of Ref. [125]. In all surveys, the galaxy samples are divided into three redshift bin, and the ranges of redshift are chosen such that the each redshift bin has same number of galaxies, $N_g/3$. The resultant redshift ranges are summarized in Table 4.3 for each mean redshift z_m .

Survey	f_{sky}	z_m	$N_g [\text{arcmin}^{-2}]$
CS-D	0.05 (1500deg 2)	1.0	35
CS-W	0.2 (6000deg 2)	0.5	12

Table 4.3: The relation between mean redshift, z_m , and the redshift ranges of i -th bin computed in the case with $N_{\text{bin}} = 3$. Using Eq. (2.139), the redshift ranges are determined such that each redshift bin has same number of galaxies.

z_m	redshift ranges		
	$z < 0.369$	$0.369 < z < 0.569$	$0.569 < z$
0.5	$z < 0.369$	$0.369 < z < 0.569$	$0.569 < z$
1.0	$z < 0.739$	$0.739 < z < 1.14$	$1.14 < z$
1.5	$z < 1.11$	$1.11 < z < 1.72$	$1.72 < z$
2.0	$z < 1.48$	$1.48 < z < 2.29$	$2.29 < z$

CS-W, respectively. The redshift distribution of galaxies is assumed to be given by Eq. (2.139), with $\alpha = 2$, $\beta = 1.5$ and $z_0 = 0.64z_m$. For simplicity, we adopt the scaling relation for the photo-z error, $\sigma(z) = 0.03(1+z)$. In Table 4.2, we summarize the basic parameters of the survey design for two surveys used in the subsequent analysis.

In a photometric survey, apart from the calibration systematics for shear estimation, the noise source for cosmic shear measurement mainly comes from the intrinsic ellipticity of galaxies, which is described by

$$N_{\ell}^{\mathcal{E}_i \mathcal{E}_j} = N_{\ell}^{\mathcal{B}_i \mathcal{B}_j} = \delta_{ij} \frac{\langle \gamma_{\text{int}}^2 \rangle}{\hat{N}_i}. \quad (4.12)$$

with \hat{N}_i being the number density of galaxies per steradians in i -th redshift bin;

$$\hat{N}_i = 3600 \bar{N}_i \left(\frac{180}{\pi} \right)^2 \text{ str}^{-1}. \quad (4.13)$$

The quantity $\langle \gamma_{\text{int}}^2 \rangle^{1/2}$ is the rms intrinsic ellipticity. We adopt the empirically derived value, $\langle \gamma_{\text{int}}^2 \rangle^{1/2} = 0.3$ [126]. In our analysis, we assume the galaxy samples are divided by three redshift bins, and the ranges of redshift are chosen such that each redshift bin has same number of galaxies, $N_g/3$ (the resultant redshift ranges are summarized in Table 4.3 for each mean redshift z_m). This is because, by dividing the galaxy samples into several subsamples, we obtain cosmic shear data from several redshifts, providing information on distance, and breaking degeneracies between cosmological parameters.

Table 4.4: Forecast results for marginalized 1σ errors for each cosmological parameter, assuming CMB-S, CMB-G and CS-D. The labels, $+ \phi$, $+ \mathcal{E}$, and $+ \phi + \mathcal{E}$, respectively indicate the cases including CMB lensing, cosmic shear, and combining both. The primary CMB information is included in all cases.

parameter	$+ \phi$	$+ \mathcal{E}$	$+ \phi + \mathcal{E}$
$\ln(\Omega_b h^2)$	0.0030	0.0029	0.0028
$\ln(\Omega_m h^2)$	0.0094	0.0084	0.0057
Ω_Λ	0.039	0.023	0.020
w_0	0.091	0.045	0.044
w_a	0.13	0.17	0.063
n_s	0.0023	0.0021	0.0021
$\ln(A_s)$	0.013	0.012	0.012
τ	0.0039	0.0039	0.0039
$\sum m_\nu$ [eV]	0.065	0.082	0.052

4.2.2 Forecast results

Implications for massive neutrinos

Here, as an example of cosmological implications with even-parity quantities (i.e., scalar-lensing potential and E-mode shear), we show the expected constraints on total mass of neutrinos from CMB experiments and galaxy imaging surveys. In Table 4.4, we summarize the marginalized 1σ (68%) errors in the case with combining CMB-S, CMB-G and CS-D. We examine following three cases:

- $+ \phi$: including CMB lensing data ($C_\ell^{\phi\phi}$ and $C_\ell^{\Theta\phi}$)
- $+ \mathcal{E}$: including cosmic shear data ($C_\ell^{\mathcal{E}_i\mathcal{E}_j}$ and $C_\ell^{\Theta\mathcal{E}_i}$)
- $+ \phi + \mathcal{E}$: combining all power spectra, i.e., $C_\ell^{\phi\phi}$, $C_\ell^{\Theta\phi}$, $C_\ell^{\mathcal{E}_i\mathcal{E}_j}$, $C_\ell^{\Theta\mathcal{E}_i}$, and $C_\ell^{\phi\mathcal{E}_i}$

Note that we use information on primary CMB anisotropies (temperature and E-mode polarization) up to $\ell_{\max} = 3000$. On the other hand, we assume to use scalar-lensing potential and E-mode shear up to $\ell_{\max} = 1000$ and $\ell_{\max} = 300$, respectively, in order to reduce uncertainty from nonlinear evolution of density fluctuations. For all cases, we add the primary (unlensed) CMB data (i.e., $C_\ell^{\Theta\Theta}$, $C_\ell^{\Theta E}$ and C_ℓ^{EE}) as prior information. We assume that the observed area of CS-D is entirely overlapped with that of CMB-G, and similarly the survey region of CMB-G is totally included in the nearly full-sky survey with CMB-S. Overall, the constraints obtained from the single experiments ($+ \phi$ or $+ \mathcal{E}$) are almost comparable, and combining all the lensing observations ($+ \phi + \mathcal{E}$) improves the constraints on cosmological parameters. The total mass of neutrinos can be detected with $\sim 2\sigma$ significance for a fiducial value $\sum m_\nu = 0.1$ eV. Note that the constraints on massive neutrinos would be further improved by adding information on E-mode shear at small scales ($\ell > 300$), where we have to accurately predict non-linear evolution of density fluctuations including massive neutrinos. However, a treatment of the non-linear evolutions with massive neutrinos is still difficult in both theoretical and numerical studies, and would significant bias on the constraints (e.g., [127, 128, 129, 130]). In this respect, the constraints given in Table 4.4 are conservative.

In Fig 4.4, to elucidate the impact of upcoming lensing experiments on cosmological parameters, we plot the expected 1σ (68% C.L.) contours on $\ln \Omega_m h^2$ and $\sum m_\nu$. The two panels show the results from CMB-S and CMB-G combining with CS-D or CS-W, respectively. Comparing with the constraints coming from the primary CMB data alone, the CMB lensing and cosmic shear experiments greatly improve the constraints from the primary CMB information, and these can be used as an independent cross check for extracting cosmological information in an unbiased way. Hence, science benefit for combining two lensing experiments is valuable.

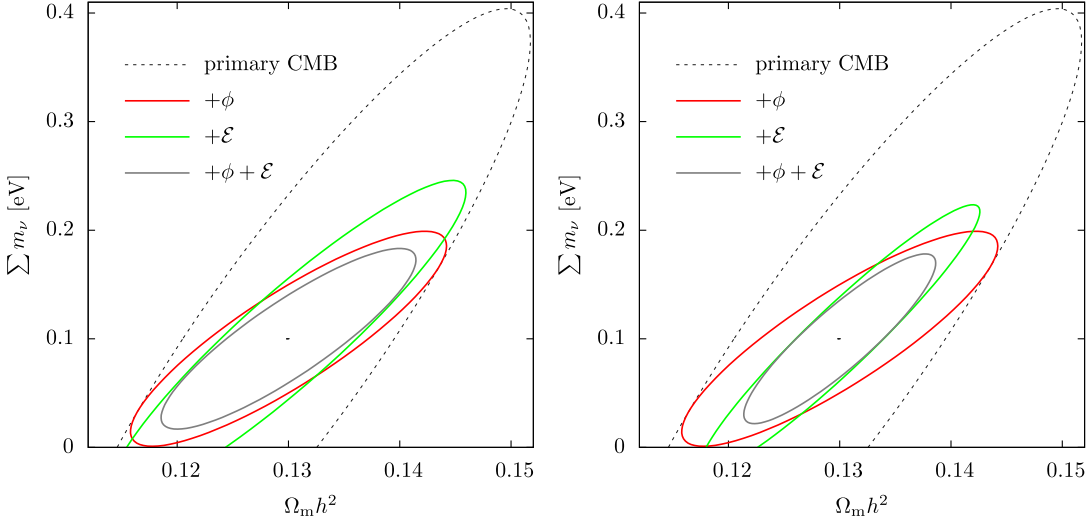


Figure 4.4: Expected 1σ error contours on $\ln \Omega_m h^2 - \sum m_\nu$ plane assuming CMB-S, CMB-G with CS-D (right) or CS-W (left). The gray dotted lines represent the results from primary CMB, while the red solid and green dashed lines indicate the results further including CMB lensing and cosmic shear, respectively. The blue filled ellipse are the results of all measurements.

Implications for primordial GWs and cosmic strings

Next, we illustrate the usefulness of odd-parity quantities (curl mode and B-mode shear) as a diagnosis of the vector/tensor perturbations. Here we specifically focus on the curl mode induced by two cases; primordial GWs produced during inflation, and cosmic strings (e.g., Refs. [92, 131]).

We first show the case with the curl mode. Note that, similar to the case of gradient mode, we assume to obtain curl mode of deflection angle with the reconstruction technique given in the next chapter, and the noise spectrum, N_ℓ^ϖ , is defined as Eq. (4.11) but replacing ϕ with ϖ .

In the left two panels of Fig. 4.5, the angular power spectrum from primordial GWs and the signal-to-noise ratio (SNR) are shown. The plotted errors are estimated from

$$\Delta C_\ell = \frac{C_\ell^{\varpi\varpi} + N_\ell^\varpi}{\sqrt{(\ell + 1/2)f_{\text{sky}}\Delta\ell}}, \quad (4.14)$$

where $\Delta\ell$ is the size of multipole bin, and we set $\Delta\ell = (i + 1)^3 - i^3$ for i -th bin, just for illustration. For CMB-G combined with CMB-S, we evaluate the errors as

$$\Delta C_\ell = \{(\Delta C_{\ell:\text{G}})^2 + (\Delta C_{\ell:\text{S}})^2\}^{1/2}, \quad (4.15)$$

where the errors arising from CMB-G survey region, $\Delta C_{\ell:\text{G}}^{XY}$, are computed according to Eq. (4.14) with $f_{\text{sky}} = 0.1$ and $N_\ell^\varpi = N_{\ell:\text{G}}^\varpi$. Similarly, the errors from CMB-S survey area, $\Delta C_{\ell:\text{S}}^{XY}$, are obtained from Eq. (4.14) with $f_{\text{sky}} = 0.55$ and $N_\ell^\varpi = N_{\ell:\text{S}}^\varpi$. On the other hand, for the cosmic-variance limit (CV-limit), we compute the errors with $f_{\text{sky}} = 1.0$ and the instrumental noise power spectra being zero. The SNR for the curl-mode angular power spectrum is defined by

$$\left(\frac{\text{S}}{\text{N}}\right)_{<\ell} = \left\{ \sum_{\ell'=2}^{\ell} \left(\frac{C_{\ell'}^{\varpi\varpi}}{\Delta C_{\ell'}} \right)^2 \right\}^{1/2}. \quad (4.16)$$

As is expected, it is hard to detect the signature of primordial GWs from lensing reconstruction. For CMB-G+CMB-S, the SNR is less than 0.1. Even with CV-limit, the SNR is ~ 2 . For the tensor-to-scalar ratio below the current upper limit [77], the SNR would be further worsen. This is true as long as we adopt the quadratic estimator.

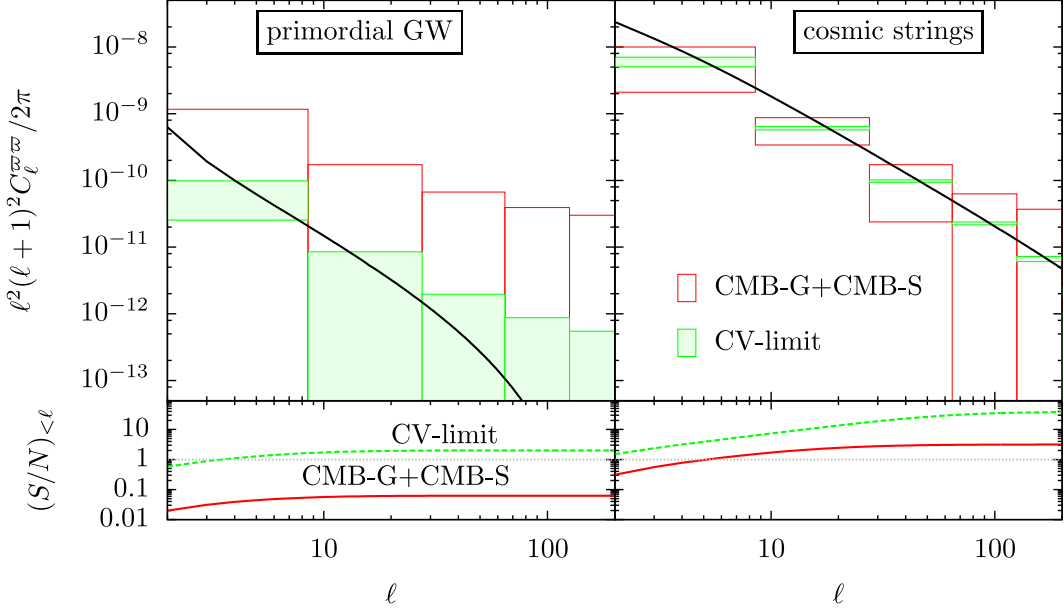


Figure 4.5: Angular power spectra of the curl mode from primordial GWs with the tensor-to-scalar ratio, $r = 0.1$ (top left), and a specific model of cosmic strings with $G\mu = 10^{-8}$ and $P = 10^{-3}$ (top right). The error boxes show expected uncertainties of angular power spectrum from CMB-G+CMB-S (red) and cosmic-variance limit (green). The bottom two panels show the SNR as a function of a maximum multipole, for primordial GWs (bottom left) and cosmic strings (bottom right).

On the other hand, the right panels of Fig. 4.5 shows the case of the cosmic strings, with $G\mu = 10^{-8}$ and $P = 10^{-3}$ [132]. Note that these values are consistent with the constraint from the temperature angular power spectrum using the Gott-Kaiser-Stebbins (GKS) effect [133, 134] induced by the gravitational potential of a moving string [92]. Although the result depends on the parameters of comic strings, the SNR is ~ 3 even for CMB-G+CMB-S case. In the cosmic variance limit, the SNR becomes ~ 30 . Note that, we have ignored the tensor metric perturbations from cosmic strings which also induce the curl mode, and the inclusion of the contributions from the tensor perturbations would further increase the SNR. The GKS effect observed via temperature map would have larger SNR than the curl mode [92]. However, the temperature anisotropies at small angular scales are usually dominated by point source contaminations and the Sunyaev-Zel'dovich (SZ) effect [135]. In this respect, the curl mode is useful to check systematics and biases in the derived constraints on cosmic strings from GKS effect.

The information on large scales would be important for detecting the curl mode from cosmic strings, and the full-sky formalism for lensing reconstruction is indispensable. Fig. 4.8 shows the dependence of SNR on the string parameters $G\mu$ and P . The SNR for curl-mode signal scales as $(S/N)_{<\ell}^{\varpi\varpi} \propto (G\mu)^2 P^{-5/2}$, and the CMB-lensing experiment is capable of detecting a string network with small P compared to the case with GKS effect.

Fig. 4.7 shows the same plot of Fig. 4.5, but for the B-mode shear angular power spectra induced by a cosmic string network. Each panel of Fig. 4.7 shows the expected errors (top) and SNRs (bottom) for three representative surveys. Typically, the B-mode spectrum has a large power with a flat shape at large angular scales $\ell \lesssim 100$, and it rapidly falls off at small angular scales. These features are irrespective of the survey design, and are determined by the properties of cosmic string network and the lensing kernel. On the other hand, the expected amplitude of the power spectrum depends not only on string parameters but also on the survey depth, and the resultant SNR for B-mode spectrum is rather sensitive to the survey specification. The results show that a deep survey such as CS-D would be capable of detecting the cosmic strings with high SNR ($S/N \sim 30$) compared to a wide survey. In Fig. 4.8, we show the same plot of Fig. 4.8, but for B-mode shear. Similar to the curl mode, the SNR for B-mode signal scales

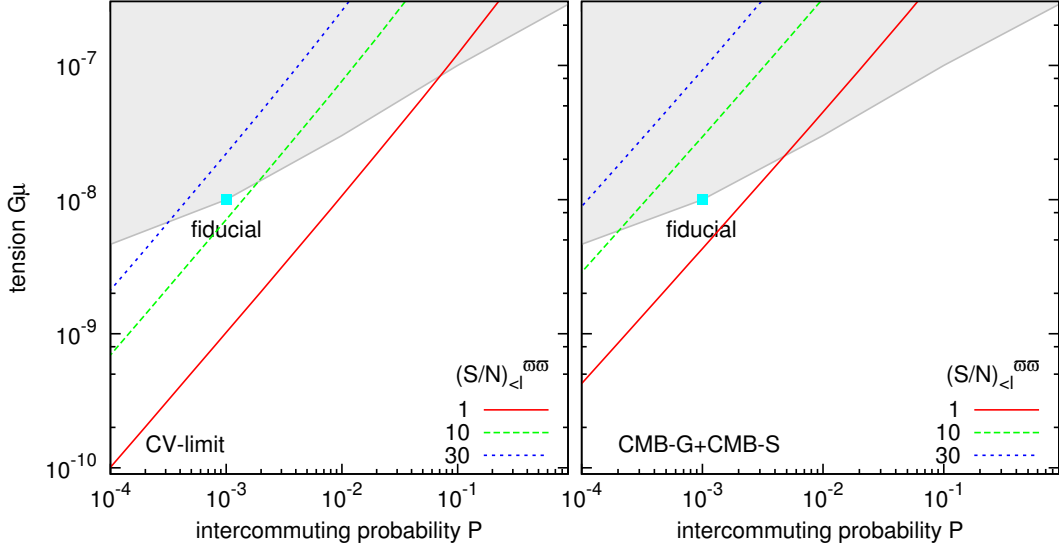


Figure 4.6: The contours of the SNR, $(S/N)_{<l}^{\varpi\varpi}$, as a function of the tension $G\mu$ and intercommuting probability P for CV-limit (left) and CMB-G+CMB-S (panel). The lines show the points with the same SNR. The shaded region is excluded from the GKS effect obtained from Ref. [92].

as $(S/N)_{<l}^{BB} \propto (G\mu)^2 P^{-5/2}$.

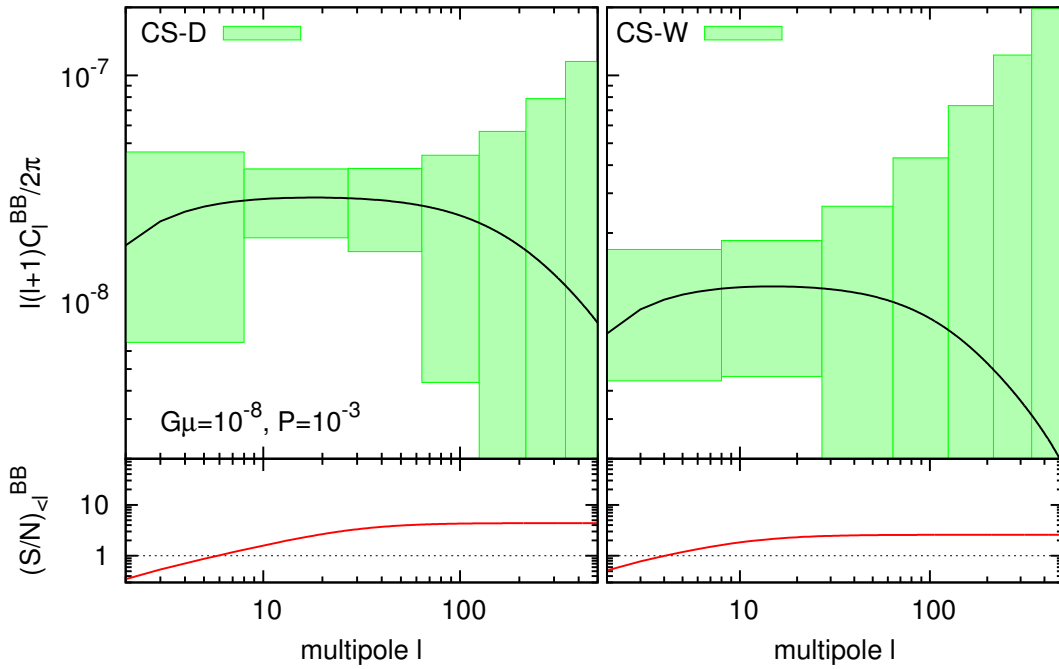


Figure 4.7: The angular power spectra of the B-mode shear from a specific model of cosmic string with $G\mu = 10^{-8}$, $P = 10^{-3}$ for CS-D (left) and CS-W (right). The error boxes in each figure show the expected variance of angular power spectrum from each experiments. The bottom panels show the SNR as a function of maximum multipole.

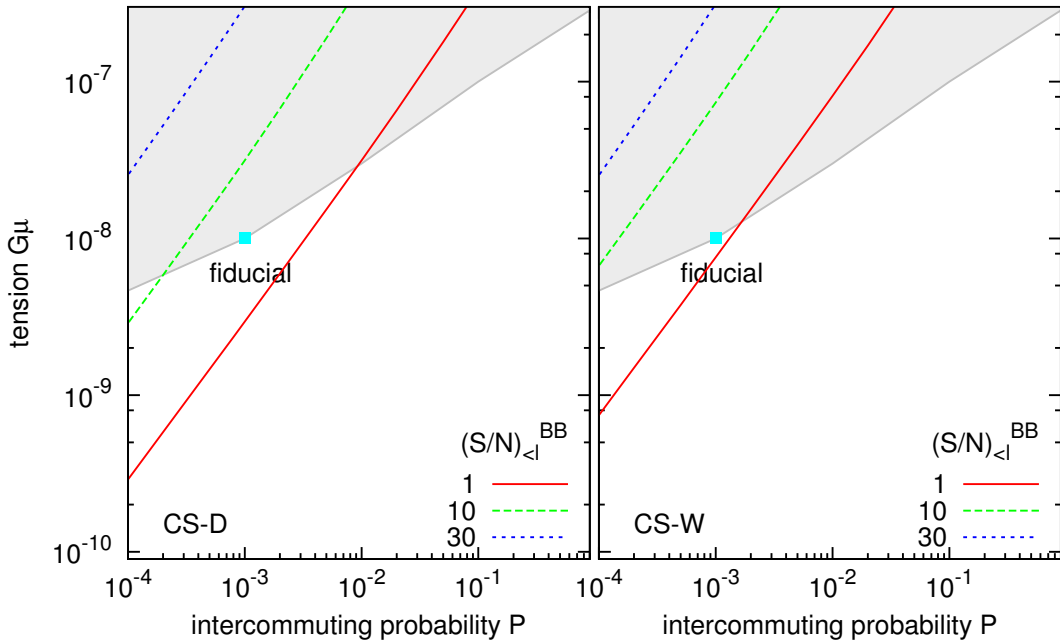


Figure 4.8: Same as Fig. but for the B-mode shear, $(S/N)_{\ell}^{BB}$.

Chapter 5

CMB Lensing Reconstruction for Gradient and Curl Modes

Unlike cosmic shear, lensing estimators for CMB utilize the fact that a fixed lensing potential introduces statistical anisotropy into the observed CMB, in the form of a correlation between the CMB temperature and its gradient (e.g., [6, 7, 8, 9, 10, 136]). With a large number of observed CMB modes, this correlation may be used to form estimates of the lensing potential. The power spectrum of the lensing potential may in turn be studied by taking the power spectrum of these lensing estimates.

In the most of these studies, the estimator is constructed only for scalar lensing potential. But, as mentioned in chapter 1, the curl-mode reconstruction is also useful to cosmological analysis. The reconstruction of the curl mode has been previously discussed in Ref. [34]. In Ref. [34], they empirically defined a quadratic estimator of the curl mode in the flat-sky limit, and claimed that estimator of the lensing potential is biased in the presence of the curl mode.

In this chapter, we derive estimators for both the gradient and curl modes in an unbiased way, and also discuss method for estimating power spectrum of lensing potentials. In section 5.1, reconstruction methods for the gradient and curl modes are derived, based on quadratic statistics (e.g., Refs. [8, 9]), and show that, thanks to the distinctive property of parity, the estimator of the lensing potential is not biased even in the presence of the curl mode, and remains the same form derived in previous studies without curl mode. We also show that the resultant estimator is similar to that from the maximum likelihood approach. Then, we compare the flat-sky estimator with the full-sky estimator, and show that the empirically defined estimator in Ref. [34] can be derived from the full-sky estimator. Even in the flat-sky, we show that the lensing potential estimator is not modified by the presence of the curl mode. Finally, in section 5.2, we summarize a method to estimate angular power spectrum of the gradient and curl modes.

Note that, in Table 5.1, we summarize the meaning and definition of the quantities used to reconstruct the lensing potentials from observed CMB maps.

5.1 Estimating CMB lensing potentials

5.1.1 Formalism of standard optimal quadratic estimator

Lensing potentials as quadratic statistics

To get insight into the reconstruction of the lensing potentials, we consider an idealistic situation; we can take the ensemble average over primary CMB anisotropies alone, under a given realization of the lensing potentials. Hereafter, we denote this average by $\langle \dots \rangle_{\text{CMB}}$, to distinguish it from the usual meaning of the ensemble average, $\langle \dots \rangle$. Under the situation, in the correlation of lensed CMB anisotropies, $\langle \tilde{X}_{LM} \tilde{Y}_{L'M'} \rangle_{\text{CMB}}$, the lensing potentials are included in the non-zero off-diagonal terms ($L \neq L'$, $M \neq -M'$). This is because the lensing effect causes a non-trivial

Table 5.1: Notations for quantities used in this chapter.

Symbol	Definition	Meaning
Full sky / Flat sky	Full sky / Flat sky	
$X_{\ell m} / X_{\ell}$	—	unlensed CMB maps
$\tilde{X}_{\ell m} / \tilde{X}_{\ell}$	—	lensed CMB maps
$\hat{X}_{\ell m} / \hat{X}_{\ell}$	—	lensed CMB maps including instrumental noise
α (or β)	—	A pair of two CMB maps, X and Y
$\hat{x}_{\ell m}^{(\alpha)} / \hat{x}_{\ell}^{(\alpha)}$	Eq. (5.10) / Eq. (5.38)	Estimator
$\bar{F}_{\ell L L'}^{x,(\alpha)} / F_{\ell, \mathbf{L}, \mathbf{L}'}^{x,(\alpha)}$	Eq. (5.27) / Eq. (5.39)	Weight function
$\bar{N}_{\ell}^{x,(\alpha)} / N_{\ell}^{x,(\alpha)}$	Eq. (5.26) / Eq. (5.37)	Noise spectrum
$\bar{g}_{\ell L L'}^{x,(\alpha)} / g_{\ell, \mathbf{L}, \mathbf{L}'}^{x,(\alpha)}$	Eq. (5.21) / Eq. (5.36)	—
$\bar{f}_{\ell L L'}^{x,(\alpha)} / f_{\ell, \mathbf{L}, \mathbf{L}'}^{x,(\alpha)}$	Table 5.2 / 5.3	—
$S^{0,x}$	Eq. (2.91)	—
$S^{\pm 2,x}$	Eq. (2.104)	—
$S^{\pm,x}$	Eq. (2.108)	-
$\hat{x}_{\ell m}^{(c)} / \hat{x}_{\ell}^{(c)}$	Eq. (5.29) / Eq. (5.41)	Optimal combination
$\bar{N}_{\ell}^{x,(c)} / N_{\ell}^{x,(c)}$	Eq. (5.30) / Eq. (5.42)	Noise spectrum for optimal combination
$\bar{N}_{\ell}^{x,(\alpha,\beta)} / N_{\ell}^{x,(\alpha,\beta)}$	Eq. (5.31) / Eq. (5.43)	Noise cross-spectrum
$- / f_{\ell, \mathbf{L}}^x$	$- / \text{Table 5.3}$	Equivalent to $f_{\ell, \mathbf{L}, \ell - \mathbf{L}}^{x,(\Theta\Theta)}$
$- / N_{\ell}^{x,(0)}$	$- / \text{Eq. (5.37)}$	Equivalent to $N_{\ell}^{x,(\Theta\Theta)}$

Table 5.2: The functional forms of $\bar{f}_{\ell LL'}^{\phi, (XY)}$ and $\bar{f}_{\ell LL'}^{\varpi, (XY)}$ appeared in Eq. (5.1). The label “even” and “odd” indicate that the function are non-zero only when $\ell + L + L'$ is even or odd, respectively.

XY	$\bar{f}_{\ell LL'}^{\phi, (XY)}$	$\bar{f}_{\ell LL'}^{\varpi, (XY)}$
$\Theta\Theta$	$S_{L\ell L'}^{0,\phi} C_{L'}^{\Theta\Theta} + S_{L'\ell L}^{0,\phi} C_L^{\Theta\Theta}$ (even) $S_{L\ell L'}^{0,\varpi} C_{L'}^{\Theta\Theta} - S_{L'\ell L}^{0,\varpi} C_L^{\Theta\Theta}$ (odd),	
ΘE	$S_{L\ell L'}^{0,\phi} C_{L'}^{\Theta E} + S_{L'\ell L}^{+,\phi} C_L^{\Theta E}$ (even) $S_{L\ell L'}^{0,\varpi} C_{L'}^{\Theta E} - S_{L'\ell L}^{+,\varpi} C_L^{\Theta E}$ (odd)	
ΘB	$-S_{L'\ell L}^{-,\phi} C_L^{\Theta E}$ (odd)	$S_{L'\ell L}^{-,\varpi} C_L^{\Theta E}$ (even)
EE	$S_{L\ell L'}^{+,\phi} C_{L'}^{EE} + S_{L'\ell L}^{+,\phi} C_L^{EE}$ (even) $S_{L\ell L'}^{+,\varpi} C_{L'}^{EE} - S_{L'\ell L}^{+,\varpi} C_L^{EE}$ (odd)	
EB	$-S_{L\ell L'}^{-,\phi} C_L^{BB} - S_{L'\ell L}^{-,\phi} C_L^{EE}$ (odd) $-S_{L\ell L'}^{-,\varpi} C_L^{BB} + S_{L'\ell L}^{-,\varpi} C_L^{EE}$ (even)	
BB	$S_{L\ell L'}^{+,\phi} C_{L'}^{BB} + S_{L'\ell L}^{+,\phi} C_L^{BB}$ (even) $S_{L\ell L'}^{+,\varpi} C_{L'}^{BB} - S_{L'\ell L}^{+,\varpi} C_L^{BB}$ (odd)	

mode-coupling between the primary CMB anisotropies and lensing potentials (see Eqs. (2.86), (2.105) and (2.106)), and the lensed CMB anisotropies are not statistically isotropic for a given realization of the lensing potentials. Thus, it is possible to reconstruct the lensing potentials by extracting the off-diagonal terms of $\langle \tilde{X}_{LM} \tilde{Y}_{L'M'} \rangle_{\text{CMB}}$.

To see this, let us write the correlation of the lensed CMB anisotropies in the harmonic space. With Eqs. (2.86), (2.105) and (2.106), we obtain

$$\begin{aligned} \langle \tilde{X}_{LM} \tilde{Y}_{L'M'} \rangle_{\text{CMB}} &= C_L^{XY} \delta_{LL'} \delta_{M,-M'} (-1)^M \\ &\quad + \sum_{\ell m} (-1)^m \begin{pmatrix} \ell & L & L' \\ -m & M & M' \end{pmatrix} [\bar{f}_{\ell LL'}^{\phi, (XY)} \phi_{\ell m} + \bar{f}_{\ell LL'}^{\varpi, (XY)} \varpi_{\ell m}], \end{aligned} \quad (5.1)$$

with the coefficients, $\bar{f}_{\ell LL'}^{\phi, (XY)}$ and $\bar{f}_{\ell LL'}^{\varpi, (XY)}$, summarized in Table 5.2. The conditions, “even” and “odd”, in Table 5.2 come from the parity symmetry in the lensing potentials and primary CMB anisotropies. To extract the off-diagonal terms and find the solutions for $\phi_{\ell m}$ and $\varpi_{\ell m}$, we multiply

$$(-1)^{m'} \begin{pmatrix} \ell' & L & L' \\ -m' & M & M' \end{pmatrix} \bar{f}_{\ell' LL'}^{\phi, (XY)}, \quad (5.2)$$

in both sides of Eq. (5.1). Note that the multipoles, L and L' , are chosen so that $\bar{f}_{\ell' LL'}^{\phi, (XY)} \neq 0$. Then, summing up the equation over M and M' , and using the formulas, Eqs. (F.4) and (F.5), we find¹

$$\phi_{\ell m} = \frac{2\ell + 1}{\bar{f}_{\ell LL'}^{\phi, (XY)}} \sum_{MM'} (-1)^m \begin{pmatrix} \ell & L & L' \\ -m & M & M' \end{pmatrix} \langle \tilde{X}_{LM} \tilde{Y}_{L'M'} \rangle_{\text{CMB}}. \quad (5.3)$$

¹In deriving Eq. (5.3), we have ignored the zero-mode (C_0^{XY}), arising from the first term in Eq. (5.1).

Notice that the term involving ϖ in Eq. (5.1) vanishes. This is because, for all ℓ , L and L' , the parity symmetry of $\bar{f}_{\ell LL'}^{\phi, (XY)}$ and $\bar{f}_{\ell LL'}^{\varpi, (XY)}$ (Table 5.2) leads to

$$\bar{f}_{\ell LL'}^{\phi, (XY)} \bar{f}_{\ell LL'}^{\varpi, (XY)} = 0. \quad (5.4)$$

Similarly, following the procedure described in Eq. (5.2) below, but replacing $\bar{f}_{\ell LL'}^{\phi, (XY)}$ with $\bar{f}_{\ell LL'}^{\varpi, (XY)}$, the solution for $\varpi_{\ell m}$ is obtained, and the result is

$$\varpi_{\ell m} = \frac{2\ell + 1}{\bar{f}_{\ell LL'}^{\varpi, (XY)}} \sum_{MM'} (-1)^m \begin{pmatrix} \ell & L & L' \\ -m & M & M' \end{pmatrix} \langle \tilde{X}_{LM} \tilde{Y}_{L'M'} \rangle_{\text{CMB}}. \quad (5.5)$$

The above equations, (5.3) and (5.5), can not be used for a definition of the estimator of lensing potentials, because these equations include the ensemble average over the primary CMB anisotropies alone, $\langle \dots \rangle_{\text{CMB}}$. But, the above equations imply that, by summing the quadratic combination of lensed fields over multipoles appropriately, it is possible to separately construct the estimators for ϕ and ϖ .

Formalism

Based on Eqs. (5.3) and (5.5), we first naively define the estimator for the lensing potential x ($= \phi$ or ϖ) as follows:

$$\frac{2\ell + 1}{\bar{f}_{\ell LL'}^{x, (\alpha)}} \sum_{MM'} (-1)^m \begin{pmatrix} \ell & L & L' \\ -m & M & M' \end{pmatrix} \hat{X}_{LM} \hat{Y}_{L'M'}, \quad (5.6)$$

where the subscript, α , means a pair of two CMB maps, e.g., $\alpha = \Theta\Theta$ or EB . The quantities, \hat{X} and \hat{Y} , are the lensed CMB maps including isotropic and homogeneous instrumental noise. The multipoles, L and L' , are chosen so that $\bar{f}_{\ell LL'}^{x, (\alpha)} \neq 0$. With Eqs. (5.3) and (5.5), the estimator is rewritten as

$$\text{Eq.(5.6)} = x_{\ell m} + n_{\ell m LL'}^{x, (\alpha)}, \quad (5.7)$$

where the quantity, $n_{\ell m LL'}^{x, (\alpha)}$, is given by

$$n_{\ell m LL'}^{x, (\alpha)} = (-1)^m \frac{2\ell + 1}{\bar{f}_{\ell LL'}^{x, (\alpha)}} \sum_{MM'} \begin{pmatrix} \ell & L & L' \\ -m & M & M' \end{pmatrix} \left(\hat{X}_{LM} \hat{Y}_{L'M'} - \langle \hat{X}_{LM} \hat{Y}_{L'M'} \rangle_{\text{CMB}} \right). \quad (5.8)$$

Note that the above equation can be expressed without the quantity, $\langle \dots \rangle_{\text{CMB}}$. For instance, in the case using the temperature anisotropies alone (i.e., $\alpha = \Theta\Theta$), the above equation is rewritten as

$$\begin{aligned} n_{\ell m LL'}^{x, (\Theta\Theta)} &= (-1)^m \frac{2\ell + 1}{\bar{f}_{\ell LL'}^{x, (\Theta\Theta)}} \sum_{MM'} \begin{pmatrix} \ell & L & L' \\ -m & M & M' \end{pmatrix} \left\{ \Theta_{LM} \Theta_{L'M'} - C_L^{\Theta\Theta} \delta_{LL'} \delta_{M, -M'} (-1)^M \right. \\ &\quad + \sum_{x'=\phi, \varpi} \sum_{\ell' m'} \left\{ \sum_{L'' M''} \left[(-1)^{M'} \begin{pmatrix} L' & \ell' & L'' \\ -M' & m' & M'' \end{pmatrix} {}_0 S_{L' \ell L''}^{x'} \Theta_{L'' M''} \Theta_{LM} \right. \right. \\ &\quad \left. \left. + (-1)^M \begin{pmatrix} L & \ell' & L'' \\ -M & m' & M'' \end{pmatrix} {}_0 S_{L \ell L''}^{x'} \Theta_{L'' M''} \Theta_{L'M'} \right] \right. \\ &\quad \left. \left. - (-1)^{m'} \begin{pmatrix} \ell' & L & L' \\ -m' & M & M' \end{pmatrix} \bar{f}_{\ell' LL'}^{x', (\Theta\Theta)} \right\} x'_{\ell' m'} \right\}, \end{aligned} \quad (5.9)$$

where, in the above, the instrumental noise is ignored for simplicity. The above estimator (5.6) suffers from several drawbacks in practical application to observation. At first, we should know about the primary CMB angular power

spectra included in $\bar{f}_{\ell LL'}^{x,(\alpha)}$ a priori. Another problem is that the estimator includes the contribution from the term $n_{\ell m LL'}^{x,(\alpha)}$ which leads to a noisy reconstruction of the lensing potentials. Nevertheless, for the former point, the primary CMB angular power spectrum can be theoretically inferred if we know a set of fiducial cosmological parameters from other observations. On the other hand, for the latter point, we redefine the estimator for ϕ and ϖ by introducing a weight function, $\bar{F}_{\ell LL'}^{x,(\alpha)}$, in order to reduce the contribution from $n_{\ell m LL'}^{x,(\alpha)}$. Summing up all combination of L and L' , we write the estimator of the lensing potentials as

$$\hat{x}_{\ell m}^{(\alpha)} = \sum_{LL'} \bar{F}_{\ell LL'}^{x,(\alpha)} \sum_{MM'} (-1)^m \begin{pmatrix} \ell & L & L' \\ -m & M & M' \end{pmatrix} \hat{X}_{LM} \hat{Y}_{L'M'} . \quad (5.10)$$

The functional form of the weight function is determined so that the noise contribution is minimized.

In what follows, we determine the functional form of the weight function so that the estimator is unbiased and the noise term is minimized. Eq. (5.10) can be recast as

$$\begin{aligned} \hat{x}_{\ell m}^{(\alpha)} &= \sum_{LL'} \bar{F}_{\ell LL'}^{x,(\alpha)} \sum_{x'=\phi,\varpi} \frac{\bar{f}_{\ell LL'}^{x',(\alpha)}}{2\ell+1} x'_{\ell m} + n_{\ell m}^{x,(\alpha)} \\ &= \sum_{x'=\phi,\varpi} [\bar{F}^x, \bar{f}^{x'}]_{\ell}^{(\alpha)} x'_{\ell m} + n_{\ell m}^{x,(\alpha)}, \end{aligned} \quad (5.11)$$

where the inner product $[a^x, b^{x'}]_{\ell}^{(\alpha)}$ for arbitrary two quantities, $a_{\ell LL'}^{x,(\alpha)}$ and $b_{\ell LL'}^{x',(\alpha)}$, is defined by

$$[a^x, b^{x'}]_{\ell}^{(\alpha)} \equiv \frac{1}{2\ell+1} \sum_{LL'} a_{\ell LL'}^{x,(\alpha)} b_{\ell LL'}^{x',(\alpha)} . \quad (5.12)$$

The quantity, $n_{\ell m}^{x,(\alpha)}$, is defined as

$$n_{\ell m}^{x,(\alpha)} \equiv \sum_{LL'} \bar{F}_{\ell LL'}^{x,(\alpha)} \frac{\bar{f}_{\ell LL'}^{x,(\alpha)}}{2\ell+1} n_{\ell m,LL'}^{x,(\alpha)} . \quad (5.13)$$

Eq. (5.11) implies that the estimator would be an unbiased estimator if we impose the following condition:

$$[\bar{F}^x, \bar{f}^{x'}]_{\ell}^{(\alpha)} = \delta_{x,x'} . \quad (5.14)$$

Mathematically, this is equivalent to $\langle \hat{x}_{\ell m}^{(\alpha)} \rangle_{\text{CMB}} = x_{\ell m}$. Also, we wish to suppress the noise contributions, $n_{\ell m}^{x,(\alpha)}$, imposing the following condition:

$$\frac{\delta}{\delta \bar{F}_{\ell LL'}^{x,(\alpha)}} \langle |n_{\ell m}^{x,(\alpha)}|^2 \rangle = 0 . \quad (5.15)$$

Let us determine the functional form of the weight function under the conditions, (5.14) and (5.15), with the Lagrange-multiplier method. The variance of $n_{\ell m}^{(\alpha)}$ is given by

$$\begin{aligned} \langle |n_{\ell m}^{(\alpha)}|^2 \rangle &= \frac{1}{2\ell+1} \sum_{LL'} (\bar{F}_{\ell LL'}^{x,(\alpha)})^* \\ &\times \left(\bar{F}_{\ell LL'}^{x,(\alpha)} \hat{C}_L^{XX'} \hat{C}_{L'}^{YY'} + \bar{F}_{\ell L',L}^{x,(\alpha)} (-1)^{\ell+L+L'} \hat{C}_L^{XY'} \hat{C}_{L'}^{X'Y} \right) , \end{aligned} \quad (5.16)$$

where the quantity, \hat{C}_L^{XY} , is the lensed angular power spectrum including the contributions from instrumental noise. The detailed calculation for the noise variance, $\langle |n_{\ell m}^{(\alpha)}|^2 \rangle$, is presented in appendix C. Then, Eq. (5.15) under the

constraint (5.14) is equivalent to

$$\begin{aligned} \frac{\delta}{\delta \bar{F}_{\ell LL'}^{x,(\alpha)}} & \left\{ \frac{1}{2\ell+1} \sum_{LL'} (\bar{F}_{\ell LL'}^{x,(\alpha)})^* \left(\bar{F}_{\ell LL'}^{x,(\alpha)} \hat{C}_L^{XX} \hat{C}_{L'}^{YY} + (-1)^{\ell+L+L'} \bar{F}_{\ell L',L}^{x,(\alpha)} \hat{C}_L^{XY} \hat{C}_{L'}^{XY} \right) \right. \\ & \left. + \sum_{x'=\phi,\varpi} \lambda_{x'}^x \left([\bar{F}^x, \bar{f}^{x'}]_\ell^{(\alpha)} - \delta_{xx'} \right) \right\} = 0. \end{aligned} \quad (5.17)$$

The quantities, λ_{ϕ}^x and λ_{ϖ}^x , are the Lagrange multiplier whose functional form is specified below. Eq. (5.17) leads to

$$(\bar{F}_{\ell LL'}^{x,(\alpha)})^* \hat{C}_L^{XX} \hat{C}_{L'}^{YY} + (\bar{F}_{\ell L',L}^{x,(\alpha)})^* (-1)^{\ell+L+L'} \hat{C}_L^{XY} \hat{C}_{L'}^{XY} + \sum_{x'=\phi,\varpi} \lambda_{x'}^x \bar{f}_{\ell LL'}^{x',(\alpha)} = 0. \quad (5.18)$$

In the above, interchanging L and L' , we also obtain

$$(\bar{F}_{\ell L',L}^{x,(\alpha)})^* \hat{C}_{L'}^{XX} \hat{C}_L^{YY} + (\bar{F}_{\ell LL'}^{x,(\alpha)})^* (-1)^{\ell+L+L'} \hat{C}_L^{XY} \hat{C}_{L'}^{XY} + \sum_{x'=\phi,\varpi} \lambda_{x'}^x \bar{f}_{\ell L',L}^{x',(\alpha)} = 0. \quad (5.19)$$

Multiplying the factors $\hat{C}_{L'}^{XX} \hat{C}_L^{YY}$ and $-(-1)^{\ell+L+L'} \hat{C}_L^{XY} \hat{C}_{L'}^{XY}$ with Eqs. (5.18) and (5.19), respectively, the sum of Eqs. (5.18) and (5.19) gives

$$\bar{F}_{\ell LL'}^{x,(\alpha)} + \sum_{x'=\phi,\varpi} (\lambda_{x'}^x)^* \bar{g}_{\ell LL'}^{x',(\alpha)} = 0, \quad (5.20)$$

where we define

$$\bar{g}_{\ell LL'}^{x,(\alpha)} = \frac{(\bar{f}_{\ell LL'}^{x,(\alpha)})^* \hat{C}_{L'}^{XX} \hat{C}_L^{YY} - (-1)^{\ell+L+L'} \hat{C}_L^{XY} \hat{C}_{L'}^{XY} (\bar{f}_{\ell L',L}^{x,(\alpha)})^*}{\hat{C}_L^{XX} \hat{C}_{L'}^{YY} \hat{C}_{L'}^{XX} \hat{C}_L^{YY} - (\hat{C}_L^{XY} \hat{C}_{L'}^{XY})^2}. \quad (5.21)$$

Substituting Eq. (5.20) into Eq. (5.14), we obtain

$$-\sum_{x''} (\lambda_{x''}^x)^* [\bar{g}^{x''}, \bar{f}^{x'}]_\ell^{(\alpha)} = \delta_{xx'}. \quad (5.22)$$

From Eq. (5.4), we find

$$[\bar{g}^{x''}, \bar{f}^{x'}]_\ell^{(\alpha)} = \delta_{x''x'} [\bar{g}^{x'}, \bar{f}^{x'}]_\ell^{(\alpha)}. \quad (5.23)$$

Combining the above equation with Eq. (5.22), we obtain the explicit form of the Lagrange multiplier

$$(\lambda_{x'}^x)^* = -\frac{\delta_{xx'}}{[\bar{f}^x, \bar{g}^x]_\ell^{(\alpha)}}. \quad (5.24)$$

Then, from Eq. (5.20), we finally obtain the expression for the weight function:

$$\bar{F}_{\ell LL'}^{x,(\alpha)} = \frac{\bar{g}_{\ell LL'}^{x,(\alpha)}}{[\bar{f}^x, \bar{g}^x]_\ell^{(\alpha)}}. \quad (5.25)$$

Note that, with the explicit expression (5.25), the noise variance, $\bar{N}_{\ell}^{x,(\alpha)}$, given in Eq. (5.16) becomes

$$\begin{aligned} \bar{N}_{\ell}^{x,(\alpha)} & \equiv \langle |n_{\ell m}^{x,(\alpha)}|^2 \rangle \\ & = \frac{1}{2\ell+1} \frac{1}{[\bar{f}^x, \bar{g}^x]_\ell^{(\alpha)}} \sum_{LL'} (\bar{g}_{\ell LL'}^{x,(\alpha)})^* \\ & \quad \times \left(\bar{F}_{\ell LL'}^{x,(\alpha)} \hat{C}_L^{XX} \hat{C}_{L'}^{YY} + \bar{F}_{\ell L',L}^{x,(\alpha)} (-1)^{\ell+L+L'} \hat{C}_L^{XY} \hat{C}_{L'}^{XY} \right) \\ & = \frac{1}{[\bar{f}^x, \bar{g}^x]_\ell^{(\alpha)}}, \end{aligned} \quad (5.26)$$

where we use the relations given in Eqs. (5.18) and (5.24). Thus, the weight function can be recast as

$$\bar{F}_{\ell LL'}^{x,(\alpha)} = \bar{N}_\ell^{x,(\alpha)} \bar{g}_{\ell LL'}^{x,(\alpha)}. \quad (5.27)$$

With the weight function given above, the estimators defined by Eq. (5.10) become optimal, i.e., the noise contribution is minimized. Eq. (5.25) or Eq. (5.27) is one of the main results in this thesis. Note that, if the curl mode is absent, $\varpi = 0$, the resultant form of the weight function for ϕ exactly coincides with the one obtained in Ref. [9]. The difference appears when the angular power spectrum of the curl mode, $C_\ell^{\varpi\varpi}$, included in the lensed angular power spectrum becomes non-vanishing. Note again that, in practical case, to use the estimator, the angular power spectrum of primary CMB anisotropies should be a priori known (i.e., $\bar{f}_{\ell LL'}^{\phi,(\alpha)}$ and $\bar{f}_{\ell LL'}^{\varpi,(\alpha)}$ are given).

Naive optimal combination

As discussed in Ref. [9], the noise contribution can be further suppressed by combining multiple observables. Summing up the whole possible combination of temperature and polarization anisotropies, the optimal combination of the minimum variance estimators are given by

$$\hat{x}_{\ell m}^{(c)} = \sum_{\alpha} W^{x,(\alpha)} \hat{x}_{\ell m}^{(\alpha)}. \quad (5.28)$$

The weight functions, $W^{x,(\alpha)}$, are determined so that the estimator satisfies the unbiased condition ($\langle \hat{x}_{\ell m}^{(c)} \rangle_{\text{CMB}} = x_{\ell m}$), and the variance of the noise contribution is minimum. The optimal combination of the minimum variance estimator is then determined by the same analogy as in Ref. [9], and the result is

$$\hat{x}_{\ell m}^{(c)} = \bar{N}_\ell^{x,(c)} \sum_{\alpha, \beta} \{(\bar{N}_\ell^x)^{-1}\}^{\alpha, \beta} \hat{x}_{\ell m}^{(\alpha)}, \quad (5.29)$$

where the variance, $\bar{N}_\ell^{x,(c)}$, is defined by

$$\bar{N}_\ell^{x,(c)} = \left[\sum_{\beta, \beta'} \{(\bar{N}_\ell^x)^{-1}\}_{\beta \beta'} \right]^{-1}. \quad (5.30)$$

The component of the matrix, $\{\bar{N}_\ell^x\}_{\alpha, \beta}$, is the covariance of $n_{\ell m}^{x,(\alpha)}$ and $n_{\ell m}^{x,(\beta)}$ which is given by

$$\begin{aligned} \bar{N}_\ell^{x,(\alpha, \beta)} &\equiv \langle (n_{\ell m}^{x,(\alpha)})^* n_{\ell m}^{x,(\beta)} \rangle \\ &= \frac{1}{2\ell + 1} \sum_{LL'} (\bar{F}_{\ell LL'}^{x,(\alpha)})^* \\ &\quad \times \left(\bar{F}_{\ell LL'}^{x,(\beta)} \hat{C}_L^{XX'} \hat{C}_{L'}^{YY'} + \bar{F}_{\ell L', L}^{x,(\beta)} (-1)^{\ell+L+L'} \hat{C}_L^{XY'} \hat{C}_{L'}^{X'Y} \right). \end{aligned} \quad (5.31)$$

The derivation of the above equation is given in appendix C.

5.1.2 Lensing estimator in flat-sky

The quadratic estimator for the curl mode has been empirically derived in [34], based on the flat-sky approximation. Here, we show that our full-sky estimator can reproduce the flat-sky estimator of Ref. [34] (Eqs. (10)-(12) of Ref. [34]), in the flat-sky limit, $\ell, L, L' \ll 1$.

Table 5.3: Functional forms of $f_{\ell, \mathbf{L}, \mathbf{L}'}^{\phi, (XY)}$ and $f_{\ell, \mathbf{L}, \mathbf{L}'}^{\varpi, (XY)}$ in the flat-sky case.

XY	$f_{\ell, \mathbf{L}, \mathbf{L}'}^{\phi, (XY)}$	$f_{\ell, \mathbf{L}, \mathbf{L}'}^{\varpi, (XY)}$
$\Theta\Theta$	$C_L^{\Theta\Theta} \boldsymbol{\ell} \cdot \mathbf{L} + C_{L'}^{\Theta\Theta} \boldsymbol{\ell} \cdot \mathbf{L}'$	$C_L^{\Theta\Theta} (\star\boldsymbol{\ell}) \cdot \mathbf{L} + C_{L'}^{\Theta\Theta} (\star\boldsymbol{\ell}) \cdot \mathbf{L}'$
ΘE	$C_L^{\Theta E} \boldsymbol{\ell} \cdot \mathbf{L} \cos 2\varphi_{LL'} + C_{L'}^{\Theta E} \boldsymbol{\ell} \cdot \mathbf{L}'$	$C_L^{\Theta E} (\star\boldsymbol{\ell}) \cdot \mathbf{L} \cos 2\varphi_{LL'} + C_{L'}^{\Theta E} (\star\boldsymbol{\ell}) \cdot \mathbf{L}'$
ΘB	$C_L^{\Theta E} \boldsymbol{\ell} \cdot \mathbf{L} \sin 2\varphi_{LL'}$	$C_L^{\Theta E} (\star\boldsymbol{\ell}) \cdot \mathbf{L} \sin 2\varphi_{LL'}$
$E E$	$[\boldsymbol{\ell} \cdot \mathbf{L} C_L^{EE} + \boldsymbol{\ell} \cdot \mathbf{L}' C_{L'}^{EE}] \cos 2\varphi_{LL'}$	$[(\star\boldsymbol{\ell}) \cdot \mathbf{L} C_L^{EE} + (\star\boldsymbol{\ell}) \cdot \mathbf{L}' C_{L'}^{EE}] \cos 2\varphi_{LL'}$
$E B$	$[\boldsymbol{\ell} \cdot \mathbf{L} C_L^{EE} - \boldsymbol{\ell} \cdot \mathbf{L}' C_{L'}^{BB}] \sin 2\varphi_{LL'}$	$[(\star\boldsymbol{\ell}) \cdot \mathbf{L} C_L^{EE} - (\star\boldsymbol{\ell}) \cdot \mathbf{L}' C_{L'}^{BB}] \sin 2\varphi_{LL'}$
$B B$	$[\boldsymbol{\ell} \cdot \mathbf{L} C_L^{BB} + \boldsymbol{\ell} \cdot \mathbf{L}' C_{L'}^{BB}] \cos 2\varphi_{LL'}$	$[(\star\boldsymbol{\ell}) \cdot \mathbf{L} C_L^{BB} + (\star\boldsymbol{\ell}) \cdot \mathbf{L}' C_{L'}^{BB}] \cos 2\varphi_{LL'}$

Let us first rewrite the full-sky estimator (5.10) in Fourier space. Using Eqs. (2.66) and (2.67), and combining Eq. (5.27), the full-sky estimator (5.10) in Fourier space is re-expressed as

$$\hat{x}_{\boldsymbol{\ell}}^{(\alpha)} = \sum_{LL'} LL' \int \frac{d\varphi_L}{2\pi} \int \frac{d\varphi_{L'}}{2\pi} \mathcal{T}_{\boldsymbol{\ell}, \mathbf{L}, \mathbf{L}'} \bar{N}_{\boldsymbol{\ell}}^{x, (\alpha)} \bar{g}_{\ell LL'}^{x, (\alpha)} \tilde{X}_{\mathbf{L}} \tilde{Y}_{\mathbf{L}'}, \quad (5.32)$$

where we define

$$\begin{aligned} \mathcal{T}_{\boldsymbol{\ell}, \mathbf{L}, \mathbf{L}'} &\equiv \left(\frac{(2L+1)(2L'+1)}{4\pi(2\ell+1)(LL')^2} \right)^{1/2} \sum_{mMM'} (-1)^m \begin{pmatrix} \ell & L & L' \\ -m & M & M' \end{pmatrix} \\ &\quad \times e^{im\varphi_{\ell}} e^{-iM\varphi_L} e^{-iM'\varphi_{L'}} i^{-m+M+M'} . \end{aligned} \quad (5.33)$$

To go further, we approximate the quantities, $\mathcal{T}_{\boldsymbol{\ell}, \mathbf{L}, \mathbf{L}'} g_{\ell LL'}^{x, (\alpha)}$ and $\bar{N}_{\boldsymbol{\ell}}^{x, (\alpha)}$, taking the flat-sky limit. To do this, we use the following relation valid under the flat-sky approximation, $\ell \gg 1$ [80]:

$$e^{\pm si(\varphi_{\ell}-\varphi)} e^{i\boldsymbol{\ell} \cdot \hat{\mathbf{n}}} \simeq (\pm i)^s \sqrt{\frac{2\pi}{\ell}} \sum_m i^m Y_{\ell m}^{\pm s}(\hat{\mathbf{n}}) e^{-im\varphi_{\ell}} \quad (s = 0, 2) . \quad (5.34)$$

We also note that the delta function is given by [80]:

$$\delta_{\boldsymbol{\ell}} = \int \frac{d^2 \hat{\mathbf{n}}}{(2\pi)^2} e^{i\boldsymbol{\ell} \cdot \hat{\mathbf{n}}} . \quad (5.35)$$

Using Eqs. (2.87), (2.101), (5.34) and (5.35), we find that, under the flat-sky approximation,

$$\begin{aligned} \mathcal{T}_{\ell, \mathbf{L}, \mathbf{L}'} \bar{g}_{\ell, \mathbf{L}, \mathbf{L}'}^{x,(\alpha)} &\simeq \delta_{\mathbf{L}+\mathbf{L}'-\ell} \left\{ \frac{\widehat{C}_{L'}^{XX} \widehat{C}_L^{YY} (f_{\ell, \mathbf{L}, \mathbf{L}'}^{x,(\alpha)})^* - \widehat{C}_L^{XY} \widehat{C}_{L'}^{XY} (f_{\ell, \mathbf{L}', \mathbf{L}}^{x,(\alpha)})^*}{\widehat{C}_{L'}^{XX} \widehat{C}_L^{YY} \widehat{C}_L^{XX} \widehat{C}_{L'}^{YY} - (\widehat{C}_L^{XY} \widehat{C}_{L'}^{XY})^2} \right\} \\ &\equiv \delta_{\mathbf{L}+\mathbf{L}'-\ell} g_{\ell, \mathbf{L}, \mathbf{L}'}^{x,(\alpha)}, \end{aligned} \quad (5.36)$$

$$\begin{aligned} \bar{N}_{\ell}^{x,(\alpha)} &\simeq \left\{ \int \frac{d^2 \mathbf{L}}{(2\pi)^2} \int d^2 \mathbf{L}' \delta_{\mathbf{L}+\mathbf{L}'-\ell} f_{\ell, \mathbf{L}, \mathbf{L}'}^{x,(\alpha)} g_{\ell, \mathbf{L}, \mathbf{L}'}^{x,(\alpha)} \right\}^{-1} \\ &\equiv N_{\ell}^{x,(\alpha)}, \end{aligned} \quad (5.37)$$

where the function, $f_{\ell, \mathbf{L}, \mathbf{L}'}^{x,(\alpha)}$, is given in Table 5.3 for each x and α . Note that the quantity, $N_{\ell}^{x,(\alpha)}$, is the flat-sky counterpart of the minimum variance, $\bar{N}_{\ell}^{x,(\alpha)}$. The detailed derivation of Eqs. (5.36) and (5.37) is given in appendix C. Then, Eq. (5.32) is rewritten as

$$\hat{x}_{\ell}^{(\alpha)} = \int \frac{d^2 \mathbf{L}}{(2\pi)^2} \int d^2 \mathbf{L}' \delta_{\mathbf{L}+\mathbf{L}'-\ell} F_{\ell, \mathbf{L}, \mathbf{L}'}^{x,(\alpha)} \tilde{X}_{\mathbf{L}} \tilde{Y}_{\mathbf{L}'} \quad (x = \phi, \varpi), \quad (5.38)$$

where we define the function, $F_{\ell, \mathbf{L}, \mathbf{L}'}^{x,(\alpha)}$, as

$$F_{\ell, \mathbf{L}, \mathbf{L}'}^{x,(\alpha)} = N_{\ell}^{x,(\alpha)} g_{\ell, \mathbf{L}, \mathbf{L}'}^{x,(\alpha)}. \quad (5.39)$$

Eq. (5.38) is the flat-sky counterpart of Eq. (5.10), which exactly coincides with that empirically defined in Ref. [34]. Ref. [34] mentioned that their estimator does not satisfy the unbiased condition, and may detect some non-zero signals of ϖ even in the absence of the curl mode. But our result show that their estimator satisfies the condition, $\langle \hat{x}_{\ell}^{(\alpha)} \rangle_{\text{CMB}} = x_{\ell}$, and becomes zero when the curl modes vanish².

Before closing this section, we also give the expression for the optimal combination of the flat-sky estimator used in the next section. With Eq. (2.67), the optimal combination (5.29) is rewritten as

$$\hat{x}_{\ell}^{(c)} = \bar{N}_{\ell}^{x,(c)} \sum_{\alpha, \beta} \{(\bar{N}_{\ell}^x)^{-1}\}^{\alpha, \beta} \hat{x}_{\ell}^{(\alpha)}, \quad (5.40)$$

and the minimum variance is obtained from Eq. (5.30). Then, denoting the flat-sky counterpart of $\bar{N}_{\ell}^{x,(c)}$ and \bar{N}_{ℓ}^x as $N_{\ell}^{x,(c)}$ and N_{ℓ}^x , respectively, the optimal combination in the flat-sky limit is described by

$$\hat{x}_{\ell}^{(c)} = N_{\ell}^{x,(c)} \sum_{\alpha, \beta} \{(N_{\ell}^x)^{-1}\}^{\alpha, \beta} \hat{x}_{\ell}^{(\alpha)}, \quad (5.41)$$

with the variance, $N_{\ell}^{x,(c)}$, given by

$$\frac{1}{N_{\ell}^{x,(c)}} = \sum_{\beta, \beta'} \{(N_{\ell}^x)^{-1}\}_{\beta \beta'}. \quad (5.42)$$

The component of the matrix, $\{N_{\ell}^x\}_{\alpha, \beta}$, is obtained by computing the flat-sky counterpart of Eq. (5.31)) and the result is

$$\begin{aligned} N_{\ell}^{x,(\alpha, \beta)} &= \int \frac{d^2 L}{(2\pi)^2} \int d^2 \mathbf{L}' \delta_{\mathbf{L}+\mathbf{L}'-\ell} (F_{\ell, \mathbf{L}, \mathbf{L}'}^{x,(\alpha)})^* \\ &\times \left(F_{\ell, \mathbf{L}, \mathbf{L}'}^{x,(\beta)} \widehat{C}_L^{XX'} \widehat{C}_{L'}^{YY'} + F_{\ell, \mathbf{L}', \mathbf{L}}^{x,(\beta)} \widehat{C}_L^{XY'} \widehat{C}_{L'}^{X'Y} \right). \end{aligned} \quad (5.43)$$

The detailed calculation of Eq. (5.43) is given in appendix C.

²In fact, the integrand in Eq.(14) of Ref. [34] is an odd function in terms of the angle of ℓ_1 , and the right-hand side of Eq.(14) vanishes.

5.1.3 Maximum likelihood estimator

Instead of the above derivation, given a set of observed CMB anisotropies, one of the useful way to derive the optimal estimator is the maximum-likelihood approach [137, 10, 138]. Here we compare the quadratic estimator with the maximum-likelihood estimator in the presence of both gradient and curl modes.

Formalism

Here we briefly summarize the maximum likelihood estimator given in Ref. [138]. We start from the Gaussian likelihood for unlensed CMB anisotropies which is given by [10]

$$\ln \mathcal{L} = -\frac{1}{2}[\boldsymbol{\Lambda}^{-1}\hat{\mathbf{X}}]^\dagger \mathbf{C}^{-1}[\boldsymbol{\Lambda}^{-1}\hat{\mathbf{X}}]^\dagger + \frac{1}{2} \ln \det \mathbf{C}^{-1} + \text{const.}, \quad (5.44)$$

where $\hat{\mathbf{X}}$ is a vector of CMB temperature and polarization multipoles, $\mathbf{C} \equiv \langle \hat{\mathbf{X}}\hat{\mathbf{X}}^\dagger \rangle|_{d=0}$, is the covariance matrix for unlensed CMB including contributions from instrumental noise, and the matrix, $\boldsymbol{\Lambda}$, is defined so that $\boldsymbol{\Lambda}\mathbf{X}(\hat{\mathbf{n}}) = \mathbf{X}(\hat{\mathbf{n}} + \mathbf{d})$. With the above likelihood, following Ref. [138], the lensing potentials, $x_{\ell m} = \phi_{\ell m}$ and $\varpi_{\ell m}$, which maximize the likelihood is obtained by solving

$$\frac{\partial \ln \mathcal{L}}{\partial x_{\ell m}} = \mathcal{H}_{\ell m}(x_{\ell m}) - \langle \mathcal{H}_{\ell m}(x_{\ell m}) \rangle = 0, \quad (5.45)$$

where the quantity, $\mathcal{H}_{\ell m}(x_{\ell m})$ is given as

$$\mathcal{H}_{\ell m}(x_{\ell m}) = \bar{\mathbf{X}}^\dagger \frac{\partial \boldsymbol{\Lambda}}{\partial x_{\ell m}} \mathbf{C} \boldsymbol{\Lambda}^\dagger \bar{\mathbf{X}}, \quad (5.46)$$

with the inverse-variance filtered map, $\bar{\mathbf{X}} = \mathbf{C}^{-1}\hat{\mathbf{X}}$. Note that the second term in Eq. (5.45) is obtained with the formula, $\text{Tr}(\mathbf{A}) = \langle \mathbf{x} \mathbf{A} \mathbf{C}^{-1} \mathbf{x} \rangle$, where \mathbf{A} is any matrix and \mathbf{x} is a Gaussian field. The maximum-likelihood estimator is the solution of Eq. (5.45), i.e., the estimator satisfies

$$\mathcal{H}_{\ell m}(\hat{x}_{\ell m}^{(c)}) - \langle \mathcal{H}_{\ell m}(\hat{x}_{\ell m}^{(c)}) \rangle = 0 \quad (5.47)$$

To obtain the estimator, we have to solve the above equation. But the estimator given in Eq. (5.47) is numerically unstable to solve, and Ref. [10] further adds Gaussian prior on lensing potentials to the formulation of estimator and adopts an iterative method, but still numerically cost.

Comparison with quadratic estimator

In the Fisher limit, the maximum-likelihood estimator can be simplified in the following form:

$$\begin{aligned} \hat{x}_{\ell m}^{(c)} &= \bar{N}_\ell^{x,(c)} \sum_{(XY),(ZW)} \sum_{LL'}^{L \leq L'} \{\hat{\mathbf{C}}_{LL'}^{-1}\}^{(XY),(ZW)} (\bar{f}_{\ell LL'}^{x,(ZW)})^* \\ &\quad \times \sum_{M,M'} (-1)^m \begin{pmatrix} \ell & L & L' \\ -m & M & M' \end{pmatrix} \hat{X}_{LM} \hat{Y}_{L'M'}, \end{aligned} \quad (5.48)$$

where X, Y, Z and W is the temperature or E/B mode polarizations, and we define the normalization as

$$\bar{N}_\ell^{x,(c)} = \left\{ \frac{1}{2\ell+1} \sum_{\alpha,\beta} \sum_I \{\hat{\mathbf{C}}_I^{-1}\}^{\alpha,\beta} (\bar{f}_{\ell I}^{x,\alpha})^* \bar{f}_{\ell I}^{x,\beta} \right\}^{-1}, \quad (5.49)$$

and the covariance is

$$\hat{C}_{(LL')}^{(XY),(ZW)} = \begin{cases} \hat{C}_L^{XZ}\hat{C}_{L'}^{YW} & (L < L') \\ \hat{C}_L^{XZ}\hat{C}_{L'}^{YW} + \hat{C}_L^{XW}\hat{C}_{L'}^{YZ} & (L = L') \end{cases}. \quad (5.50)$$

The above estimator is the same as the quadratic estimator but using unlensed CMB in the covariance matrix. Ignoring higher-order corrections involving C_ℓ^{xx} , the error of the above estimator is given by $\bar{N}_\ell^{x,(c)} + C_\ell^{xx}$.

For gradient mode, Ref. [137] shows that the expression of the maximum-likelihood estimator is nearly identical to that of quadratic estimator in temperature case. On the other hand, as shown in Ref. [10], the maximum likelihood estimator for B-mode polarization significantly decreases the amplitude of $\bar{N}_\ell^{x,(c)}$ compared to the quadratic estimator. However, the Fisher limit is not valid for polarizations estimators, i.e., the estimators with polarizations have highly non-Gaussian behavior, and the error of the above estimator has additional correction (higher-order terms of C_ℓ^{xx}) to $\bar{N}_\ell^{x,(c)} + C_\ell^{xx}$ [10]. although the maximum likelihood estimator is numerically hard to compute and further theoretical developments are required. These situations are also similar for curl mode. If we use the maximum-likelihood estimator for curl mode, the detectability would be increased but the numerical evaluation is challenging.

5.2 Estimating CMB lensing power spectrum

For cosmological analysis, we are interested in the statistical power of lensing potentials rather than the lensing field itself. In this section, we describe a method to measure lensing power spectra from lensing estimators, which will be used in chapter 6 for CMB lensing reconstruction from current data. Note that, to simplify the discussion, here the all quantities are expressed with the flat-sky approximation and we focus on the lensing reconstruction from the temperature anisotropies. Since we focus on the temperature case, hereafter, the quantities, $\hat{x}_\ell^{(\Theta\Theta)}$, $f_{\ell,L,\ell-L}^{x,(\Theta\Theta)}$ and $N_\ell^{x,(\Theta\Theta)}$, are denoted by \hat{x}_ℓ , $f_{\ell,L}^x$ and $N_\ell^{x,(0)}$, respectively.

5.2.1 From lensing potentials to lensing power spectrum

Power spectrum of lensing estimators

The power spectrum of the lensing potential may be studied through the power spectra of the quadratic estimators discussed in the previous section. The lensing estimator in the flat-sky approximation for temperature case given in Eq. (5.38) is rewritten as

$$\hat{x}_\ell = \frac{1}{2}N_\ell^{x,(0)} \int \frac{d^2\mathbf{L}}{(2\pi)^2} f_{\ell,\mathbf{L}}^x \bar{\Theta}_{\mathbf{L}} \bar{\Theta}_{\ell-\mathbf{L}}, \quad (5.51)$$

where we define filtered multipoles, $\bar{\Theta}_{\mathbf{L}}$, as

$$\bar{\Theta}_{\mathbf{L}} = \frac{1}{\hat{C}_L^{\Theta\Theta}} \hat{\Theta}_{\mathbf{L}}. \quad (5.52)$$

The power spectrum of the quadratic estimator is given by

$$\langle |\hat{x}_\ell|^2 \rangle = \frac{1}{4}(N_\ell^{x,(0)})^2 \int \frac{d^2\mathbf{L}}{(2\pi)^2} \int \frac{d^2\mathbf{L}'}{(2\pi)^2} f_{\ell,\mathbf{L}}^x f_{\ell,\mathbf{L}'}^x \langle \bar{\Theta}_{\mathbf{L}} \bar{\Theta}_{\ell-\mathbf{L}} (\bar{\Theta}_{\mathbf{L}'} \bar{\Theta}_{\ell-\mathbf{L}'})^* \rangle. \quad (5.53)$$

This quantity probes the 4-point function of the lensed CMB, and can be usefully broken into disconnected and connected parts as

$$\langle |\hat{x}_\ell|^2 \rangle = \langle |\hat{x}_\ell|^2 \rangle_D + \langle |\hat{x}_\ell|^2 \rangle_C. \quad (5.54)$$

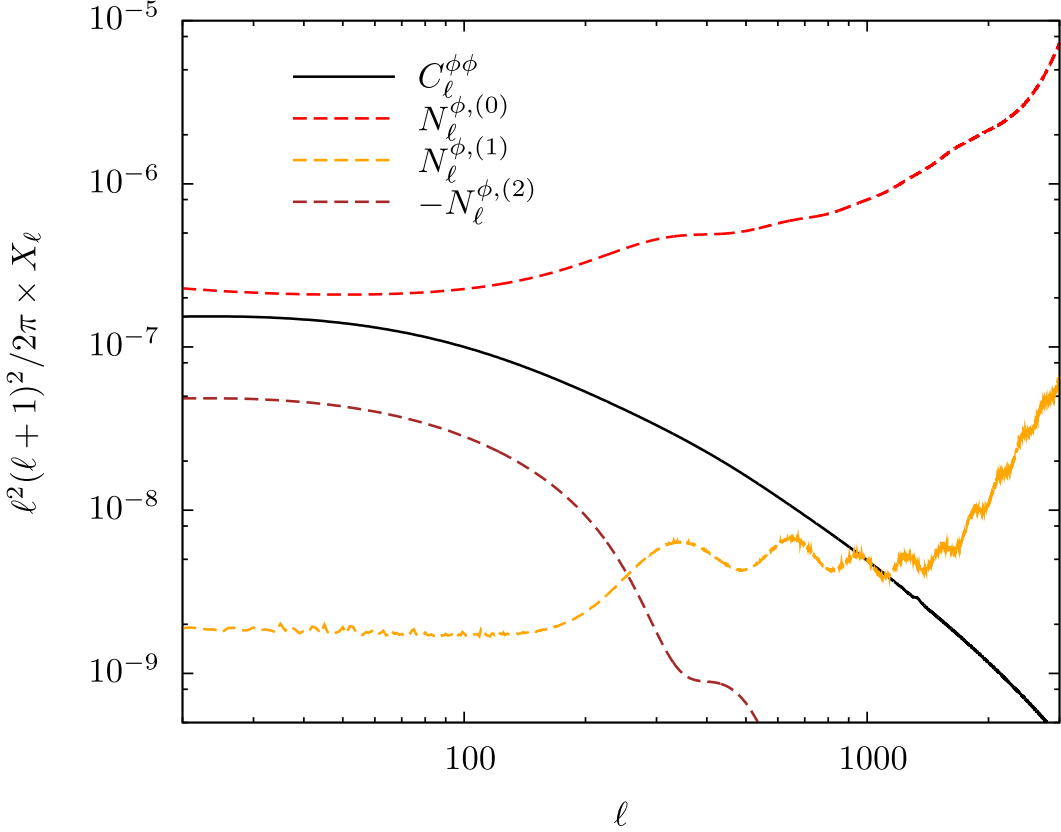


Figure 5.1: Contribution of N1 and N2 bias terms to the lensing estimator [139]. The solid line show the lensing power spectrum, $C_\ell^{\phi\phi}$, while the dashed lines show the biases in a measurement of lensing power spectrum, $N_\ell^{\phi,(0)}$, $N_\ell^{\phi,(1)}$ and $N_\ell^{\phi,(2)}$ (see text for their definitions).

The disconnected part, $\langle \cdots \rangle_D$, contains the contributions which would be expected if $\bar{\Theta}_L$ were a Gaussian random variable, while the connected part, $\langle \cdots \rangle_C$, contains the non-Gaussian contributions which are a distinctive signature of lensing. The disconnected part, usually referred to as ‘‘Gaussian noise bias’’, must be accurately subtracted from Eq. (5.54) to obtain a clean measurement of the lensing signal.

To obtain the explicit form of the Gaussian noise bias, we write the disconnected part of the four-point correlation as

$$\langle \hat{\Theta}_L \hat{\Theta}_{\ell-L} (\hat{\Theta}_{L'} \hat{\Theta}_{\ell-L'})^* \rangle_D = [\delta_D(\mathbf{L} + \mathbf{L}') + \delta_D(\mathbf{L} + \mathbf{L}' - \ell)] \widehat{C}_L^{\Theta\Theta} \widehat{C}_{|\ell-\mathbf{L}|}^{\Theta\Theta}. \quad (5.55)$$

Substituting Eq. (5.55) into Eq. (5.53), and using the expression of the normalization $N_\ell^{x,(0)}$, the power spectrum of estimator induced by the disconnected part becomes

$$\langle |\hat{x}_\ell|^2 \rangle_D = N_\ell^{x,(0)} = \left\{ \int \frac{d^2 \mathbf{L}}{(2\pi)^2} \frac{(f_{\mathbf{L},\mathbf{L}}^x)^2}{2\widehat{C}_L^{\Theta\Theta} \widehat{C}_{|\ell-\mathbf{L}|}^{\Theta\Theta}} \right\}^{-1}. \quad (5.56)$$

The power spectrum of the connected part of the quadratic estimator is given on the full sky by [141]

$$\langle |\hat{x}_\ell|^2 \rangle_C = C_\ell^{xx} + N_\ell^{x,(1)} + \mathcal{O}[(C_\ell^{xx})^2]. \quad (5.57)$$

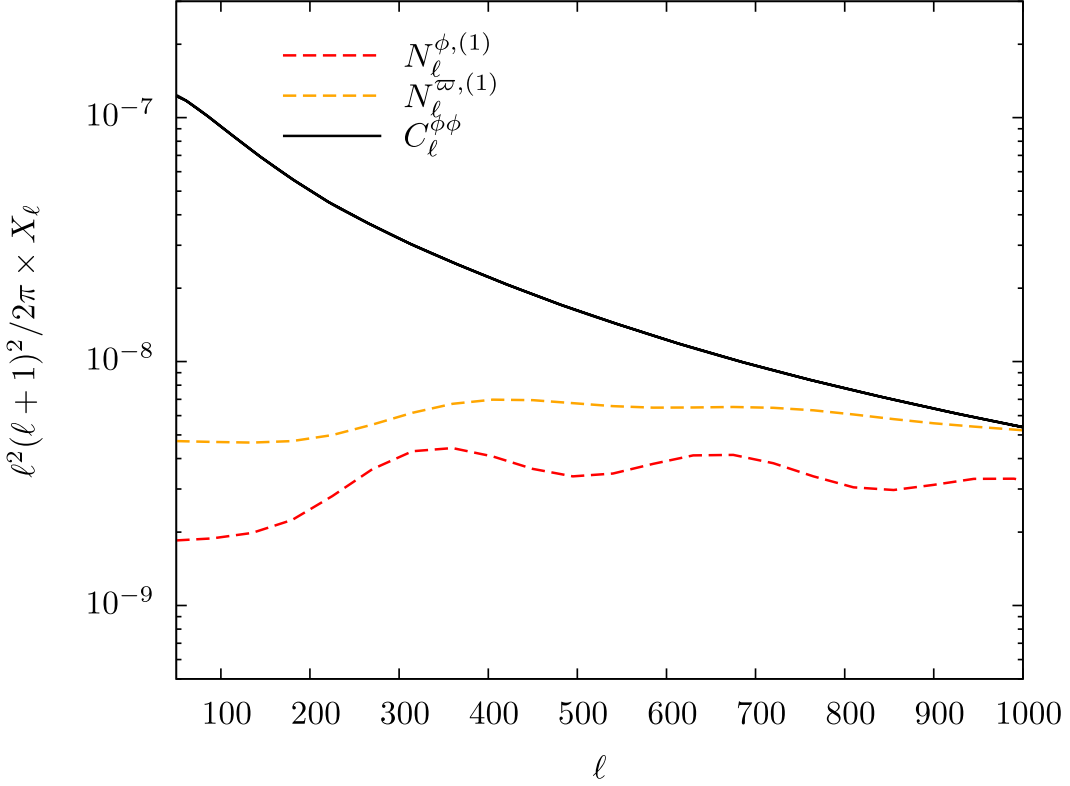


Figure 5.2: Comparison of N1-bias contributions on gradient and curl mode estimators [140]. We also show the lensing power spectrum, $C_\ell^{\phi\phi}$.

Here C_ℓ^{xx} is the lensing potential power spectrum which we have to estimate, while $N_\ell^{x,(1)}$ is a nuisance term coming from the “secondary” lensing contractions of the trispectrum [142] which is usually called N1 bias.

Finally, the power spectrum of estimator is given by

$$\langle |\hat{x}_\ell|^2 \rangle = C_\ell^{xx} + N_\ell^{x,(0)} + N_\ell^{x,(1)} + \mathcal{O}[(C_\ell^{xx})^2]. \quad (5.58)$$

Fig. 5.1 shows the bias terms, $N_\ell^{\phi,(0)}$, $N_\ell^{\phi,(1)}$, comparing with the lensing power spectrum, $C_\ell^{\phi\phi}$, in the case of PLANCK experimental specification [143]. Note that the bias contribution from second order of lensing power spectrum is also shown, and denoted by $N_\ell^{\phi,(2)}$, which is usually referred to as N2 bias. To measure the lensing power spectrum from lensing estimator, the contributions from the N1 and N2 biases should be corrected. In Fig. 5.2, we show the contributions of N1 bias for the curl mode estimator, comparing with the gradient mode estimator. Even in the absence of curl mode, the curl mode estimator after subtraction of the Gaussian noise bias does not vanish, $\langle |\hat{\varpi}_\ell|^2 \rangle - N_\ell^{\omega,(0)} = N_\ell^{\omega,(1)}$, since $N_\ell^{\omega,(1)}$ is generated by $C_\ell^{\phi\phi}$.

Eq. (5.58) means that the angular power spectrum of lensing potentials, C_ℓ^{xx} , is computed from the estimator by evaluating $N_\ell^{x,(0)}$ and $N_\ell^{x,(1)}$. In principle, these two quantities, $N_\ell^{x,(0)}$ and $N_\ell^{x,(1)}$, can be computed analytically, i.e., from Eq. (5.56) and Eq. (30) in [143], respectively. However, the exact calculation of these two quantities is numerically expensive because of the evaluation of the Wigner 3j and 6j symbols. In the followings, as an alternative to the exact calculation, we describe a method based on the Monte Carlo simulation.

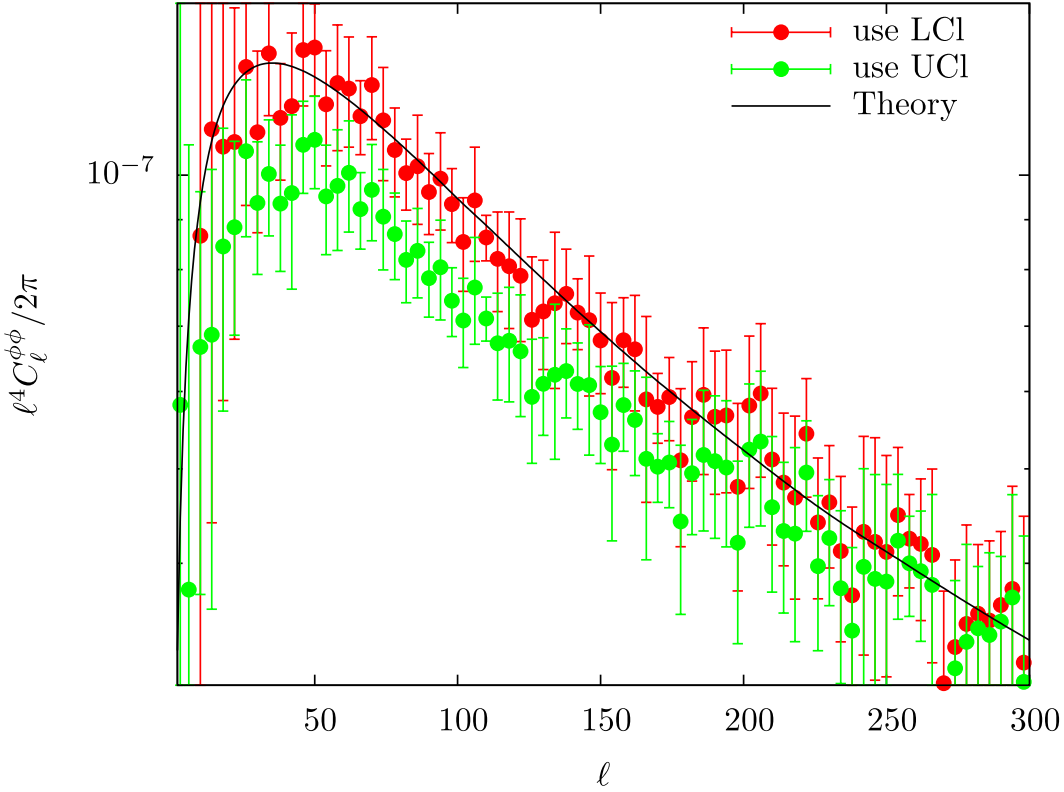


Figure 5.3: Power spectrum of lensing potential estimator after subtraction of the leading order bias, $|\hat{\phi}_\ell|^2 - N_\ell^{\phi,(0)}$, where the estimator is computed with the lensed (LCl) or unlensed (UCl) power spectrum involved in the weight function (see Table 5.2). The solid line shows the lensing power spectrum, $C_\ell^{\phi\phi}$. The error bars show the cosmic variance.

5.2.2 Estimating bias terms from Monte Carlo simulation

Estimating Gaussian noise

As shown in the above, the Gaussian noise is equivalent to the variance of estimator induced by the disconnected part of four-point correlation of lensed temperature anisotropies. By generating n_r realizations of Gaussian maps whose variance in Fourier space is the lensed angular power spectrum, the Gaussian noise is computed from

$$\hat{N}_\ell^{x,(0)} = \frac{1}{n_r} \sum_{i=1}^{n_r} \int \frac{d\varphi_\ell}{2\pi} |\hat{x}_\ell^{(0),i}|^2, \quad (5.59)$$

where the estimator $\hat{x}_\ell^{g,i}$ is obtained from i -th realization of the Gaussian map.

Estimating N1 bias

The N1 bias, $N_\ell^{x,(1)}$, can be computed by creating n_r number of realizations of lensed maps with a single realization of lensing potential, x_ℓ^{fix} . Computing estimators from each realization of lensed map, we obtain the following quantity:

$$\begin{aligned} & \frac{1}{n_r(n_r - 1)} \sum_{i \neq j} \int \frac{d\varphi_\ell}{2\pi} \hat{x}_\ell^{\text{fix},i} (\hat{x}_\ell^{\text{fix},j})^* \\ &= (N_\ell^{x,(0)})^2 \int \frac{d\varphi_\ell}{2\pi} \int \frac{d^2 \mathbf{L}}{(2\pi)^2} \int \frac{d^2 \mathbf{L}'}{(2\pi)^2} \frac{f_{\ell,\mathbf{L}}^x}{2\hat{C}_L^{\Theta\Theta} \hat{C}_{|\ell-\mathbf{L}|}^{\Theta\Theta}} \frac{f_{\ell,\mathbf{L}'}^x}{2\hat{C}_{L'}^{\Theta\Theta} \hat{C}_{|\ell-\mathbf{L}'|}^{\Theta\Theta}} \\ & \quad \times \frac{1}{n_r(n_r - 1)} \sum_{i \neq j} \hat{\Theta}_\mathbf{L}^{\text{fix},i} \hat{\Theta}_{\ell-\mathbf{L}}^{\text{fix},i} (\hat{\Theta}_{\mathbf{L}'}^{\text{fix},j} \hat{\Theta}_{\ell-\mathbf{L}'}^{\text{fix},j})^*, \end{aligned} \quad (5.60)$$

where we denote i -th realization of the temperature maps lensed by x_ℓ^{fix} as $\Theta_\ell^{\text{fix},i}$, and the estimator from these map is $\hat{x}_\ell^{\text{fix},i}$. The trispectrum included in the above equation becomes

$$\begin{aligned} & \frac{1}{n_r(n_r - 1)} \sum_{i \neq j} \hat{\Theta}_\mathbf{L}^{\text{fix},i} \hat{\Theta}_{\ell-\mathbf{L}}^{\text{fix},i} (\hat{\Theta}_{\mathbf{L}'}^{\text{fix},j} \hat{\Theta}_{\ell-\mathbf{L}'}^{\text{fix},j})^* \\ & \simeq \frac{2}{n_r(n_r - 1)} \sum_{i=1}^{n_r} \hat{\Theta}_\mathbf{L}^{\text{fix},i} \hat{\Theta}_{\ell-\mathbf{L}}^{\text{fix},i} \sum_{j=i+1}^{n_r} (\hat{\Theta}_{\mathbf{L}'}^{\text{fix},j} \hat{\Theta}_{\ell-\mathbf{L}'}^{\text{fix},j})^* \\ & \simeq f_{\ell,\mathbf{L}}^x f_{\ell,\mathbf{L}'}^x |x_\ell|^2, \end{aligned} \quad (5.61)$$

where, from left to middle, we ignore the products of lensed map between different realizations, and, from middle to right, we assume

$$\sum_{i=1}^{n_r} \hat{\Theta}_\mathbf{L}^{\text{fix},i} \hat{\Theta}_{\ell-\mathbf{L}}^{\text{fix},i} \simeq \langle \hat{\Theta}_\mathbf{L}^{\text{fix},i} \hat{\Theta}_{\ell-\mathbf{L}}^{\text{fix},i} \rangle_{\text{CMB}} = f_{\ell,\mathbf{L}}^x x_\ell^{\text{fix}}, \quad (5.62)$$

with $\langle \dots \rangle_{\text{CMB}}$ denoting the ensemble average over primary temperature anisotropies under a fixed lensing potential. Substituting Eq. (5.61) into Eq. (5.60), and using the definition of Gaussian noise given in Eq. (5.56), we obtain

$$\begin{aligned} & \frac{1}{n_r(n_r - 1)} \sum_{i \neq j} \int \frac{d\varphi_\ell}{2\pi} \hat{x}_\ell^{\text{fix},i} (\hat{x}_\ell^{\text{fix},j})^* \\ & \simeq (N_\ell^{x,(0)})^2 \int \frac{d\varphi_\ell}{2\pi} \int \frac{d^2 \mathbf{L}}{(2\pi)^2} \frac{(f_{\ell,\mathbf{L}}^x)^2}{2\hat{C}_L^{\Theta\Theta} \hat{C}_{|\ell-\mathbf{L}|}^{\Theta\Theta}} \int \frac{d^2 \mathbf{L}'}{(2\pi)^2} \frac{(f_{\ell,\mathbf{L}'}^x)^2}{2\hat{C}_{L'}^{\Theta\Theta} \hat{C}_{|\ell-\mathbf{L}'|}^{\Theta\Theta}} |x_\ell^{\text{fix}}|^2 \\ & = \int \frac{d\varphi_\ell}{2\pi} |x_\ell^{\text{fix}}|^2. \end{aligned} \quad (5.63)$$

The above quantity corresponds to the angular power spectrum of lensing potentials, and $N_\ell^{x,(1)}$ would be estimated by

$$\hat{N}_\ell^{x,(1)} = \frac{1}{n_r} \sum_i \int \frac{d\varphi_\ell}{2\pi} |\hat{x}_\ell^{\text{fix},i}|^2 - \hat{N}_\ell^{x,(0)} - \frac{1}{n_r(n_r - 1)} \sum_{i \neq j} \int \frac{d\varphi_\ell}{2\pi} \hat{x}_\ell^{\text{fix},i} (\hat{x}_\ell^{\text{fix},j})^*, \quad (5.64)$$

where $\hat{N}_\ell^{x,(0)}$ is computed from Eq. (5.59).

Estimating other bias terms

Second-order biases of $C_\ell^{\phi\phi}$ can be reduced by using lensed power spectrum instead of unlensed spectrum in the weight function [144]. In Fig. 5.3, we show the reconstructed lensing power spectrum with lensed/unlensed power spectrum in the weight function. The bias on large scales is reduced by using lensed power spectrum.

Chapter 6

An Improved Method For CMB Lensing Reconstruction

In the previous chapters we discuss what we can probe by weak lensing measurements and how to measure lensing, in particular, from CMB maps in the idealistic situation (i.e., full-sky coverage, homogeneous map noise, with a delta function instrumental beam, and so on). When applying lens reconstruction on a realistic dataset, there are at least two sources of bias which must be corrected for:

1. Statistical anisotropy from non-lensing sources such as a sky mask, inhomogeneous map noise, and asymmetry of the instrumental beam can be misinterpreted as lensing, generating a spurious lensing “mean-field bias”, i.e., the theoretical ensemble average of the estimator, $\langle \hat{x}_\ell \rangle$, does not vanish.
2. In the estimation of lensing power spectrum as described in Sec. 5.2, there can be a large contribution from the “Gaussian noise bias”, $\langle |\hat{x}_\ell|^2 \rangle_D$, which must be subtracted.

With perfect statistical understanding of the CMB, foregrounds, and instrumental response to the sky, these sources of bias are always computable (although potentially only through the use of Monte Carlo simulations), and may be subtracted from the lensing potential and power spectrum estimates. However, the mean-field ($\langle \hat{x}_\ell \rangle$) and Gaussian noise ($\langle |\hat{x}_\ell|^2 \rangle_D$), are often quite large in comparison to the signals of interest, i.e., the lensing field (x_ℓ) and lensing power spectrum C_ℓ^{xx} , respectively. The uncertainties in the power spectrum of the CMB fluctuations, the shape of the instrumental beam and its transfer function, the contribution from unresolved (and therefore unmasked) point sources, and the instrumental noise level can all lead to problematic uncertainties for these bias terms.

Multiple approaches have been proposed in the literature to mitigate these problems. For mean-field biases, most studies have focused on the issue of masking. One approach is to explicitly avoid masked regions [12, 51]. Another is inpainting, in which masked regions are filled with simulated signal, therefore reducing the large gradients at the mask boundary [145, 146]. Published analyses from the ACT and SPT experiments have used either source subtraction [15] or inpainting via Wiener filtering [16] to deal with resolved point sources, and apodization to reduce spurious gradients at the survey boundary. The reduction of uncertainties in the estimation of Gaussian noise has also been discussed in the literature. For full-sky coverage, with homogeneous map noise and a symmetric beam, the Gaussian noise may be estimated directly from the power spectrum of the map [142, 147]. This approach has the added benefit of suppressing terms in the covariance of the reconstructed power spectrum [143]. For several specific choices of apodization/inpainting, it has been found that the full-sky equations can be quite accurate even for cut-sky data [15, 146]. In principle, the Gaussian noise may be avoided entirely by taking the cross-spectrum of two estimators with independent noise realizations [142]. This is a more difficult proposition than for power spectrum, where the only source of noise is instrumental and independent surveys of the same region of sky may usually be obtained. In the case of lensing, a large fraction of the Gaussian noise comes from the CMB fluctuations themselves, and so the construction of estimators with independent noise realizations requires slicing the Fourier plane into disjoint regions,

such as the odd/even parity split [142] or the in/out split [148]. There is usually a substantial loss of signal-to-noise associated with such splits. Additionally, for a realistic observation, some mode mixing is induced by the sky mask and instrumental response, and it is necessary to introduce buffer regions between the disjoint pieces of the Fourier plane from which the lensing estimates are formed, leading to further degradation of signal-to-noise.

In this chapter, we discuss new methods for constructing lensing estimators which have significantly reduced mean-field bias and uncertainties in the Gaussian noise, with minimal loss of signal-to-noise. These “bias-hardened” estimators can be constructed in conjunction with any of the data processing methods (such as inpainting, apodization, inverse-variance filtering) described above. They are useful to deal not only with the complications induced by masking, but also with other effects such as noise inhomogeneity, beam asymmetry, and uncertainty in the primary CMB power spectrum.

6.1 Formalism of Estimators

In this section we propose methods to mitigate the mean-field bias and the uncertainties in the Gaussian noise bias.

6.1.1 Conventional approach

Here we first discuss the conventional approach to reduce biases from mode coupling which is generated by, e.g., masking effect, beam asymmetry, inhomogeneous noise and so on. Hereafter, we consider CMB lensing reconstruction from temperature alone in the flat-sky limit.

In addition to the quadratic estimator in the idealistic case, a practical estimator contains the subtraction of the mean-field bias:

$$\hat{x}_{\ell}^C = \hat{x}_{\ell}^S - \langle \hat{x}_{\ell}^S \rangle, \quad (6.1)$$

where \hat{x}_{ℓ}^S is the estimator in the idealistic case given in Eq. (5.51):

$$\hat{x}_{\ell}^S = \frac{1}{2} A_{\ell}^x \int \frac{d^2 L}{(2\pi)^2} f_{\ell L}^x \bar{\Theta}_L \bar{\Theta}_{\ell-L}. \quad (6.2)$$

In the above, we denote the normalization as A_{ℓ}^x since the estimator with the normalization, $N_{\ell}^{x,(0)}$, is in general biased in practical cases. It is still incredibly useful to assume $A_{\ell}^x = N_{\ell}^{x,(0)}$, however, if the effective normalization is close to $N_{\ell}^{x,(0)}$.

For idealistic case, the filtered multipoles, $\bar{\Theta}_L$, are given with the diagonal filter (see Eq. (5.52)). However, the filtered sky map $\bar{\Theta}_L$ given in Eq. (5.52) is no longer unbiased optimal estimator if there are additional mode couplings in the observed anisotropies (or, in other words, the covariance matrix of the filtered multipoles is not diagonal matrix). In the presence of additional contributions from non-lensing signals, inverse-variance (or “ C^{-1} ”) filtering can reduce the off-diagonal terms of covariance matrix, in which the filtered multipoles are obtained by filtering the lensed map, $\hat{\Theta}_L$, as

$$\bar{\Theta}_L = \sum_{L'} \{\hat{C}_{LL'}\}^{-1} \hat{\Theta}_{L'}, \quad (6.3)$$

where $\hat{C}_{LL'} \equiv \langle \hat{\Theta}_L \hat{\Theta}_{L'} \rangle$ is the covariance matrix for observed temperature map. Note that the diagonal filter (5.52) is simple to implement, and can be used even on the masked sky, with the penalty of large spurious gradients at the mask boundary [12]. Intermediate between full C^{-1} filtering and the diagonal approximation is the approach of using an apodized sky mask to reduce the creation of spurious gradients at the mask boundary (apodization). The details of apodization technique is given in Sec. 6.2.

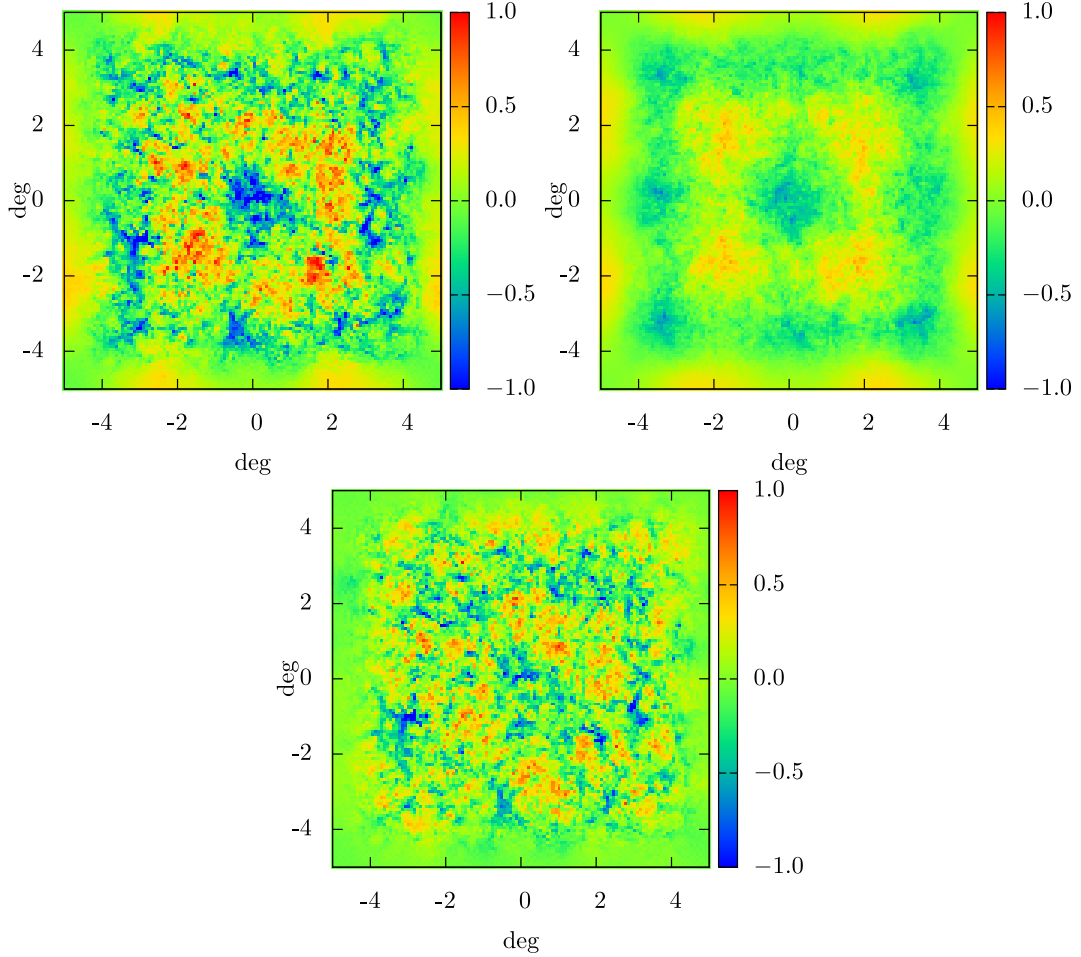


Figure 6.1: An example of the mean-field bias. The simulated temperature maps are generated with a fiducial temperature spectrum on $10 \times 10 \text{ deg}^2$ region. Then the maps are masked. *top left*: reconstructed field from one realization of masked map, $\hat{\phi}$. *top right*: reconstructed field averaged over several realizations, $\langle \hat{\phi} \rangle$. *bottom*: reconstructed field with mean-field subtraction, $\hat{\phi} - \langle \hat{\phi} \rangle$.

With the above filtering technique, we can reduce the mean-field and Gaussian noise bias. To illustrate subtraction of the mean-field bias, in Fig. 6.1, we show an example. In the top left, we show the reconstructed field from a masked map, $\hat{\phi}(\hat{n})$. It is clearly shown that there are some features associated with large scale modes. In fact, as shown in top right, if we average the reconstructed fields over 20 realizations, there are some residual field, which is just as the mean-field bias, $\langle \hat{\phi}(\hat{n}) \rangle$. In the conventional approach, the mean-field bias is estimated with many realizations of simulated maps, and then subtracted (see bottom). However, this is robust only when we know all systematics affected on temperature anisotropies, and simulated maps reproduce the *true* temperature map. Therefore an alternative method for cross check should be required.

Finally we discuss the uncertainties in the estimation of Gaussian noise bias:

$$\langle |\hat{x}_\ell|^2 \rangle_D = \frac{1}{2} (N_\ell^{x,(0)})^2 \int \frac{d^2 L}{(2\pi)^2} \int \frac{d^2 L'}{(2\pi)^2} f_{\ell L}^x f_{\ell L'}^x \bar{C}_{L,\ell-L'} \bar{C}_{\ell-L,L'}, \quad (6.4)$$

where $\bar{C}_{LL'} = \langle \bar{\Theta}_L \bar{\Theta}_{L'} \rangle$ is the covariance matrix of the filtered map. Given a model for this covariance matrix and a method to simulate Gaussian realizations of it, this disconnected bias may be evaluated by Monte Carlo simulations.

However, the uncertainties in the covariance matrix leads to problematic systematics for estimating Gaussian noise bias.

Before moving to the next section, we note on the fast computation technique for the quadratic estimator. A numerical approach to fast computation of the generic quadratic estimator is to rewrite Eq. (6.2) as a convolution of two maps, $\bar{\Theta}_\ell$, and $\alpha_\ell = i\ell \tilde{C}_\ell^{\Theta\Theta} \bar{\Theta}_\ell$ [8]:

$$\hat{x}_\ell^S = A_\ell^x \int \frac{d^2 L}{(2\pi)^2} \bar{\Theta}_L [\ell \odot_x \alpha_{L-L}] . \quad (6.5)$$

With the convolution theorem, in real space this can be written as

$$\hat{x}_\ell^S = A_\ell^x \int d^2 \hat{n} e^{-i\hat{n}\cdot\ell} \bar{\Theta}(\hat{n}) [\ell \odot_x \alpha(\hat{n})] , \quad (6.6)$$

where $\bar{\Theta}(\hat{n})$ and $\alpha(\hat{n})$ are the map space counterpart of $\bar{\Theta}_\ell$ and α_ℓ , respectively. Eq. (6.6) means that the estimator can be computed by FFT.

6.1.2 Bias-reduced lensing estimator

We begin by discussing a method to reduce the mean-field bias. Our approach is straightforward; we construct a new estimator which is optimized to detect the source of the mean-field bias, and use this estimate to correct the lensing estimator accordingly. This allows the construction of a new hybrid lensing estimator which has intrinsically much smaller mean-fields than the standard one.

To illustrate this approach, it is useful to consider the mean-field bias introduced by a specific form of statistical anisotropy. We consider a modulation of the observed temperature fluctuations by a function $\epsilon(\hat{n})$:

$$\widehat{\Theta}^{\text{mod}}(\hat{n}) = [1 - \epsilon(\hat{n})] \widehat{\Theta}(\hat{n}) , \quad (6.7)$$

Note that the above modulation is induced by, e.g., masking, beam asymmetry, inhomogeneous map noise [149, 52], and so on. From Eq. (6.7) the Fourier modes of observed temperature are related to the underlying fluctuations as

$$\widehat{\Theta}_\ell^{\text{mod}} = \int d^2 \hat{n} e^{-i\hat{n}\cdot\ell} \widehat{\Theta}^{\text{mod}}(\hat{n}) = \widehat{\Theta}_\ell - \int \frac{d^2 \ell'}{(2\pi)^2} \epsilon_{\ell-\ell'} \widehat{\Theta}_{\ell'} , \quad (6.8)$$

where ϵ_ℓ is the Fourier mode of $\epsilon(\hat{n})$. The covariance matrix is given by

$$\langle \widehat{\Theta}_L^{\text{mod}} \widehat{\Theta}_{L-L}^{\text{mod}} \rangle_{\text{CMB},n} = \delta_\ell \widehat{C}_L^{\Theta\Theta} + \sum_{x=\phi,\varpi} f_{\ell L}^x x_\ell + f_{\ell L}^\epsilon \epsilon_\ell + \mathcal{O}(\epsilon_\ell^2) , \quad (6.9)$$

where $\widehat{C}^{\Theta\Theta}$ is the power spectrum of underlying temperature map, and we define

$$f_{\ell L}^\epsilon = -\widehat{C}_L^{\Theta\Theta} - \widehat{C}_{|\ell-L|}^{\Theta\Theta} . \quad (6.10)$$

The operation $\langle \dots \rangle_{\text{CMB},n}$ means the ensemble average over the realizations of CMB and noise with a fixed realizations of lensing potentials. At first order in ϵ , with diagonal filtering, Eq. (6.9) leads to the following bias in ϕ -estimator:

$$\langle \widehat{\phi}_\ell^S \rangle_{\text{CMB},n} = \phi_\ell + A_\ell^\phi \left[\int \frac{d^2 L}{(2\pi)^2} \frac{f_{\ell L}^\phi f_{\ell L}^\epsilon}{2\widehat{C}_L^{\Theta\Theta} \widehat{C}_{|\ell-L|}^{\Theta\Theta}} \right] \epsilon_\ell . \quad (6.11)$$

We see that ϵ leads to a mean-field which directly traces the modulation field ϵ_ℓ . Unlike ϕ , the curl-mode estimator is unmodified at first order in ϵ , i.e., this kind of modulation fields does not introduce a large mean-field into the curl-mode estimator.

An estimator for the modulation field can be constructed analogous to that for lensing:

$$\hat{\epsilon}_{\ell}^S = \frac{1}{2} A_{\ell}^{\epsilon} \int \frac{d^2 L}{(2\pi)^2} f_{\ell L}^{\epsilon} \bar{\Theta}_L \bar{\Theta}_{\ell-L}, \quad (6.12)$$

where A_{ℓ}^{ϵ} is the same as Eq. (5.56) but with the mask weight function $f_{\ell L}^{\epsilon}$.

Now we consider the joint estimation of both the modulation and lensing fields simultaneously. The standard quadratic estimator is biased by modulation field as Eq. (6.11). Correspondingly, the naive ϵ estimator of Eq. (6.12) is biased by lensing as

$$\langle \hat{\epsilon}_{\ell}^S \rangle_{\text{CMB,n}} = \epsilon_{\ell} + \left[A_{\ell}^{\epsilon} \int \frac{d^2 L}{(2\pi)^2} \frac{f_{\ell L}^{\epsilon} f_{\ell L}^{\phi}}{2 \hat{C}_L^{\Theta\Theta} \hat{C}_{|\ell-L|}^{\Theta\Theta}} \right] \phi_{\ell}. \quad (6.13)$$

In matrix form, we can write (temporarily ignoring the mean-field corrections for both estimators)

$$\begin{pmatrix} \langle \hat{\phi}_{\ell}^S \rangle_{\text{CMB,n}} \\ \langle \hat{\epsilon}_{\ell}^S \rangle_{\text{CMB,n}} \end{pmatrix} = \begin{pmatrix} 1 & R_{\ell}^{\phi\epsilon} \\ R_{\ell}^{\epsilon\phi} & 1 \end{pmatrix} \begin{pmatrix} \phi_{\ell} \\ \epsilon_{\ell} \end{pmatrix}, \quad (6.14)$$

where the ensemble average is taken over CMB and noise realizations and we define the response function R_{ℓ}^{ab} , for $a, b = \phi, \epsilon$,

$$R_{\ell}^{ab} = A_{\ell}^a \int \frac{d^2 L}{(2\pi)^2} \frac{f_{\ell,L}^a f_{\ell,L}^b}{2 \hat{C}_L^{\Theta\Theta} \hat{C}_{|\ell-L|}^{\Theta\Theta}}. \quad (6.15)$$

By inverting Eq. (6.14), we obtain

$$\begin{pmatrix} \phi_{\ell} \\ \epsilon_{\ell} \end{pmatrix} = \frac{1}{1 - R_{\ell}^{x\epsilon} R_{\ell}^{\epsilon x}} \begin{pmatrix} 1 & -R_{\ell}^{x,\epsilon} \\ -R_{\ell}^{\epsilon x} & 1 \end{pmatrix} \begin{pmatrix} \langle \hat{\phi}_{\ell}^S \rangle_{\text{CMB,n}} \\ \langle \hat{\epsilon}_{\ell}^S \rangle_{\text{CMB,n}} \end{pmatrix}. \quad (6.16)$$

A bias-free estimator for the scalar lensing potential may therefore be formed as

$$\hat{\phi}_{\ell}^{\text{BR}} = \frac{\hat{\phi}_{\ell}^S - R_{\ell}^{x\epsilon} \hat{\epsilon}_{\ell}^S}{1 - R_{\ell}^{x\epsilon} R_{\ell}^{\epsilon x}}. \quad (6.17)$$

This lensing estimator has no mean-field contribution from the modulation field (up to the ϵ^2 term in Eq. (6.9)).

Let us consider the case of mean-field bias induced by masking. In this case the estimator of Eq. (6.17) will not be completely free of mask bias, since the ϵ^2 term may produce a significant mean-field contribution. Also if non-diagonal filtering of the map is utilized then the response terms of Eq. (6.15) are only approximate. Even in such situations, however, the estimator of Eq. (6.17) should have a smaller mask mean-field than the standard estimator. We therefore refer to this as a ‘‘bias-reduced (BR) estimator’’. In Sec. 6.2 we will test the behavior of this estimator for several choices of filtering and mask. The procedure above can be easily generalized to mitigate multiple sources of mean-field simultaneously.

Mean-field bias from other sources

Our intention for the construction of the BR estimators is to mitigate the mean-field bias generated by the field, ϵ_{ℓ} . But there are other sources of possible error for the mean-field subtraction of Eq. (6.2). Suppose, for example, that our analysis is performed using a slightly incorrect estimate $\hat{C}_L^{\Theta\Theta}$ (denoted by a cursive \mathcal{C}) for the ensemble average map power spectrum $\hat{C}_L^{\Theta\Theta}$, with

$$\hat{C}_L^{\Theta\Theta} = \hat{C}_L^{\Theta\Theta} - \Sigma_L. \quad (6.18)$$

This propagates directly to an error $f_{\ell,L}^\Sigma = -\Sigma_L - \Sigma_{|\ell-L|}$ in the weight function of Eq. (6.9). If the mean field is removed by averaging over masked CMB realizations with power spectrum given by Eq. (6.18), there will be an uncorrected mean field given by

$$\langle \hat{\phi}_\ell^C \rangle = \mathcal{R}^{\phi\Sigma} \epsilon_\ell, \quad (6.19)$$

where \mathcal{R}_ℓ^{ab} is the same as Eq. (6.15) but using the incorrect power spectrum. For the BR estimator, however, the uncorrected contribution is given by

$$\langle \hat{\phi}_\ell^{\text{BR}} \rangle = \frac{\mathcal{R}^{\phi\Sigma} - \mathcal{R}^{\phi\epsilon} \mathcal{R}^{\epsilon\Sigma}}{1 - \mathcal{R}_\ell^{\phi\epsilon} \mathcal{R}_\ell^{\epsilon\phi}} \epsilon_\ell. \quad (6.20)$$

It is in principle possible that the residual mean-field in this case is *worse* than for the standard approach, for example if $\mathcal{R}^{\phi\Sigma}$ is zero but $\mathcal{R}^{\epsilon\Sigma}$ is not. If a source of non-lensing statistical anisotropy has sufficient resemblance to lensing to produce a significant mean-field, such a situation seems somewhat pathological however and we do not believe it to be common. A more likely situation is that of a calibration error, for example $f_{\ell,L}^\Sigma = b f_{\ell,L}^\epsilon$, for some small coefficient b . In this case the residual mean-field will be completely avoided by the BR estimator. If bounds on Σ can be obtained for a specific experiment, the usefulness of the BR estimators can be explored using Eqs. (6.19) and (6.20). In any case, agreement between the standard and BR estimators provides a useful consistency test.

Derivation of BR estimator with optimal/unbiased conditions

Here we show that the BR estimator is the optimal unbiased estimator in the presence of uncertainties in both lensing and mask fields, i.e., the above estimator is uniquely determined by imposing the unbiased and optimal conditions on both the lensing and mask estimators. This is the same analogy of [35], but now we consider the lensing and mask fields simultaneously, which do not separately estimate each other. Thus we have to consider the response induced by the other as shown in Eq. (6.15).

Let us define optimal estimators for two fields, ϕ and ϵ , as

$$\hat{a}_\ell = \int \frac{d^2 L}{(2\pi)^2} F_{\ell L}^a \hat{\Theta}_L \hat{\Theta}_{\ell-L}, \quad (6.21)$$

with $a = \phi$ or ϵ . Note that the above estimator is unchanged with $L \rightarrow \ell - L$. We derive the functional form of, $F_{\ell L}^a$, so that the estimators satisfy the unbiased condition,

$$\langle \hat{a}_\ell \rangle_{\text{CMB}} = a_\ell, \quad (6.22)$$

and the optimal condition. Neglecting higher order corrections and zero-mode ($C_0 = 0$), we obtain

$$\langle \text{Eq. (6.21)} \rangle_{\text{CMB}} = \int \frac{d^2 L}{(2\pi)^2} F_{\ell L}^a \langle \hat{\Theta}_L \hat{\Theta}_{\ell-L} \rangle_{\text{CMB}} \quad (6.23)$$

$$= \int \frac{d^2 L}{(2\pi)^2} F_{\ell L}^a \sum_b f_{\ell L}^b b_\ell \quad (6.24)$$

$$= \sum_b [F^a, f^b]_\ell b_\ell, \quad (6.25)$$

with

$$[A, B]_\ell = \int \frac{d^2 L}{(2\pi)^2} A_{\ell L} B_{\ell L}. \quad (6.26)$$

This leads to

$$[F^a, f^b]_{\ell} = \delta_b^a. \quad (6.27)$$

Next, we determine the function F^a from the optimal condition by using the Lagrange-Multiplier method. The Gaussian variance of the estimator is

$$\begin{aligned} \langle (\hat{a}_{\ell})^* \hat{a}_{\ell} \rangle_G &= \int \frac{d^2 \mathbf{L}}{(2\pi)^2} \int \frac{d^2 \mathbf{L}'}{(2\pi)^2} (F_{\ell \mathbf{L}}^a)^* F_{\ell \mathbf{L}'}^a \langle \hat{\Theta}_{\mathbf{L}}^* \hat{\Theta}_{\ell - \mathbf{L}}^* \hat{\Theta}_{\mathbf{L}'} \hat{\Theta}_{\ell - \mathbf{L}'} \rangle_D \\ &= 2 \int \frac{d^2 \mathbf{L}}{(2\pi)^2} (F_{\ell \mathbf{L}}^a)^* F_{\ell \mathbf{L}}^a \hat{C}_L^{\Theta\Theta} \hat{C}_{|\ell - \mathbf{L}|}^{\Theta\Theta}, \end{aligned} \quad (6.28)$$

where we use $F_{\ell \mathbf{L}}^a = F_{\ell, \ell - \mathbf{L}}^a$. The functional form is given by solving the following equation:

$$0 = \frac{\partial}{\partial F_{\ell \mathbf{L}}^a} \langle (\hat{a}_{\ell})^* \hat{a}_{\ell} \rangle_G = 2(F_{\ell \mathbf{L}}^a)^* \hat{C}_L^{\Theta\Theta} \hat{C}_{|\ell - \mathbf{L}|}^{\Theta\Theta} - \sum_c \lambda_c^a f_{\ell, \mathbf{L}}^c. \quad (6.29)$$

where $\{\lambda_{\ell}\}_c^b$ denotes the Lagrange multiplier. Then, we obtain relations between F^a and λ_c^a :

$$F_{\ell \mathbf{L}}^a = \frac{\sum_c (\lambda_c^a)^* (f_{\ell \mathbf{L}}^c)^*}{2 \hat{C}_L^{\Theta\Theta} \hat{C}_{|\ell - \mathbf{L}|}^{\Theta\Theta}}. \quad (6.30)$$

Using Eq. (6.27), we find

$$\int \frac{d^2 \mathbf{L}}{(2\pi)^2} \frac{\sum_c (\lambda_c^a)^* f_{\ell \mathbf{L}}^b (f_{\ell \mathbf{L}}^c)^*}{2 \hat{C}_L^{\Theta\Theta} \hat{C}_{|\ell - \mathbf{L}|}^{\Theta\Theta}} = \delta_b^a. \quad (6.31)$$

Introducing normalizations and correlation coefficients as

$$R_{\ell}^{ab} = \int \frac{d^2 \mathbf{L}}{(2\pi)^2} \frac{f_{\ell \mathbf{L}}^a (f_{\ell \mathbf{L}}^b)^*}{2 \hat{C}_L^{\Theta\Theta} \hat{C}_{|\ell - \mathbf{L}|}^{\Theta\Theta}}, \quad (6.32)$$

we obtain

$$\sum_c (\lambda_c^a)^* R_{\ell}^{bc} = \delta_b^a. \quad (6.33)$$

This is equivalent to

$$(\lambda_b^a)^* = \{\mathbf{R}_{\ell}^{-1}\}_b^a, \quad (6.34)$$

where \mathbf{R} is a correlation matrix whose (a, b) component is given by $R^{a,b}$. Finally we obtain the functional form of the filter function and estimator as

$$F_{\ell, \mathbf{L}}^a = \sum_b \{\mathbf{R}_{\ell}^{-1}\}_b^a \frac{(f_{\ell, \mathbf{L}}^b)^*}{2 \hat{C}_L^{\Theta\Theta} \hat{C}_{|\ell - \mathbf{L}|}^{\Theta\Theta}}, \quad (6.35)$$

$$\hat{a}_{\ell} = \sum_b \{\mathbf{R}_{\ell}^{-1}\}_b^a \int \frac{d^2 \mathbf{L}}{(2\pi)^2} \frac{(f_{\ell, \mathbf{L}}^b)^*}{2 \hat{C}_L^{\Theta\Theta} \hat{C}_{|\ell - \mathbf{L}|}^{\Theta\Theta}} \hat{\Theta}_{\mathbf{L}} \hat{\Theta}_{\ell - \mathbf{L}}. \quad (6.36)$$

Note that if R^{ab} is diagonal, e.g., $a = \phi$ and $b = \varpi$, we obtain

$$F_{\ell, \mathbf{L}}^a = N_{\ell}^a \frac{(f_{\ell, \mathbf{L}}^a)^*}{2 \hat{C}_L^{\Theta\Theta} \hat{C}_{|\ell - \mathbf{L}|}^{\Theta\Theta}}, \quad (6.37)$$

where we introduce the normalization as

$$N_\ell^a \equiv [R_\ell^{aa}]^{-1} = \left\{ \int \frac{d^2 \mathbf{L}}{(2\pi)^2} \frac{f_{\ell \mathbf{L}}^a (f_{\ell \mathbf{L}}^a)^*}{2\bar{C}_L^{\Theta\Theta} \bar{C}_{|\ell - \mathbf{L}|}^{\Theta\Theta}} \right\}^{-1}. \quad (6.38)$$

If the mode coupling is only induced by one field or induced by multi-independent components, the normalization equals to the Gaussian noise of each estimator. If we define an uncorrelated estimator as

$$\hat{a}_\ell^{\text{uc}} = N_\ell^a \int \frac{d^2 \mathbf{L}}{(2\pi)^2} \frac{(f_{\ell \mathbf{L}}^a)^*}{2\bar{C}_L^{\Theta\Theta} \bar{C}_{|\ell - \mathbf{L}|}^{\Theta\Theta}} \hat{\Theta}_{\mathbf{L}} \hat{\Theta}_{\ell - \mathbf{L}}, \quad (6.39)$$

the correlated estimator is expressed as

$$\begin{aligned} \hat{a}_\ell &= \frac{\hat{a}_\ell^{\text{uc}} / (N_\ell^b N_\ell^a) - R_\ell^{ab} \hat{b}_\ell^{\text{uc}} / N_\ell^b}{1 / (N_\ell^a N_\ell^b) - R_\ell^{ab} R_\ell^{ba}}, \\ &= \frac{\hat{a}_\ell^{\text{uc}} - \mathcal{R}_\ell^{ab} \hat{b}_\ell^{\text{uc}}}{1 - \mathcal{R}_\ell^{ab} \mathcal{R}_\ell^{ba}}. \end{aligned} \quad (6.40)$$

6.1.3 Gaussian noise estimator

We turn now to the issue of estimating the Gaussian noise bias to obtain lensing power spectrum, given by Eq. (6.4), which is dependent on the covariance matrix of the filtered CMB modes $\bar{C}_{\mathbf{LL}'}$. Similar to the case of the BR lensing estimator above, we suppose that we are in possession of an imperfect model $\bar{C}_{\mathbf{LL}'}$ for the ensemble-average covariance matrix of the filtered CMB modes

$$\bar{C}_{\mathbf{LL}'} = \bar{C}_{\mathbf{LL}'} - \Sigma_{\mathbf{LL}'}, \quad (6.41)$$

where $\Sigma_{\mathbf{LL}'}$ is an error matrix. An estimate of the Gaussian noise made by substituting \mathcal{C} for C in Eq. (6.4) will have $\mathcal{O}(\Sigma)$ contributions from the error matrix. We would therefore like to construct an estimator to determine the Gaussian noise more directly from the data.

For full-sky coverage and diagonal filtering, where the covariance matrix is given by $\bar{C}_{\mathbf{LL}'} = \delta_{\ell - \mathbf{L}'} \bar{C}_{\mathbf{L}}$, this can be done simply, by replacing the ensemble average $\bar{C}_{\mathbf{L}}$ in Eq. (6.4) with the (realization-dependent) power spectrum of the filtered map [142, 147]. This method of correcting the disconnected bias has the added advantage that it removes the largest off-diagonal contributions to the covariance matrix of the power spectrum estimates [143]. In more realistic situations where the covariance matrix has off-diagonal elements this procedure is not guaranteed to work, although for some specific forms of filtering it has been found adequate [15, 16, 146].

Here we motivate a new approach which utilizes both data and the imperfect covariance. It is more robust than relying entirely on $\bar{C}_{\mathbf{L}, \mathbf{L}'}$, and also does not depend on the accuracy of full-sky equations which neglect any off-diagonal correlations due to masking, inhomogeneity of the instrumental noise, etc. The method is again straightforward, we simply estimate the reconstruction noise bias with Eq. (6.4), substituting the imperfect model for one of the covariance matrices and the data itself for the other:

$$\widehat{\langle |\hat{x}_\ell|^2 \rangle}_D = (A_\ell^x)^2 \frac{1}{2} \int \frac{d^2 \mathbf{L}}{(2\pi)^2} \int \frac{d^2 \mathbf{L}'}{(2\pi)^2} f_{\ell \mathbf{L}}^x f_{\ell \mathbf{L}'}^x (2\bar{C}_{\mathbf{L}, \ell - \mathbf{L}'} \bar{\Theta}_{\ell - \mathbf{L}} \bar{\Theta}_{\ell - \mathbf{L}'} - \bar{C}_{\mathbf{L}, \ell - \mathbf{L}'} \bar{C}_{\ell - \mathbf{L}, \mathbf{L}'}) , \quad (6.42)$$

This approach to removal of the disconnected bias emerges naturally when deriving optimal trispectrum estimators from an Edgeworth expansion of the CMB likelihood (see e.g. [150] for a thorough derivation). The calculation of the bias in this manner is only sensitive to uncertainties in the CMB covariance at $\mathcal{O}(\Sigma^2)$, an improvement over an entirely model-based determination of the reconstruction noise. It also maintains the property of suppressing off-diagonal contributions to the covariance matrix of the reconstructed power spectrum. We refer to the approach above as the ‘‘Gaussian noise estimator’’.

6.2 Numerical Tests

In this section, we test the usefulness of the BR estimator for several different choices of filtering and characteristic masking. As discussed in Sec. 6.1.2, we expect significant reduction of the mask mean-field bias using these estimators, which reduces the ability for some uncertainties in the primary CMB and instrument properties to leave residual biases in the estimated lensing potential. We do not test the noise bias estimator, as the only potential limitation of its usefulness is in the size of the Σ^2 matrix in Eq. (6.41), and this must be evaluated on an experiment-specific basis. We will, however, compare the noise bias and normalization for the BR estimators to the approximation of Eq. (5.56) as a cross-check on how closely they agree with the full-sky expectation for various choices of filtering, with or without the use of the BR estimators.

For lensing reconstruction, we use 100 realizations of Gaussian unlensed and lensed temperature fluctuations. These fluctuations are simulated on a $10 \times 10 \text{ deg}^2$ map, and the lensed maps are generated using the ray-tracing simulations described in Appendix G. We generate simulated source masks by cutting N_m randomly located square regions with angular size r_m on each side. In our analysis, we choose $N_m = 70$ and $r_m = 10'$ or $20'$. Note that the case with $N_m = 70$ and $r_m = 10'$ roughly corresponds to the case of SPT lensing analysis [16]. To consider experiments with high-angular resolution such as PolarBear, ACTPol and SPTPol, and also to avoid contamination by SZ and unresolved point sources, we assume a delta function instrumental beam, but truncate the temperature multipoles at $\ell_{\max} = 3000$. We assume homogeneous map noise, with a level of $1 \mu\text{K}$ arcmin. The angular power spectrum of the lensed/unlensed temperature and scalar lensing potential is computed using CAMB [82].

6.2.1 Filtering

We use three approaches to filtering our simulated sky maps: the straightforward diagonal filtering of Eq. (5.52), on a masked map, diagonal filtering on the map with an apodized mask, and C^{-1} filtering. The apodization and C^{-1} procedures are described in more detail below.

Apodization

One approach to reduce mode coupling from sky cuts, often used in power spectrum estimation (e.g., [151]), is apodization; to smooth the mask somewhat so that its Fourier counterpart more closely resembles a delta function. To apodize the survey boundary, for example, we can use a window function given by (as in Eq. (6.7))

$$W^s(x, y; s_0) = w^s(x; s_0)w^s(y; s_0). \quad (6.43)$$

We will use a sine apodization function given by

$$w^s(s; s_0) = \frac{1}{w_1} \times \begin{cases} 1 & |s| < as_0 \\ \sin\left(\frac{\pi}{2} \frac{1 - |s|}{1 - s_0}\right) & as_0 \leq |s| < a \\ 0 & a \leq |s| \end{cases} \quad (6.44)$$

The parameter, s_0 , indicates the width of the region where the apodization is applied, and the prefactor, $w_1 \equiv 2a[s_0 + 2(1 - s_0)/\pi]$, is used so that $\int_{-\infty}^{\infty} ds w^s(s; s_0) = 1$. In Fig. 6.2, we show the Fourier counterpart of the above function:

$$w^s(\ell; s_0) = \int_{-\infty}^{\infty} ds e^{i\ell s} w^s(s; s_0). \quad (6.45)$$

The Fourier counterpart with $s_0 = 0.0$ has a high-contrast peak at $\ell = 0$ relative to that of the top-hat function ($s_0 = 1.0$). This implies that the function $W^s(\hat{n}; s_0)$ given by Eq. (6.44) with $s_0 = 0.0$ would be a better choice to

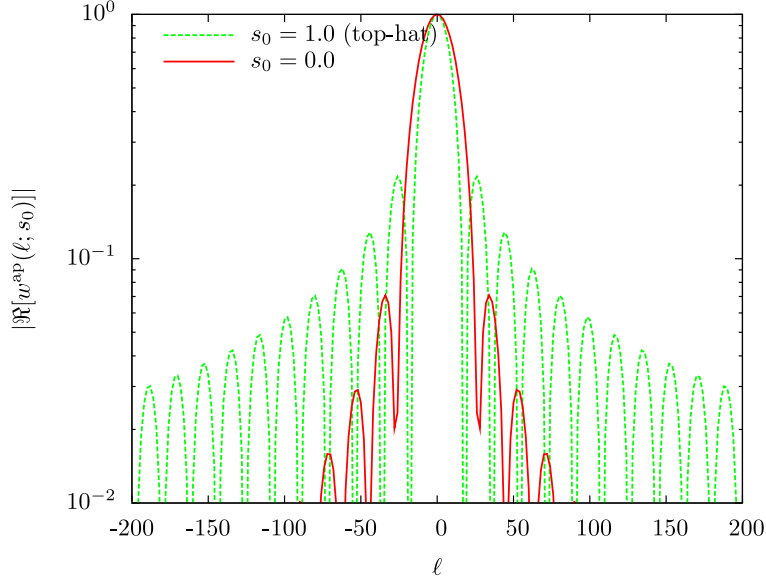


Figure 6.2: Real part of the apodizing function in Fourier space given in Eq. (6.44) with $s_0 = 0.0$ (red solid) compared with that of the top-hat function ($s_0 = 1.0$; green dashed). We choose $a = 10$ deg.

reduce mode coupling, compared to that with $s_0 = 1.0$. From here forward, the parameter, s_0 in all of our survey boundary apodization is set to $s_0 = 0.0$.

We now construct an apodization function for both the survey boundaries and detected point sources. Let us consider an observed map given on an $S = [-a : a] \times [-a : a]$ plane with N_m detected point sources, each of which we would like to mask. For simplicity, we will use a square mask function, with a length of r_m on each size. We apply an apodizing window function to the observed map, given as

$$W(\hat{\mathbf{n}}; s_0, t_0) = \frac{1}{W_1(s_0, t_0)} W^s(\hat{\mathbf{n}}; s_0) \prod_{i=1}^{N_m} (1 - W_{(i)}^m(\hat{\mathbf{n}}; t_0)), \quad (6.46)$$

The function, $W^s(\hat{\mathbf{n}}; s_0)$, is used to apodize the edges of the survey region, while the functions $1 - W_{(i)}^m(\hat{\mathbf{n}}; t_0)$, apodize the point sources. The factor W_1 is given by

$$W_1(s_0, t_0) = \int d^2\hat{\mathbf{n}} e^{-i\hat{\mathbf{n}} \cdot \boldsymbol{\ell}} W^s(\hat{\mathbf{n}}; s_0) \prod_{i=1}^{N_m} (1 - W_{(i)}^m(\hat{\mathbf{n}}; t_0)), \quad (6.47)$$

and the functions, $W_{(i)}^m(\hat{\mathbf{n}}; t_0)$ ($i = 1, 2, \dots, N_m$), are defined as

$$W_{(i)}^m(x, y; t_0) = w_{(i)}^m(x - x_i; t_0) w_{(i)}^m(y - y_i; t_0), \quad (6.48)$$

with

$$w_{(i)}^m(t; t_0) = \begin{cases} 1 & |t| < b \\ \sin\left(\frac{\pi}{2} \frac{b(1+t_0) - |t|}{bt_0}\right) & b \leq |t| < b(1+t_0) \\ 0 & b(1+t_0) \leq |t| \end{cases}. \quad (6.49)$$

(x_i, y_i) denotes coordinate of the i th point-source mask, and $b = r_m/2$. The parameter t_0 is the length of the apodization for each mask. Similar to $W^s(\hat{\mathbf{n}}; s_0)$, the Fourier counterpart of the mask function has a sharp peak

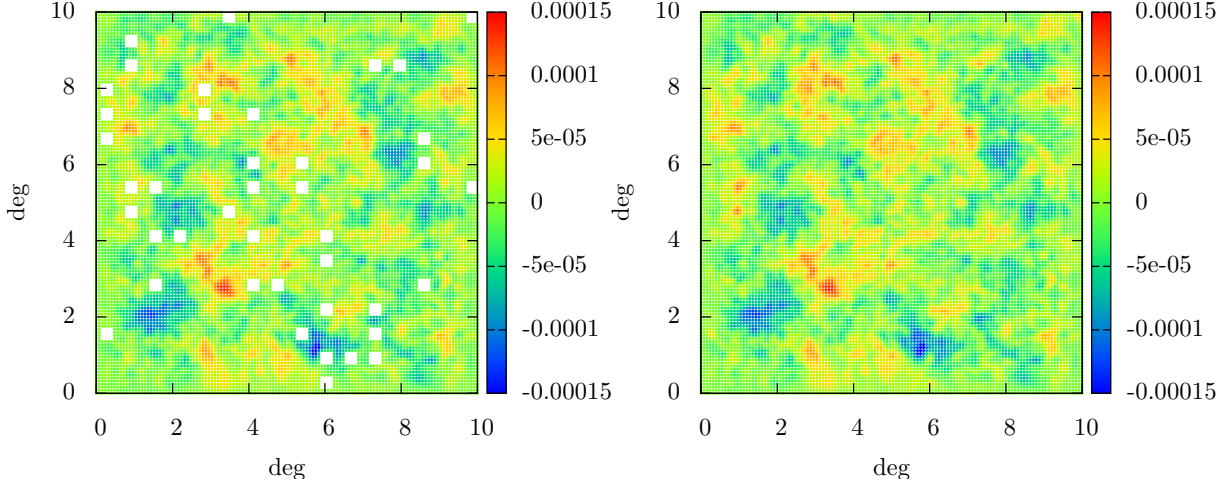


Figure 6.3: An example of C^{-1} filtering. *Left:* CMB temperature maps with point source masks. *Right:* C^{-1} filtered map.

around $\ell \sim 0$ at large values of t_0 . If both survey window and mask functions have a sharp peak at $\ell \sim 0$ in Fourier space, the Fourier transform of $W(\hat{\mathbf{n}}; s_0, t_0)$ is approximately a delta function.

C^{-1} filtering

The minimum-variance filtering which emerges from likelihood-based derivations of lensing estimators is known as C^{-1} filtering. For a data model given as

$$\widehat{\Theta}(\hat{\mathbf{n}}) = \Theta(\hat{\mathbf{n}}) + n(\hat{\mathbf{n}}), \quad (6.50)$$

the inverse-variance filtered multipoles, $\bar{\Theta}_\ell$, are obtained by solving

$$\left[1 + \mathbf{C}^{1/2} \mathbf{N}^{-1} \mathbf{C}^{1/2} \right] (\mathbf{C}^{1/2} \bar{\Theta}) = \mathbf{C}^{1/2} \mathbf{N}^{-1} \widehat{\Theta}. \quad (6.51)$$

Here $\bar{\Theta}$ is a vector whose components are $\bar{\Theta}_\ell$. \mathbf{C} is the covariance of the lensed or unlensed CMB anisotropies;

$$\{\mathbf{C}\}_{\ell_i, \ell_j} = \delta_{\ell_i - \ell_j} C_{\ell_i}^{\Theta \Theta}, \quad (6.52)$$

The matrix $\mathbf{N} = \langle \mathbf{n}^\dagger \mathbf{n} \rangle$ is the noise covariance. \mathbf{N} in Fourier space is obtained from that in real space $\overline{\mathbf{N}}$ as

$$\mathbf{N}^{-1} = \mathbf{Y}^\dagger \overline{\mathbf{N}}^{-1} \mathbf{Y}, \quad (6.53)$$

where the pointing matrix, \mathbf{Y} , is defined by

$$\{\mathbf{Y}\}_{\hat{\mathbf{n}}_i, \ell_j} = \exp(i \hat{\mathbf{n}}_i \cdot \ell_j). \quad (6.54)$$

The mask is incorporated by setting the noise level of masked pixels to infinity, and therefore the inverse of the noise covariance in real space $\overline{\mathbf{N}}^{-1}$ to zero for masked pixels. The inversion of the matrix on the left-hand side of Eq. (6.51) can be numerically cost but may be evaluated by the conjugate descent with careful preconditioning [11].

For our C^{-1} results, after applying the C^{-1} filter we additionally apply an apodizing function to account for the survey boundary, given by Eq. (6.44).

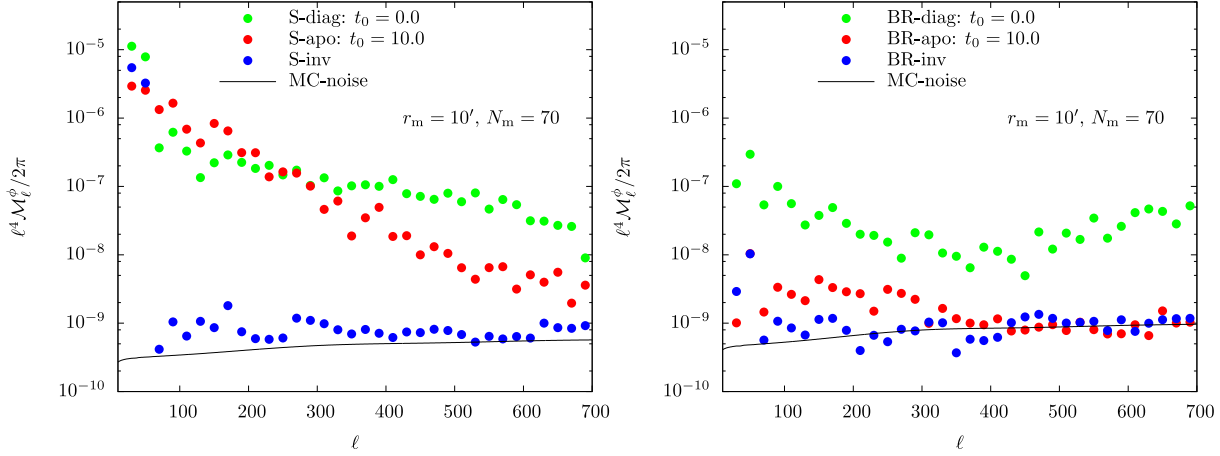


Figure 6.4: Mask mean-field spectrum computed with 100 Gaussian unlensed map realizations using the standard estimator (left) and the BR estimator (right). In each panel, we show the case with diagonal filtering (S-diag, BR-diag), apodization (S-apo, BR-apo), and C-inverse filtered map (S-inv, BR-inv). The black line shows the Monte-Carlo noise, $N_\ell^{\phi,(0)} / 20$. The multipoles are used up to $\ell_{\text{max}} = 3000$. The number and size of masks, N_m and r_m , are fixed with 70 and $10'$, respectively; the total fraction of masked area is $\sim 2\%$.

6.2.2 Mean-field power spectrum

We now proceed to our numerical results. We start by looking at the mean-field power spectrum for both the standard and BR estimators.

In Fig. 6.4, we plot the power spectrum

$$\mathcal{M}_\ell^x \equiv \frac{1}{W_2} \int \frac{d\varphi_\ell}{2\pi} \left| \frac{1}{100} \sum_{i=1}^{100} \hat{x}_\ell^{g,i} \right|^2, \quad (6.55)$$

where $\hat{x}_\ell^{g,i}$ is reconstructed from i -th realization of an unlensed Gaussian map without mean-field subtraction, and W_2 is derived (in analogy to appendix B in Ref. [75]) as

$$W_2 \equiv \int d^2 \hat{\mathbf{n}} W^2(\hat{\mathbf{n}}; s_0, t_0). \quad (6.56)$$

We construct source masks with $N_m = 70$ and $r_m = 10'$. To show the usefulness of the BR estimator, we compute

- the standard quadratic estimator, Eq. (6.2), or
- the BR estimator, Eq. (6.17),

where the filtering is taken to be

- the diagonal filter with no apodization of source holes ($t_0 = 0$, denoted as S-diag) or
- the diagonal filter with apodized source holes (non-zero t_0 , denoted as S-apo), or
- the inverse-variance filtered map (denoted as S-inv).

As noted above, in all cases we use $s_0 = 0.0$. The results for the BR estimator are prefixed by ‘‘BR’’.

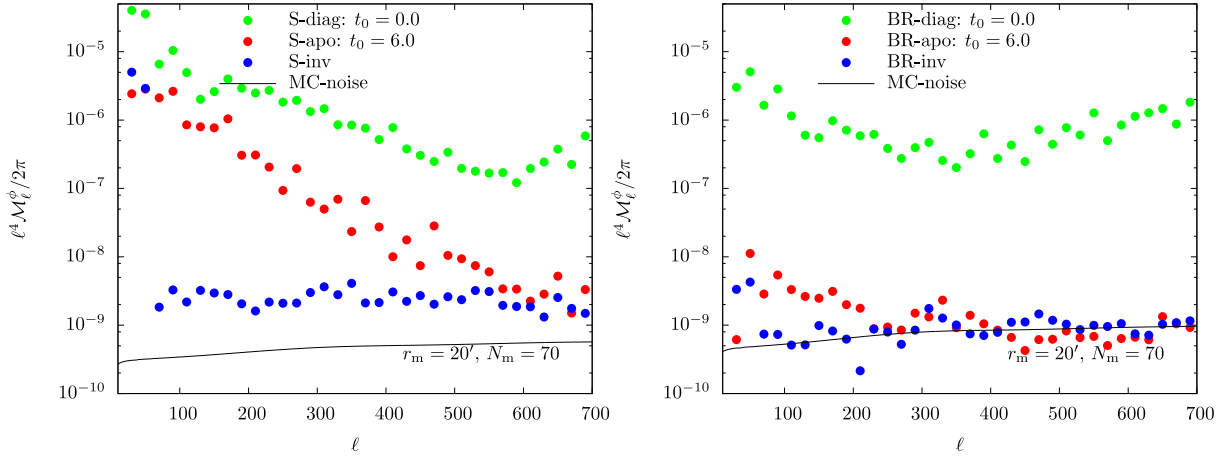


Figure 6.5: Same as Fig. 6.4, but for $r_m = 20'$; the total fraction of masked area is $\sim 8\%$.

It is clear that the mean field bias from the standard quadratic estimator is large particularly on large scales, $\ell \lesssim 500$. For the standard quadratic estimator, the mean-field on large scales still has a large amplitude even with source apodization or C^{-1} filtering. When we use the inverse-variance filtering, the mean-field contribution from source holes is suppressed significantly. This is because the α_ℓ term in the estimator (c.f. Eq. (6.5)) in the case of C^{-1} filtering corresponds to Wiener filtering, which is able to reconstruct the component of the masked signal which is due to modes larger than the holes themselves. Most of the power in the CMB gradient is due to scales greater than $r_m = 10'$, and so this inpainting aspect of the C^{-1} filter significantly reduces the generation of spurious gradients near the source boundary. Even for C^{-1} filtering, however, there exists a mean-field on large scales $\ell \lesssim 100$ due to the survey boundary in the standard estimator. On the other hand, even without source apodization, the BR estimator suppresses the mean-field significantly. If we use the source apodization or C^{-1} filtering, the mean-field is suppressed significantly, and the amplitude close to the Monte-Carlo noise level.

In Fig. 6.5, we show the case with $r_m = 20'$. Even in this case, for standard quadratic estimator, either the source apodization or C^{-1} filtering suppresses the mean field significantly compared to the case without these two filtering methods, but, similar to $r_m = 10'$, there are still large mean field at large scales. For the BR estimator, the mean field is suppressed down to the Monte-Carlo noise floor.

6.2.3 Power spectrum of lensing estimator

Next, we show the power spectrum of the lensing estimator computed from unlensed Gaussian simulations, i.e., the reconstruction noise bias. The reconstruction noise bias of the i -th realization map is computed as

$$\hat{N}_\ell^{xx,i} = \frac{1}{W_4} \int \frac{d\varphi_\ell}{2\pi} |\hat{x}_\ell^{g,i}|^2, \quad (6.57)$$

and then the mean of 100 realizations is compared with the full-sky, diagonal filtering expectation. Note that, for the reduced bias estimator, the noise bias is modified, i.e., the standard reconstruction noise bias divided by $(1 - R_\ell^{\phi,M} R_\ell^{M,\phi})$.

Fig. 6.6 shows the reconstruction noise bias, for the same cases as shown in Fig. 6.4. For both the apodization and C^{-1} filtering, the reconstruction noise bias agrees well with the analytical approximation using either the standard estimator (after a perfect mean-field subtraction) or the BR estimator. The errors using the BR estimator are not so degraded compared to the that using the standard approach.

Now we discuss the errors of estimator in the presence of incomplete mean-field subtraction in the standard approach. The advantage of the BR estimator is that it may be less sensitive on how accurately we model the statistics

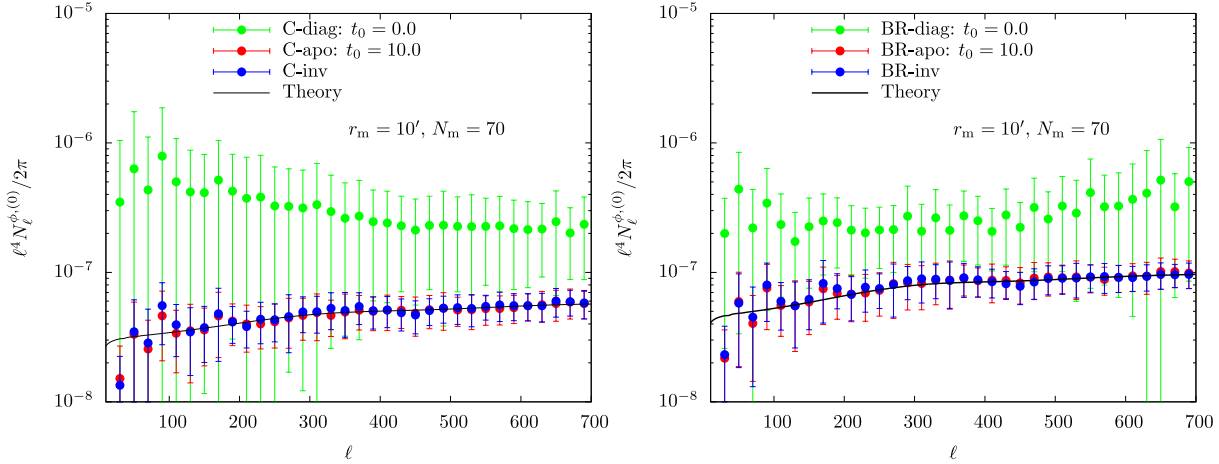


Figure 6.6: The angular spectrum of lensing estimator with Gaussian simulation using the standard estimator with the subtraction of the mean-field bias Eq. (6.1) (left) and the BR estimator of Eq. (6.17) (right). The mean and error bars of angular power spectrum are computed by 100 realizations of the simulation.

of the underlying fluctuations. In the above analysis, although the errors for the BR result are slightly larger than those for the standard result, the uncertainties in the mean-filed bias is completely ignored, and inclusion of other possible sources for mean-field bias degrades the accuracy in the standard approach. To see this, we consider a case with the uncertainty in mean-field bias generated by, e.g., calibration error as discussed in the previous section, and the resultant estimator is

$$\hat{\phi}^C \rightarrow \hat{\phi}^C + \epsilon \langle \hat{\phi}_\ell^S \rangle, \quad (6.58)$$

where ϵ is a small parameter. Fig. 6.7 shows the expected errors taking into account this uncertainty, normalized by the minimum variance, $(N_\ell^{\phi,(0)})^{1/2}$: $(1 + \epsilon^2 \mathcal{M}_\ell^\phi / N_\ell^{\phi,(0)})^{1/2}$. We also show the error bars expected from the BR estimator, $1/(1 - R_\ell^{\phi M} R_\ell^{M\phi})^{1/2}$. The mean-field spectrum, \mathcal{M}_ℓ^ϕ , is computed for $N_m = 70$ and $r_m = 10'$. As clearly shown, the result with the BR estimator is accurate on large scales ($\ell \lesssim 100$) where the lensing signals are dominated compared to that with the conventional approach.

In Fig. 6.8, we show the curl mode. The reconstruction noise of the curl mode is modified and the normalization is biased by the mode coupling due to the presence of sky cuts and masks. Note that there is no characteristic feature at large scales as there is for the scalar-lensing potential. This is because the estimator of the curl mode is not significantly biased by the masking mean-field, as discussed in the previous section. Similar to the case with the BR estimator, using source apodization, the reconstruction noise agrees well with the analytical prediction for small source holes.

Finally, in Fig. 6.9, to see how well the bias can be reduced even in the presence of lensing field, as well as how well the estimator normalization is described by the full-sky equation, we show the angular power spectrum of lensing estimator, computed from Eq. (6.57) but using the estimator reconstructed from i th realization of simulated lensed map. The theoretical prediction is the sum of the reconstruction noise, $N_\ell^{x,(0)} = A_\ell^x$, and the lensing spectrum, $C_\ell^{\phi\phi}$. The results are similar to that in the case with the unlensed Gaussian simulation.

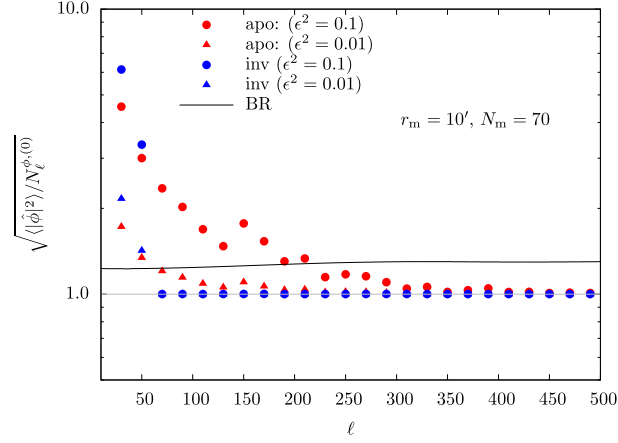


Figure 6.7: The error of estimator in the presence of residuals in the subtraction of mean-field bias. The points show the error in the case with apodization (red) or C^{-1} filtering (blue), assuming $\epsilon^2 = 0.1$ or $\epsilon^2 = 0.01$. For comparison, we also show the error of the BR estimator.

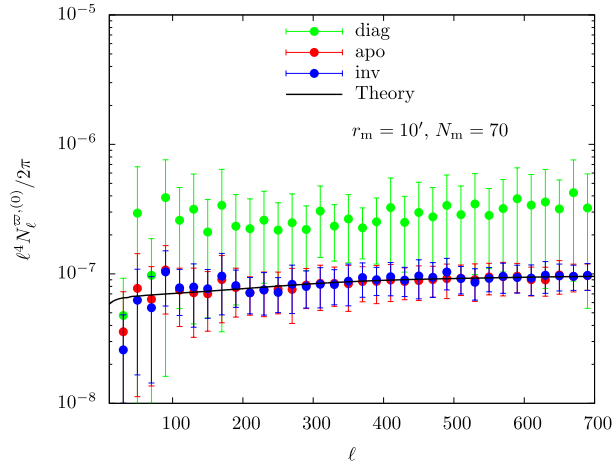


Figure 6.8: Curl-mode estimator spectrum in the case with $N_m = 70$ and $r_m = 10'$.

6.3 Application of Bias-Reduced Estimator to CMB data

In this section, we apply the BR estimator to ACT data which is obtained from the website¹, and see whether measured lensing signals with the BR estimator are consistent with that obtained in Ref. [15]. We also measure the curl-mode spectrum from ACT data and show cosmological implications from curl mode.

6.3.1 Maps used for reconstruction and measured temperature angular power spectrum

For CMB lensing reconstruction, we avoid survey boundaries and choose a region where the noise level is around $\sim 30\mu\text{K}\text{-arcmin}$, and divide into four square regions. Area of each map is $\sim 70 \text{ deg}^2$ (1024^2 pixels where size of each pixel is $0.5 \text{ arcmin-square}$). We also apply apodization window function given in previous section with $s_0 = 0.0$, and filtered out Fourier modes $\ell \leq 300$ and $\ell \geq 7000$.

¹<http://lambda.gsfc.nasa.gov/>

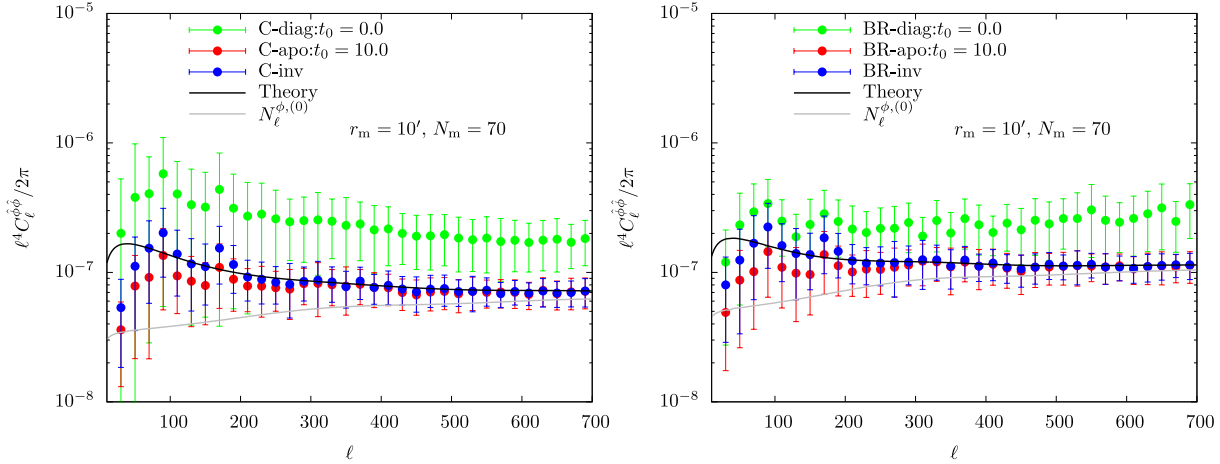


Figure 6.9: Same as Fig. 6.6, but using simulated lensed temperature maps. The gray lines show the theoretical reconstruction noise bias, $N_\ell^{\phi,(0)}$.

As a check of our code, Fig. 6.10 shows measured temperature angular power spectrum (red circles), compared with the expected temperature power spectrum, i.e., power spectrum convolved with beam transfer function including instrumental noise (black triangles). Other plots show the theoretical power spectrum with beam transfer function (solid line; $B_\ell C_\ell$) and measured noise spectrum (green points; N_ℓ). As a reference, we also show the white noise spectrum with $28.6 \mu\text{K}\text{-arcmin}$, which is the lowest instrumental noise in this map. Since the measured noise spectrum approaches the white noise spectrum at high multipole, the noise level of this map is almost minimum within the ACT full map. Note that the noise power spectra are measured from cross-correlation of four independent maps. Beam function and four independent maps are also obtained from LAMBDA website. The instrumental noise dominates the angular power spectrum at $\ell \gtrsim 3000$ and $\ell \lesssim 500$, and we use the temperature multipoles for $500 \leq \ell \leq 3000$.

6.3.2 Angular power spectra of lensing potentials

Scalar lensing potential

In Fig. 6.11, we show power spectrum of lensing estimators of scalar-lensing potential using the standard estimator without Monte Carlo correction, $|\hat{\phi}^S|^2$ (left) or the BR estimator, $|\hat{\phi}^{\text{BR}}|^2$ (right). The black solid line shows the expected power spectrum of the lensing estimator, $\langle |\phi|^2 \rangle$, theoretically calculated with the best fit values obtained from ACT temperature map combined with WMAP data [152]. On the other hand, the gray solid line shows the Gaussian noise spectrum computed with the observed temperature spectrum according to Eq. (5.56), assuming the diagonal covariance matrix of observed temperature anisotropies.²

As a cross check, we perform the ℓ -splitting technique [148]. In this method, the temperature multipole range is divided into two disjoint annular regions. The estimated cross-power spectrum between these two reconstructed maps has no Gaussian noise bias, although the SNR for the lensing power spectrum decreases compared to the usual technique. We compute two reconstructed fields using temperature multipoles with $500 \leq \ell \leq 1850$ and $1950 \leq \ell \leq 3000$, which maximize the SNR for ℓ -splitting. Then cross-correlation of these two estimators are calculated.

The left panel of Fig. 6.12 shows the results of ℓ -splitting technique, compared with the theoretically computed

²We also show the expected binned spectrum of the lensing estimator (black) and Gaussian noise spectrum (gray), with the same binning used for measurement of estimator power spectrum. Comparing the dots with the lines, the binned spectrum deviates from the unbinned spectrum on large scales, and the results of lensing estimator power spectrum should compare with the binned power spectrum.

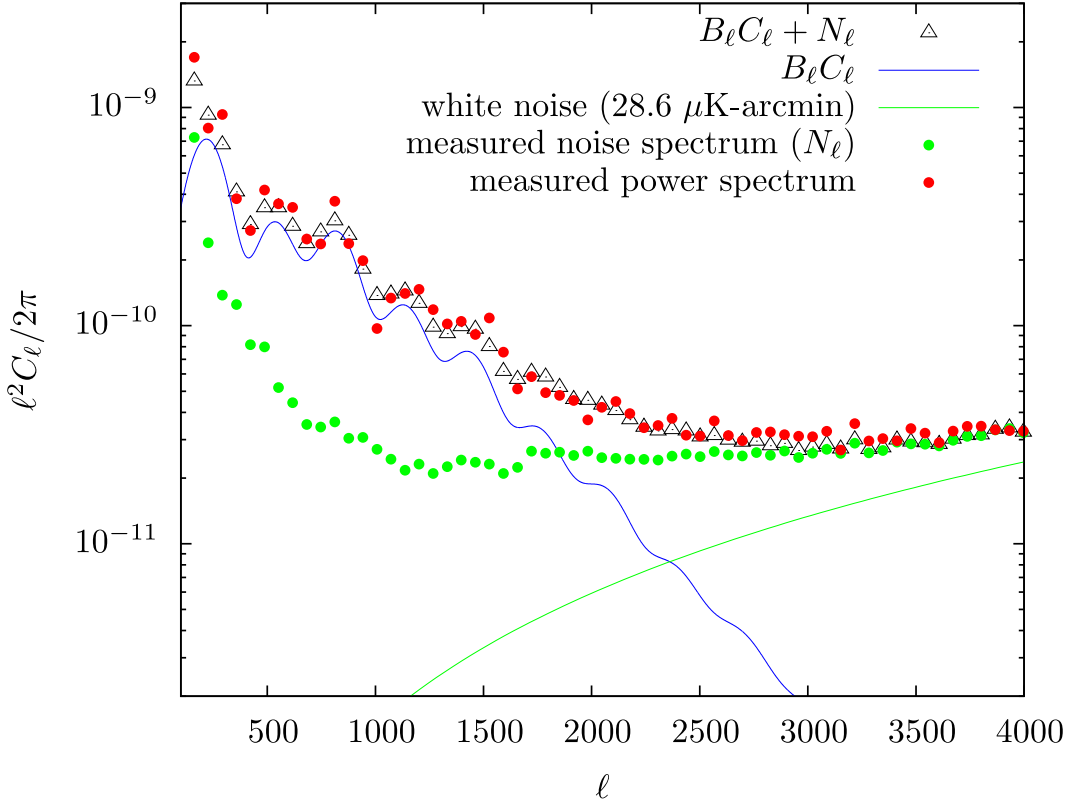


Figure 6.10: Measured temperature spectra (red circles). Other plots show the theoretical power spectrum expected from Ref. [152] multiplied by the beam transfer function (solid line; $B_\ell C_\ell$), further including measured noise spectrum (black triangles; $B_\ell C_\ell + N_\ell$), and measured noise spectrum from four split maps (green points; N_ℓ). As a reference, we also show the white noise spectrum with $28.6\mu\text{K-arcmin}$, which is the lowest instrumental noise within the ACT map.

lensing power spectrum, $C_\ell^{\phi\phi}$, with the best fit cosmological parameters from ACT + WMAP data [152]. The BR estimator reduces the bias even on large scales, and consistent with the expected power spectrum. Our results are also consistent with those from Ref. [15]. To compare our results with the previous work more quantitatively, we constrain a parameter A_L which is defined as $C_\ell^{\phi\phi} = A_L C_\ell^{\phi\phi,\text{fid}}$ with $C_\ell^{\phi\phi,\text{fid}}$ denoting the expected power spectrum. We only marginalize A_L with varying its value between 0.0 and 3.0. The results of likelihood for A_L are shown in the right of Fig. 6.12. The BR estimator with the ℓ -splitting technique leads to $A_L = 1.02 \pm 0.39(1\sigma)$. This result is also consistent with the previous result obtained in Ref. [15]: $A_L = 1.16 \pm 0.29(1\sigma)$.

Pseudo-scalar lensing potential

In Fig. 6.13 and the left of Fig. 6.14 we show the same as Fig. 6.11 and the left of Fig. 6.12, respectively, but for the measured curl spectrum. The measured curl-mode spectrum is found to be consistent with zero. The curl spectrum obtained from SPT data [16] is also consistent with zero and with our results.

Finally we note that the constraints on cosmic-string parameters, $G\mu$ and P , are obtained based on the measured power spectrum. To constrain the parameters, $G\mu$ and P , we compute the likelihood on the two-dimensional parameter space. The resultant likelihood contour is shown in the right of Fig. 6.14. With the measured curl spectrum the cosmic strings model with $G\mu = 10^{-9}$ and $P = 10^{-5}$ is excluded with more than 95% confidence level, which is not yet ruled out with the GKS effect on temperature angular power spectrum [92]. For strings with $P \lesssim 10^{-4}$, we

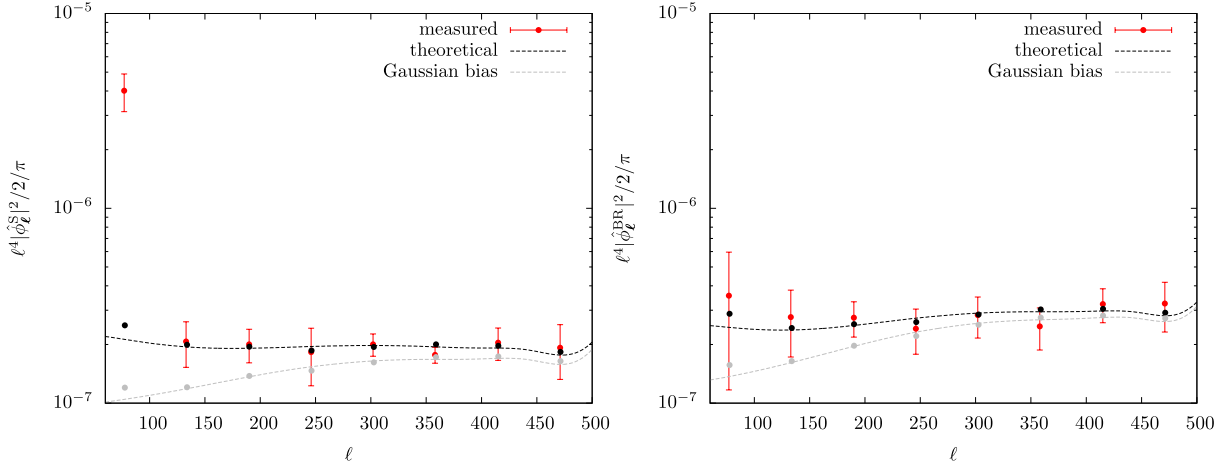


Figure 6.11: Measured lensing spectrum in the case with the standard estimator without Monte Carlo correction (left) and the BR estimator (right), denoted by red points. The solid lines show the expected power spectrum of lensing estimator, $\langle |\phi|^2 \rangle$, (black) and the estimated Gaussian noise spectrum (gray). The points show the binned power spectrum of lensing estimator (black) and Gaussian noise (gray).

find that the tighter constraint on $G\mu$ come from weak lensing compared to the temperature angular power spectrum obtained in Ref. [132]. As discussed in chapter 4, the constraints to these parameters would be further improved with the upcoming and next generation experiments.

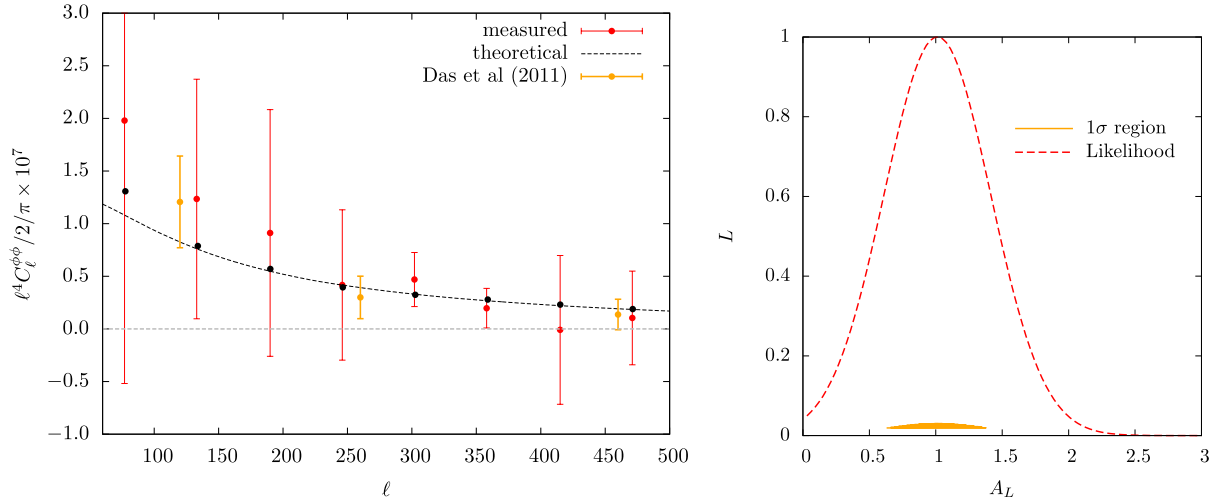


Figure 6.12: *Left:* Estimate of the lensing spectrum with the ℓ -splitting technique (red). The results from Das et al 2011 [15] are also shown (orange). The expected power spectrum from ACT + WMAP 7yr is shown in black solid line and its binned spectrum is shown in black symbols. *Right:* One dimensional likelihood for parameter, A_L , (see text for the definition). Note that the value of likelihood is normalized by the maximum value.

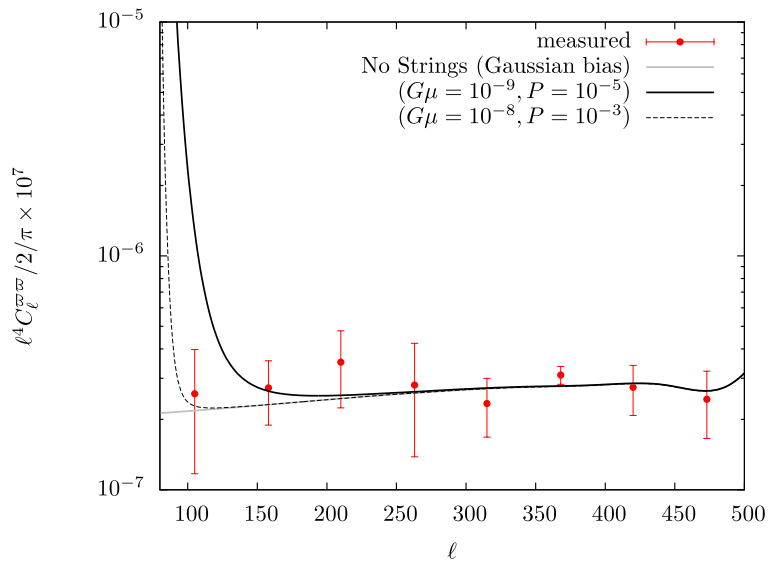


Figure 6.13: Measured estimator power spectrum of the curl mode, denoted by red symbols. We also show the theoretical power spectrum of Gaussian bias (gray solid line) and the case in the presence of cosmic strings between the last-scattering surface and the observer (black lines).

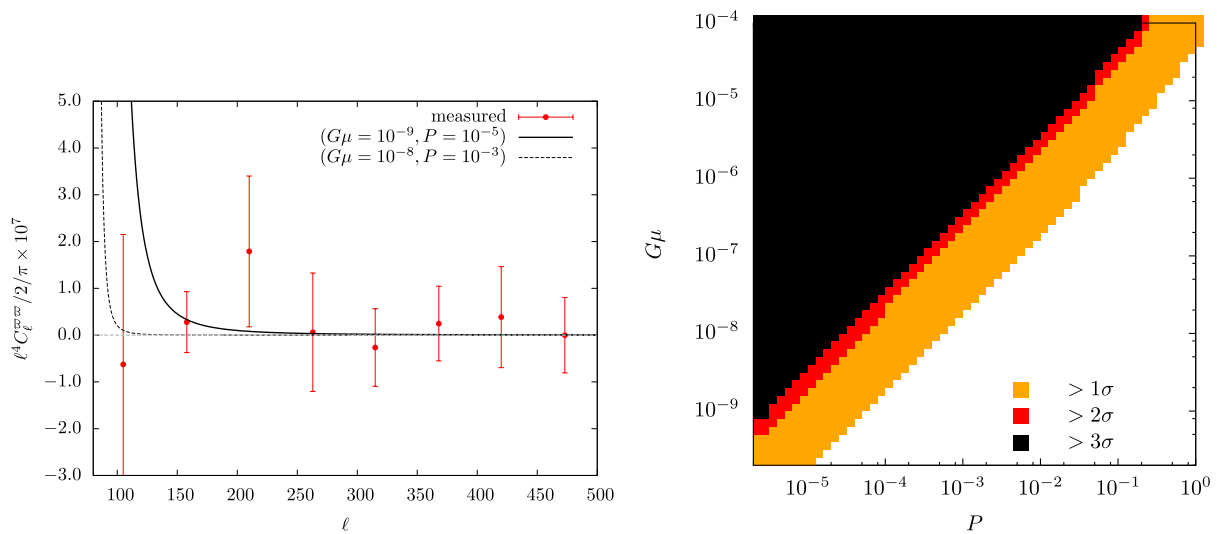


Figure 6.14: *Right:* The results of ℓ -splitting technique for the curl mode. The solid lines show the theoretical curl mode power spectrum generated by a specific model of cosmic strings, with $(P = 10^{-3}, G\mu = 10^{-8})$ or $(P = 10^{-5}, G\mu = 10^{-9})$. *Left:* Two-dimensional likelihood for parameters, P and $G\mu$. The colored regions (black, red and orange) are excluded (with $> 3\sigma$, $> 2\sigma$ and $> 1\sigma$ statistical significance).

Chapter 7

Summary and Conclusion

In this thesis, we mainly discussed the following subjects:

- what we can probe from even/odd parity modes of weak lensing, i.e., lensing potential, curl modes and E/B-mode shear,
- how to measure these lensing signals, and
- how accurately we can measure these signals particularly in CMB lensing reconstruction

In chapter 3, we have discussed observational signatures of the vector and tensor metric perturbations through the effect of the weak gravitational lensing. In the presence of the non-scalar perturbations, non-vanishing signals for the curl mode and B-mode shear appear, and would be a unique signature of any vector and tensor sources. Solving the geodesic and geodesic deviation equations, we have then derived the full-sky formulas for angular power spectra of weak lensing signals, and give the explicit expressions for the lensing potential and curl mode [Eq. (3.78) with Eqs. (3.80) and (3.85)], and for E/B-mode shear [Eq. (3.90) with Eqs. (3.92) and (3.97)].

In chapter 4, we explored cosmological implications expected to obtain from upcoming and future experiments. Assuming specific experiments, we explicitly evaluated the noise spectra, and prospects for reconstructing the gradient and curl modes is discussed. Then, we showed that the SNR for even/odd parity modes of weak lensing would be significantly improved enough to constrain, e.g., massive neutrinos from even-parity mode and cosmic strings from odd-parity mode.

In chapter 5, we derived a full-sky algorithm for reconstructing the lensing potential and curl modes simultaneously. We defined the estimator as a quadratic combination of observed anisotropies, and introduced the weight function to reduce the noise contribution (see Eq. (5.10)). The functional form of the optimal weight which minimizes the noise contribution is given by Eq. (5.27) with Eqs. (5.21) and (5.26). Thanks to the distinct feature of the parity symmetry between the lensing potential and curl mode, they can be separately reconstructed. The quantities used to reconstruct the lensing signals are summarized in Table 5.1. In the flat-sky limit, we showed that the estimator reduces to the one empirically defined in Ref. [34].

The formalism given in chapter 5 relies on several idealistic assumptions, e.g., the higher-order terms of the deflection angle are negligible, and observed CMB maps are given on the full sky without foregrounds and the inhomogeneous noise. However, at small scales, the lowest-order approximation (e.g., ignoring the higher-order terms in Eq. (??) for the temperature anisotropies) would not be valid for high resolution experiments [153]. The higher-order terms of deflection angle produce additional contributions in the lensed anisotropies, and the lensing potential and curl mode estimators include the contributions from the higher-order terms of the deflection angle [143]. Also, the masking effect [136, 50, 51], foreground contaminations from point sources and thermal/kinematic SZ effect [153, 15], and the inhomogeneous noise [149] induce the additional non-zero off-diagonal terms in Eq. (5.1) and the estimated lensing signals would be biased.

In chapter 6, toward a more realistic situation, we consider a method for CMB lensing reconstruction to mitigate especially focusing on masking effect. We have discussed methods to reduce the “mean-field” and “Gaussian noise” biases which must be accounted for in CMB lensing reconstruction. Our approach focuses on estimating these biases directly from the data itself, reducing sensitivity to the uncertainties of sky model. Then, we performed numerical tests of the mean-field reduction approach for several different choices of filtering, finding it particularly useful for the reduction of the large-scale component of the mean-field. Finally, we apply our estimator to the actual data and measure lensing potential power spectra. We also obtain the curl-mode power spectrum and we give some implications for cosmic strings.

In near the future, more precise cosmological data can be available, and we can tackle more advanced and fundamental questions. As constraints on cosmological parameters become tighter, we have to treat observed data more accurately, otherwise the estimated parameters would be biased. One of the way to improve accuracy is the cross-correlation analysis, in which statistical correlations of two independent data sets are measured. The cross correlations are in principle independent of the intrinsic uncertainties in each data, and therefore more accurate compared to the auto correlations. In the next decades, the cross correlations of CMB lensing and cosmic shear would be an useful statistical tool and would provide tighter constraint on massive neutrinos and properties of the dark energy. The establishment of cross-correlation analysis and estimation of expected constraints obtained from the cross correlations with realistic maps are worth investigating and will be explored in the future work.

CMB lensing now becomes one of the tool to obtain cosmological information. A measurement of B-mode polarizations in the future will significantly improve the precision of lensing signals from CMB. In our derivation of bias-reduced methods described in chapter 6, however, we have focused on the temperature fluctuations, since the current polarization data is too noisy to reconstruct the lensing fields and its power spectrum. As shown in this thesis, the reconstructed lensing power spectrum including polarization would become a powerful probe of, e.g., massive neutrinos and vector/tensor sources. Our current understanding of lensing reconstruction from polarization maps is very poor, and we still do not know how significantly the higher-order bias terms affects on the estimation of lensing power spectrum, even in the idealistic situation. The lensing reconstruction from realistic polarization maps is worth investigating. The method investigated in this thesis may be also applicable to the polarization maps, and the usefulness of our method to the lensing reconstruction from polarization maps will be explored in our future work.

Acknowledgment

It is my great pleasure to express my sincere thanks and gratitude to Assistant Professor Atsushi Taruya for introducing me to the field and for his continuous encouragements and advices. Successive discussions with him were always fruitful. Special thanks are as well due to Duncan Hanson for his continuous help. His advices for my research were always proper and he kindly gave me a data for the higher-order biases of lensing reconstruction. I also appreciate it that Alexander van Engelen for kindly providing me a data for power spectrum of N1-bias term including both gradient and curl modes. I would like to acknowledge my collaborators, Shun Saito, Tomohiro Okamura, Daisuke Yamauchi, and Ryuichi Takahashi. I also express my sincere gratitude to my supervisor Professor Yasushi Suto for his valuable supports. I express my sincere appreciation to all of the members in the University of Tokyo Theoretical Astrophysics (UTAP) and Research Center for the Early Universe (RESCEU) for providing me a comfortable research environment, particularly grateful to Teruyuki Hirano and Yuka Fujii for their assistances and encouragements. Finally I wish to specially thank my family and friends for their supports.

Appendix A

Evolution Equations for Fluctuations

A.1 Evolution Equations for Fluctuations

For discussing the physical process of generating CMB anisotropies and evolution of gravitation fields in the universe, we briefly summarize the basic evolution equations for baryons, CDM, photons, neutrinos and gravitational fields. The evolution equations for each component and linearized Einstein equation is derived in Ref. [76].

A.1.1 Scalar Perturbations

Harmonics

We chose the harmonics for the scalar perturbations as

$$Q^{(0)} = e^{i\mathbf{k}\cdot\mathbf{x}}. \quad (\text{A.1})$$

Harmonics for scalar perturbations from divergence-less vector and symmetric divergence-less tensor is given by

$$Q_i^{(0)} = -\frac{1}{k} \nabla_i Q^{(0)}, \quad (\text{A.2})$$

$$Q_{ij}^{(0)} = \left[\frac{1}{k^2} \nabla_i \nabla_j + \frac{1}{3} \delta_{ij} \right] Q^{(0)}. \quad (\text{A.3})$$

Fluctuations of Baryons and CDM

We assume that the baryons and CDM are characterized by the energy density and velocity, and the anisotropic stress is ignored. In the fluid approximation, the density and velocity perturbations of baryons are described by [76]

$$\frac{\partial \delta_b}{\partial \eta} + k v_b^{(0)} + 3 \frac{\partial \Psi}{\partial \eta} = 0, \quad (\text{A.4})$$

$$\frac{\partial v_b^{(0)}}{\partial \eta} + \mathcal{H} v_b^{(0)} + k \Phi = \frac{1}{R} \frac{d\tau}{d\eta} (v_b^{(0)} - \Theta_1^{(0)}), \quad (\text{A.5})$$

where R is the baryon-to-photon ratio

$$R \equiv \frac{3\bar{\rho}_b}{4\bar{\rho}_\gamma}, \quad (\text{A.6})$$

and the quantity, τ , is the optical depth which is given by

$$\tau(\eta) \equiv \int_\eta^{\eta_0} d\eta' n_e(\eta') \sigma_T a(\eta'). \quad (\text{A.7})$$

with n_e and σ_T denoting the electron number density and cross section of the Thomson scattering. The term proportional to $d\tau/d\eta$ describes the exchange of the momentum between the photons and baryons thorough the Thomson scattering, since, at the early stage of the universe, photons and electrons are tightly coupled with electro-magnetic force.

Similarly, the evolution equations for CDM is given by neglecting the term related to the Thomson scattering in the above equations, and the result is [76]

$$\frac{\partial \delta_C}{\partial \eta} + k v_C^{(0)} + 3 \frac{\partial \Psi}{\partial \eta} = 0, \quad (\text{A.8})$$

$$\frac{\partial v_C^{(0)}}{\partial \eta} + \mathcal{H} v_C^{(0)} + k \Phi = 0. \quad (\text{A.9})$$

Fluctuations of photons

From the Boltzmann equation including the effect of the Thomson scattering, the evolution equations for temperature fluctuations are given by [76]

$$\frac{\partial \Theta_0^{(0)}}{\partial \eta} = -\frac{k}{3} \Theta_1^{(0)} - \frac{\partial \Psi}{\partial \eta}, \quad (\text{A.10})$$

$$\frac{\partial \Theta_1^{(0)}}{\partial \eta} = k \left[\Theta_0^{(0)} - \frac{2}{5} \Theta_2^{(0)} \right] - k \Phi + \frac{d\tau}{d\eta} (\Theta_1^{(0)} - v_b^{(0)}), \quad (\text{A.11})$$

$$\frac{\partial \Theta_2^{(0)}}{\partial \eta} = k \left[\frac{2}{3} \Theta_1^{(0)} - \frac{3}{7} \Theta_3^{(0)} \right] + \frac{d\tau}{d\eta} (\Theta_2^{(0)} - \mathcal{P}^{(0)}), \quad (\text{A.12})$$

$$\frac{\partial \Theta_\ell^{(0)}}{\partial \eta} = k \left[\frac{\ell}{2\ell-1} \Theta_{\ell-1}^{(0)} - \frac{\ell+1}{2\ell+3} \Theta_{\ell+1}^{(0)} \right] + \frac{d\tau}{d\eta} \Theta_\ell^{(0)}, \quad (\ell \geq 3) \quad (\text{A.13})$$

where the quantity, $\mathcal{P}^{(0)}$, is defined as

$$\mathcal{P}^{(0)} = \frac{1}{10} [\Theta_2^{(0)} - \sqrt{6} E_2^{(0)}]. \quad (\text{A.14})$$

On the other hand, the evolution equations for polarizations are given by [76]

$$\frac{\partial E_2^{(0)}}{\partial \eta} = -k \frac{\sqrt{5}}{7} E_3^{(0)} + \frac{d\tau}{d\eta} [E_2^{(0)} + \sqrt{6} \mathcal{P}^{(0)}], \quad (\text{A.15})$$

$$\frac{\partial E_\ell^{(0)}}{\partial \eta} = k \left[\frac{\sqrt{\ell^2-4}}{2\ell-1} E_{\ell-1}^{(0)} - \frac{\sqrt{(\ell+1)^2-4}}{2\ell+3} E_{\ell+1}^{(0)} \right] + \frac{d\tau}{d\eta} E_\ell^{(0)}, \quad (\ell \geq 3) \quad (\text{A.16})$$

$$\frac{\partial B_\ell^{(0)}}{\partial \eta} = k \left[\frac{\sqrt{\ell^2-4}}{2\ell-1} B_{\ell-1}^{(0)} - \frac{\sqrt{(\ell+1)^2-4}}{2\ell+3} B_{\ell+1}^{(0)} \right] + \frac{d\tau}{d\eta} B_\ell^{(0)}, \quad (\ell \geq 2) \quad (\text{A.17})$$

From the above equation, the E-mode polarization anisotropies is generated by the quadrupole moment of the temperature anisotropies, $\Theta_2^{(0)}$ through the Thomson scattering.

Fluctuations of relativistic neutrinos

The evolution equations for relativistic neutrinos are obtained by neglecting the terms related to the Thomson scattering in the evolution equations for photons, and the result is [76]

$$\frac{\partial \mathcal{N}_0^{(0)}}{\partial \eta} = \frac{k}{3} \mathcal{N}_1^{(0)} - \frac{\partial \Psi}{\partial \eta}, \quad (\text{A.18})$$

$$\frac{\partial \mathcal{N}_1^{(0)}}{\partial \eta} = k \left[\mathcal{N}_0^{(0)} - \frac{2}{5} \mathcal{N}_2^{(0)} \right] - \Phi, \quad (\text{A.19})$$

$$\frac{\partial \mathcal{N}_\ell^{(0)}}{\partial \eta} = k \left[\frac{\ell}{2\ell-1} \mathcal{N}_{\ell-1}^{(0)} - \frac{\ell+1}{2\ell+3} \mathcal{N}_{\ell+1}^{(0)} \right], \quad (\ell \geq 2) \quad (\text{A.20})$$

where, with the distribution function of relativistic neutrino at zeroth and first order, \bar{f}_ν and δf_ν , the quantity, Δ_ν is described by

$$\mathcal{N} = \left[\int_0^\infty 4\pi p^3 dp \bar{f}_\nu(\eta, \mathbf{p}, \mathbf{x}) \right]^{-1} \int d^3x e^{i\mathbf{k}\cdot\mathbf{x}} \int_0^\infty 4\pi p^3 dp \delta f_\nu(\eta, \mathbf{p}, \mathbf{x}). \quad (\text{A.21})$$

Gravitational fields

Finally, the evolution equations for the gravitational fields are given by [76]

$$k^2 \Psi = 4\pi G a^2 \sum_i \bar{\rho}_i \left[\delta_i + 3(1+w_i) \frac{\mathcal{H}}{k} v_i^{(0)} \right], \quad (\text{A.22})$$

$$k^2 (\Psi + \Phi) = -\frac{32\pi G a^2}{5} (\bar{\rho}_\gamma \Theta_2^{(0)} + \bar{\rho}_\nu \mathcal{N}_2^{(0)}), \quad (\text{A.23})$$

where the subscript i indicates each component in the universe, and the anisotropic stress from baryons and CDM are ignored. Note that $\delta_\gamma = 4\Theta_0^{(0)}$, $v_\gamma^{(0)} = \Theta_1^{(0)}$ and these relations are the same for relativistic neutrinos.

A.1.2 Vector Perturbations

Harmonics

We chose the harmonics for the vector perturbations as

$$\mathbf{Q}^{(\pm 1)} = -\frac{i}{\sqrt{2}} \mathbf{e}_\pm e^{i\mathbf{k}\cdot\mathbf{x}}, \quad (\text{A.24})$$

and

$$Q_{ij}^{(\pm 1)} = -\frac{1}{2k} \left[\nabla_i Q_j^{(\pm 1)} + \nabla_j Q_i^{(\pm 1)} \right]. \quad (\text{A.25})$$

We note that the trace-free condition for the vector perturbations is automatically satisfied when we consider the Fourier expansion with the above harmonics. In the followings, we only consider the equations for $n = +1$, since the equations for $n = -1$ are similar to the case with $n = +1$.

Fluctuations of Baryons and CDM

Since the density fluctuations do not generate the vector perturbations, the evolution equations of the vector perturbations for baryons and CDM are described by velocity perturbations [76]:

$$\frac{\partial[v_b^{(1)} - \sigma^{(1)}]}{\partial\eta} + \mathcal{H}[v_b^{(1)} - \sigma^{(1)}] = \frac{1}{R}\frac{d\tau}{d\eta}(v_b^{(1)} - \Theta_1^{(1)}), \quad (\text{A.26})$$

$$\frac{\partial[v_C^{(1)} - \sigma^{(1)}]}{\partial\eta} + \mathcal{H}[v_C^{(1)} - \sigma^{(1)}] = 0. \quad (\text{A.27})$$

Fluctuations of photons

The evolution equations for temperature fluctuations are given by [76]

$$\frac{\partial\Theta_1^{(1)}}{\partial\eta} = -k\frac{\sqrt{3}}{5}\Theta_3^{(1)} + \frac{\partial\sigma^{(1)}}{\partial\eta} + \frac{d\tau}{d\eta}[\Theta_1^{(1)} - v_b^{(1)}], \quad (\text{A.28})$$

$$\frac{\partial\Theta_2^{(1)}}{\partial\eta} = k\left[\frac{\sqrt{3}}{3}\Theta_1^{(1)} - \frac{2\sqrt{2}}{7}\Theta_3^{(1)}\right] + \frac{d\tau}{d\eta}(\Theta_2^{(1)} - \mathcal{P}^{(1)}), \quad (\text{A.29})$$

$$\frac{\partial\Theta_\ell^{(1)}}{\partial\eta} = k\left[\frac{\sqrt{\ell^2-1}}{2\ell-1}\Theta_{\ell-1}^{(1)} - \frac{\sqrt{(\ell+1)^2-1}}{2\ell+3}\Theta_{\ell+1}^{(1)}\right] + \frac{d\tau}{d\eta}\Theta_\ell^{(1)}, \quad (\ell \geq 3) \quad (\text{A.30})$$

where the quantity, $\mathcal{P}^{(1)}$, is defined as

$$\mathcal{P}^{(1)} = \frac{1}{10}[\Theta_2^{(1)} - \sqrt{6}E_2^{(1)}]. \quad (\text{A.31})$$

On the other hand, the evolution equations for polarizations are given by [76]

$$\frac{\partial E_2^{(1)}}{\partial\eta} = -k\left[\frac{1}{3}B_2^{(1)} + \frac{2\sqrt{10}}{7}E_3^{(1)}\right] + \frac{d\tau}{d\eta}[E_2^{(1)} + \sqrt{6}\mathcal{P}^{(1)}], \quad (\text{A.32})$$

$$\frac{\partial E_\ell^{(1)}}{\partial\eta} = k\left[a_\ell^{(1)}E_{\ell-1}^{(1)} - \frac{2}{\ell(\ell+1)}B_\ell^{(1)} - b_\ell^{(1)}E_{\ell+1}^{(1)}\right] + \frac{d\tau}{d\eta}E_\ell^{(1)}, \quad (\ell \geq 3) \quad (\text{A.33})$$

$$\frac{\partial B_\ell^{(1)}}{\partial\eta} = k\left[a_\ell^{(1)}B_{\ell-1}^{(1)} + \frac{2}{\ell(\ell+1)}E_\ell^{(1)} - b_\ell^{(1)}B_{\ell+1}^{(1)}\right] + \frac{d\tau}{d\eta}B_\ell^{(1)} \quad (\ell \geq 2), \quad (\text{A.34})$$

with $a_\ell^{(1)} = \sqrt{(\ell^2-1)(\ell^2-4)}/(2\ell^2-\ell)$ and $b_\ell^{(1)} = \sqrt{(\ell-1)\ell(\ell+2)(\ell+3)}/(2\ell^2+3\ell)$.

Fluctuations of relativistic neutrinos

The evolution equations for relativistic neutrinos are obtained by neglecting the terms related to the Thomson scattering in the evolution equations for photons, and the result is [76]

$$\frac{\partial\mathcal{N}_1^{(1)}}{\partial\eta} = -k\left[\frac{\sqrt{3}}{5}\mathcal{N}_3^{(1)}\right] - \frac{\partial B^{(1)}}{\partial\eta}, \quad (\text{A.35})$$

$$\frac{\partial\mathcal{N}_\ell^{(1)}}{\partial\eta} = k\left[\frac{\sqrt{\ell^2-1}}{2\ell-1}\mathcal{N}_{\ell-1}^{(1)} - \frac{\sqrt{(\ell+1)^2-1}}{2\ell+3}\mathcal{N}_{\ell+1}^{(1)}\right]. \quad (\ell \geq 2) \quad (\text{A.36})$$

Gravitational fields

The linearized Einstein equation for vector perturbations is given by [76]

$$\frac{1}{a^2} \frac{d(a^2 \sigma^{(1)})}{dt} = -\frac{16\pi G a^2}{5\sqrt{3}k} [\bar{\rho}_\gamma \Theta_2^{(1)} + \bar{\rho}_\nu \mathcal{N}_2^{(1)}]. \quad (\text{A.37})$$

The above equation implies that, in the absence of the anisotropic stress, the vector metric perturbation decays as $\sigma^{(1)} \propto a^{-2}$, and the vector components of the temperature and polarization anisotropies would be negligible. However, if we consider a sub-dominant component which has negligible contributions to the scalar perturbations compared to the dominant component, the vector perturbations would not decay and may be observed.

A.1.3 Tensor Perturbations

Harmonics

We chose the harmonics for the tensor perturbations as

$$\mathbf{Q}^{(\pm 2)} = -\sqrt{\frac{3}{8}} \mathbf{e}_\pm \otimes \mathbf{e}_\pm e^{i\mathbf{k}\cdot\mathbf{x}}. \quad (\text{A.38})$$

Similar to the case of the vector perturbations, in the followings, we only consider the equations for $n = +2$.

Fluctuations of photons

The evolution equations for temperature fluctuations are given by [76]

$$\frac{\partial \Theta_2^{(2)}}{\partial \eta} = -k \left[\frac{\sqrt{5}}{7} \Theta_3^{(2)} \right] - \frac{\partial D^{(2)}}{\partial \eta} + \frac{d\tau}{d\eta} (\Theta_2^{(2)} - \mathcal{P}^{(2)}), \quad (\text{A.39})$$

$$\frac{\partial \Theta_\ell^{(2)}}{\partial \eta} = k \left[\frac{\sqrt{\ell^2 - 4}}{2\ell - 1} \Theta_{\ell-1}^{(2)} - \frac{\sqrt{(\ell+1)^2 - 4}}{2\ell + 3} \Theta_{\ell+1}^{(2)} \right] + \frac{d\tau}{d\eta} \Theta_\ell^{(2)}, \quad (\ell \geq 3) \quad (\text{A.40})$$

where the quantity, $\mathcal{P}^{(2)}$, is defined as

$$\mathcal{P}^{(2)} = \frac{1}{10} [\Theta_2^{(2)} - \sqrt{6} E_2^{(2)}]. \quad (\text{A.41})$$

On the other hand, the evolution equations for polarizations are given by [76]

$$\frac{\partial E_2^{(2)}}{\partial \eta} = -k \left[\frac{2}{3} B_2^{(2)} + \frac{5}{7} E_3^{(2)} \right] + \frac{d\tau}{d\eta} [E_2^{(2)} + \sqrt{6} \mathcal{P}^{(2)}], \quad (\text{A.42})$$

$$\frac{\partial E_\ell^{(2)}}{\partial \eta} = k \left[a_\ell^{(2)} E_{\ell-1}^{(2)} - \frac{4}{\ell(\ell+1)} B_\ell^{(2)} - b_\ell^{(2)} E_{\ell+1}^{(2)} \right] + \frac{d\tau}{d\eta} E_\ell^{(2)}, \quad (\ell \geq 3) \quad (\text{A.43})$$

$$\frac{\partial B_\ell^{(2)}}{\partial \eta} = k \left[a_\ell^{(2)} B_{\ell-1}^{(2)} + \frac{4}{\ell(\ell+1)} E_\ell^{(2)} - b_\ell^{(2)} B_{\ell+1}^{(2)} \right] + \frac{d\tau}{d\eta} B_\ell^{(2)}, \quad (\ell \geq 2) \quad (\text{A.44})$$

with $a_\ell^{(2)} = (\ell^2 - 4)/(2\ell^2 - \ell)$ and $b_\ell^{(2)} = (\ell - 1)(\ell + 3)/(2\ell^2 + 3\ell)$.

Fluctuations of relativistic neutrinos

The evolution equations for relativistic neutrinos are obtained by neglecting the terms related to the Thomson scattering in the evolution equations for photons, and the result is [76]

$$\frac{\partial \mathcal{N}_2^{(2)}}{\partial \eta} = -k \left[\frac{\sqrt{5}}{7} \mathcal{N}_3^{(2)} \right] - \frac{\partial D^{(2)}}{\partial \eta}, \quad (\text{A.45})$$

$$\frac{\partial \mathcal{N}_\ell^{(2)}}{\partial \eta} = k \left[\frac{\sqrt{\ell^2 - 4}}{2\ell - 1} \mathcal{N}_{\ell-1}^{(2)} - \frac{\sqrt{(\ell + 1)^2 - 4}}{2\ell + 3} \mathcal{N}_{\ell+1}^{(2)} \right] \quad (\ell \geq 3). \quad (\text{A.46})$$

Gravitational fields

The evolution equation for the amplitude of the gravitational waves is [76]

$$\frac{d^2 D^{(2)}}{d\eta^2} + 2\mathcal{H} \frac{dD^{(2)}}{d\eta} + k^2 D^{(2)} = \frac{64\pi G a^2}{15} [\bar{\rho}_\gamma \Theta_2^{(2)} + \bar{\rho}_\nu \mathcal{N}_2^{(2)}]. \quad (\text{A.47})$$

Appendix B

Note for Weak Lensing from Scalar, Vector and Tensor Perturbations

In this appendix, we provide details of our derivations of the angular power spectrum for the E-/B-mode shear, lensing potential and curl mode generated by the scalar, vector and tensor perturbations. In Sec. B.1, we first summarize useful formulas for our calculations. In Sec. B.2.1 and B.2.2, we present the formula for the angular power spectrum of the E-/B-mode shear and the gradient-/curl-mode deflection angle. In Sec. B.2.3 we derive the explicit relation between the cosmic shear field and the deflection angle.

B.1 Useful formulas for computing weak lensing effect

B.1.1 Properties of orthonormal space-like basis

The orthonormal space-like basis satisfies the following equations:

$$\begin{aligned} (e_\chi^i)_{,a} &= e_a^i, \quad (e_a^i)_\chi = 0, \quad (e_\chi^i)_{(ab)} = -\omega_{ab} e_\chi^i, \\ (e_\theta^i)_{,\varphi} &= (e_\varphi^i)_{,\theta} = e_\varphi^i \cot \theta, \quad (e_\theta^i)_{,\theta} = -e_\chi^i, \\ (e_\varphi^i)_{,\varphi} &= -\sin \theta (\sin \theta e_\chi^i + \cos \theta e_\theta^i) e_\chi^k e_{i\chi} e_{a,b}^i = -e_\chi^k \omega_{ab}. \end{aligned} \quad (\text{B.1})$$

B.1.2 Derivatives with orthonormal space-like basis

For an arbitrary quantity, X_i , we find a following useful formula:

$$\begin{aligned} X_{i,j} e_a^i e_b^j &= \frac{1}{\chi} [X_{a,b} - X_i e_{a,b}^i] = \frac{1}{\chi} [X_{a,b} - X_k (e_\chi^k e_{i\chi} + e_c^k e_{ic}) e_{a,b}^i] \\ &= \frac{1}{\chi} [X_{a:b} - X_k e_\chi^k e_{i\chi} e_{a,b}^i] = \frac{1}{\chi} [X_{a:b} - X_\chi \omega_{ab}]. \end{aligned} \quad (\text{B.2})$$

B.1.3 Perturbed optical tidal matrix

In the absence of perturbation the photon's path is given by Eq. (3.3) and the basis vectors are given by $n_a^\mu = e_a^\mu$. The Riemann tensor at zeroth order vanishes. Then the optical tidal matrix is expanded as

$$\delta \mathcal{T}_{ab} = R_{i00j} e_a^i e_b^j - 2R_{ik0j} e_\chi^k e_a^i e_b^j + R_{iklj} e_\chi^k e_\chi^l e_a^i e_b^j, \quad (\text{B.3})$$

where the perturbed Riemann tensor is given by

$$\begin{aligned} R_{i00j} &= -\Phi_{,ij} + \frac{\partial}{\partial\eta} \frac{\sigma_{i,j} + \sigma_{j,i}}{2} + \frac{\partial^2\Psi}{\partial\eta^2}\delta_{ij} + \frac{\partial^2D_{ij}}{\partial\eta^2} \\ R_{ik0j} &= \frac{\sigma_{i,kj} - \sigma_{kj,ij}}{2} + \frac{\partial}{\partial\eta}(C_{ij,k} - C_{kj,i}) \\ R_{iklj} &= C_{ik,jl} - C_{ik,lj} + C_{ij,kl} - C_{il,kj} + C_{kl,ij} - C_{kj,il}. \end{aligned} \quad (\text{B.4})$$

Using the perturbed Riemann tensor, the first term of Eq. (B.3) becomes

$$-\frac{1}{\chi^2}\Phi_{,ij}e_a^i e_b^j + \frac{\partial^2\Psi}{\partial\eta^2}\omega_{ab} + \frac{1}{2}\frac{\partial}{\partial\eta}\left[\frac{e_a^i\sigma_{i,b} + e_b^j\sigma_{j,a}}{\chi} + 2\frac{\partial D_{ab}}{\partial\eta}\right]. \quad (\text{B.5})$$

Similarly, second term is

$$-e_\chi^k e_a^i e_b^j(\sigma_{i,kj} - \sigma_{kj,ij}) - 2\frac{\partial}{\partial\eta}\left[\omega_{ab}\Psi_{,\chi\chi} + e_a^i e_b^j D_{ij,\chi\chi} - e_\chi^k e_b^j \frac{D_{kj,a}}{\chi}\right], \quad (\text{B.6})$$

and the third term becomes

$$\omega_{ab}\Psi_{,\chi\chi} + e_a^i e_b^j D_{ij,\chi\chi} + \frac{1}{\chi}[e_\chi^k e_\chi^l e_a^i D_{kl,ib} - e_\chi^l e_a^i D_{il,b\chi} - e_\chi^k e_b^j D_{kj,a\chi}]. \quad (\text{B.7})$$

Combining the above Eqs. (B.5) - (B.7), the optical tidal matrix at liner order for scalar, vector and tensor contributions is summarized as follows:

- scalar perturbations,

$$\mathcal{T}_{ab}^{(S)} = -\frac{1}{\chi^2}(\Phi - \Psi)_{:ab} - \frac{1}{\chi}\omega_{ab}\frac{\partial(\Phi - \Psi)}{\partial\chi} + \omega_{ab}\frac{d^2\Psi}{d\chi^2}, \quad (\text{B.8})$$

- vector perturbations,

$$\begin{aligned} \mathcal{T}_{ab}^{(V)} &= \frac{\partial}{\partial\eta}\frac{e_a^i\sigma_{i,b} + e_b^j\sigma_{j,a}}{2\chi} - \frac{1}{\chi}e_\chi^k e_a^i(\sigma_{i,kb} - \sigma_{k,ib}) \\ &= \frac{1}{\chi^2}\left\{(\sigma_\chi)_{:ab} - \frac{d}{d\chi}(\chi\sigma_{(a:b)}) + \chi\omega_{ab}\frac{\partial\sigma_\chi}{\partial\eta}\right\}, \end{aligned} \quad (\text{B.9})$$

- tensor perturbations

$$\begin{aligned} \mathcal{T}_{ab}^{(T)} &= \frac{d^2D_{ab}}{d\chi^2} + 2e_\chi^k e_b^j \frac{\partial}{\partial\eta}\frac{D_{kj,a}}{\chi} + \frac{1}{\chi}[e_\chi^k e_\chi^l e_a^i D_{kl,ib} - e_\chi^l e_a^i D_{il,b\chi} - e_\chi^k e_b^j D_{kj,a\chi}] \\ &= \frac{1}{\chi^2}\left\{(D_{\chi\chi})_{:ab} - 2\frac{d}{d\chi}[\chi D_{\chi(a:b)}] + \chi\frac{d^2}{d\chi^2}[\chi D_{ab}] - \chi\omega_{ab}\left(\frac{d}{d\chi}D_{\chi\chi} - \frac{\partial}{\partial\eta}D_{\chi\chi}\right)\right\}. \end{aligned} \quad (\text{B.10})$$

B.2 Derivation of angular power spectrum

B.2.1 E-/B-mode cosmic shear

Let us now derive the explicit expression for the reduced shear and E-/B-mode angular power spectra in terms of spin-weighted quantities. Using Eqs. (F.20) and (F.22), we can rewrite Eq. (3.68) in terms of the spin operators:

$$g = [{}_2D]_0^\chi + \int_0^\chi d\chi' \frac{\chi - \chi'}{\chi\chi'} \left\{ \mathcal{J}^2\mathcal{A} - \frac{d}{d\chi'}[\chi'\mathcal{J}_1\mathcal{B}] + \chi' \frac{d^2}{d\chi'^2}[\chi'_2D] \right\}, \quad (\text{B.11})$$

where we define ${}_{\pm 1}\mathcal{B} = \mathcal{B}_i e_{\pm}^i$ and ${}_{\pm 2}D = D_{ij} e_{\pm}^i e_{\pm}^j$. Decomposing the scalar, vector and tensor perturbations into the Fourier modes, we obtain

$$\mathcal{A}(\chi, \hat{\mathbf{n}}) = \sum_{m=0,\pm 1,\pm 2} \int \frac{d^3 k}{(2\pi)^3} \mathcal{A}^{(m)}(\mathbf{k}, \chi) {}_0\mathcal{G}_{\ell}^{(m)}(\mathbf{k}, \chi \hat{\mathbf{n}}), \quad (\text{B.12})$$

$${}_{\pm 1}\mathcal{B}(\chi, \hat{\mathbf{n}}) = \sum_{m=\pm 1,\pm 2} \int \frac{d^3 k}{(2\pi)^3} \mathcal{B}^{(m)}(\mathbf{k}, \chi) {}_{\pm 1}\mathcal{G}_{\ell}^{(m)}(\mathbf{k}, \chi \hat{\mathbf{n}}), \quad (\text{B.13})$$

$${}_{\pm 2}D(\chi, \hat{\mathbf{n}}) = \sum_{m=\pm 2} \int \frac{d^3 k}{(2\pi)^3} D^{(m)}(\mathbf{k}, \chi) {}_{\pm 2}\mathcal{G}_{\ell}^{(m)}(\mathbf{k}, \chi \hat{\mathbf{n}}), \quad (\text{B.14})$$

where ${}_s\mathcal{G}_{\ell}^{(m)}(\mathbf{k}, \chi \hat{\mathbf{n}})$ is the total-angular momentum basis (see also Ref. [76]) defined by

$${}_s\mathcal{G}_{\ell}^{(m)}(\mathbf{k}, \chi \hat{\mathbf{n}}) = (-i)^{\ell} \sqrt{\frac{4\pi}{2\ell + 1}} {}_sY_{\ell,m}(\hat{\mathbf{n}}) e^{i\mathbf{k} \cdot (\chi \hat{\mathbf{n}})}. \quad (\text{B.15})$$

Following the same step as derived in the case of the spin-+2 part, we multiply $e_-^a e_-^b$ in both sides of Eq. (3.68) to construct the spin--2 part of the reduced shear:

$$g^* = [-_2D]_0^{\chi} + \int_0^{\chi} d\chi' \frac{\chi - \chi'}{\chi \chi'} \left\{ \bar{\partial}^2 \mathcal{A} - \frac{d}{d\chi'} [\chi' \bar{\partial}_{-1} \mathcal{B}] + \chi' \frac{d^2}{d\chi'^2} [_{-2}D] \right\}. \quad (\text{B.16})$$

To compute the angular power spectrum, it is useful to expand the total-angular momentum basis as

$${}_s\mathcal{G}_{\ell}^{(m)}(\mathbf{k}, \chi \hat{\mathbf{n}}) = \sum_{L=0}^{\infty} (-i)^L \sqrt{4\pi(2L+1)} {}_s\mathcal{J}_L^{\ell m}(k\chi) {}_sY_{Lm}(\hat{\mathbf{n}}), \quad (\text{B.17})$$

where we assume $\mathbf{k}/k = \mathbf{e}_z$. The exact expressions for coefficients, ${}_s\mathcal{J}_L^{\ell m}$ ($= {}_s\epsilon_L^{\ell m}(x) \pm i_s\beta_L^{\ell m}(x)$), are summarized in the following:

- $s = 0$:

$${}_0\mathcal{J}_L^{00}(x) = j_L(x), \quad (\text{B.18})$$

$${}_0\mathcal{J}_L^{10}(x) = j'_L(x), \quad (\text{B.19})$$

$${}_0\mathcal{J}_L^{1,\pm 1}(x) = \sqrt{\frac{L(L+1)}{2}} \frac{j_L(x)}{x}, \quad (\text{B.20})$$

$${}_0\mathcal{J}_L^{20}(x) = \frac{1}{2} [3j''_L(x) + j_L(x)], \quad (\text{B.21})$$

$${}_0\mathcal{J}_L^{2,\pm 1}(x) = \sqrt{\frac{3L(L+1)}{2}} \left(\frac{j_L(x)}{x} \right)', \quad (\text{B.22})$$

$${}_0\mathcal{J}_L^{2,\pm 2}(x) = \sqrt{\frac{3(L+2)!}{8(L-2)!}} \frac{j_L(x)}{x^2}. \quad (\text{B.23})$$

- $s = \pm 1$:

$${}_1\epsilon_L^{10}(x) = \sqrt{\frac{L(L+1)}{2}} \frac{j_L(x)}{x}, \quad (\text{B.24})$$

$${}_1\epsilon_L^{1,\pm 1}(x) = \frac{1}{2} \left(\frac{j_L(x)}{x} + j'_L(x) \right), \quad (\text{B.25})$$

$${}_1\epsilon_L^{20}(x) = \sqrt{\frac{3L(L+1)}{2}} \left(\frac{j_L(x)}{x} \right)', \quad (\text{B.26})$$

$${}_1\epsilon_L^{2,\pm 1}(x) = \frac{1}{2} \left(j_L(x) + 2j''_L(x) - 2\frac{j_L(x)}{x^2} + \frac{2j'_L(x)}{x} \right), \quad (\text{B.27})$$

$${}_1\epsilon_L^{2,\pm 2}(x) = \frac{\sqrt{(L-1)(L+2)}}{2} \left(\frac{j_L(x)}{x^2} + \frac{j'_L(x)}{x} \right), \quad (\text{B.28})$$

$${}_1\beta_L^{10}(x) = 0, \quad {}_1\beta_L^{1,\pm 1}(x) = \pm \frac{j_L(x)}{2}, \quad (\text{B.29})$$

$${}_1\beta_L^{20}(x) = 0, \quad {}_1\beta_L^{2,\pm 1}(x) = \pm \frac{1}{2} \left(j'_L(x) - \frac{j_L(x)}{x} \right), \quad (\text{B.30})$$

$${}_1\beta_L^{2,\pm 2}(x) = \pm \frac{\sqrt{(L-1)(L+2)}}{2} \frac{j_L(x)}{x}. \quad (\text{B.31})$$

- $s = \pm 2$:

$$\epsilon_L^{20}(x) = {}_0\mathcal{J}_L^{2,\pm 2}(x), \quad (\text{B.32})$$

$$\epsilon_L^{2,\pm 1}(x) = \frac{1}{2} \sqrt{(L-1)(L+2)} \left(\frac{j_L(x)}{x^2} + \frac{j'_L(x)}{x} \right), \quad (\text{B.33})$$

$$\epsilon_L^{2,\pm 2}(x) = \frac{1}{4} \left(-j_L(x) + j''_L(x) + 2\frac{j_L(x)}{x^2} + 4\frac{j'_L(x)}{x} \right), \quad (\text{B.34})$$

$$\beta_L^{20}(x) = 0, \quad (\text{B.35})$$

$$\beta_L^{2,\pm 1}(x) = \pm \frac{1}{2} \sqrt{(L-1)(L+2)} \frac{j_L(x)}{x}, \quad (\text{B.36})$$

$$\beta_L^{2,\pm 2}(x) = \pm \frac{1}{2} \left(j'_L(x) + 2\frac{j_L(x)}{x} \right), \quad (\text{B.37})$$

With the above expansion, we obtain

$$\mathcal{A} = \sum_{m=0,\pm 1,\pm 2} \int \frac{d^3 k}{(2\pi)^3} \mathcal{A}^{(m)}(\mathbf{k}, \eta) \sum_{L=0}^{\infty} (-i)^L \sqrt{4\pi(2L+1)} {}_0\mathcal{J}_L^{|m|,m}(k\chi) {}_0Y_{L,m}(\hat{\mathbf{n}}), \quad (\text{B.38})$$

$${}_{\pm 1}\mathcal{B} = \sum_{m=\pm 1,\pm 2} \int \frac{d^3 k}{(2\pi)^3} \mathcal{B}^{(m)}(\mathbf{k}, \eta) \sum_{L=0}^{\infty} (-i)^L \sqrt{4\pi(2L+1)} {}_{\pm 1}\mathcal{J}_L^{|m|,m}(k\chi) {}_{\pm 1}Y_{L,m}(\hat{\mathbf{n}}), \quad (\text{B.39})$$

$${}_{\pm 2}\mathcal{D} = \sum_{m=\pm 2} \int \frac{d^3 k}{(2\pi)^3} \mathcal{D}^{(m)}(\mathbf{k}, \eta) \sum_{L=0}^{\infty} (-i)^L \sqrt{4\pi(2L+1)} {}_{\pm 2}\mathcal{J}_L^{|m|,m}(k\chi) {}_{\pm 2}Y_{L,m}(\hat{\mathbf{n}}). \quad (\text{B.40})$$

This leads to

$$g = \sum_{m=0,\pm 1,\pm 2} \int \frac{d^3 k}{(2\pi)^3} \sum_{L=0}^{\infty} (-i)^L \sqrt{4\pi(2L+1)} \left\{ \begin{aligned} & [{}_{+2}\mathcal{J}_L^{[m],m}(k\chi) D^{(m)}(\mathbf{k}, \eta)]_0^\chi \\ & + \int_0^\chi d\chi' \frac{\chi - \chi'}{\chi\chi'} \left[{}_0\mathcal{J}_L^{[m],m}(k\chi) \mathcal{A}^{(m)}(\mathbf{k}, \eta) - \frac{d}{d\chi'} [{}_{+1}\mathcal{J}_L^{[m],m}(k\chi)]_+ {}_1\mathcal{B}^{(m)}(\mathbf{k}, \eta) \right. \\ & \left. + \chi' \frac{d^2}{d\chi'^2} [{}_{+2}\mathcal{J}_L^{[m],m}(k\chi)]_+ {}_2D^{(m)}(\mathbf{k}, \eta) \right] \end{aligned} \right\} {}_{+2}Y_{L,m}(\hat{\mathbf{n}}), \quad (\text{B.41})$$

and

$$g^* = \sum_{m=0,\pm 1,\pm 2} \int \frac{d^3 k}{(2\pi)^3} \sum_{L=0}^{\infty} (-i)^L \sqrt{4\pi(2L+1)} \left\{ \begin{aligned} & [{}_{-2}\mathcal{J}_L^{[m],m}(k\chi) D^{(m)}(\mathbf{k}, \eta)]_0^\chi \\ & + \int_0^\chi d\chi' \frac{\chi - \chi'}{\chi\chi'} \left[{}_0\mathcal{J}_L^{[m],m}(k\chi) \mathcal{A}^{(m)}(\mathbf{k}, \eta) - \frac{d}{d\chi'} [{}_{-1}\mathcal{J}_L^{[m],m}(k\chi)]_- {}_1\mathcal{B}^{(m)}(\mathbf{k}, \eta) \right. \\ & \left. + \chi' \frac{d^2}{d\chi'^2} [{}_{-2}\mathcal{J}_L^{[m],m}(k\chi)]_- {}_2D^{(m)}(\mathbf{k}, \eta) \right] \end{aligned} \right\} {}_{-2}Y_{L,m}(\hat{\mathbf{n}}), \quad (\text{B.42})$$

B.2.2 Lensing potential and curl mode

In this subsection we derive the explicit expression of the lensing potential, curl mode and their angular power spectra induced by the vector perturbations. The calculation of the angular power spectra are basically the same as in the case of cosmic shear in previous subsection. From Eq. (3.32) we obtain

$$\nabla^2 \phi = \int_0^\chi \frac{d\chi'}{\chi'} \left\{ \frac{\chi - \chi'}{\chi'} \partial \bar{\partial} \mathcal{A}(\bar{x}) - \frac{1}{2} [\bar{\partial} {}_{+1}\mathcal{B}(\bar{x}) + \partial {}_{-1}\mathcal{B}(\bar{x})] \right\}, \quad (\text{B.43})$$

$$\nabla^2 \varpi = \int_0^\chi \frac{d\chi'}{\chi'} \frac{1}{2} [\bar{\partial} {}_{+1}\mathcal{B}(\bar{x}) - \partial {}_{-1}\mathcal{B}(\bar{x})]. \quad (\text{B.44})$$

Similar to the case of cosmic shear we can rewrite the above equations as

$$\begin{aligned} \nabla^2 \phi &= \sum_{m=0,\pm 1,\pm 2} \int \frac{d^3 k}{(2\pi)^3} \sum_{L=0}^{\infty} (-i)^L \sqrt{4\pi(2L+1)} \\ &\times \int_0^\chi \frac{d\chi'}{\chi'} \left\{ \frac{\chi - \chi'}{\chi'} {}_0\mathcal{J}_L^{[m],m}(k\chi) \mathcal{A}^{(m)}(\mathbf{k}, \eta) \right. \\ &\left. - \frac{1}{2} [{}_{+1}\mathcal{J}_L^{[m],m}(k\chi) {}_{+1}\mathcal{B}^{(m)}(\mathbf{k}, \eta) + {}_{-1}\mathcal{J}_L^{[m],m}(k\chi) {}_{-1}\mathcal{B}^{(m)}(\mathbf{k}, \eta)] \right\} Y_{Lm}(\hat{\mathbf{n}}), \end{aligned} \quad (\text{B.45})$$

$$\nabla^2 \varpi = \int_0^\chi \frac{d\chi'}{\chi'} \frac{1}{2} [{}_{+1}\mathcal{J}_L^{[m],m}(k\chi) {}_{+1}\mathcal{B}^{(m)}(\mathbf{k}, \eta) - {}_{-1}\mathcal{J}_L^{[m],m}(k\chi) {}_{-1}\mathcal{B}^{(m)}(\mathbf{k}, \eta)] Y_{Lm}(\hat{\mathbf{n}}). \quad (\text{B.46})$$

B.2.3 Derivation of shear-deflection relation

In this subsection, we derive the explicit relation between cosmic shear and deflection angle in terms of the spin operators. In the absence of the metric shear (3.69) can be further reduced to a simplified form in the harmonic space. With $\nabla^2 Y_{\ell m}(\hat{\mathbf{n}}) = -\ell(\ell+1)Y_{\ell m}(\hat{\mathbf{n}})$ we have

$$\phi_{\ell m} = 2 \frac{(\ell-2)!}{(\ell+2)!} \int d^2 \hat{\mathbf{n}} Y_{\ell m:ab}^* \gamma_{cd} \omega^{ac} \omega^{bd}, \quad (\text{B.47})$$

$$\varpi_{\ell m} = 2 \frac{(\ell-2)!}{(\ell+2)!} \int d^2 \hat{\mathbf{n}} Y_{\ell m:ab}^* \gamma_{cd} \omega^{ac} \epsilon^{bd}. \quad (\text{B.48})$$

We then rewrite the metric on the sphere, ω^{ab} , the Levi-Civita pseudo-tensor, ϵ^{ab} , in terms of the basis vector e_{\pm}^a and spin operators:

$$\begin{aligned}\phi_{\ell m} &= 2 \frac{(\ell-2)!}{(\ell+2)!} \int d^2 \hat{\mathbf{n}} Y_{\ell m:ab}^* \gamma_{cd} e_+^{(a} e_-^{c)} e_+^{(b} e_-^{d)} \\ &= - \frac{(\ell-2)!}{(\ell+2)!} \int d^2 \hat{\mathbf{n}} \left[(\partial^2 Y_{\ell m}(\hat{\mathbf{n}}))^* g(\hat{\mathbf{n}}) + (\bar{\partial}^2 Y_{\ell m}(\hat{\mathbf{n}}))^* g^*(\hat{\mathbf{n}}) \right],\end{aligned}\quad (\text{B.49})$$

$$\begin{aligned}\varpi_{\ell m} &= 2i \frac{(\ell-2)!}{(\ell+2)!} \int d^2 \hat{\mathbf{n}} Y_{\ell m:ab}^* \gamma_{cd} e_+^{(a} e_-^{c)} e_+^{[b} e_-^{d]} \\ &= i \frac{(\ell-2)!}{(\ell+2)!} \int d^2 \hat{\mathbf{n}} \left[(\partial^2 Y_{\ell m}(\hat{\mathbf{n}}))^* g(\hat{\mathbf{n}}) - (\bar{\partial}^2 Y_{\ell m}(\hat{\mathbf{n}}))^* g^*(\hat{\mathbf{n}}) \right],\end{aligned}\quad (\text{B.50})$$

where we have used the traceless condition for the shear, namely $\gamma_{ab} \omega^{ab} = \gamma_{ab} e_+^a e_-^b = 0$. We then rewrite $\partial^2 Y_{\ell m}$ and $\bar{\partial}^2 Y_{\ell m}$ in terms of the spin- ± 2 spherical harmonics ${}_{\pm 2} Y_{\ell m}$:

$$\begin{aligned}\phi_{\ell m} &= - \sqrt{\frac{(\ell-2)!}{(\ell+2)!}} \int d^2 \hat{\mathbf{n}} \left\{ {}_{+2} Y_{\ell m}^* (\hat{\mathbf{n}}) g(\hat{\mathbf{n}}) + {}_{-2} Y_{\ell m}^* (\hat{\mathbf{n}}) g^*(\hat{\mathbf{n}}) \right\} \\ &= - \sqrt{\frac{(\ell-2)!}{(\ell+2)!}} \left({}_{+2} g_{\ell m} + {}_{-2} g_{\ell m} \right),\end{aligned}\quad (\text{B.51})$$

$$\begin{aligned}\varpi_{\ell m} &= i \sqrt{\frac{(\ell-2)!}{(\ell+2)!}} \int d^2 \hat{\mathbf{n}} \left\{ {}_{+2} Y_{\ell m}^* (\hat{\mathbf{n}}) g(\hat{\mathbf{n}}) - {}_{-2} Y_{\ell m}^* (\hat{\mathbf{n}}) g^*(\hat{\mathbf{n}}) \right\} \\ &= i \sqrt{\frac{(\ell-2)!}{(\ell+2)!}} \left({}_{+2} g_{\ell m} - {}_{-2} g_{\ell m} \right).\end{aligned}\quad (\text{B.52})$$

Recalling that the combination $({}_{+2} g_{\ell m} \pm {}_{-2} g_{\ell m})$ can be rewritten in terms of the E-/B-mode cosmic shear field, we obtain the explicit relations between $\phi_{\ell m}$, $\varpi_{\ell m}$, $\mathcal{E}_{\ell m}$ and $\mathcal{B}_{\ell m}$:

$$\phi_{\ell m} = 2 \sqrt{\frac{(\ell-2)!}{(\ell+2)!}} \mathcal{E}_{\ell m}, \quad \varpi_{\ell m} = 2 \sqrt{\frac{(\ell-2)!}{(\ell+2)!}} \mathcal{B}_{\ell m}. \quad (\text{B.53})$$

Appendix C

Note for derivation of lensing estimator

C.1 Noise covariance

Here we derive Eqs. (5.16) and (5.31). Since Eq. (5.16) is obtained by setting $\beta = \alpha$, in what follows, we derive the expression for the noise covariance given in Eq. (5.31).

C.1.1 Relation between noise and estimator covariance

First we rewrite the noise variance using the variance of the estimator. Since $n_{\ell m}^{x,(\alpha)} = \hat{x}_{\ell m}^{(\alpha)} - x_{\ell m}$, the noise variance is rewritten as

$$\langle (n_{\ell m}^{x,(\alpha)})^* n_{\ell m}^{x,(\beta)} \rangle = \langle (\hat{x}_{\ell m}^{(\alpha)})^* \hat{x}_{\ell m}^{(\beta)} \rangle - \langle (x_{\ell m})^* \hat{x}_{\ell m}^{(\beta)} \rangle - \langle (\hat{x}_{\ell m}^{(\alpha)})^* x_{\ell m} \rangle + C_\ell^{xx}. \quad (\text{C.1})$$

Note here that

$$\begin{aligned} & \langle (x_{\ell m})^* \tilde{X}_{LM} \tilde{Y}_{L'M'} \rangle \\ &= \sum_{x'} \sum_{\ell' m'} \sum_{L'' M''} \sum_{Z=\Theta, E, B} \\ & \quad \times \left\{ (-1)^{M'} \begin{pmatrix} L' & \ell' & L'' \\ -M' & m' & M'' \end{pmatrix} s_{L'\ell'L''}^{x', (ZY)} \langle (x_{\ell m})^* Z_{L''M''} x'_{\ell'm'} X_{LM} \rangle \right. \\ & \quad \left. + (-1)^M \begin{pmatrix} L & \ell' & L'' \\ -M & m' & M'' \end{pmatrix} s_{L\ell'L''}^{x', (ZX)} \langle (x_{\ell m})^* Z_{L''M''} x'_{\ell'm'} Y_{L'M'} \rangle \right\}, \end{aligned} \quad (\text{C.2})$$

where we use Eqs. (2.86), (2.105) and (2.106), and introduce the coefficients, $s_{L\ell L'}^{x, (XY)}$, defined by

$$s_{L\ell L'}^{x, (\Theta\Theta)} = S_{L\ell L'}^{0,x}, \quad s_{L\ell L'}^{x, (EE)} = s_{L\ell L'}^{x, (BB)} = S_{L\ell L'}^{+,x}, \quad s_{L\ell L'}^{x, (EB)} = -s_{L\ell L'}^{x, (BE)} = S_{L\ell L'}^{-,x}, \quad (\text{C.3})$$

and $s_{L\ell L'}^{x, (XY)} = 0$ for the other combinations of XY . Assuming that the lensing potentials and primary CMB anisotropies are a random Gaussian field, and the correlations between the lensing potentials and primary CMB anisotropies are negligible, the above equation (C.2) reduces to

$$\langle (x_{\ell m})^* \tilde{X}_{LM} \tilde{Y}_{L'M'} \rangle = (-1)^m \begin{pmatrix} \ell & L & L' \\ -m & M & M' \end{pmatrix} \bar{f}_{\ell LL'}^{x, (XY)} C_\ell^{xx}. \quad (\text{C.4})$$

With Eq. (F.5) this leads to the following equation:

$$\langle (x_{\ell m})^* \hat{x}_{\ell m}^{(\alpha)} \rangle = \sum_{LL'} \bar{F}_{\ell LL'}^{x, (\alpha)} \sum_{MM'} \begin{pmatrix} \ell & L & L' \\ -m & M & M' \end{pmatrix} \begin{pmatrix} \ell & L & L' \\ -m & M & M' \end{pmatrix} \bar{f}_{\ell LL'}^{x, (XY)} C_\ell^{xx} = C_\ell^{xx}. \quad (\text{C.5})$$

As a result Eq. (C.1) becomes

$$\langle (n_{\ell m}^{x,(\alpha)})^* n_{\ell m}^{x,(\beta)} \rangle = \langle (\hat{x}_{\ell m}^{(\alpha)})^* \hat{x}_{\ell m}^{(\beta)} \rangle - C_\ell^{xx}. \quad (\text{C.6})$$

C.1.2 Estimator covariance

Next we compute the estimator covariance, $\langle (\hat{x}_{\ell m}^{(\alpha)})^* \hat{x}_{\ell m}^{(\beta)} \rangle$. From Eq. (5.10), the covariance is given by

$$\begin{aligned} \langle (\hat{x}_{\ell m}^{(\alpha)})^* \hat{x}_{\ell m}^{(\beta)} \rangle &= \sum_{L_1 L'_1} \sum_{L_2 L'_2} \sum_{M_1 M'_1} \sum_{M_2 M'_2} \begin{pmatrix} \ell & L_1 & L'_1 \\ -m & M_1 & M'_1 \end{pmatrix} \begin{pmatrix} \ell & L_2 & L'_2 \\ -m & M_2 & M'_2 \end{pmatrix} \\ &\times (\bar{F}_{\ell L_1 L'_1}^{x,(\alpha)})^* \bar{F}_{\ell L_2 L'_2}^{x,(\beta)} \langle \hat{X}_{L_1 M_1}^* \hat{Y}_{L'_1 M'_1}^* \hat{Z}_{L_2 M_2} \hat{W}_{L'_2 M'_2} \rangle . \end{aligned} \quad (\text{C.7})$$

To compute the r.h.s. of Eq. (C.7) we need to evaluate the four-point correlation of the observed CMB anisotropies:

$$\langle \hat{X}_{L_1 M_1}^* \hat{Y}_{L'_1 M'_1}^* \hat{Z}_{L_2 M_2} \hat{W}_{L'_2 M'_2} \rangle . \quad (\text{C.8})$$

In general the four-point correlation (C.8) is described by

$$\begin{aligned} &\langle \hat{X}_{L_1 M_1}^* \hat{Y}_{L'_1 M'_1}^* \hat{Z}_{L_2 M_2} \hat{W}_{L'_2 M'_2} \rangle \\ &= \langle \hat{X}_{L_1 M_1}^* \hat{Y}_{L'_1 M'_1}^* \hat{Z}_{L_2 M_2} \hat{W}_{L'_2 M'_2} \rangle_{\text{G}} + \langle \hat{X}_{L_1 M_1}^* \hat{Y}_{L'_1 M'_1}^* \hat{Z}_{L_2 M_2} \hat{W}_{L'_2 M'_2} \rangle_{\text{C}} . \end{aligned} \quad (\text{C.9})$$

The first term is defined by

$$\begin{aligned} &\langle \hat{X}_{L_1, M_1}^* \hat{Y}_{L'_1, M'_1}^* \hat{Z}_{L_2, M_2} \hat{W}_{L'_2, M'_2} \rangle_{\text{G}} \\ &= \hat{C}_{L_1}^{XY} \hat{C}_{L'_1}^{ZW} \Delta_{(1,1'),(2,2')} + \hat{C}_{L_1}^{XZ} \hat{C}_{L'_1}^{YW} \Delta_{(1,2),(1',2')} + \hat{C}_{L_1}^{XW} \hat{C}_{L'_1}^{YZ} \Delta_{(1,2'),(1',2)} , \end{aligned} \quad (\text{C.10})$$

where the quantity \hat{C} is the observed angular power spectrum, and $\Delta_{(1,1'),(2,2')}$, $\Delta_{(1,2),(1',2')}$ and $\Delta_{(1,2'),(1',2)}$ denote

$$\Delta_{(1,1'),(2,2')} \equiv \delta_{L_1 L'_1} \delta_{L_2 L'_2} \delta_{M_1, -M'_1} \delta_{M_2, -M'_2} , \quad (\text{C.11})$$

$$\Delta_{(1,2),(1',2')} \equiv \delta_{L_1 L_2} \delta_{L'_1 L'_2} \delta_{M_1 M_2} \delta_{M'_1 M'_2} , \quad (\text{C.12})$$

$$\Delta_{(1,2'),(1',2)} \equiv \delta_{L_1 L'_2} \delta_{L'_1 L_2} \delta_{M_1 M'_2} \delta_{M'_1 M_2} . \quad (\text{C.13})$$

The other terms included in the four-point correlation are represented by the second term in Eq. (C.9). If the quantities, $\tilde{X}_{L_1 M_1}$, $\tilde{Y}_{L'_1 M'_1}$, $\tilde{Z}_{L_2 M_2}$ and $\tilde{W}_{L'_2 M'_2}$, are random Gaussian fields, the second term vanishes. From Eq. (C.9) the covariance is decomposed into two parts:

$$\langle (\hat{x}_{\ell m}^{(\alpha)})^* \hat{x}_{\ell m}^{(\beta)} \rangle = G_{\ell m}^{x,(\alpha,\beta)} + C_{\ell m}^{x,(\alpha,\beta)} , \quad (\text{C.14})$$

where we define the Gaussian and connected parts, $G_{\ell m}^{x,(\alpha,\beta)}$ and $C_{\ell m}^{x,(\alpha,\beta)}$, as

$$\begin{aligned} G_{\ell m}^{x,(\alpha,\beta)} &= \sum_{L_1 L'_1} \sum_{L_2 L'_2} \sum_{M_1 M'_1} \sum_{M_2 M'_2} \begin{pmatrix} \ell & L_1 & L'_1 \\ -m & M_1 & M'_1 \end{pmatrix} \begin{pmatrix} \ell & L_2 & L'_2 \\ -m & M_2 & M'_2 \end{pmatrix} \\ &\times (\bar{F}_{\ell L_1 L'_1}^{x,(\alpha)})^* \bar{F}_{\ell L_2 L'_2}^{x,(\beta)} \langle \hat{X}_{L_1 M_1}^* \hat{Y}_{L'_1 M'_1}^* \hat{Z}_{L_2 M_2} \hat{W}_{L'_2 M'_2} \rangle_{\text{G}} , \end{aligned} \quad (\text{C.15})$$

$$\begin{aligned} C_{\ell m}^{x,(\alpha,\beta)} &= \sum_{L_1 L'_1} \sum_{L_2 L'_2} \sum_{M_1 M'_1} \sum_{M_2 M'_2} \begin{pmatrix} \ell & L_1 & L'_1 \\ -m & M_1 & M'_1 \end{pmatrix} \begin{pmatrix} \ell & L_2 & L'_2 \\ -m & M_2 & M'_2 \end{pmatrix} \\ &\times (\bar{F}_{\ell L_1 L'_1}^{x,(\alpha)})^* \bar{F}_{\ell L_2 L'_2}^{x,(\beta)} \langle \hat{X}_{L_1 M_1}^* \hat{Y}_{L'_1 M'_1}^* \hat{Z}_{L_2 M_2} \hat{W}_{L'_2 M'_2} \rangle_{\text{C}} . \end{aligned} \quad (\text{C.16})$$

Let us first compute the Gaussian part, $G_{\ell m}^{x,(\alpha,\beta)}$. Substituting Eq. (C.10) into Eq. (C.15) the Gaussian part of the covariance is given by

$$G_{\ell m}^{x,(\alpha,\beta)} = \sum_{L_1 L'_1 L_2 L'_2 M_1 M'_1 M_2 M'_2} \begin{pmatrix} \ell & L_1 & L'_1 \\ -m & M_1 & M'_1 \end{pmatrix} \begin{pmatrix} \ell & L_2 & L'_2 \\ -m & M_2 & M'_2 \end{pmatrix} \times (\bar{F}_{\ell L_1 L'_1}^{x,(\alpha)})^* \bar{F}_{\ell L_2 L'_2}^{x,(\beta)} \left\{ \hat{C}_{L_1}^{XY} \hat{C}_{L'_1}^{ZW} \Delta_{(1,1'),(2,2')} + \hat{C}_{L_1}^{XZ} \hat{C}_{L'_1}^{YW} \Delta_{(1,2),(1',2')} + \hat{C}_{L_1}^{XW} \hat{C}_{L'_1}^{YZ} \Delta_{(1,2'),(1',2)} \right\}. \quad (\text{C.17})$$

Using Eq. (F.4) the term proportional to $\Delta_{(1,1'),(2,2')}$ gives $\delta_{\ell,0}$, and we neglect this term to consider $\ell > 0$. Then Eq. (C.17) becomes

$$\begin{aligned} G_{\ell m}^{x,(\alpha,\beta)} &= \sum_{L_1 L'_1 L_2 L'_2 M_1 M'_1 M_2 M'_2} \begin{pmatrix} \ell & L_1 & L'_1 \\ -m & M_1 & M'_1 \end{pmatrix} \begin{pmatrix} \ell & L_2 & L'_2 \\ -m & M_2 & M'_2 \end{pmatrix} \times (\bar{F}_{\ell L_1 L'_1}^{x,(\alpha)})^* \bar{F}_{\ell L_2 L'_2}^{x,(\beta)} \{ \hat{C}_{L_1}^{XZ} \hat{C}_{L'_1}^{YW} \Delta_{(1,2),(1',2')} + \hat{C}_{L_1}^{XW} \hat{C}_{L'_1}^{YZ} \Delta_{(1,2'),(1',2)} \} \\ &= \sum_{L_1 L_1 M_1 M'_1} (\bar{F}_{\ell L_1 L'_1}^{x,(\alpha)})^* \times \left\{ \bar{F}_{\ell L_1 L'_1}^{x,(\beta)} \hat{C}_{L_1}^{XZ} \hat{C}_{L'_1}^{YW} \begin{pmatrix} \ell & L_1 & L'_1 \\ -m & M_1 & M'_1 \end{pmatrix} \begin{pmatrix} \ell & L_1 & L'_1 \\ -m & M_1 & M'_1 \end{pmatrix} + \bar{F}_{\ell L'_1 L_1}^{x,(\beta)} \hat{C}_{L_1}^{XW} \hat{C}_{L'_1}^{YZ} \begin{pmatrix} \ell & L_1 & L'_1 \\ -m & M_1 & M'_1 \end{pmatrix} \begin{pmatrix} \ell & L'_1 & L_1 \\ -m & M'_1 & M_1 \end{pmatrix} \right\}. \end{aligned} \quad (\text{C.18})$$

Using Eq. (F.2) the above equation reduces to

$$\begin{aligned} G_{\ell m}^{x,(\alpha,\beta)} &= \sum_{L_1 L_1} (\bar{F}_{\ell L_1 L'_1}^{x,(\alpha)})^* (\bar{F}_{\ell L_1 L'_1}^{x,(\beta)} \hat{C}_{L_1}^{XZ} \hat{C}_{L'_1}^{YW} + (-1)^{\ell+L_1+L'_1} \bar{F}_{\ell L'_1 L_1}^{x,(\beta)} \hat{C}_{L_1}^{XW} \hat{C}_{L'_1}^{YZ}) \\ &\quad \times \sum_{M_1 M'_1} \begin{pmatrix} \ell & L_1 & L'_1 \\ -m & M_1 & M'_1 \end{pmatrix} \begin{pmatrix} \ell & L_1 & L'_1 \\ -m & M_1 & M'_1 \end{pmatrix} \\ &= \frac{1}{2\ell+1} \sum_{L_1 L_1} (\bar{F}_{\ell L_1 L'_1}^{x,(\alpha)})^* \times \left(\bar{F}_{\ell L_1 L'_1}^{x,(\beta)} \hat{C}_{L_1}^{XZ} \hat{C}_{L'_1}^{YW} + \bar{F}_{\ell L'_1 L_1}^{x,(\beta)} (-1)^{\ell+L_1+L'_1} \hat{C}_{L_1}^{XW} \hat{C}_{L'_1}^{YZ} \right). \end{aligned} \quad (\text{C.19})$$

Note that we use Eq. (F.5) from the first to the last equation.

Next we compute the connected part of the covariance (C.16). Even if the primordial CMB temperature and polarization anisotropies are random Gaussian fields, the connected part of the four-point correlations is arising from the secondary effects such as the weak lensing. Assuming that the connected part is arising from the lensing effect, the connected part of the four-point correlations is given as

$$\begin{aligned} &\langle \tilde{X}_{L_1 M_1}^* \tilde{Y}_{L'_1 M'_1}^* \tilde{Z}_{L_2 M_2} \tilde{W}_{L'_2 M'_2} \rangle_C \\ &\simeq \sum_{\ell'' m''} \begin{pmatrix} \ell'' & L_1 & L'_1 \\ -m'' & M_1 & M'_1 \end{pmatrix} \begin{pmatrix} \ell'' & L_2 & L'_2 \\ -m'' & M_2 & M'_2 \end{pmatrix} \sum_{x'} (\bar{f}_{\ell'' L_1 L'_1}^{x'(\alpha)})^* \bar{f}_{\ell'' L_2 L'_2}^{x'(\beta)} C_{\ell''}^{x' x'}. \end{aligned} \quad (\text{C.20})$$

Other terms included in the connected part of four-point correlation, such as the non-Gaussian terms introduced in Ref. [154], induce additional noise term in Eq. (5.31) but the terms may be an order of magnitude smaller than $G_{\ell}^{x,(\alpha,\beta)}$

[141, 154, 143]. Substituting Eq. (C.20) into Eq. (C.16) the connected part of the covariance is rewritten as

$$\begin{aligned} C_{\ell m}^{x,(\alpha,\beta)} &= \sum_{L_1 L'_1 L_2 L'_2 M_1 M'_1 M_2 M'_2} \binom{\ell}{-m} \binom{L_1}{M_1} \binom{L'_1}{M'_1} \binom{\ell}{-m} \binom{L_2}{M_2} \binom{L'_2}{M'_2} \\ &\quad \times (\bar{F}_{\ell L_1 L'_1}^{x,(\alpha)})^* \bar{F}_{\ell L_2 L'_2}^{x,(\beta)} \sum_{\ell'' m''} \binom{\ell''}{-m''} \binom{L_1}{M_1} \binom{L'_1}{M'_1} \binom{\ell''}{-m''} \binom{L_2}{M_2} \binom{L'_2}{M'_2} \\ &\quad \times \sum_{x'} (\bar{f}_{\ell'' L_1 L'_1}^{x',(\alpha)})^* \bar{f}_{\ell'' L_2 L'_2}^{x',(\beta)} C_{\ell''}^{x' x'} . \end{aligned} \quad (\text{C.21})$$

With Eq. (F.5) the above equation is rewritten as

$$\begin{aligned} C_{\ell m}^{x,(\alpha,\beta)} &= \sum_{L_1 L'_1 L_2 L'_2 \ell'' m''} \sum_{x'} \frac{\delta_{\ell \ell''} \delta_{m m''}}{2\ell + 1} \frac{\delta_{\ell \ell''} \delta_{m m''}}{2\ell + 1} \\ &\quad \times (\bar{F}_{\ell L_1 L'_1}^{x,(\alpha)})^* \bar{F}_{\ell L_2 L'_2}^{x,(\beta)} (\bar{f}_{\ell'' L_1 L'_1}^{x',(\alpha)})^* \bar{f}_{\ell'' L_2 L'_2}^{x',(\beta)} C_{\ell}^{x' x'} \\ &= \sum_{x'} \left([\bar{F}^x, \bar{f}^{x'}]_{\ell}^{(\alpha)} \right)^* [\bar{F}^x, \bar{f}^{x'}]_{\ell}^{(\beta)} C_{\ell}^{x' x'} . \end{aligned} \quad (\text{C.22})$$

Using Eq. (5.14) we obtain

$$C_{\ell m}^{x,(\alpha,\beta)} = C_{\ell}^{xx} . \quad (\text{C.23})$$

Finally, substituting the resultant form of the Gaussian (C.19) and connected parts (C.23) into Eq. (C.6) we obtain Eq. (5.31).

C.2 Flat-sky limit

In this appendix, using Eqs. (2.66) and (5.34), we derive Eqs. (5.36) and (5.37) and the noise cross-spectrum in the flat-sky limit (5.43).

We first consider the expression for $\mathcal{T}_{\ell, L, L'} g_{\ell, L, L'}^{x,(\alpha)}$ (5.36) in the flat-sky limit. From Eq. (5.21) we obtain

$$\mathcal{T}_{\ell L L'} \bar{g}_{\ell L L'}^{x,(\alpha)} = \frac{\hat{C}_{L'}^{XX} \hat{C}_L^{YY} \mathcal{T}_{\ell L L'} (\bar{f}_{\ell L L'}^{x,(\alpha)})^* - \hat{C}_L^{XY} \hat{C}_{L'}^{XY} \mathcal{T}_{\ell, L', L} (\bar{f}_{\ell L' L}^{x,(\alpha)})^*}{\hat{C}_{L'}^{XX} \hat{C}_L^{YY} \hat{C}_L^{XX} \hat{C}_{L'}^{YY} - (\hat{C}_L^{XY} \hat{C}_{L'}^{XY})^2} . \quad (\text{C.24})$$

Note that, we use

$$\mathcal{T}_{\ell L L'} = (-1)^{\ell+L+L'} \mathcal{T}_{\ell L' L} . \quad (\text{C.25})$$

Then, we need to compute the quantity, $(\mathcal{T}_{\ell L L'})^* \bar{f}_{\ell L L'}^{x,(\alpha)}$. As shown in Table 5.2, this quantity includes $(\mathcal{T}_{\ell L L'})^* S_{L' \ell L}^{s,x}$ and $(\mathcal{T}_{\ell L L'})^* S_{L \ell L'}^{s,x}$ where $s = 0$ or ± 2 . From Eqs. (2.91) and (2.104), we obtain

$$\begin{aligned} (\mathcal{T}_{\ell L L'})^* S_{L' \ell L}^{s,x} &= \left(\frac{(2L+1)(2L'+1)}{4\pi(2\ell+1)(LL')^2} \right)^{1/2} \sum_{m M M'} e^{-im\varphi_{\ell}} e^{iM\varphi_L} e^{iM'\varphi_{L'}} (-1)^{m+M'} \\ &\quad \times i^{m-M-M'} \int d^2 \hat{n} (Y_{L', -M'}^s(\hat{n}))^* [\nabla Y_{\ell-m}(\hat{n})] \odot_x [\nabla_s Y_{LM}(\hat{n})] . \end{aligned} \quad (\text{C.26})$$

Note here that, the r.h.s of Eqs. (2.91) and (2.104) is a real/imaginary number for gradient/curl mode, since the l.h.s of these equations is a real/imaginary number. Thus Eq. (C.26) is rewritten as

$$\begin{aligned}
 (\mathcal{T}_{\ell LL'})^* S_{L'\ell L}^{s,x} &= \left(\frac{(2L+1)(2L'+1)}{4\pi(2\ell+1)(LL')^2} \right)^{1/2} \sum_{mMM'} e^{-im\varphi_\ell} e^{iM\varphi_L} e^{iM'\varphi_{L'}} (-1)^{m+M'} \\
 &\quad \times i^{m-M-M'} \int d^2\hat{\mathbf{n}} Y_{L',-M'}^s(\hat{\mathbf{n}}) [\nabla(Y_{LM}^s(\hat{\mathbf{n}}))^*] \odot_x [\nabla Y_{\ell,-m}^*(\hat{\mathbf{n}})] \\
 &= \left(\frac{\ell(2L+1)(2L'+1)}{2(2\ell+1)LL'} \right)^{1/2} \\
 &\quad \times \sum_{mMM'} \sqrt{\frac{2\pi}{\ell}} i^m e^{-im\varphi_\ell} \sqrt{\frac{2\pi}{L}} i^{-M} e^{iM\varphi_L} \sqrt{\frac{2\pi}{L'}} i^{-M'} e^{iM'\varphi_{L'}} \\
 &\quad \times \int \frac{d^2\hat{\mathbf{n}}}{(2\pi)^2} (Y_{L'M'}^s(\hat{\mathbf{n}}))^* [\nabla(Y_{LM}^s(\hat{\mathbf{n}}))^*] \odot_x [\nabla Y_{\ell m}(\hat{\mathbf{n}})]. \tag{C.27}
 \end{aligned}$$

Using Eq. (5.34) and assuming $\ell, L, L' \gg 1$, the above equation reduces to

$$(\mathcal{T}_{\ell LL'})^* S_{L'\ell L}^{s,x} \simeq e^{si(\varphi_{L'} - \varphi_L)} \mathbf{L} \odot_x \ell \int \frac{d^2\hat{\mathbf{n}}}{(2\pi)^2} e^{i(\ell - \mathbf{L} - \mathbf{L}') \cdot \hat{\mathbf{n}}}. \tag{C.28}$$

From Eq. (5.35) we obtain

$$(\mathcal{T}_{\ell LL'})^* S_{L'\ell L}^{s,x} \simeq \delta_{\mathbf{L} + \mathbf{L}' - \ell} \mathbf{L} \odot_x \ell \times \begin{cases} 1 & (s = 0) \\ \cos 2\varphi_{LL'} & (s = +) \\ -\sin 2\varphi_{LL'} & (s = -) \end{cases}, \tag{C.29}$$

with $\varphi_{LL'} = \varphi_L - \varphi_{L'}$. Similarly, the flat-sky counterpart of $(\mathcal{T}_{\ell LL'})^* S_{L'\ell L}^{s,x}$ is obtained by interchanging \mathbf{L} and \mathbf{L}' in Eq. (C.29) if $\ell + L + L'$ is an even integer. If $\ell + L + L'$ is an odd integer, we further multiply it by minus sign. From Eq. (C.29) we can define the following quantity:

$$f_{\ell LL'}^{x,(\alpha)} \delta_{\mathbf{L} + \mathbf{L}' - \ell} = (\mathcal{T}_{\ell LL'})^* \bar{f}_{\ell LL'}^{x,(\alpha)}. \tag{C.30}$$

The functional form of $f_{\ell LL'}^{x,(\alpha)}$ is summarized in Table 5.3 for each x and α . Substituting Eq. (C.30) into Eq. (C.24) we obtain the following expression:

$$\begin{aligned}
 \mathcal{T}_{\ell LL'} \bar{g}_{\ell LL'}^{x,(\alpha)} &= \delta_{\mathbf{L} + \mathbf{L}' - \ell} \frac{\widehat{C}_{L'}^{XX} \widehat{C}_L^{YY} (f_{\ell LL'}^{x,(\alpha)})^* - \widehat{C}_L^{XY} \widehat{C}_{L'}^{XY} (f_{\ell LL'}^{x,(\alpha)})^*}{\widehat{C}_{L'}^{XX} \widehat{C}_L^{YY} \widehat{C}_L^{XX} \widehat{C}_{L'}^{YY} - (\widehat{C}_L^{XY} \widehat{C}_{L'}^{XY})^2} \\
 &= \delta_{\mathbf{L} + \mathbf{L}' - \ell} g_{\ell LL'}^{x,(\alpha)}, \tag{C.31}
 \end{aligned}$$

with the quantity $\bar{g}_{\ell LL'}^{x,(\alpha)}$ being

$$g_{\ell LL'}^{x,(\alpha)} = \frac{\widehat{C}_{L'}^{XX} \widehat{C}_L^{YY} (f_{\ell LL'}^{x,(\alpha)})^* - \widehat{C}_L^{XY} \widehat{C}_{L'}^{XY} (f_{\ell LL'}^{x,(\alpha)})^*}{\widehat{C}_{L'}^{XX} \widehat{C}_L^{YY} \widehat{C}_L^{XX} \widehat{C}_{L'}^{YY} - (\widehat{C}_L^{XY} \widehat{C}_{L'}^{XY})^2}. \tag{C.32}$$

Next, we consider the flat-sky counterpart of Eq. (5.31) and show Eqs. (5.37) and (5.43). Using Eq. (F.5) the

covariance (5.31) is rewritten as

$$\begin{aligned}
 \bar{N}_\ell^{x,(\alpha\beta)} &= \sum_{mMM'm'M''M'''} \frac{(-1)^{m+m'}}{2\ell+1} \binom{\ell}{-m} \binom{L}{M} \binom{L'}{M'} \binom{\ell}{-m'} \binom{L}{M''} \binom{L'}{M'''} \\
 &\quad \times \sum_{LL'} (\bar{F}_{\ell LL'}^{x,(\alpha)})^* \left(\bar{F}_{\ell LL'}^{x,(\beta)} \hat{C}_L^{XX'} \hat{C}_{L'}^{YY'} + \bar{F}_{\ell L'L}^{x,(\beta)} (-1)^{\ell+L+L'} \hat{C}_L^{XY'} \hat{C}_{L'}^{X'Y} \right) \\
 &= \sum_{mMMm'm'M'''M'''} \frac{(-1)^{m+m'}}{2\ell+1} \binom{\ell}{-m} \binom{L}{M} \binom{L'}{M'} \binom{\ell}{-m'} \binom{L}{M''} \binom{L'}{M'''} \\
 &\quad \times \int \frac{d\varphi_\ell}{2\pi} e^{-i(m-m')\varphi} \int \frac{d\varphi_L}{2\pi} e^{-i(M-M'')\varphi_L} \int \frac{d\varphi_{L'}}{2\pi} e^{-i(M'-M''')\varphi_{L'}} \\
 &\quad \times \sum_{LL'} (\bar{F}_{\ell LL'}^{x,(\alpha)})^* \left(\bar{F}_{\ell LL'}^{x,(\beta)} \hat{C}_L^{XX'} \hat{C}_{L'}^{YY'} + \bar{F}_{\ell L'L}^{x,(\beta)} (-1)^{\ell+L+L'} \hat{C}_L^{XY'} \hat{C}_{L'}^{X'Y} \right), \tag{C.33}
 \end{aligned}$$

where, for arbitrary integers, M_1 and M_2 , we use the following equation:

$$\delta_{M_1 M_2} = \int \frac{d\varphi}{2\pi} e^{-i(M_1 - M_2)\varphi}. \tag{C.34}$$

With the quantity defined in Eq. (5.33) the expression for the covariance (C.33) is rewritten as

$$\begin{aligned}
 \bar{N}_\ell^{x,(\alpha\beta)} &= \int \frac{d\varphi_\ell}{2\pi} \sum_{LL'} \left(\frac{(2L+1)(2L'+1)}{4\pi(LL')^2} \right)^{-1} \int \frac{d\varphi_L}{2\pi} \int \frac{d\varphi_{L'}}{2\pi} (\mathcal{T}_{\ell LL'})^* \mathcal{T}_{\ell LL'} \\
 &\quad \times (\bar{F}_{\ell LL'}^{x,(\alpha)})^* \left(\bar{F}_{\ell LL'}^{x,(\beta)} \hat{C}_L^{XX'} \hat{C}_{L'}^{YY'} + \bar{F}_{\ell L'L}^{x,(\beta)} (-1)^{\ell+L+L'} \hat{C}_L^{XY'} \hat{C}_{L'}^{X'Y} \right). \tag{C.35}
 \end{aligned}$$

In the flat-sky limit, we can define the following quantity:

$$\delta_{\mathbf{L}+\mathbf{L}'-\boldsymbol{\ell}} F_{\ell \mathbf{L}' \mathbf{L}}^{x,(\beta)} \simeq \mathcal{T}_{\ell LL'} \bar{F}_{\ell LL'}^{x,(\beta)}. \tag{C.36}$$

This is because, from Eq. (C.31), the r.h.s of the above equation is proportional to the delta function, $\delta_{\mathbf{L}+\mathbf{L}'-\boldsymbol{\ell}}$. Using Eq. (C.36) and $\delta_0 = 1/\pi$ and assuming $\ell, L, L' \gg 1$, (C.35) becomes

$$\begin{aligned}
 \bar{N}_\ell^{x,(\alpha\beta)} &\simeq \int \frac{d\varphi_\ell}{2\pi} \sum_{LL'} LL' \int \frac{d\varphi_L}{2\pi} \int \frac{d\varphi_{L'}}{2\pi} \delta_{\mathbf{L}+\mathbf{L}'-\boldsymbol{\ell}} \\
 &\quad \times (F_{\ell, \mathbf{L}, \mathbf{L}'}^{x,(\alpha)})^* \left(F_{\ell, \mathbf{L}, \mathbf{L}'}^{x,(\beta)} \hat{C}_L^{XX'} \hat{C}_{L'}^{YY'} + F_{\ell, \mathbf{L}', \mathbf{L}}^{x,(\beta)} \hat{C}_L^{XY'} \hat{C}_{L'}^{X'Y} \right). \tag{C.37}
 \end{aligned}$$

In the right-hand side, we can choose two-dimensional coordinate system for the variables of integration, \mathbf{L} and \mathbf{L}' , so that the integrand of φ_ℓ does not depend on φ_ℓ . Then, the above equation reduces to

$$\begin{aligned}
 N_\ell^{x,(\alpha\beta)} &= \int \frac{d^2 \mathbf{L}}{(2\pi)^2} \int d^2 \mathbf{L}' \delta_{\mathbf{L}+\mathbf{L}'-\boldsymbol{\ell}} (F_{\ell, \mathbf{L}, \mathbf{L}'}^{x,(\alpha)})^* \\
 &\quad \times \left(F_{\ell, \mathbf{L}, \mathbf{L}'}^{x,(\beta)} \hat{C}_L^{XX'} \hat{C}_{L'}^{YY'} + F_{\ell, \mathbf{L}', \mathbf{L}}^{x,(\beta)} \hat{C}_L^{XY'} \hat{C}_{L'}^{X'Y} \right). \tag{C.38}
 \end{aligned}$$

The noise in the flat-sky limit, $N_\ell^{x,(\alpha)}$, is obtained by $\alpha = \beta$ in the above equation:

$$\begin{aligned}
 N_\ell^{x,(\alpha)} &= \int \frac{d^2 \mathbf{L}}{(2\pi)^2} \int d^2 \mathbf{L}' \delta_{\mathbf{L}+\mathbf{L}'-\boldsymbol{\ell}} (F_{\ell, \mathbf{L}, \mathbf{L}'}^{x,(\alpha)})^* \\
 &\quad \times \left(F_{\ell, \mathbf{L}, \mathbf{L}'}^{x,(\alpha)} \hat{C}_L^{XX'} \hat{C}_{L'}^{YY'} + F_{\ell, \mathbf{L}', \mathbf{L}}^{x,(\alpha)} \hat{C}_L^{XY'} \hat{C}_{L'}^{X'Y} \right). \tag{C.39}
 \end{aligned}$$

Note that the quantity $F_{\ell, \mathbf{L}, \mathbf{L}'}^{x,(\alpha)}$ is described by

$$F_{\ell, \mathbf{L}, \mathbf{L}'}^{x,(\alpha)} = N_{\ell}^{x,(\alpha)} g_{\ell, \mathbf{L}, \mathbf{L}'}^{x,(\alpha)}. \quad (\text{C.40})$$

Substituting Eq. (C.40) into Eq. (C.39) we obtain the expression for the noise spectrum in the flat-sky limit:

$$N_{\ell}^{x,(\alpha)} = \left\{ \int \frac{d^2 \mathbf{L}}{(2\pi)^2} \int d^2 \mathbf{L}' \delta_{\mathbf{L} + \mathbf{L}' - \ell} f_{\ell, \mathbf{L}, \mathbf{L}'}^{x,(\alpha)} g_{\ell, \mathbf{L}, \mathbf{L}'}^{x,(\alpha)} \right\}^{-1}. \quad (\text{C.41})$$

Appendix D

Derivation of correlations of a cosmic string network

Let us consider a Nambu-Goto string segment at the position $\mathbf{r} = \mathbf{r}(\sigma, \eta)$ where η and σ are the time and position on the string worldsheet. In the transverse gauge, the stress-energy tensor for a string segment can be described as [87]

$$\delta T^{\mu\nu}(\mathbf{r}, \eta) = \mu \int d\sigma \begin{pmatrix} 1 & -\dot{r}^i \\ -\dot{r}^j & \dot{r}^i \dot{r}^j - r^{ij} \dot{r}^{j'} \end{pmatrix} \delta^3(\mathbf{r} - \mathbf{r}(\sigma, \eta)), \quad (\text{D.1})$$

where the dot () and the prime ('') denote the derivative with respect to η and σ . Comparing to Eqs. (D.1) and (D.2), the velocity perturbations, $v^{(\pm 1)}$, due to a segment are given by

$$v^{(\pm 1)}(\mathbf{k}, \eta) = \mu \int d\sigma \dot{r}^i(\sigma, \eta) e_{\pm, i}^*(\hat{\mathbf{k}}) e^{i\mathbf{k}\cdot\mathbf{r}(\sigma, \eta)}. \quad (\text{D.2})$$

Since the correlations can be described by a summation of the contribution of each segment, we can estimate the equal-time auto-power spectrum for the vector perturbations as

$$\begin{aligned} P_{\sigma\sigma}(k; \eta, \eta) &= 2 \frac{(16\pi G)^2 a^4}{k^4} \frac{1}{\mathcal{V}} \langle v^{(\pm 1)*}(\mathbf{k}, \eta) v^{(\pm 1)}(\mathbf{k}, \eta) \rangle \\ &= 2 \frac{(16\pi G \mu)^2 a^4}{k^4} n_s dV \frac{1}{\mathcal{V}} e_{\pm, i}^*(\hat{\mathbf{k}}) e_{\pm, j}(\hat{\mathbf{k}}) \\ &\quad \times \left\langle \int d\sigma_1 d\sigma_2 \dot{r}^i(\sigma_1, \eta) \dot{r}^j(\sigma_2, \eta) e^{i\mathbf{k}\cdot(\mathbf{r}(\sigma_1, \eta) - \mathbf{r}(\sigma_2, \eta))} \right\rangle. \end{aligned} \quad (\text{D.3})$$

where $dV = 4\pi\chi^2/H$ is the differential comoving volume element, $n_s = a^3 \xi^{-3}$ is the comoving number density of string segments, and $\mathcal{V} = (2\pi)^3 \delta^3(\mathbf{0})$ is the comoving box size. For the string averaging, we can use a very simple model developed in [88, 89, 90]. The assumption in this model is that all correlators can be expressed in terms of two-point correlations for $\dot{r}^i(\sigma, \eta)$ and $\dot{r}^j(\sigma, \eta)$. Assuming that $\dot{r}^i(\sigma, \eta)$ and $\dot{r}^j(\sigma, \eta)$ are exactly Gaussian and isotropic distributed with mean zero and variances $\langle \dot{r}^i(\sigma, \eta) \dot{r}^j(0, \eta) \rangle \equiv \frac{1}{3} \delta^{ij} V_s(\sigma)$, and $\langle \dot{r}^i(\sigma, \eta) \dot{r}^j(0, \eta) \rangle \equiv \frac{1}{3} \delta^{ij} T_s(\sigma)$, we can compute the equal-time auto-power spectrum for the vector perturbations as

$$P_{\sigma\sigma}(k, \eta, \eta) = \frac{(16\pi G \mu)^2 a^4}{k^4} n_s dV \frac{1}{3\mathcal{V}} \int d\sigma_+ d\sigma_- V_s(\sigma_-) \exp \left[-\frac{1}{6} k^2 \Gamma_s(\sigma_-) \right], \quad (\text{D.4})$$

where $\sigma_{\pm} = \sigma_1 \pm \sigma_2$, we have introduced $\Gamma_s(\sigma) = \int_0^\sigma d\sigma_3 d\sigma_4 T_s(\sigma_3 - \sigma_4)$. On scale larger than the correlation length, the correlators are expected to be damped, and the correlators on scale $\sigma < \xi/a$ can be approximated as $V_s \approx v_{\text{rms}}^2$, $\Gamma_s \approx (1 - v_{\text{rms}}^2) \sigma^2$. Once we determine the region of the integration, we can calculate the auto-power spectrum of

the velocity perturbations by integrating Eq. (D.4). Since the term $\int d\sigma_+/\mathcal{V}$ corresponds to the length of the string segment within the unit volume and the correlators, V_s and Γ_s , are damped at $\sigma_- \gg \xi/a$, we take the region of the integration as $\int d\sigma_+/\mathcal{V} = a^2/\xi^2 \sqrt{1 - v_{\text{rms}}^2}$ and $|\sigma_-| \leq \xi/2a\sqrt{1 - v_{\text{rms}}^2}$ hereafter. Then, we have

$$P_{\sigma\sigma}(k; \eta, \eta) \approx (16\pi G\mu)^2 \frac{2\sqrt{6\pi} v_{\text{rms}}^2}{3(1 - v_{\text{rms}}^2)} \frac{4\pi\chi^2 a^4}{H} \left(\frac{a}{k\xi}\right)^5 \text{erf}\left(\frac{k\xi/a}{2\sqrt{6}}\right). \quad (\text{D.5})$$

Appendix E

Conjugate Gradient Method for Inpainting

Let us consider the solution of the following equation:

$$Ax = b, \quad (\text{E.1})$$

where A is a $n \times n$ Hermite matrix, $A^\dagger = A$, and positive definite. If the inverse of A is numerically hard to compute because of very large n , the following conjugate gradient method (e.g., [155]) is an useful method to solve the above equation.

Note that we can apply the method for general case by rewriting the equation by

$$(A^\dagger A)x = A^\dagger b. \quad (\text{E.2})$$

This is because, denoting $\mathcal{A} = A^\dagger A$, the matrix is Hermite, $\mathcal{A}^\dagger = \mathcal{A}$, and, for arbitrary non-zero vector, \mathbf{u} , $\mathbf{u}^\dagger A^\dagger A \mathbf{u} = |\mathbf{A}\mathbf{u}|^2 > 0$.

Concept

The solution of $Ax = b$ minimize the following function:

$$f(x) = \frac{1}{2}x^\dagger Ax - x^\dagger b. \quad (\text{E.3})$$

Hereafter, we denote the solution as x_* .

Given non-zero vector, \mathbf{v} , a conjugate vector, \mathbf{u} , in terms of A is defined so that

$$\mathbf{u}^\dagger A \mathbf{v} = 0. \quad (\text{E.4})$$

Since $\mathbf{u}^\dagger A \mathbf{v} = \mathbf{v}^\dagger A \mathbf{u}$ and, for non-zero vectors, $\mathbf{u}^\dagger A \mathbf{u} > 0$, we can define a product: $(\mathbf{u}, \mathbf{v})_A \equiv \mathbf{u}^\dagger A \mathbf{v}$.

Consider a set of vectors, $\{\mathbf{p}_k\}_{k=1,\dots,n}$, which satisfy $(\mathbf{p}_i, \mathbf{p}_j)_A = 0$ if $i \neq j$. These vectors consist a basis in n -dimensional space, and the solution, x_* , is expressed with the basis vectors:

$$x_* = \sum_{k=1}^n \frac{\mathbf{p}_k^\dagger \cdot \mathbf{b}}{(\mathbf{p}_k, \mathbf{p}_k)_A} \mathbf{p}_k. \quad (\text{E.5})$$

Thus, determining $\mathbf{p}_1, \mathbf{p}_2, \dots$ in turn, we finally obtain the solution.

The squared of distance between x and y measured with these basis is defined as $\|x - y\|^2 = (x - y, x - y)_A$.

Basic algorithm

For numerically evaluating the solution, \mathbf{x}_0 , it is preferred to rewrite the equation so that the matrix A is nearly diagonal as possible. Here we consider a preconditioner matrix, \tilde{A} , which satisfy $\tilde{A}^{-1}A = I + R$ where the eigenvalues of R are all less than 1, and the equation, multiplying the preconditioner:

$$\tilde{A}^{-1}Ax = \tilde{A}^{-1}\mathbf{b}. \quad (\text{E.6})$$

At first step, we set $\mathbf{x} = \mathbf{x}_0$, and define the residual, $\mathbf{r}_0 \equiv \mathbf{b} - Ax_0$. Note that the residual multiplied by \tilde{A}^{-1} is the gradient at \mathbf{x}_0 with minus sign. Along the direction of gradient, $\tilde{A}^{-1}\mathbf{r}_0$, we move to the next point; with the search direction, $\mathbf{p}_0 = \tilde{A}^{-1}\mathbf{r}_0$, we give the next point as

$$\mathbf{x}_1 = \mathbf{x}_0 + \alpha_0 \mathbf{p}_0, \quad (\text{E.7})$$

where α_0 is chosen such that the distance between \mathbf{x}_1 and the solution, \mathbf{x}_* , in A -space, $\|\mathbf{x}_1 - \mathbf{x}_*\|_A^2$ is minimized. This requirement leads to

$$\alpha_0 = \frac{\|\mathbf{r}_0\|_{\tilde{A}^{-1}}^2}{\|\mathbf{p}_0\|_A^2}. \quad (\text{E.8})$$

For next step, we similarly define the residual, $\mathbf{r}_1 = \mathbf{b} - Ax_1$, and the gradient with minus sign, $\tilde{A}^{-1}\mathbf{r}_1$. Here, instead of choosing \mathbf{p}_1 as the minus gradient, we choose the search direction as

$$\mathbf{p}_1 = \tilde{A}^{-1}\mathbf{r}_1 + \beta_0 \mathbf{p}_0, \quad (\text{E.9})$$

where β_1 is determined so that $(\mathbf{p}_1, \mathbf{p}_0)_A = 0$. This leads to

$$\beta_0 = -\frac{(\mathbf{p}_0, \tilde{A}^{-1}\mathbf{r}_1)_A}{\|\mathbf{p}_0\|^2} = -\frac{(\mathbf{r}_1 - \mathbf{r}_0)\tilde{A}^{-1}\mathbf{r}_1}{(\mathbf{r}_1 - \mathbf{r}_0)\tilde{A}^{-1}\mathbf{r}_0} = \frac{\|\mathbf{r}_1\|_{\tilde{A}^{-1}}^2}{\|\mathbf{r}_0\|_{\tilde{A}^{-1}}^2}, \quad (\text{E.10})$$

where, from the second to last line, we use $(\mathbf{r}_1, \mathbf{r}_0)_{\tilde{A}^{-1}} = 0$. Then, we move to the next point, $\mathbf{x}_2 = \mathbf{x}_1 + \alpha_1 \mathbf{p}_1$, with the α_1 determined by the similar analogy of the determination of α_0 , and the result is

$$\alpha_1 = \frac{\|\mathbf{r}_1\|_{\tilde{A}^{-1}}^2}{\|\mathbf{p}_1\|_A^2}. \quad (\text{E.11})$$

For $n+1$ -th step, the residual is defined by $\mathbf{r}_{n+1} = \mathbf{b} - Ax_{n+1}$. The search direction, \mathbf{p}_{n+1} , is given by the direction of minus gradient, $\tilde{A}^{-1}\mathbf{r}_{n+1}$ with the former search direction, \mathbf{p}_n :

$$\mathbf{p}_{n+1} = \tilde{A}^{-1}\mathbf{r}_{n+1} + \beta_n \mathbf{p}_n. \quad (\text{E.12})$$

The parameter, β_n , is given by

$$\beta_n = -\frac{(\mathbf{p}_n, \tilde{A}^{-1}\mathbf{r}_{n+1})_A}{\|\mathbf{p}_n\|^2} = \frac{\|\mathbf{r}_{n+1}\|_{\tilde{A}^{-1}}^2}{\|\mathbf{r}_n\|_{\tilde{A}^{-1}}^2}. \quad (\text{E.13})$$

The next point is given by $\mathbf{x}_{n+1} = \mathbf{x}_n + \alpha_n \mathbf{p}_n$, with

$$\alpha_n = \frac{\|\mathbf{r}_{n+1}\|_{\tilde{A}^{-1}}^2}{\|\mathbf{p}_n\|_A^2}. \quad (\text{E.14})$$

We note that $\{\mathbf{p}_i\}_{i=1,2,\dots,n}$ and $\{\mathbf{r}_j\}_{j=1,2,\dots,n}$ are the set of basis vectors in A and \tilde{A}^{-1} space, respectively.

Finally, we summarize the algorithm for the above process: the initial condition is $\mathbf{r}_0 = \mathbf{b} - Ax_0$ and $\mathbf{p}_0 = \tilde{A}^{-1}\mathbf{r}_0$, and the recursion equations are described by

$$\mathbf{x}_{n+1} = \mathbf{x}_n + \alpha_n \mathbf{p}_n, \quad (\text{E.15})$$

$$\mathbf{r}_{n+1} = \mathbf{r}_n - \alpha_n A \mathbf{p}_n, \quad (\text{E.16})$$

$$\mathbf{p}_{n+1} = \tilde{A}^{-1}\mathbf{r}_{n+1} + \beta_n \mathbf{p}_n. \quad (\text{E.17})$$

Diagonal preconditioner (Jacobi preconditioner)

The most simple way is to use the diagonal matrix whose components are given by

$$\tilde{A} = \begin{cases} A_{ij} & (i = j) \\ 0 & (i \neq j) \end{cases} . \quad (\text{E.18})$$

Appendix F

Mathematical Note

F.1 Kronecker product

With $n \times n$ matrices, \mathbf{A} and \mathbf{B} , the Kronecker product is defined as

$$\begin{aligned} \mathbf{A} \otimes \mathbf{B} &\equiv \begin{pmatrix} A_{11}\mathbf{B} & A_{12}\mathbf{B} & \cdots & A_{1n}\mathbf{B} \\ A_{21}\mathbf{B} & A_{22}\mathbf{B} & \cdots & A_{2n}\mathbf{B} \\ \vdots & \vdots & \ddots & \vdots \\ A_{n1}\mathbf{B} & A_{n2}\mathbf{B} & \cdots & A_{nn}\mathbf{B} \end{pmatrix} \\ &= \begin{pmatrix} A_{11}B_{11} & A_{11}B_{12} & \cdots & A_{12}B_{11} & A_{12}B_{12} & \cdots & A_{1n}B_{1n} \\ A_{11}B_{21} & A_{11}B_{22} & \cdots & A_{12}B_{21} & A_{12}B_{22} & \cdots & A_{1n}B_{2n} \\ \vdots & \vdots & \ddots & \vdots & \vdots & \ddots & \vdots \\ A_{21}B_{11} & A_{21}B_{12} & \cdots & A_{22}B_{11} & A_{22}B_{12} & \cdots & A_{1n}B_{1n} \\ A_{21}B_{21} & A_{21}B_{22} & \cdots & A_{22}B_{21} & A_{22}B_{22} & \cdots & A_{2n}B_{2n} \\ \vdots & \vdots & \ddots & \vdots & \vdots & \ddots & \vdots \\ A_{n1}B_{11} & A_{n1}B_{12} & \cdots & A_{n2}B_{11} & A_{n2}B_{12} & \cdots & A_{nn}B_{1n} \\ A_{n1}B_{21} & A_{21}B_{22} & \cdots & A_{n2}B_{21} & A_{n2}B_{22} & \cdots & A_{nn}B_{2n} \\ \vdots & \vdots & \ddots & \vdots & \vdots & \ddots & \vdots \\ A_{n1}B_{n1} & A_{n1}B_{n2} & \cdots & A_{n2}B_{n1} & A_{n2}B_{n2} & \cdots & A_{nn}B_{nn} \end{pmatrix}. \end{aligned} \quad (\text{F.1})$$

Note that, if both \mathbf{A} and \mathbf{B} are the regular matrix, the inverse of the Kronecker product is given by $\mathbf{A}^{-1} \otimes \mathbf{B}^{-1}$. Note also that $\text{Tr}(A \otimes B) = \text{Tr}(A)\text{Tr}(B)$ and $\det(A \otimes B) = [\det(A) \det(B)]^n$.

F.2 Special Functions

F.2.1 Wigner-3j symbols

Following Ref. [156] and Ref. [76], we summarize the useful formulas for Wigner-3j symbols.

Symmetric properties of Wigner-3j symbols

$$\begin{pmatrix} \ell_1 & \ell_2 & \ell_3 \\ m_1 & m_2 & m_3 \end{pmatrix} = \begin{pmatrix} \ell_2 & \ell_3 & \ell_1 \\ m_2 & m_3 & m_1 \end{pmatrix} = \begin{pmatrix} \ell_3 & \ell_1 & \ell_2 \\ m_3 & m_1 & m_2 \end{pmatrix} \\ = (-1)^{\ell_1+\ell_2+\ell_3} \begin{pmatrix} \ell_3 & \ell_1 & \ell_2 \\ m_3 & m_1 & m_2 \end{pmatrix}, \quad (\text{F.2})$$

$$\begin{pmatrix} \ell_1 & \ell_2 & \ell_3 \\ m_1 & m_2 & m_3 \end{pmatrix} = (-1)^{\ell_1+\ell_2+\ell_3} \begin{pmatrix} \ell_3 & \ell_1 & \ell_2 \\ -m_3 & -m_1 & -m_2 \end{pmatrix}. \quad (\text{F.3})$$

Summation of Wigner-3j symbols

$$\sum_M (-1)^{L+M} \begin{pmatrix} \ell & L & L \\ -m & M & -M \end{pmatrix} = \delta_{\ell,0} \delta_{m,0} \sqrt{\frac{2L+1}{2\ell+1}}, \quad (\text{F.4})$$

$$\sum_{MM'} \begin{pmatrix} \ell & L & L' \\ -m & M & M' \end{pmatrix} \begin{pmatrix} \ell' & L & L' \\ -m' & M & M' \end{pmatrix} = \frac{1}{2\ell+1} \delta_{\ell\ell'} \delta_{mm'} . \quad (\text{F.5})$$

F.2.2 Legendre Polynomials

Legendre polynomials are defined by

$$P_\ell(x) = \frac{1}{2^\ell \ell!} \frac{d^\ell}{dx^\ell} (x^2 - 1)^\ell. \quad (\text{F.6})$$

The Legendre polynomials satisfy

$$P_\ell(1) = 1, \quad P_\ell(-1) = (-1)^\ell. \quad (\text{F.7})$$

and orthogonality:

$$\int_{-1}^1 dx P_\ell(x) P_{\ell'}(x) = \frac{2}{2\ell+1} \delta_{\ell,\ell'} . \quad (\text{F.8})$$

F.2.3 Associated Legendre polynomials

Using the Legendre polynomials, the associated Legendre polynomials are defined as

$$P_\ell^m = (1-x^2)^{|m|/2} \frac{d^{|m|}}{dx^{|m|}} P_\ell(x). \quad (\text{F.9})$$

The associated Legendre polynomials are a solution of the following differential equation:

$$\left[(1-x^2) \frac{d^2}{dx^2} - 2x + \left(\ell(\ell+1) - \frac{m^2}{1-x^2} \right) \right] P_\ell^m(x) = 0. \quad (\text{F.10})$$

Derivative of the associated Legendre polynomials is

$$\frac{d}{dx} P_\ell^m(x) = \frac{d}{dx} \left[(1-x^2)^{|m|/2} \frac{d^{|m|}}{dx^{|m|}} P_\ell(x) \right] = -\frac{|m|x}{1-x^2} P_\ell^m(x) + \frac{1}{1-x^2} P_\ell^{m+1}(x). \quad (\text{F.11})$$

Orthogonality of the associated Legendre polynomials is given by

$$\int_{-1}^1 d\mu P_\ell^m P_{\ell'}^m = \frac{2}{2\ell+1} \frac{(\ell+m)!}{(\ell-m)!} \delta_{\ell\ell'} . \quad (\text{F.12})$$

F.2.4 Spin operators

Definition

Spin operators acting on a spin s function are introduced by

$$\begin{aligned}\mathcal{D}_s &= -\sin^s \theta \left[\frac{\partial}{\partial \theta} + \frac{i}{\sin \theta} \frac{\partial}{\partial \varphi} \right] \sin^{-s} \theta \\ &= \frac{s}{\tan \theta} - \left(\frac{\partial}{\partial \theta} + \frac{i}{\sin \theta} \frac{\partial}{\partial \varphi} \right) \\ &= (1 - \mu^2)^{s/2} \left[\sqrt{1 - \mu^2} \frac{\partial}{\partial \mu} + \frac{-i}{\sqrt{1 - \mu^2}} \frac{\partial}{\partial \varphi} \right] (1 - \mu^2)^{-s/2}, \\ \bar{\mathcal{D}}_s &= -\sin^{-s} \theta \left[\frac{\partial}{\partial \theta} - \frac{i}{\sin \theta} \frac{\partial}{\partial \varphi} \right] \sin^s \theta \\ &= \frac{-s}{\tan \theta} - \left(\frac{\partial}{\partial \theta} - \frac{i}{\sin \theta} \frac{\partial}{\partial \varphi} \right) \\ &= (1 - \mu^2)^{-s/2} \left[\sqrt{1 - \mu^2} \frac{\partial}{\partial \mu} + \frac{i}{\sqrt{1 - \mu^2}} \frac{\partial}{\partial \varphi} \right] (1 - \mu^2)^{s/2},\end{aligned}\tag{F.13}$$

with $\mu = \cos \theta$.

Relations with covariant derivatives

Covariant derivative on the unit sphere is rewritten by the spin operator as

$$\begin{aligned}\partial^i &= e_\theta^i \frac{\partial}{\partial \theta} + \frac{e_\varphi^i}{\sin \theta} \frac{\partial}{\partial \varphi} = \frac{e_-^i + e_+^i}{2} \frac{\partial}{\partial \theta} + \frac{i}{\sin \theta} \frac{e_-^i - e_+^i}{2} \frac{\partial}{\partial \varphi} \\ &= \frac{e_-^i}{2} \left(\frac{\partial}{\partial \theta} + \frac{i}{\sin \theta} \frac{\partial}{\partial \varphi} \right) + \frac{e_+^i}{2} \left(\frac{\partial}{\partial \theta} - \frac{i}{\sin \theta} \frac{\partial}{\partial \varphi} \right) \\ &= \frac{e_-^i}{2} \left(-\mathcal{D}_s + \frac{s}{\tan \theta} \right) + \frac{e_+^i}{2} \left(-\bar{\mathcal{D}}_s - \frac{s}{\tan \theta} \right) = -\frac{e_-^i \mathcal{D}_s + e_+^i \bar{\mathcal{D}}_s}{2} - \frac{is}{\tan \theta} e_\varphi^i,\end{aligned}\tag{F.14}$$

where we use the polarization vectors, e_{\pm} , defined by Eq.(2.37), but using $e_1 = e_\theta$ and $e_2 = e_\varphi$. The Laplacian is given by

$$\begin{aligned}\nabla \cdot \nabla &= -\frac{s^2}{\tan^2 \theta} + \frac{s}{\tan \theta} \frac{\mathcal{D}_s - \bar{\mathcal{D}}_s}{2} + \frac{(e_-^i \mathcal{D}_s + e_+^i \bar{\mathcal{D}}_s)^2}{4} \\ &= -\frac{s^2}{\tan^2 \theta} + \frac{s}{\tan \theta} \frac{\mathcal{D}_s - \bar{\mathcal{D}}_s}{2} + \frac{1}{4} [e_-^i \mathcal{D}_s e_+^i \bar{\mathcal{D}}_s + e_+^i \bar{\mathcal{D}}_s e_-^i \mathcal{D}_s] \\ &= -\frac{s^2}{\tan^2 \theta} + \frac{1}{2} \left[\left(\frac{1}{\tan \theta} + \bar{\mathcal{D}}_s \right) \mathcal{D}_s + \left(\frac{1}{\tan \theta} + \mathcal{D}_s \right) \bar{\mathcal{D}}_s \right] \\ &= -\frac{s^2}{\tan^2 \theta} + \frac{\mathcal{D}_{s-1} \bar{\mathcal{D}}_s + \bar{\mathcal{D}}_{s+1} \mathcal{D}_s}{2}.\end{aligned}\tag{F.15}$$

Other useful formulas

To see the relation between the intrinsic covariant derivatives on the unit sphere and the spin-raising/lowering operators, one can verify

$$\chi e_\pm^j \partial_j e_\pm^i = \cot \theta e_\pm^i, \quad \chi e_\pm^j \partial_j e_\mp^i = -2 e_\chi^i - \cot \theta e_\mp^i.\tag{F.16}$$

In terms of the spin basis, these are reduced to

$$e_{\pm:b}^a e_{\pm}^b = \cot \theta e_{\pm}^a, \quad e_{\pm:b}^a e_{\mp}^b = -\cot \theta e_{\pm}^a. \quad (\text{F.17})$$

A spin- s function, ${}_s X$, can be written in terms of the spin basis and a symmetric trace-free rank- s tensor, $X_{a_1 \dots a_s}$, as

$$X^s = X_{a_1 \dots a_s} e_+^{a_1} \cdots e_+^{a_s}, \quad (s \geq 0), \quad X^s = X_{a_1 \dots a_{|s|}} e_-^{a_1} \cdots e_-^{a_{|s|}}, \quad (s < 0), \quad (\text{F.18})$$

with $e_{\pm}^a \equiv e_i^a e_{\pm}^i$. With these notations, we can easily prove the following useful relations:

$$(X^0)_{:a} e_+^a = -\partial X^0, \quad (X^0)_{:a} e_-^a = -\bar{\partial} X^0, \quad (\text{F.19})$$

$$X_{a:b} e_+^a e_+^b = -\partial X^1, \quad X_{a:b} e_-^a e_-^b = -\bar{\partial} X^{-1}, \quad (\text{F.20})$$

$$X_{a:b} e_-^a e_+^b = -\partial X^{-1}, \quad X_{a:b} e_+^a e_-^b = -\bar{\partial} X^1, \quad (\text{F.21})$$

$$(X^0)_{:ab} e_+^a e_+^b = \partial^2 X^0, \quad (X^0)_{:ab} e_-^a e_-^b = \bar{\partial}^2 X^0, \quad (\text{F.22})$$

$$(X^0)_{:ab} e_+^a e_-^b = \partial \bar{\partial} X^0 = \bar{\partial} \partial X^0. \quad (\text{F.23})$$

F.2.5 Spherical harmonics

Definition

Spherical harmonics are defined by

$$Y_{\ell m}(\theta, \varphi) = (-1)^{(-m+|m|)/2} \sqrt{\frac{2\ell+1}{4\pi} \frac{(\ell-|m|)!}{(\ell+|m|)!}} e^{im\varphi} P_{\ell}^{|m|}(\cos \theta). \quad (\text{F.24})$$

Generally, spin- s spherical harmonics are introduced as

$$Y_{\ell m}^s(\theta, \varphi) = \sqrt{\frac{(\ell-s)!}{(\ell+s)!}} [\partial_s \cdots \partial_0] Y_{\ell m}(\theta, \varphi). \quad (\text{F.25})$$

Complex conjugate and space inversion:

$$(Y_{\ell m}^s)^*(\hat{\mathbf{n}}) = (-1)^{s+m} Y_{\ell, -m}^{-s}(\hat{\mathbf{n}}), \quad Y_{\ell m}^s(-\hat{\mathbf{n}}) = (-1)^{\ell} Y_{\ell m}^{-s}(\hat{\mathbf{n}}). \quad (\text{F.26})$$

Special values

If $\theta = 0$ and $\varphi = 0$, the spin-0 spherical harmonics becomes

$$Y_{\ell m}(0, 0) = \sqrt{\frac{2\ell+1}{4\pi}} \delta_{m,0}. \quad (\text{F.27})$$

For the spin- s spherical harmonics,

$$Y_{\ell,1}^{-1}(0, 0) = Y_{\ell,1}^1(0, 0) = -\sqrt{\frac{2\ell+1}{4\pi}}. \quad (\text{F.28})$$

Another expression

The spin- s spherical harmonics are expressed with the elementary functions as

$$\begin{aligned} Y_{\ell m}^s(\theta, \varphi) &= (-1)^{(-m+|m|)/2} \sqrt{\frac{2\ell+1}{4\pi} \frac{(\ell-|m|)!(\ell+|m|)!}{(\ell+s)!(\ell-s)!}} e^{im\varphi} \left(\frac{1-\mu^2}{4} \right)^{\ell} \\ &\times \sum_r \frac{(\ell-s+r)!}{(\ell-s)!r!} \frac{(\ell-m+2s+r)!}{(\ell+s)!(r+s-m)!} (-1)^{\ell-r-s} \left(\frac{\mu}{2\sqrt{1-\mu^2}} \right)^{2r+s-m}. \end{aligned} \quad (\text{F.29})$$

Orthogonality

The two spin- s spherical harmonics satisfies the following orthogonality:

$$\int d^2\hat{\mathbf{n}} (Y_{\ell m}^s(\hat{\mathbf{n}}))^* Y_{\ell m}^s(\hat{\mathbf{n}}) = \delta_{\ell\ell'} \delta_{mm'} , \quad (\text{F.30})$$

$$\sum_{\ell m} (Y_{\ell m}^s(\hat{\mathbf{n}}))^* Y_{\ell m}^s(\hat{\mathbf{n}}') = \delta(\cos \theta - \cos \theta') \delta(\varphi - \varphi') . \quad (\text{F.31})$$

Spherical harmonic transform

A function on unit sphere, $X(\hat{\mathbf{n}})$, is expanded by the spherical harmonics, and coefficients are given by

$$X_{\ell m}^s = \int d^2\hat{\mathbf{n}} X(\hat{\mathbf{n}}) Y_{\ell m}^s(\hat{\mathbf{n}}) . \quad (\text{F.32})$$

Multiplying $Y_{\ell m}^*(\hat{\mathbf{n}}')$ in both sides of Eq.(F.32), and summing up both sides in terms of ℓ and m , we obtain

$$X(\hat{\mathbf{n}}) = \sum_{\ell m} X_{\ell m}^s Y_{\ell m}^s(\hat{\mathbf{n}}) . \quad (\text{F.33})$$

Relations between spherical harmonics and Wigner-3j symbols

The spherical harmonics is related to the Clebsch-Gordan coefficients:

$$Y_{\ell_1 m_1}(\hat{\mathbf{n}}) Y_{\ell_2 m_2}(\hat{\mathbf{n}}) = \sum_{LM} \sqrt{(2\ell_1 + 1)(2\ell_2 + 1)} 4\pi (2L + 1) C_{\ell_1, 0, \ell_2, 0}^{L, 0} C_{\ell_1, m_1, \ell_2, m_2}^{LM, 0} Y_{LM}(\hat{\mathbf{n}}) . \quad (\text{F.34})$$

The above equation leads to

$$\begin{aligned} \int d^2\hat{\mathbf{n}} Y_{\ell_1 m_1}(\hat{\mathbf{n}}) Y_{\ell_2 m_2}(\hat{\mathbf{n}}) Y_{\ell_3 m_3}(\hat{\mathbf{n}}) &= \sqrt{\frac{(2\ell_1 + 1)(2\ell_2 + 1)(2\ell_3 + 1)}{4\pi}} \\ &\times \begin{pmatrix} \ell_1 & \ell_2 & \ell_3 \\ 0 & 0 & 0 \end{pmatrix} \begin{pmatrix} \ell_1 & \ell_2 & \ell_3 \\ m_1 & m_2 & m_3 \end{pmatrix} . \end{aligned} \quad (\text{F.35})$$

More general form is (see e.g. Ref.[80])

$$\begin{aligned} \int d^2\hat{\mathbf{n}} Y_{\ell_1 m_1}^{s_1}(\hat{\mathbf{n}}) Y_{\ell_2 m_2}^{s_2}(\hat{\mathbf{n}}) Y_{\ell_3 m_3}^{s_3}(\hat{\mathbf{n}}) &= \sqrt{\frac{(2\ell_1 + 1)(2\ell_2 + 1)(2\ell_3 + 1)}{4\pi}} \\ &\times \begin{pmatrix} \ell_1 & \ell_2 & \ell_3 \\ -s_1 & -s_2 & -s_3 \end{pmatrix} \begin{pmatrix} \ell_1 & \ell_2 & \ell_3 \\ m_1 & m_2 & m_3 \end{pmatrix} . \end{aligned} \quad (\text{F.36})$$

Relations between spherical harmonics and Wigner D-matrix

The spin spherical harmonics is related to the Wigner D-matrix as

$$Y_{\ell m}^s(\theta, \phi) = (-1)^m \sqrt{\frac{2\ell + 1}{4\pi}} D_{-m, s}^\ell(\phi, \theta, 0) . \quad (\text{F.37})$$

The Wigner d-function is

$$D_{mm'}^j(\alpha, \beta, \gamma) = e^{-im\alpha} d_{mm'}^j(\beta) e^{-im'\gamma} , \quad (\text{F.38})$$

where the quantities α , β and γ are the Euler angle. For spin weighted harmonics,

$$\begin{aligned}\sum_m (Y_{\ell m}^{s_1})^*(\theta, \phi) Y_{\ell m}^{s_2}(\theta + \beta, \phi) &= \sqrt{\frac{2\ell + 1}{4\pi}} Y_{\ell, -s_1}^{s_2}(\beta, 0) \\ &= \sqrt{\frac{2\ell + 1}{4\pi}} d_{s_2, -s_1}^\ell(\beta) Y_{\ell, -s_1}^{s_2}(\mathbf{0}).\end{aligned}\quad (\text{F.39})$$

Derivatives of spherical harmonics

Derivatives of spherical harmonics in terms of the spin operator are

$$\partial Y_{\ell m}^s = \sqrt{(\ell - s)(\ell + s + 1)} Y_{\ell m}^{s+1}, \quad (\text{F.40})$$

$$\bar{\partial} Y_{\ell m}^s = -\sqrt{(\ell + s)(\ell - s + 1)} Y_{\ell m}^{s-1}. \quad (\text{F.41})$$

This leads to

$$\begin{aligned}\partial^i Y_{\ell m} &= \frac{e_-^i \partial + e_+^i \bar{\partial}}{\sqrt{2}} Y_{\ell m} \\ &= \sqrt{\ell(\ell + 1)} \frac{e_-^i Y_{\ell m}^1 + e_+^i Y_{\ell m}^{-1}}{\sqrt{2}}.\end{aligned}\quad (\text{F.42})$$

Using Eq.(F.15), divergence of the spherical harmonics is

$$\nabla^2 Y_{\ell m}^s = -(\ell - s)(\ell + s + 1) Y_{\ell m}^s, \quad (\star \nabla) \cdot \nabla Y_{\ell m}^s = 0. \quad (\text{F.43})$$

Integration of spherical harmonics

Here we define the integral

$$I_{\ell_1 \ell_2 \ell_3 m_1 m_2 m_3}^{s_1 s_2 s_3} \equiv c^{ij} \int d^2 \hat{\mathbf{n}} Y_{\ell_1 m_1}^{s_1} [\partial_i Y_{\ell_2 m_2}^{s_2}] [\partial_j Y_{\ell_3 m_3}^{s_3}], \quad (\text{F.44})$$

where c^{ij} is δ^{ij} or ϵ^{ij} . Computing integral by parts, we obtain

$$\begin{aligned}I_{\ell_1 \ell_2 \ell_3 m_1 m_2 m_3}^{s_1 s_2 s_3} &= -c^{ij} \int d^2 \hat{\mathbf{n}} \{ [\partial_j Y_{\ell_1 m_1}^{s_1}] [\partial_i Y_{\ell_2 m_2}^{s_2}] Y_{\ell_3 m_3}^{s_3} + Y_{\ell_1 m_1}^{s_1} [\partial_i \partial_j Y_{\ell_2 m_2}^{s_2}] Y_{\ell_3 m_3}^{s_3} \} \\ &= c^{ij} \int d^2 \hat{\mathbf{n}} \{ [\partial_j Y_{\ell_1 m_1}^{s_1}] Y_{\ell_2 m_2}^{s_2} [\partial_i Y_{\ell_3 m_3}^{s_3}] \\ &\quad + [\partial_i \partial_j Y_{\ell_1 m_1}^{s_1}] Y_{\ell_2 m_2}^{s_2} Y_{\ell_3 m_3}^{s_3} - Y_{\ell_1 m_1}^{s_1} [\partial_i \partial_j Y_{\ell_2 m_2}^{s_2}] Y_{\ell_3 m_3}^{s_3} \} \\ &= -a I_{\ell_1 \ell_2 \ell_3 m_1 m_2 m_3}^{s_1 s_2 s_3} + c^{ij} \int d^2 \hat{\mathbf{n}} \{ -Y_{\ell_1 m_1}^{s_1} Y_{\ell_2 m_2}^{s_2} [\partial_j \partial_i Y_{\ell_3 m_3}^{s_3}] \\ &\quad + [\partial_i \partial_j Y_{\ell_1 m_1}^{s_1}] Y_{\ell_2 m_2}^{s_2} Y_{\ell_3 m_3}^{s_3} - Y_{\ell_1 m_1}^{s_1} [\partial_i \partial_j Y_{\ell_2 m_2}^{s_2}] Y_{\ell_3 m_3}^{s_3} \},\end{aligned}\quad (\text{F.45})$$

where $a = 1$ for $c = \delta$ and -1 for $c = \epsilon$. Thus, if we choose $c^{ij} = \delta^{ij}$, we obtain

$$\begin{aligned}
 & I_{\ell_1, \ell_2, \ell_3, m_1, m_2, m_3}^{s_1, s_2, s_3} \\
 &= \frac{\delta^{ij}}{2} \int d^2 \hat{n} \{ -Y_{\ell_1 m_1}^{s_1} Y_{\ell_2 m_2}^{s_2} [\partial_j \partial_i Y_{\ell_3 m_3}^{s_3}] \\
 &\quad + [\partial_i \partial_j Y_{\ell_1 m_1}^{s_1}] Y_{\ell_2 m_2}^{s_2} Y_{\ell_3 m_3}^{s_3} - Y_{\ell_1 m_1}^{s_1} [\partial_i \partial_j Y_{\ell_2 m_2}^{s_2}] Y_{\ell_3 m_3}^{s_3} \} \\
 &= \frac{-(\ell_1 - s_1)(\ell_1 + s_1 + 1) + (\ell_2 - s_2)(\ell_2 + s_2 + 1) + (\ell_3 - s_3)(\ell_3 + s_3 + 1)}{2} \\
 &\quad \times \int d^2 \hat{n} Y_{\ell_1 m_1}^{s_1} Y_{\ell_2 m_2}^{s_2} Y_{\ell_3 m_3}^{s_3}. \tag{F.46}
 \end{aligned}$$

Further, using Eq. (F.36), we obtain the useful relation

$$\begin{aligned}
 & \int d^2 \hat{n} Y_{\ell_1 m_1}^{s_1} [\nabla Y_{\ell_2 m_2}^{s_2}] \cdot [\nabla Y_{\ell_3 m_3}^{s_3}] \\
 &= [-(\ell_1 - s_1)(\ell_1 + s_1 + 1) + (\ell_2 - s_2)(\ell_2 + s_2 + 1) + (\ell_3 - s_3)(\ell_3 + s_3 + 1)] \\
 &\quad \times \sqrt{\frac{(2\ell_1 + 1)(2\ell_2 + 1)(2\ell_3 + 1)}{16\pi}} \begin{pmatrix} \ell_1 & \ell_2 & \ell_3 \\ -s_1 & -s_2 & -s_3 \end{pmatrix} \begin{pmatrix} \ell_1 & \ell_2 & \ell_3 \\ m_1 & m_2 & m_3 \end{pmatrix}. \tag{F.47}
 \end{aligned}$$

This relations is also derived in Ref.([80, 9]). On the other hand, if we choose $c^{ij} = \epsilon^{ij}$, we obtain

$$\begin{aligned}
 & \epsilon^{ij} \int d^2 \hat{n} \{ -Y_{\ell_1 m_1}^{s_1} Y_{\ell_2 m_2}^{s_2} [\partial_j \partial_i Y_{\ell_3 m_3}^{s_3}] \\
 &\quad + [\partial_i \partial_j Y_{\ell_1 m_1}^{s_1}] Y_{\ell_2 m_2}^{s_2} Y_{\ell_3 m_3}^{s_3} - Y_{\ell_1 m_1}^{s_1} [\partial_i \partial_j Y_{\ell_2 m_2}^{s_2}] Y_{\ell_3 m_3}^{s_3} \} = 0. \tag{F.48}
 \end{aligned}$$

This result is consistent with the fact that $(\star \nabla) \cdot \nabla = 0$. To relate $I_{\ell_1 \ell_2 \ell_3 m_1 m_2 m_3}^{s_1 s_2 s_3}$ with the Wigner 3j symbols, we use

$$\begin{aligned}
 & [(\star \nabla) Y_{\ell_2 m_2}^{s_2}] [\nabla Y_{\ell_3 m_3}^{s_3}] \\
 &= \frac{1}{2} [((\star \bar{e}) \bar{\partial} + (\star e) \bar{\partial}) Y_{\ell_2 m_2}^{s_2}] [(\bar{e} \bar{\partial} + e \bar{\partial}) Y_{\ell_3 m_3}^{s_3}] \\
 &= \frac{i}{2} [(\bar{\partial} Y_{\ell_2 m_2}^{s_2})(\bar{\partial} Y_{\ell_3 m_3}^{s_3}) - (\bar{\partial} Y_{\ell_2 m_2}^{s_2})(\bar{\partial} Y_{\ell_3 m_3}^{s_3})] \\
 &= \frac{-i}{2} \left[\sqrt{(\ell_2 - s_2)(\ell_2 + s_2 + 1)(\ell_3 + s_3)(\ell_3 - s_3 + 1)} Y_{\ell_2 m_2}^{s_2+1} Y_{\ell_3 m_3}^{s_3-1} \right. \\
 &\quad \left. - \sqrt{(\ell_2 + s_2)(\ell_2 - s_2 + 1)(\ell_3 - s_3)(\ell_3 + s_3 + 1)} Y_{\ell_2 m_2}^{s_2-1} Y_{\ell_3 m_3}^{s_3+1} \right]. \tag{F.49}
 \end{aligned}$$

Then we obtain

$$\begin{aligned}
& \int d^2 \hat{\mathbf{n}} Y_{\ell_1 m_1}^{s_1} [(\star \nabla) Y_{\ell_2 m_2}^{s_2}] [\nabla s_3 Y_{\ell_3 m_3}] \\
&= \frac{-i}{2} \left[\sqrt{(\ell_2 - s_2)(\ell_2 + s_2 + 1)(\ell_3 + s_3)(\ell_3 - s_3 + 1)} \int d^2 \hat{\mathbf{n}} Y_{\ell_1 m_1}^{s_1} Y_{\ell_2 m_2}^{s_2+1} Y_{\ell_3 m_3}^{s_3-1} \right. \\
&\quad - \sqrt{(\ell_2 + s_2)(\ell_2 - s_2 + 1)(\ell_3 - s_3)(\ell_3 + s_3 + 1)} \int d^2 \hat{\mathbf{n}} Y_{\ell_1 m_1}^{s_1} Y_{\ell_2 m_2}^{s_2-1} Y_{\ell_3 m_3}^{s_3+1} \left. \right] \\
&= -i \left[\sqrt{(\ell_2 - s_2)(\ell_2 + s_2 + 1)(\ell_3 + s_3)(\ell_3 - s_3 + 1)} \right. \\
&\quad \times \sqrt{\frac{(2\ell_1 + 1)(2\ell_2 + 1)(2\ell_3 + 1)}{16\pi}} \begin{pmatrix} \ell_1 & \ell_2 & \ell_3 \\ -s_1 & -s_2 - 1 & -s_3 + 1 \end{pmatrix} \begin{pmatrix} \ell_1 & \ell_2 & \ell_3 \\ m_1 & m_2 & m_3 \end{pmatrix} \\
&\quad - \sqrt{(\ell_2 + s_2)(\ell_2 - s_2 + 1)(\ell_3 - s_3)(\ell_3 + s_3 + 1)} \\
&\quad \times \sqrt{\frac{(2\ell_1 + 1)(2\ell_2 + 1)(2\ell_3 + 1)}{16\pi}} \begin{pmatrix} \ell_1 & \ell_2 & \ell_3 \\ -s_1 & -s_2 + 1 & -s_3 - 1 \end{pmatrix} \begin{pmatrix} \ell_1 & \ell_2 & \ell_3 \\ m_1 & m_2 & m_3 \end{pmatrix} \left. \right] \\
&= -i \left[\sqrt{(\ell_2 - s_2)(\ell_2 + s_2 + 1)(\ell_3 + s_3)(\ell_3 - s_3 + 1)} \begin{pmatrix} \ell_1 & \ell_2 & \ell_3 \\ -s_1 & -s_2 - 1 & -s_3 + 1 \end{pmatrix} \right. \\
&\quad - \sqrt{(\ell_2 + s_2)(\ell_2 - s_2 + 1)(\ell_3 - s_3)(\ell_3 + s_3 + 1)} \begin{pmatrix} \ell_1 & \ell_2 & \ell_3 \\ -s_1 & -s_2 + 1 & -s_3 - 1 \end{pmatrix} \left. \right] \\
&\quad \times \sqrt{\frac{(2\ell_1 + 1)(2\ell_2 + 1)(2\ell_3 + 1)}{16\pi}} \begin{pmatrix} \ell_1 & \ell_2 & \ell_3 \\ m_1 & m_2 & m_3 \end{pmatrix}. \tag{F.50}
\end{aligned}$$

This result is consistent with the equation derived in Ref. [46]

F.2.6 Bessel function

The Bessel and Neumann functions are the solution of the following differential equation:

$$\frac{d^2 f}{dz^2} + \frac{1}{z} \frac{df}{dz} + \left(1 - \frac{\nu^2}{z^2} \right) f = 0. \tag{F.51}$$

The Bessel function is

$$J_\nu(z) = \left(\frac{z}{2} \right)^\nu \sum_{m=0}^{\infty} \frac{(-1)^m}{m! \Gamma(\nu + m + 1)} \left(\frac{z}{2} \right)^{2m}. \tag{F.52}$$

The Neumann function is

$$Y_\nu(z) = \frac{J_\nu(z) \cos \nu \pi - J_{-\nu}(z)}{\sin \nu \pi}. \tag{F.53}$$

Spherical Bessel function

The spherical Bessel function is the solutions of the following equation:

$$\frac{d^2 f}{dx^2} + \frac{2}{x} \frac{df}{dx} + \left(1 - \frac{\nu(\nu + 1)}{x} \right) f = 0. \tag{F.54}$$

The expressions for the spherical Bessel functions are

$$j_\nu(x) = \left(\frac{x}{2}\right)^\nu \sum_{n=0}^{\infty} \frac{(-1)^n (x/2)^{2n}}{n! \Gamma(\nu + n + 1)}, \quad (\text{F.55})$$

$$n_\nu(x) = \frac{J_\nu(x) \cos(\nu\pi) - J_{-\nu}(x)}{\sin(\nu\pi)}. \quad (\text{F.56})$$

The derivative of the spherical Bessel function is

$$\frac{d}{dx} x^{n+1} j_n = x^{n+1} j_{n-1}(x). \quad (\text{F.57})$$

The following formula is usually referred to as the partial wave expansion (or Rayleigh expansion):

$$\begin{aligned} e^{-ix\mu} &= \sum_{n=0}^{\infty} (2n+1)(-i)^n j_n(x) P_n(\mu) \\ &= \sum_{\ell=0}^{\infty} \sum_{m=-\ell}^{\ell} 4\pi (-i)^\ell j_\ell(x) Y_{\ell m}(\hat{\mathbf{n}}) Y_{\ell m}^*(\hat{\mathbf{n}}'). \end{aligned} \quad (\text{F.58})$$

with $\mu = \hat{\mathbf{n}} \cdot \hat{\mathbf{n}}'$. From this formula, we can also derive

$$(-1)^m (1 - \mu^2)^{m/2} (-ix)^m e^{-ix\mu} = \sum_{n=0}^{\infty} (2n+1)(-i)^n j_n(x) P_n^m(\mu). \quad (\text{F.59})$$

Appendix G

Numerical simulation of lensed CMB maps

In this section, we describe our method to generate lensed CMB maps, based on the ray-tracing of large-scale structure simulations (e.g., [157, 158]).

Fig. G.1 shows a schematic picture of our ray-tracing simulation. We have multiple lens planes but use a flat-sky approximation. The horizontal axis is the comoving distance r from the observer. The thick vertical lines are the lens and source planes, which are placed at equal-distance intervals of L , and located at $r = (i - 1/2) \times L$ with an integer $i = 1, 2, \dots, N$. Here, $i = N$ corresponds to the source plane. We place the source plane at the last scattering surface ($z_s = 1090$). The distance to the last scattering surface is $r_{\text{LSS}} = r(z_s = 1090) = 9900 h^{-1} \text{Mpc}$ in our fiducial cosmological model. We place 19 lens planes up to the last scattering surface, i.e., we set $N = 20$. We determine the interval L from the distance to the last scattering surface divided by the number of lens planes, $L = r_{\text{LSS}}/(N - 1/2) = r_{\text{LSS}}/(20 - 1/2) = 507.6 h^{-1} \text{Mpc}$. Light rays are emitted from the observer and are deflected at each lens plane before reaching the source plane. In our simulation, the field of view is $10 \times 10 \text{ deg}^2$. We impose a periodic boundary condition on the lens planes.

G.1 N -body Simulations

In order to obtain the particle distribution and the gravitational potential on the lens planes, we run N -body simulations in a cubic box, and then project the particle positions into two dimensions perpendicular to the line-of-sight. We use the numerical simulation code Gadget2 [159, 160]. We generate the initial conditions based on the second-order Lagrangian perturbation theory (2LPT; [161, 162]) with the initial linear power spectrum calculated by CAMB. We employ 1024^3 dark matter particles in the simulation box of $L = 507.6 h^{-1} \text{Mpc}$ on a side. The initial redshift is $z_{\text{init}} = 70$, and we dump the outputs (the particle positions) at the redshifts corresponding to the positions of the lens planes $r = L \times (i - 1/2)$, shown in Fig. G.1. The softening length is fixed to be 5% of the mean particle separations, which correspond to $25 h^{-1} \text{kpc}$. We prepare five independent realizations to reduce the sample variance.

G.2 Ray-tracing Simulations

We briefly explain the procedure to trace light rays through N -body data and obtain the maps of the lensing fields on the source plane (see also, e.g., [157, 158]). We use the code RAYTRIX [163] which follows the standard multiple lens plane algorithm. In the standard multiple lens plane algorithm, the distance between observer and source galaxies is divided into several intervals. In our case, as shown in Fig. G.1, we adopt a fixed interval whose value is the same as simulation box L on a side. Particle positions are projected onto two dimensional lens planes (xy , yz , zx planes) every L . Using the Triangular-Shaped Cloud method [164], we assign the particles onto N_g^2 grids in lens planes, then compute the projected density contrast at each plane. We use $N_g^2 = 2048^2$ throughout this paper. The two-dimensional gravitational potential is solved via the Poisson equation using a Fast Fourier Transform. Finally, two dimensional

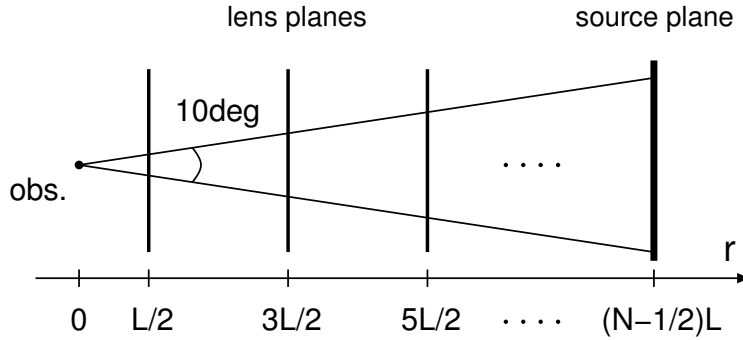


Figure G.1: A schematic picture of our ray-tracing simulation. The horizontal axis is the comoving distance r from the observer. The vertical thick lines denote the positions of the lens planes and the source plane, which are located at $r = (i - 1/2) \times L$ with $i = 1, 2, \dots, N$. Here, we set $N = 20$. We have multiple lens planes but use the flat-sky approximation. Light rays are emitted from the observer and are deflected at the lens planes before reaching the source plane. The field of view is $10 \times 10 \text{ deg}^2$.

sky maps of the convergence, shear, and angular positions of light rays are obtained by solving the evolution equation of Jacobian matrix along the light-ray path which is obtained by solving the multiple lens equation. At high redshifts ($z > 12$), the density fluctuations are very small and give only $< 10\%$ contribution to the angular power spectrum of the lensing potential at the multipole $\ell = 100 - 1000$ (see [98]). Hence, at high redshifts ($z > 12$) we do not include the density fluctuations in our calculation. We solve the multiple lens equation up to $z = 12$ and further redshifts the light rays are assumed to propagate in straight lines.

We prepare 20 realizations by randomly choosing the projecting direction and shifting the two dimensional positions. In each realization, we emit 1024^2 light-rays in the field-of-view $10 \times 10 \text{ deg}^2$. Then, the angular resolution is $10\text{deg}/1024 \simeq 0.6'$.

In order to check the accuracy of our ray-tracing simulation, we calculate the power spectrum of scalar lensing potential and compare it with the theoretical model. Fig. G.2 shows the power spectrum, $\ell^4 C_\ell^{\phi\phi} / 2\pi$, as a function of multipole ℓ at the last scattering surface ($z = 1090$). The dots with error bars are the simulation results calculated from the 20 realizations of $10 \times 10 \text{ deg}^2$ convergence maps. The black curve is the theoretical prediction in which the power spectrum of scalar lensing potential is given by the projected (three-dimensional) matter power spectrum weighted with the radial lensing kernel along the line-of-sight (e.g., [101]). Here, we use the halo-fit model [109] to calculate the non-linear power spectrum. As clearly seen in the figure, our simulation results agree with the theoretical model very well.

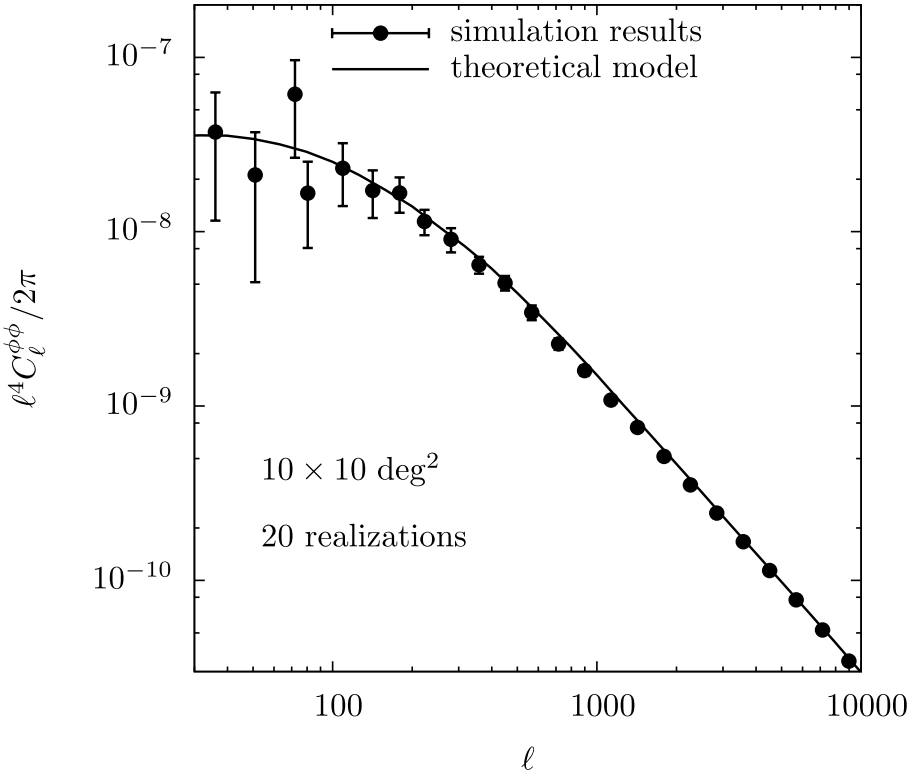


Figure G.2: The power spectrum of the scalar lensing potential at the last scattering surface ($z = 1090$). The dots with error bars are our ray-tracing simulation results calculated from the 20 realizations of $10 \times 10 \text{ deg}^2$ convergence maps. The black curve is the theoretical prediction.

G.3 Lensed CMB Temperature Map

In this subsection, we introduce our procedure for making lensed CMB temperature maps. We prepare these maps as follows:

1. We obtain the power spectrum of the unlensed CMB temperature fluctuations using CAMB.
2. We make an unlensed temperature map on a square $\sqrt{4\pi}$ radian ($\simeq 203 \text{ deg}$) on a side assuming Gaussian fluctuations based on the unlensed power spectrum. The angular resolution of the temperature fluctuations is set to be $10 \text{ deg}/1024 \simeq 0.6'$. We prepare 20 such unlensed maps.
3. Finally, we calculate the deflection angle $d(\hat{n})$ at the angular position \hat{n} using the ray-tracing simulation for the 1024^2 light rays. Then, we obtain the lensed temperature map by shifting the positions $\hat{n} \rightarrow \hat{n} + d(\hat{n})$ on the unlensed map, according to Eq. (??). We have 20 lensed CMB temperature maps of $10 \times 10 \text{ deg}^2$ with 1024^2 grids.

We calculate the power spectrum from the 20 lensed CMB temperature maps, and the result is shown in Fig. G.3. The figure shows the angular power spectrum of lensed temperature fluctuations as a function of multipole ℓ . The dots

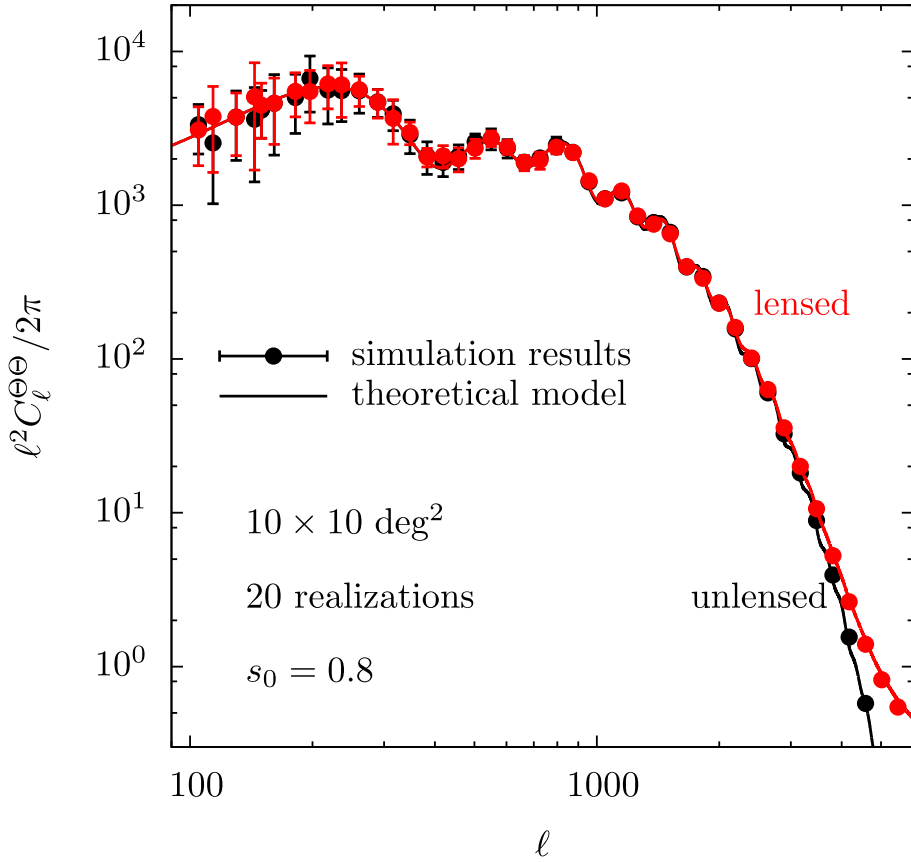


Figure G.3: The lensed CMB temperature power spectrum. The red symbols are the lensed power spectrum, while the black symbols are unlensed one. The dots with error bars are our simulation results calculated from the 20 realizations of $10 \times 10 \text{ deg}^2$ lensed maps. Here, we use $s_0 = 0.8$ in the apodization. The solid curves are the results from CAMB.

with error bars are the mean values and the dispersions calculated from the 20 realizations. We use $s_0 = 0.8$ in the apodization. The red symbols are the lensed power spectrum, while the black symbols are unlensed. The solid curves are the theoretical prediction calculated by CAMB. Our simulation results agree with the theoretical predication very well.

Bibliography

- [1] S. Dodelson, *Modern Cosmology*. 2003.
- [2] S. Weinberg, *Cosmology*. Oxford University Press, 2008.
- [3] C. Reichardt, P. Ade, J. Bock, J. R. Bond, J. Brevik, *et al.*, *High resolution cmb power spectrum from the complete acbar data set*, *Astrophys.J.* **694** (2009) 1200–1219, [[arXiv:0801.1491](#)].
- [4] S. Das, T. A. Marriage, P. A. Ade, P. Aguirre, M. Amir, *et al.*, *The atacama cosmology telescope: A measurement of the cosmic microwave background power spectrum at 148 and 218 ghz from the 2008 southern survey*, *Astrophys.J.* **729** (2011) 62, [[arXiv:1009.0847](#)].
- [5] R. Keisler, C. Reichardt, K. Aird, B. Benson, L. Bleem, *et al.*, *A measurement of the damping tail of the cosmic microwave background power spectrum with the south pole telescope*, *Astrophys.J.* **743** (2011) 28, [[arXiv:1105.3182](#)].
- [6] M. Zaldarriaga and U. Seljak, *Reconstructing projected matter density from cosmic microwave background*, *Phys. Rev. D* **59** (1999) 123507, [[astro-ph/9810257](#)].
- [7] U. Seljak and M. Zaldarriaga, *Measuring dark matter power spectrum from cosmic microwave background*, *Phys. Rev. Lett.* **82** (1999) 2636–2639, [[astro-ph/9810092](#)].
- [8] W. Hu and T. Okamoto, *Mass reconstruction with cmb polarization*, *Astrophys. J.* **574** (2002) 566–574, [[astro-ph/0111606](#)].
- [9] T. Okamoto and W. Hu, *Cmb lensing reconstruction on the full sky*, *Phys. Rev. D* **67** (2003) 083002, [[astro-ph/0301031](#)].
- [10] C. M. Hirata and U. Seljak, *Reconstruction of lensing from the cosmic microwave background polarization*, *Phys. Rev. D* **68** (2003) 083002, [[astro-ph/0306354](#)].
- [11] K. M. Smith, O. Zahn, and O. Dore, *Detection of gravitational lensing in the cosmic microwave background*, *Phys. Rev. D* **76** (2007) 043510, [[arXiv:0705.3980](#)].
- [12] C. M. Hirata, S. Ho, N. Padmanabhan, U. Seljak, and N. A. Bahcall, *Correlation of cmb with large-scale structure: Ii. weak lensing*, *Phys. Rev. D* **78** (2008) 043520, [[arXiv:0801.0644](#)].
- [13] B. D. Sherwin, S. Das, A. Hajian, G. Addison, J. R. Bond, *et al.*, *The atacama cosmology telescope: Cross-correlation of cmb lensing and quasars*, [arXiv:1207.4543](#).
- [14] L. Bleem, A. van Engelen, G. Holder, K. Aird, R. Armstrong, *et al.*, *A measurement of the correlation of galaxy surveys with cmb lensing convergence maps from the south pole telescope*, [arXiv:1203.4808](#).
- [15] S. Das *et al.*, *Detection of the power spectrum of cosmic microwave background lensing by the atacama cosmology telescope*, *Phys. Rev. Lett.* **107** (2011) 021301, [[arXiv:1103.2124](#)].

- [16] A. van Engelen, R. Keisler, O. Zahn, K. Aird, B. Benson, *et al.*, *A measurement of gravitational lensing of the microwave background using south pole telescope data*, arXiv:1202.0546.
- [17] **Planck** Collaboration, *The scientific programme*, astro-ph/0604069.
- [18] J. Errard *et al.*, *The new generation cmb b-mode polarization experiment: Polarbear*, arXiv:1011.0763.
- [19] L. Bleem, M. Lueker, S. Padin, E. Shirokoff, and J. Vieira, *An overview of the sptpol experiment*, *Journal of Low Temperature Physics* (2012) 859–864.
- [20] M. D. Niemack *et al.*, *Actpol: A polarization-sensitive receiver for the atacama cosmology telescope*, arXiv:1006.5049.
- [21] K. M. Smith *et al.*, *Cmbpol mission concept study: Gravitational lensing*, arXiv:0811.3916.
- [22] L. van Waerbeke, Y. Mellier, T. Erben, J. Cuillandre, F. Bernardeau, *et al.*, *Detection of correlated galaxy ellipticities on cfht data: First evidence for gravitational lensing by large scale structures*, *Astron.Astrophys.* **358** (2000) 30–44, [astro-ph/0002500].
- [23] D. J. Bacon, A. R. Refregier, and R. S. Ellis, *Detection of weak gravitational lensing by large-scale structure*, *Mon.Not.Roy.Astron.Soc.* **318** (2000) 625, [astro-ph/0003008].
- [24] D. M. Wittman, J. A. Tyson, D. Kirkman, I. Dell’Antonio, and G. Bernstein, *Detection of weak gravitational lensing distortions of distant galaxies by cosmic dark matter at large scales*, *Nature* **405** (2000) 143–149, [astro-ph/0003014].
- [25] N. Kaiser, G. Wilson, and G. A. Luppino, *Large scale cosmic shear measurements*, astro-ph/0003338.
- [26] T. Schrabback, J. Hartlap, B. Joachimi, M. Kilbinger, P. Simon, *et al.*, *Evidence for the accelerated expansion of the universe from weak lensing tomography with cosmos*, *Astron.Astrophys.* **516** (2010) A63, [arXiv:0911.0053].
- [27] E. M. Huff, T. Eifler, C. M. Hirata, R. Mandelbaum, D. Schlegel, *et al.*, *Seeing in the dark. 2. cosmic shear in the sloan digital sky survey*, arXiv:1112.3143.
- [28] **SDSS Collaboration** Collaboration, H. Lin *et al.*, *The sdss coadd: Cosmic shear measurement*, arXiv:1111.6622.
- [29] M. J. Jee, J. A. Tyson, M. D. Schneider, D. Wittman, S. Schmidt, *et al.*, *Cosmic shear results from the deep lens survey - i: Joint constraints on omega_m and sigma_8 with a two-dimensional analysis*, arXiv:1210.2732.
- [30] T. Abbott *et al.*, *The dark energy survey*, .
- [31] **HSC Collaboration** Collaboration, *Hyper suprime-cam design review*, .
- [32] **LSST Collaboration** Collaboration, *Lsst science book, version 2.0*, .
- [33] A. Stebbins, *Weak lensing on the celestial sphere*, astro-ph/9609149.
- [34] A. Cooray, M. Kamionkowski, and R. R. Caldwell, *Cosmic shear of the microwave background: The curl diagnostic*, *Phys. Rev. D* **D71** (2005) 123527, [astro-ph/0503002].
- [35] T. Namikawa, D. Yamauchi, and A. Taruya, *Full-sky lensing reconstruction of gradient and curl modes from cmb maps*, *JCAP* **1201** (2012) 007, [arXiv:1110.1718].

- [36] M. Kamionkowski, A. Babul, C. M. Cress, and A. Refregier, *Theory and statistics of weak lensing from large scale mass inhomogeneities*, *Mon.Not.Roy.Astron.Soc.* **301** (1998) 1064, [[astro-ph/9712030](#)].
- [37] W. Hu, *Dark synergy: Gravitational lensing and the cmb*, *Phys. Rev. D* **65** (2002) 023003, [[astro-ph/0108090](#)].
- [38] A. Albrecht *et al.*, *Report of the dark energy task force*, [astro-ph/0609591](#).
- [39] S. Das and D. N. Spergel, *Measuring distance ratios with cmb-galaxy lensing cross-correlations*, *Phys. Rev. D* **79** (2009) 043509, [[arXiv:0810.3931](#)].
- [40] T. Namikawa, S. Saito, and A. Taruya, *Probing dark energy and neutrino mass from upcoming lensing experiments of cmb and galaxies*, *JCAP* **1012** (2010) 027, [[arXiv:1009.3204](#)].
- [41] K. N. Abazajian and S. Dodelson, *Neutrino mass and dark energy from weak lensing*, *Phys.Rev.Lett.* **91** (2003) 041301, [[astro-ph/0212216](#)].
- [42] S. Hannestad, H. Tu, and Y. Y. Y. Wong, *Measuring neutrino masses and dark energy with weak lensing tomography*, *JCAP* **0606** (2006) 025, [[astro-ph/0603019](#)].
- [43] J. Lesgourgues and S. Pastor, *Massive neutrinos and cosmology*, *Phys. Rept.* **429** (2006) 307–379, [[astro-ph/0603494](#)].
- [44] R. de Putter, O. Zahn, and E. V. Linder, *Cmb lensing constraints on neutrinos and dark energy*, *Phys. Rev. D* **79** (2009) 065033, [[arXiv:0901.0916](#)].
- [45] S. Dodelson, E. Rozo, and A. Stebbins, *Primordial gravity waves and weak lensing*, *Phys. Rev. Lett.* **91** (2003) 021301, [[astro-ph/0301177](#)].
- [46] C. Li and A. Cooray, *Weak lensing of the cosmic microwave background by foreground gravitational waves*, *Phys. Rev. D* **74** (2006) 023521, [[astro-ph/0604179](#)].
- [47] D. Sarkar, P. Serra, A. Cooray, K. Ichiki, and D. Baumann, *Cosmic shear from scalar-induced gravitational waves*, *Phys. Rev. D* **77** (2008) 103515, [[arXiv:0803.1490](#)].
- [48] K. W. Masui and U.-L. Pen, *Primordial gravity wave fossils and their use in testing inflation*, *Phys.Rev.Lett.* **105** (2010) 161302, [[arXiv:1006.4181](#)].
- [49] L. Book, M. Kamionkowski, and F. Schmidt, *Lensing of 21-cm fluctuations by primordial gravitational waves*, *Phys.Rev.Lett.* **108** (2012) 211301, [[arXiv:1112.0567](#)].
- [50] C. S. Carvalho and K. Moodley, *Real space estimator for the weak lensing convergence from the cmb*, *Phys. Rev. D* **81** (2010) 123010, [[arXiv:1005.4288](#)].
- [51] C. S. Carvalho and I. Tereno, *Real space cmb lensing reconstruction with point source masks*, *Phys. Rev. D* **84** (2011) 063001, [[arXiv:1103.2305](#)].
- [52] D. Hanson, A. Lewis, and A. Challinor, *Asymmetric beams and cmb statistical anisotropy*, *Phys. Rev. D* **81** (2010) 103003, [[arXiv:1003.0198](#)].
- [53] R. Catena and A. Notari, *Cosmological parameter estimation: impact of cmb aberration*, [arXiv:1210.2731](#).
- [54] M. Su, A. P. Yadav, M. McQuinn, J. Yoo, and M. Zaldarriaga, *An improved forecast of patchy reionization reconstruction with cmb*, [arXiv:1106.4313](#).

- [55] V. Gluscevic, M. Kamionkowski, and D. Hanson, *Patchy screening of the cosmic microwave background by inhomogeneous reionization*, arXiv:1210.5507.
- [56] C. Hikage, M. Takada, T. Hamana, and D. Spergel, *Shear power spectrum reconstruction using pseudo-spectrum method*, *Mon.Not.Roy.Astron.Soc.* **412** (2011) 65–74, [arXiv:1004.3542].
- [57] A. Heavens, A. Refregier, and C. Heymans, *Intrinsic correlation of galaxy shapes: Implications for weak lensing measurements*, *Mon.Not.Roy.Astron.Soc.* **319** (2000) 649, [astro-ph/0005269].
- [58] R. A. Croft and C. A. Metzler, *Weak lensing surveys and the intrinsic correlation of galaxy ellipticities*, *Astrophys.J.* **545** (2000) 561–571, [astro-ph/0005384].
- [59] R. G. Crittenden, P. Natarajan, U.-L. Pen, and T. Theuns, *Spin induced galaxy alignments and their implications for weak lensing measurements*, *Astrophys.J.* **559** (2001) 552–571, [astro-ph/0009052].
- [60] P. Catelan, M. Kamionkowski, and R. D. Blandford, *Intrinsic and extrinsic galaxy alignment*, *Mon.Not.Roy.Astron.Soc.* **320** (2001) L7–L13, [astro-ph/0005470].
- [61] C. M. Hirata and U. Seljak, *Intrinsic alignment-lensing interference as a contaminant of cosmic shear*, *Phys. Rev. D* **70** (2004) 063526, [astro-ph/0406275].
- [62] C. Heymans, L. Van Waerbeke, D. Bacon, J. Berge, G. Bernstein, et al., *The shear testing programme. 1. weak lensing analysis of simulated ground-based observations*, *Mon.Not.Roy.Astron.Soc.* **368** (2006) 1323–1339, [astro-ph/0506112].
- [63] N. Kaiser, G. Squires, and T. J. Broadhurst, *A method for weak lensing observations*, *Astrophys.J.* **449** (1995) 460–475, [astro-ph/9411005].
- [64] D. Huterer, M. Takada, G. Bernstein, and B. Jain, *Systematic errors in future weak lensing surveys: Requirements and prospects for self-calibration*, *Mon.Not.Roy.Astron.Soc.* **366** (2006) 101–114, [astro-ph/0506030].
- [65] B. Jain, A. Connolly, and M. Takada, *Color tomography*, *JCAP* **0703** (2007) 013, [astro-ph/0609338].
- [66] G. Bernstein and D. Huterer, *Catastrophic photometric redshift errors: weak lensing survey requirements*, arXiv:0902.2782.
- [67] A. J. Nishizawa, M. Takada, T. Hamana, and H. Furusawa, *A clipping method to mitigate the impact of catastrophic photometric redshift errors on weak lensing tomography*, arXiv:1002.2476.
- [68] M. Crocce and R. Scoccimarro, *Nonlinear evolution of baryon acoustic oscillations*, *Phys. Rev. D* **77** (2008) 023533, [arXiv:0704.2783].
- [69] T. Matsubara, *Resumming cosmological perturbations via the lagrangian picture: One-loop results in real space and in redshift space*, *Phys. Rev. D* **77** (2008) 063530, [arXiv:0711.2521].
- [70] M. Pietroni, *Flowing with time: a new approach to nonlinear cosmological perturbations*, *JCAP* **0810** (2008) 036, [arXiv:0806.0971].
- [71] T. Hiramatsu and A. Taruya, *Chasing the non-linear evolution of matter power spectrum with numerical resummation method: solution of closure equations*, *Phys. Rev. D* **79** (2009) 103526, [arXiv:0902.3772].
- [72] A. Taruya, T. Nishimichi, S. Saito, and T. Hiramatsu, *Non-linear evolution of baryon acoustic oscillations from improved perturbation theory in real and redshift spaces*, *Phys. Rev. D* **80** (2009) 123503, [arXiv:0906.0507].

- [73] E. Lawrence, K. Heitmann, M. White, D. Higdon, C. Wagner, *et al.*, *The coyote universe iii: Simulation suite and precision emulator for the nonlinear matter power spectrum*, *Astrophys.J.* **713** (2010) 1322–1331, [[arXiv:0912.4490](#)].
- [74] D. Yamauchi, T. Namikawa, and A. Taruya, *Weak lensing generated by vector perturbations and detectability of cosmic strings*, [arXiv:1205.2139](#).
- [75] T. Namikawa, D. Hanson, and R. Takahashi, *Bias-hardened cmb lensing*, [arXiv:1209.0091](#).
- [76] W. Hu and M. J. White, *Cmb anisotropies: Total angular momentum method*, *Phys. Rev. D* **56** (1997) 596–615, [[astro-ph/9702170](#)].
- [77] **WMAP Collaboration** Collaboration, E. Komatsu *et al.*, *Seven-year wilkinson microwave anisotropy probe (wmap) observations: Cosmological interpretation*, *Astrophys.J.Suppl.* **192** (2011) 18, [[arXiv:1001.4538](#)].
- [78] K. K. Wu, O. Lahav, and M. J. Rees, *The large-scale smoothness of the universe*, *Nature* **397** (1999) 225–230, [[astro-ph/9804062](#)].
- [79] W. Hu, *Cmb temperature and polarization anisotropy fundamentals*, *Annals Phys.* **303** (2003) 203–225, [[astro-ph/0210696](#)].
- [80] W. Hu, *Weak lensing of the cmb: A harmonic approach*, *Phys. Rev. D* **62** (2000) 043007, [[astro-ph/0001303](#)].
- [81] R. K. Sachs and A. M. Wolfe, *Perturbations of a cosmological model and angular variations of the microwave background*, *Astrophys. J.* **147** (jan, 1967) 73.
- [82] A. Lewis, A. Challinor, and A. Lasenby, *Efficient computation of cmb anisotropies in closed frw models*, *Astrophys. J.* **538** (2000) 473–476, [[astro-ph/9911177](#)].
- [83] C. J. A. P. Martins and E. P. S. Shellard, *Quantitative string evolution*, *Phys. Rev. D* **54** (1996) 2535–2556, [[hep-ph/9602271](#)].
- [84] C. J. A. P. Martins and E. P. S. Shellard, *Extending the velocity-dependent one-scale string evolution model*, *Phys. Rev. D* **65** (2002) 043514, [[hep-ph/0003298](#)].
- [85] A. Avgoustidis and E. P. S. Shellard, *Effect of reconnection probability on cosmic (super)string network density*, *Phys. Rev. D* **73** (2006) 041301, [[astro-ph/0512582](#)].
- [86] K. Takahashi *et al.*, *Non-gaussianity in cosmic microwave background temperature fluctuations from cosmic (super-)strings*, *JCAP* **0910** (2009) 003, [[arXiv:0811.4698](#)].
- [87] A. Vilenkin and E. P. S. Shellard, *Cosmic Strings and Other Topological Defects*. 2000.
- [88] G. R. Vincent, M. Hindmarsh, and M. Sakellariadou, *Correlations in cosmic string networks*, *Phys. Rev. D* **55** (1997) 573–581, [[astro-ph/9606137](#)].
- [89] A. Albrecht, R. A. Battye, and J. Robinson, *Detailed study of defect models for cosmic structure formation*, *Phys. Rev. D* **59** (1999) 023508, [[astro-ph/9711121](#)].
- [90] M. Hindmarsh, *Small scale microwave background fluctuations from cosmic strings*, *Astrophys.J.* **431** (1994) 534–542, [[astro-ph/9307040](#)].
- [91] J. Magueijo, A. Albrecht, D. Coulson, and P. Ferreira, *Doppler peaks from active perturbations*, *Phys.Rev.Lett.* **76** (1996) 2617–2620, [[astro-ph/9511042](#)].

- [92] D. Yamauchi, K. Takahashi, Y. Sendouda, C.-M. Yoo, and M. Sasaki, *Analytical model for cmb temperature angular power spectrum from cosmic (super-)strings*, *Phys. Rev. D* **82** (2010) 063518, [[arXiv:1006.0687](#)].
- [93] A. Kashlinsky, *Small-scale fluctuations in the microwave background radiation and multiple gravitational lensing*, *Astrophys.J.* **331** (1988) L1.
- [94] M. Sasaki, *Gravitational lens effect on anisotropies of the cosmic microwave background*, *Mon. Not. Roy. Astron. Soc.* **240** (1989) 415–420.
- [95] K. Tomita and K. Watanabe, *Gravitational lens effect on the cosmic background radiation\due to nonlinear inhomogeneities*, *Progress of Theoretical Physics* **82** (1989) 563–580.
- [96] T. Fukushige, J. Makino, and T. Ebisuzaki, *The effect of gravitational scattering on the anisotropy of the cosmic background radiation*, *Astrophys. J.* **436** (1994) L107–L110, [[arXiv:astro-ph/9409069](#)].
- [97] U. Seljak, *Gravitational lensing effect on cosmic microwave background anisotropies: A power spectrum approach*, *Astrophys.J.* **463** (1996) 1, [[astro-ph/9505109](#)].
- [98] A. Lewis and A. Challinor, *Weak gravitational lensing of the cmb*, *Phys. Rep.* **429** (2006) 1–65, [[astro-ph/0601594](#)].
- [99] D. Hanson, A. Challinor, and A. Lewis, *Weak lensing of the cmb*, *Gen. Rel. Grav.* **42** (2010) 2197–2218, [[arXiv:0911.0612](#)].
- [100] F. Bernardeau, C. Bonvin, and F. Vernizzi, *Full-sky lensing shear at second order*, *Phys. Rev. D* **81** (2010) 083002, [[arXiv:0911.2244](#)].
- [101] M. Bartelmann and P. Schneider, *Weak gravitational lensing*, *Phys. Rept.* **340** (2001) 291–472, [[astro-ph/9912508](#)].
- [102] A. Amara and A. Refregier, *Optimal surveys for weak lensing tomography*, *Mon. Not. Roy. Astron. Soc.* **381** (2007) 1018–1026, [[astro-ph/0610127](#)].
- [103] W. Hu and R. Scranton, *Measuring dark energy clustering with cmb-galaxy correlations*, *Phys. Rev. D* **70** (2004) 123002, [[astro-ph/0408456](#)].
- [104] S. Dodelson, C. Shapiro, and M. J. White, 1, *Reduced shear power spectrum*, *Phys. Rev. D* **73** (2006) 023009, [[astro-ph/0508296](#)].
- [105] C. Shapiro, *Biased dark energy constraints from neglecting reduced shear in weak lensing surveys*, *Astrophys. J.* **696** (2009) 775–784, [[arXiv:0812.0769](#)].
- [106] A. Cooray and W. Hu, *Second order corrections to weak lensing by large-scale structure*, *Astrophys. J.* **574** (2002) 19, [[astro-ph/0202411](#)].
- [107] A. R. Zentner, D. H. Rudd, and W. Hu, *Self calibration of tomographic weak lensing for the physics of baryons to constrain dark energy*, *Phys. Rev. D* **77** (2008) 043507, [[arXiv:0709.4029](#)].
- [108] H. Zhan and L. Knox, *Effect of hot baryons on the weak-lensing shear power spectrum*, *Astrophys. J.* **616** (2004) L75–L78, [[astro-ph/0409198](#)].
- [109] **The Virgo Consortium** Collaboration, R. E. Smith *et al.*, *Stable clustering, the halo model and nonlinear cosmological power spectra*, *Mon. Not. Roy. Astron. Soc.* **341** (2003) 1311, [[astro-ph/0207664](#)].

- [110] R. Takahashi, M. Sato, T. Nishimichi, A. Taruya, and M. Oguri, *Revising the halofit model for the nonlinear matter power spectrum*, arXiv:1208.2701.
- [111] M. Sasaki, *The magnitude - redshift relation in a perturbed friedmann universe*, Mon. Not. Roy. Astron. Soc. **228** (1987) 653–669.
- [112] S. A. B. T. Blandford, R.D. and J. Villumsen, *The distortion of distant galaxy images by large-scale structure*, Mon. Not. Roy. Astron. Soc. **251** (1991) 600.
- [113] S. Seitz, P. Schneider, and J. Ehlers, *Light propagation in arbitrary spacetimes and the gravitational lens approximation*, Classical and Quantum Gravity **11** (1994) 2345–2373, [arXiv:astro-ph/9403056].
- [114] N. Kaiser, *Weak lensing and cosmology*, Astrophys.J. **498** (1998) 26, [astro-ph/9610120].
- [115] R. M. Wald, *General relativity*. 1984.
- [116] R. Sachs, *Gravitational waves in general relativity. vi. the outgoing radiation condition*, Royal Society of London Proceedings Series A **264** (1961) 309–338.
- [117] P. Schneider, J. Ehlers, and E. E. Falco, *Gravitational Lenses*. 1992.
- [118] F. Schmidt and D. Jeong, *Cosmic rulers*, arXiv:1204.3625.
- [119] M. Tegmark, A. Taylor, and A. Heavens, *Karhunen-loeve eigenvalue problems in cosmology: how should we tackle large data sets?*, Astrophys. J. **480** (1997) 22, [astro-ph/9603021].
- [120] M. Takada and B. Jain, *The impact of non-gaussian errors on weak lensing surveys*, arXiv:0810.4170.
- [121] R. Takahashi *et al.*, *Non-gaussian error contribution to likelihood analysis of the matter power spectrum*, arXiv:0912.1381.
- [122] L. Perotto, J. Lesgourgues, S. Hannestad, H. Tu, and Y. Y. Y. Wong, *Probing cosmological parameters with the cmb: Forecasts from full monte carlo simulations*, JCAP **0610** (2006) 013, [astro-ph/0606227].
- [123] L. Knox, *Determination of inflationary observables by cosmic microwave background anisotropy experiments*, Phys. Rev. D **52** (1995) 4307–4318, [astro-ph/9504054].
- [124] L. Verde, H. Peiris, and R. Jimenez, *Optimizing cmb polarization experiments to constrain inflationary physics*, JCAP **0601** (2006) 019, [astro-ph/0506036].
- [125] T. Namikawa, T. Okamura, and A. Taruya, *Magnification effect on the detection of primordial non-gaussianity from photometric surveys*, Phys. Rev. D **83** (2011) 123514, [arXiv:1103.1118].
- [126] G. M. Bernstein and M. Jarvis, *Shapes and shears, stars and smears: Optimal measurements for weak lensing*, Astron. J. **123** (2002) 583–618, [astro-ph/0107431].
- [127] S. Saito, M. Takada, and A. Taruya, *Nonlinear power spectrum in the presence of massive neutrinos: perturbation theory approach, galaxy bias and parameter forecasts*, Phys. Rev. D **80** (2009) 083528, [arXiv:0907.2922].
- [128] J. Brandbyge and S. Hannestad, *Resolving cosmic neutrino structure: A hybrid neutrino n-body scheme*, JCAP **1001** (2010) 021, [arXiv:0908.1969].
- [129] S. Agarwal and H. A. Feldman, *The effect of massive neutrinos on the matter power spectrum*, Mon.Not.Roy.Astron.Soc. **410** (2011) 1647, [arXiv:1006.0689].

- [130] S. Hannestad, T. Haugbolle, and C. Schultz, *Neutrinos in non-linear structure formation - a simple sph approach*, *JCAP* **1202** (2012) 045, [[arXiv:1110.1257](#)].
- [131] D. Yamauchi *et al.*, *Skewness in cmb temperature fluctuations from curved cosmic (super-)strings*, *JCAP* **1005** (2010) 033, [[arXiv:1004.0600](#)].
- [132] D. Yamauchi, K. Takahashi, Y. Sendouda, and C.-M. Yoo, *Weak lensing of cmb by cosmic (super-)strings*, [arXiv:1110.0556](#).
- [133] N. Kaiser and A. Stebbins, *Microwave anisotropy due to cosmic strings*, *Nature* **310** (1984) 391–393.
- [134] J. R. Gott, *Gravitational lensing effects of vacuum strings - exact solutions*, *Astrophys. J.* **288** (1985) 422.
- [135] Y. Zeldovich and R. Sunyaev, *The interaction of matter and radiation in a hot-model universe*, *Astrophysics and Space Science* **4** (1969) 301.
- [136] M. Bucher, C. S. Carvalho, K. Moodley, and M. Remazeilles, *Cmb lensing reconstruction in real space*, *Phys. Rev. D* **85** (2012) 043016, [[arXiv:1004.3285](#)].
- [137] C. M. Hirata and U. Seljak, *Analyzing weak lensing of the cosmic microwave background using the likelihood function*, *Phys. Rev. D* **67** (2003) 043001, [[astro-ph/0209489](#)].
- [138] D. Hanson and A. Lewis, *Estimators for cmb statistical anisotropy*, *Phys. Rev. D* **80** (2009) 063004, [[arXiv:0908.0963](#)]. add missed ref. to Gordon et. al. 2005.
- [139] D. Hanson, *(private communication)*, .
- [140] A. van Engelen, *(private communication)*, .
- [141] M. H. Kesden, A. Cooray, and M. Kamionkowski, *Lensing reconstruction with cmb temperature and polarization*, *Phys. Rev. D* **67** (2003) 123507, [[astro-ph/0302536](#)].
- [142] W. Hu, *Angular trispectrum of the cmb*, *Phys. Rev. D* **64** (2001) 083005, [[astro-ph/0105117](#)].
- [143] D. Hanson, A. Challinor, G. Efstathiou, and P. Bielewicz, *Cmb temperature lensing power reconstruction*, *Phys. Rev. D* **83** (2011) 043005, [[arXiv:1008.4403](#)].
- [144] A. Lewis, A. Challinor, and D. Hanson, *The shape of the cmb lensing bispectrum*, *JCAP* **1103** (2011) 018, [[arXiv:1101.2234](#)].
- [145] L. Perotto, J. Bobin, S. Plaszczynski, J.-L. Starck, and A. Lavabre, *Reconstruction of the cmb lensing for planck*, *Astron. Astrophys.* **519** (september, 2010) A4, [[arXiv:0903.1308](#)].
- [146] S. Plaszczynski, A. Lavabre, L. Perotto, and J.-L. Starck, *An hybrid approach to cmb lensing reconstruction on all-sky intensity maps*, *Astron. Astrophys.* (2012) [[arXiv:1201.5779](#)].
- [147] C. Dvorkin and K. M. Smith, *Reconstructing patchy reionization from the cosmic microwave background*, *Phys. Rev. D* **79** (2009) 043003, [[arXiv:0812.1566](#)].
- [148] B. D. Sherwin and S. Das, *Cmb lensing - power without bias*, [arXiv:1011.4510](#).
- [149] D. Hanson, G. Rocha, and K. Gorski, *Lensing reconstruction from planck sky maps: inhomogeneous noise*, *Mon. Not. Roy. Astron. Soc.* **400** (2009) 2169–2173, [[arXiv:0907.1927](#)].
- [150] D. Regan, E. Shellard, and J. Fergusson, *General cmb and primordial trispectrum estimation*, *Phys. Rev. D* **82** (2010) 023520, [[arXiv:1004.2915](#)].

- [151] S. Das and P. Bode, *A large sky simulation of the gravitational lensing of the cosmic microwave background*, *Astrophys. J.* **682** (2008) 1, [[arXiv:0711.3793](#)].
- [152] J. Dunkley *et al.*, *The atacama cosmology telescope: Cosmological parameters from the 2008 power spectra*, [arXiv:1009.0866](#).
- [153] A. Amblard, C. Vale, and M. J. White, 1, *Weak lensing of the cmb by large-scale structure*, *New Astron.* **9** (2004) 687–704, [[astro-ph/0403075](#)].
- [154] A. Cooray and M. Kesden, *Weak lensing of the cmb: Extraction of lensing information from the trispectrum*, *New Astron.* **8** (2003) 231–253, [[astro-ph/0204068](#)].
- [155] W. Press, S. Teukolsky, W. Vetterling, and B. Flannery, *Numerical Recipes in Fortran 90*. 1986.
- [156] D. Varshalovich, A. Moskalev, and V. Kersonskii, *Quantum Theory of Angular Momentum*. 1989.
- [157] M. Sato, T. Hamana, R. Takahashi, M. Takada, N. Yoshida, *et al.*, *Simulations of wide-field weak lensing surveys i: Basic statistics and non-gaussian effects*, *Astrophys. J.* **701** (2009) 945–954, [[arXiv:0906.2237](#)].
- [158] R. Takahashi, M. Oguri, M. Sato, and T. Hamana, *Probability distribution functions of cosmological lensing: Convergence, shear, and magnification*, *Astrophys. J.* **742** (2011) 15, [[arXiv:1106.3823](#)].
- [159] V. Springel, N. Yoshida, and S. D. White, *Gadget: A code for collisionless and gasdynamical cosmological simulations*, *New Astron.* **6** (2001) 79, [[astro-ph/0003162](#)].
- [160] V. Springel, *The cosmological simulation code gadget-2*, *Mon. Not. Roy. Astron. Soc.* **364** (2005) 1105–1134, [[astro-ph/0505010](#)].
- [161] M. Crocce, S. Pueblas, and R. Scoccimarro, *Transients from initial conditions in cosmological simulations*, *Mon. Not. Roy. Astron. Soc.* **373** (2006) 369–381, [[astro-ph/0606505](#)].
- [162] T. Nishimichi, A. Shirata, A. Taruya, K. Yahata, S. Saito, *et al.*, *Modeling nonlinear evolution of baryon acoustic oscillations: Convergence regime of n-body simulations and analytic models*, *PASJ* **61** (2009) 321–332, [[arXiv:0810.0813](#)].
- [163] T. Hamana and Y. Mellier, *Numerical study of statistical properties of the lensing excursion angles*, *Mon. Not. Roy. Astron. Soc.* **327** (2001) 169, [[astro-ph/0101333](#)].
- [164] R. W. Hockney and J. Eastwood, *Computer simulation using particles*. 1988.